APPLICATIONS OF MICROCOMPUTERS IN INTERACTIVE IMAGE PROCESSING

A thesis

presented for the Degree

of

Doctor of Philosophy

in Electrical Engineering

in the

University of Canterbury

Christchurch, New Zealand

by

F.M. CADY B.S.E.E. (Penn. State), M.S.E.E. (Cal. Tech)

ABSTRACT

Interactive image processing systems are reviewed and a system incorporating a charge coupled device imaging array, a microprocessor computing element, and a real time image display is described. Applications are given, including the description of a system capable of collecting multispectral images for satellite imagery calibration.

A new technique, called *shift and add*, which allows nearly diffraction limited images to be formed of objects viewed through a randomly distorted, turbulent media is formulated. The successful simulation of the method in an optical laboratory is reported. Results are given which show that if the method is applied in large telescope, optical astronomical imaging, nearly diffraction limited images may be obtained through the earth's atmosphere. It is shown that this can be achieved even though the telescope may have severe aberrations and when using a much wider bandwidth than that used at present in stellar Speckle Interferometry.

ACKNOWLEDGEMENTS

I am deeply grateful to Professor R.H.T. Bates, my colleague and supervisor, for his help, encouragement and guidance during the course of the project. Professor Bates negotiated the initial contract for research into solid state sensors which led to the development of the University of Canterbury Image Processing System. The development of the image processing hardware has been a joint effort with Dr R.M. Hodgson. To him goes my gratitude for taking care of research contract reports and for helping make the decisions which led to our useful image processing system. Mr W.K. Kennedy, also, was especially active in this area during the early design phases. I acknowledge the immense contribution to the hardware and software design and construction made by post-graduate students A.J. Ireland, G.A. Duncan, J.K.N. Murphy, D. Pairman, M.A. Rodgers and C.B. Lake. Without their enthusiastic help the system would still be very primitive. I extend many thanks to the rest of my colleagues in the Electrical Engineering Department, especially to Mr W.K. Kennedy, for putting up with my recent dedication to this task to the detriment of some of my other duties.

This thesis is much better for the proof-reading and English corrections made by my wife Katie.

I also acknowledge that generous financial support for the project has been received from a number of

University of Canterbury research grants and from research contracts with the Department of Scientific and Industrial Development. The enthusiasm and support of Dr Peter Ellis and the staff of the Remote Sensing Section of D.S.I.R. was very helpful.

CONTENTS

Page

Page

GLOSSARY

α	Scaling factor in CLEAN.
γ	Transfer characteristic of film.
γ_E	Region of error in Feinup algorithm.
$\delta(\cdot)$	Dirac delta function.
$\Delta\lambda$	Bandwidth.
$\Delta\nu$	Range of frequencies in a finite bandwidth.
$\Delta(\cdot)$	Array of delta functions.
$\hat{\Delta}(\cdot)$	Estimate of $\Delta(\cdot)$
$\Delta_n(\cdot)$	Array of delta functions at the centres of the bright speckles in a speckle image.
$\overline{\Delta}_n(\cdot)$	Fourier transform of $\Delta_n(\cdot)$
ΔD_F	Change in density of film.
ΔL	Differences in path length.
$\overline{\Delta Q_o^2}$	Mean square fluctuation at the input of a detector.
$\overline{\Delta R^2}$	Mean square fluctuation at the output of a detector.
Δt	Coherence time.
ΔV	Uncertainty in input voltage.
ϵ	One-dimensional spatial frequency phase.
ζ, η	Cartesian coordinates in object plane.
θ	Angular separation.
$\overline{\lambda}$	Mean wavelength.
μJ	Microjoules.
μm	Micrometres.
ν	Frequency of light.
ρ	Loop gain in CLEAN.

Σ	Summation.
τ	Short exposure time interval.
ϕ_H	CCD horizontal clock waveform.
ϕ_p	CCD photogate clock waveform.
ϕ_v	CCD vertical clock waveform.
$\Phi(\omega)$	Phase of optical transfer function.
ψ	Multiplicative constant in Fienup algorithm.
ω	One-dimensional spatial frequency.
$a(\cdot)$	Point spread function of limited aperture.
a_n	Location of the brightest point in a one-dimensional speckle image.
$A(\cdot)$	Fourier transform of $a(\cdot)$.
A	Area of one pixel in CCD.
A/D	Analog-to-digital.
ASCII	American Standard Code for Information Interchange.
ATR	Analog transport register.
b	Number of bytes per data point.
$b(\cdot)$	Point spread function due to aberrations in a receptor.
$B(\cdot)$	Fourier transform of $b(\cdot)$.
c	Speed of light.
C	Celsius.
C_d	Contrast for dark targets.
C_l	Contrast for light targets.
C_m	Contrast as modulation.
C_n	Valid command in PIKKY.
C_r	Contrast ratio.
$C(\omega)$	Real part of the optical transfer function.

CCD	Charge Coupled Device.
CID	Charge Injection Device.
cm	Centimetre.
CP/M	Control Program Monitor floppy disk operating system.
CPU	Central processor unit.
CRT	Cathode ray tube.
CTF	Contrast transfer function.
D	Diameter of receptor.
D_F	Density of film.
D/A	Digital-to-analog.
DB	Dirty beam.
DM	Dirty map.
DMA	Direct memory access.
D.S.I.R.	Department of Scientific and Industrial Research.
DQE	Detective quantum efficiency.
E_F^2	Mean square error criteria in Fourier domain.
E_o^2	Mean square error criteria in object domain.
exp	Exponential.
$f(\cdot)$	True image resolved to the diffraction limit.
f_M	Maximum frequency.
$f_T(\cdot)$	Total diffraction limited object consisting of an extended object and an unresolvable object.
FADS	Fast Area Digitizing Scanner.
FDOS	Floppy Disk Operating System.
FFT	Fast Fourier Transform.
FT	Fourier Transform.
$\mathcal{F}$	Fourier transform operation.
g	Gain of a detector.

$g(\cdot)$	True diffraction limited image convolved with the average speckle.
$\hat{g}(\cdot)$	Estimate of $g(\cdot)$.
$G_m(\cdot)$	Members of an ensemble of random processes.
h	CCD horizontal clock period.
$h(\cdot)$	Point spread function.
$h_n(\cdot)$	Point spread function at the time of the nth speckle image.
$\hat{h}(\cdot)$	Point spread function of shift and add process.
H	CCD vertical clock period.
$H(\cdot)$	Fourier transform of $h(\cdot)$.
$\hat{H}(\cdot)$	Fourier transform of $\hat{h}(\cdot)$.
$i(\cdot)$	Intensity distribution in image plane.
$i_L(\cdot)$	Long time exposure image.
$i_n(\cdot)$	Nth speckle image.
$I_n(\cdot)$	Fourier transform of $i_n(\cdot)$.
I_o	Brightest point in a dirty map.
I/O	Input/Output.
$i_n i_n(\cdot)$	Autocorrelation of $i_n(\cdot)$.
j	$\sqrt{-1}$.
J	Joule.
k	Wave number.
K	Feedforward tape for recursive filter.
K bytes	1024 bytes.
kg	Kilogram.
$l(\cdot)$	Line spread function.
L	Feedback tap for recursive filter.
L_1	Maximum luminance.
L_2	Minimum luminance.

L_b	Background luminance.
L_c	Coherence length.
L_o	Average luminance.
L_t	Target luminance.
LSB	Least significant bit.
mV	Millivolts.
M_{in}	Input modulation.
M x M	Spatial filter size.
$M(\omega)$	Modulus of optical transfer function.
mHz	Megahertz.
MIS	Metal-insulator-semiconductor.
mm	Millimetre.
ms	Millisecond.
MTF	Modulation transfer function.
n	Number of bits in a digital word.
n_p	Number of photons.
N	Noise.
$\tilde{N}$	Noise plus the less bright speckles.
N x N	Size of an image.
nm	Nanometres.
ns	Nanoseconds.
$o(\cdot)$	Intensity distribution in object plane.
$O(\cdot)$	Fourier transform of $o(\cdot)$.
otf	Optical transfer function.
p_n	Parameter in PIKKY command.
$p(\cdot)$	Shift and add processed image.
$P(\cdot)$	Fourier transform of $p(\cdot)$.
P	Number of iterations to obtain a spatial filter.
PROM	Programmable read only memory.

psf	Point spread function.
psi	Point spread invariant.
$q(\cdot)$	Transmission function.
Q	Quanta.
QE	Quantum efficiency.
r	Number of bits in the exponent.
r_o	Average size of a seeing cell.
R	Mean output level of a detector.
R_I	Relative intensity ratio.
RAM	Random access memory.
RMS	Root-mean-square.
s	Number of bits in the mantissa.
S	Storage area in bytes.
S_E	Saturation exposure.
s_k	Intensity of kth speckle.
$S(\omega)$	Imaginary part of the optical transfer function.
SI	Speckle Interferometry.
sipsf	Spatially invariant point spread function.
SNR	Ratio of partial scale signal to noise.
t	Processing time.
T	Redistribution time of the atmosphere.
t_{AP}	Aperture time.
t_{cy}	Memory cycle time.
$T(\omega)$	Optical transfer function.
$\hat{u}$	Spatial frequency where A(u,v) has significant value.
$\check{u}$	Seeing limited frequency.
u,v	Spatial frequencies in the x,y directions.
U(x,y)	Complex field distribution at point x,y.

UCIPS	University of Canterbury Image Processing System.
UCSD	University of California at San Diego.
V	Volts.
V_M	Maximum voltage amplitude.
V_N	Noise voltage.
V_{RMS}	RMS value of noise voltage.
V_{SAT}	Saturated output voltage.
V_T	Total noise voltage.
VDSI	Visual Display Store Interrogator.
W	Watts.
x,y	Cartesian coordinates in image or observation plane.
z	Distance between aperture and observation plane.
$\overset{*}{\times}$	Correlation operation.
$\ominus$	Convolution operation.
(•)	One or two dimensional parameters.
<•>	Ensemble average.
<CR>	Carriage return keystroke.
<ESC>	Escape keystroke.
<ETX>	Control-C keystroke.

To Katie and Elizabeth

"When you take stuff from one writer, it's plagiarism; but when you take it from many writers, it's research."

Wilson Mizner

APPLICATIONS OF MICROCOMPUTERS IN INTERACTIVE IMAGE PROCESSING

Preface

Microprocessors and other large scale integrated circuit devices are having a profound effect on many fields of activity, including digital image processing. The latter is normally performed with expensive, large scale equipment but the recently developed solid state imaging array, combined with the microprocessor as a computing element, can lead to low cost but dramatically effective image processing equipment.

Any digital image processing system can be subdivided into three parts. These are:

(i) the digitization of the image,

(ii) the performance of an image processing calculation or transformation, and

(iii) the display of the processed image.

Rapid technological advances are occurring in each of these areas. Input transducers for image processing are now being fabricated as two dimensional arrays of sensors using integrated circuit technology. For example, a 400x400 element charge coupled device imaging array with a resolution of 20 line pairs per millimetre has been constructed (Smith 1976). Charge coupled devices have dynamic ranges of up to 1000:1, possess quantum efficiencies as high as 50% and, when operated at a low temperature, allow very faint images to be recorded.

The processing of images can be done with microprocessor computing elements. These large scale integrated circuits will soon have up to 100,000 transistors per chip (Capece 1978) and are rapidly increasing in computer power. Shepard (1977) has predicted that a thirty-two bit microprocessor will soon be available on a single chip. The processed image is usually displayed with conventional television techniques, often in colour, which is used either as an alternative method of distinguishing between gray levels (false colour) or as a means of presenting multispectral imagery (e.g. using data gathered by satellites).

In this thesis digital image processing is approached from the viewpoint of using simple image processing equipment in an interactive manner. Chapter 1 reviews interactive image processing systems, discussing the image chain from the original object, through the sensor, the digital processing stage, and finally to the display of the processed image. Interactive image processing requirements are considered. Chapter 2 illustrates a stand-alone microprocessor and charge coupled device (CCD) interactive image processing system that has been developed in our laboratory. Our approach to utilizing real-time image capture and microprocessor-based computing seems to differ significantly from what has been developed elsewhere. The equipment is simple and inexpensive (less than $10,000) but it has been remarkably effective in several areas. Its prime use has been in the development of a multispectral scanning system suitable for the calibration of data from

an earth resources sensing satellite (Landsat). The performance of the charge coupled device sensor used in the image processing system is discussed in detail in Chapter 3.

The image processing system described in Chapter 2 has been used to develop and evaluate image processing techniques which form a diffraction limited image of an object viewed through a randomly turbulent media. This problem is exemplified by the imaging of celestial objects with large earthbound telescopes. The image processing system is used to acquire images in real time from an optical laboratory simulation. A review of techniques which can form diffraction limited images in optical astronomy is presented in Chapter 4. Chapter 5 describes a method developed jointly with Prof. Bates which extends the processing techniques of Bates and Milner (1979) and allows images to be formed with nearly diffraction limited accuracy. Chapter 6 presents results that have been achieved when using this new process in astronomical imaging simulations. Chapter 7 concludes with a discussion of the implementation of the method in actual astronomical imaging. The author's contribution to this new imaging method has been in generating test simulations and exploring the limitations and characteristics of the methods described.

It is appropriate here to acknowledge the "student power" which has contributed so much to the imaging system

described in Chapter 2. As a full time member of the academic staff of the Electrical Engineering Department, University of Canterbury, part of my duties included the supervision of final year and postgraduate student projects. (Note that in American parlance a postgraduate student is a graduate student.) A list of these is given in Appendix G and specific acknowledgement is given in the text where appropriate. Postgraduate students Ireland (1977), Duncan (1978), Murphy (1979) and Pairman (1980) contributed much to the hardware design and construction of the system. My primary function during this stage of development was to serve as chief engineer and to help overall progress.

A number of papers describing the imaging system, its uses, and the new method developed for processing astronomical image data have been published or are in preparation. These include:

Cady, F.M. and Bates, R.H.T. "Speckle processing gives diffraction limited true images from severely aberrated instruments," Optics Letters. submitted for publication April 1980.

Bates, R.H.T. and Cady, F.M. "Towards true imaging by wideband speckle interferometry," Opt. Commun. Vol. 32, No. 3, 1980, pp. 365-369.

Cady, F.M., Hodgson, R.M., Ireland, A.J. and Duncan, G.A. "A CCD based image processing system," NZIE Proc. Tech. Groups, Vol. 4, No. 2E(ETG), 1979.

Cady, F.M., Pairman, D. and Hodgson, R.M. "PIKKY - A floppy disk based image processing system," presented at NELCON 79, Aug. 29-31, 1979, Christchurch, N.Z.

Hodgson, R.M., Cady, F.M. and Murphy, J.K.N. "The development of a multispectral scanner to be flown in a light aircraft," Proc. Landsat 79, 1st. Australasian Landsat Conference, May 22-25, 1979, Sydney, Australia.

Cady, F.M. and Hodgson, R.M. "A microprocessor based interactive image processing system," IEE Journal of Computers and Digital Techniques. submitted for publication January 1980.

Hodgson, R.M. and Cady, F.M. "Remote sensing from light aircraft using solid state arrays," Photogrammetric Engineering & Remote Sensing. submitted for publication January 1980.

Cady, F.M., Hodgson, R.M., Pairman, D., Rodgers, M. and Atkinson G.J. "Interactive image processing software for a microcomputer," in preparation for IEE Journal of Computers and Digital Techniques.

Cady, F.M., Bates, R.H.T. and Berzins, G. "Imaging through fluctuating distorting media. I Experimental techniques and image processing applications; II Theory of speckle interferometry and its extensions; III The shift and add procedure; IV Imaging with aberrated instruments and wide band light," in preparation.

CHAPTER 1

INTERACTIVE IMAGE PROCESSING SYSTEMS

1.0 INTRODUCTION

An interactive image processing system, as illustrated in Figure 1.1, consists of three major sub-systems. These are the image conversion system which converts the two dimensional image to an array of digital words, the digital processing section which performs some transformation of the picture data, and the image display system which presents the processed image for viewing by the operator of the image processing system.

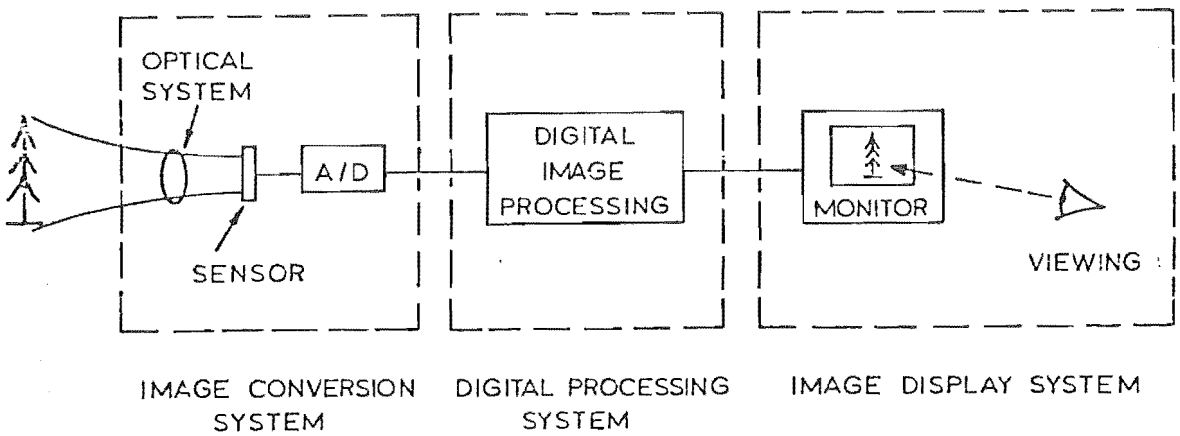

Figure 1.1 Design factors in image processing.

Image processing terminology tends to be used in slightly different ways by different authors. Green (1977) suggests that there are two broad categories of image processing. These are the *subjective enhancement* and the *quantitative enhancement* of images. Subjective enhancement is designed to re-display image data for viewing by a human observer. Particular qualities or features of the image are enhanced to allow optimal interpretation by the observer. These enhancement techniques are usually performed in an interactive manner to allow the viewer to find an optimum strategy. Quantitative enhancement, on the other hand, is based on some mathematical model and is not normally an interactive procedure. Quantitative enhancement techniques include geometrical transformations to correct for optical distortion in the picture recording process and the removal of defects caused by the input transducer (Bernstein 1976; Van Wie and Stein 1977). Other authors (Huang 1975; McDonnell 1975; Andrews and Hunt 1977) distinguish between the terms *restoration* and *enhancement*. Restoration refers to processing which is designed to reconstruct an image that has been degraded by some process. Enhancement is an attempt to improve the appearance of the image for human viewing. Restoration techniques include geometrical transformations and defect corrections mentioned above. They also encompass those techniques by which the degrading process, such as blurring, is represented by a mathematical model. An attempt is made to restore the degraded image by applying the inverse of the degrading process. The term *reconstruction* also appears in the literature (Peters 1973;

Mersereau 1974; Lewitt and Bates 1978). This term is used to describe the production of an image from data which is generated or gathered in a transform plane, e.g. the Fourier transform plane. Examples of this kind of image reconstruction are found in computer aided tomography (CAT) scanners (Peters 1973; Bates *et al.* 1975) and synthetic aperture imaging systems (Tomiyasu 1978).

A combination of these similar views and terms seems appropriate. It is convenient to consider techniques grouped according to their suitability for use in an interactive image processing situation. Some techniques may be used to restore an image interactively, particularly when the degradation process is not well understood and parameters must be varied to obtain the 'best' image. Other techniques may be used in a batch mode of operation. This is often the case when the results of a processing step, e.g. the geometrical rectification of non-linear scanning distortions, are well understood and must be applied before other processing is undertaken. Batch mode operations are also used when the processing is lengthy or requires considerable computational power as in a Fast Fourier Transform (FFT).

In general, one key factor determines whether or not an image processing procedure is used in an interactive manner. This factor is the total time between the start of the process and the time when the operator views the image on a display. The major part of this delay in interactive image processing is the time spent processing the image by the computer. In batch mode operations, the delay is

predominately the time spent by the program waiting in the job queue. Elapsed time, along with the amount of storage required, can be used to determine if image processing procedures can be performed interactively, and if the equipment upon which the processing will be carried out is suitable. These factors are considered in more detail in §1.3.

Interactive digital image processing is reviewed in this chapter. The concept of an imaging system is discussed and the limits of interactive image processing are defined. The component subsystems, including the image conversion system (§1.2), the digital image processing procedures (§1.3), and the display and hard copy of the processed image (§1.4) are also discussed.

1.1 INTERACTIVE DIGITAL IMAGE PROCESSING

Interactive digital image processing can be characterized by the following scenario. First, an image is presented for viewing. The image, which is sampled and digitized either during or before the processing, may have been pre-processed to remove geometrical distortions or input transducer effects before display. From a menu of alternatives, the operator then selects a process which seems appropriate to the particular problem. The process is invoked and the operator waits for the processed image to appear. The processed image is evaluated, usually by comparing it with the original, unprocessed version. If it seems necessary, further processing is undertaken, or else another processing strategy is tried on the original image.

For the purposes of the following discussion, an interactive digital image processing system is defined to include the following:

(i) A means of digitizing an image in the visible or near-infrared wavelength bands. This restriction is made because the following sections deal with sensors which are active in the visible to near-infrared wavelengths. Other types of sensors, such as those sensitive to thermal or x-radiation, are not discussed. The production of images by synthetic aperture techniques is also not discussed.

(ii) A digital processing element. This thesis is based on the use of microcomputers in image processing and specific examples of their use are given. A further limitation is imposed to limit the discussion to dedicated systems rather than to include time sharing systems.

(iii) A method of displaying an image. Various techniques are reviewed and it is shown that the display of images, and particularly the hard copy of images, is an area in which technological advances need to be made.

1.1.1 Imaging Systems Analysis

There are many factors affecting the imaging process which must be considered in the design or the analysis of an imaging system. A convenient grouping of these factors is shown in Figure 1.1. In this case, three major blocks have been identified. These are:

(i) the image conversion system which converts the desired input image into a digital representation,

(ii) the processing applied to the input image information, and

(iii) the output or display of the resultant processed image.

A methodology for the analysis of the imaging problem in general is known as image chain analysis (Booth and Schroeder 1977). Figure 1.2 shows a number of the items which should be considered in analyzing the image chain. Each are components of the three major blocks identified above. The following sections deal with each of the three major blocks and analyze the components within the blocks.

1.2 IMAGE CONVERSION SYSTEM

The two-dimensional distribution of intensities over an object must be converted to a digital representation before it can be processed by a digital computer. The intensity of the image is detected by a sensor, or an array of sensors, to give an appropriate analog signal. This signal may either be an electrical signal or the exposure of a photographic film. The detection process requires that the two-dimensional distribution be spatially quantized into picture elements, or pixels. In addition to the spatial quantization, the intensity is also quantized when the analog signal produced by the detector(s) is converted to a digital value.

The image conversion system analysis must consider items 1-9 in Figure 1.2. The optics (5) and the detector (6)

	Item	Typical characterizing parameters
1	Scene	- Reflectivity as a function of wavelength - Emissivity as a function of wavelength - Object or feature size - Object or feature geometry
2	Illumination	- Intensity - Angle - Coherent or non-coherent - Spectral distribution - Specular or diffuse
3	Path	- Absorption as a function of wavelength - Scatter as a function of wavelength - Turbulence - Bandwidth - Other noise sources
4	Imaging conditions (to include original image, reproductions and final image or display)	- Image motion - Aspect angle - Distance
5	Optics (to include original sensing, digitizer and printer)	- Numerical aperture - Focal length - Spectral transmission - Aberrations - Modulation Transfer Function - Distortions
6	Detector (to include original image, reproductions and digitizer-film and solid state	- Quantum efficiency - Gamma - Modulation transfer function - Dynamic range - Spectral sensitivity - Noise characteristics - Geometrical fidelity
7	A/D Converter (electronic readout)	- Accuracy - Precision - Noise
8	Digitizer (film)	- Geometric accuracy
9	Quantizer	- Sensitivity - Accuracy - Precision - Noise characteristics - Dynamic range - Spot shape
10	Processor	- Algorithm - Precision
11	D/A Converter	- Accuracy - Precision - Noise
12	Printer (film)	- Geometrical fidelity - Spot shape - Light source characteristics - Modulator accuracy, precision and noise - Gamma correction
13	Photographic processing (film)	- Chemistry type - Condition of baths - Accuracy of process control
14	CRT display (electronic readout)	- Luminance range - Luminance constancy over format - Contrast ratio (large and small area) - Geometric fidelity over format - Spot size/line spacing - Color characteristics
15	Visual system	- Sensitivity - Acuity - Contrast response - Pattern recognition - Color response

Figure 1.2 Image chain. (From Booth and Schroeder 1977)

must be matched to the conditions established by the scene (1), illumination (2), path (3) and imaging conditions (4). For example, in remote sensing for land use classification, the reflectivity of the target vegetation in the near infrared band (800-1100 nanometers) is important in determining the health of the vegetation (Bauer 1976). Therefore the sensor chosen must be sensitive to radiation in this band. The detector is also dependent on the level of the illumination. In very low light level applications, such as in surveillance work or in astronomical imaging, the sensor must have high quantum efficiency. The type of optics used in the imaging system depends to a large extent on the physical attributes of the imaging situation. The aperture determines the intensity of illumination 'seen' by the detector and can be adjusted for differing conditions. The focal length determines the field of view and ground resolution of each pixel. Recently, a spy satellite was reported to have a camera with a six metre focal length lens which could resolve whether or not a person on the ground was wearing civilian or military clothes (Richardson 1978). In the Landsat III remote sensing satellite, a ground coverage of 79 metres square for each picture element is achieved (Bauer 1976). The remote sensing system described in §2.3.1 was required to have a field of view of 0.35^{o} so that when flying at an altitude of 6400 metres the ground coverage would be 30 metres square for each picture element. This system requires a 6.4 mm focal length lens.

The optical components of an imaging system set a limit on the image quality also. All lenses have

aberrations and distortions which produce geometrical defects in the image (Thomas 1973; Jenkins and White 1976). Lenses also act as band pass filters. Normal glass lenses, for example, cut off the radiation in the infrared and ultraviolet but quartz lenses have an enhanced response in the infrared relative to glass lenses.

1.2.1 Image Formation

The term image has been used loosely in the previous sections to describe a two-dimensional radiant field which is detected by a sensor and converted to a digital representation by an analog-to-digital process. However, as Castleman (1979) points out, the dictionary definition of an image is "...a representation, likeness, or imitation of an object or thing..." Henceforth, the term image refers to the reproduction of the object's two-dimensional radiant field.

Following Dainty and Shaw (§6.2, 1974) the formation of an image can be represented as in Figure 1.3.

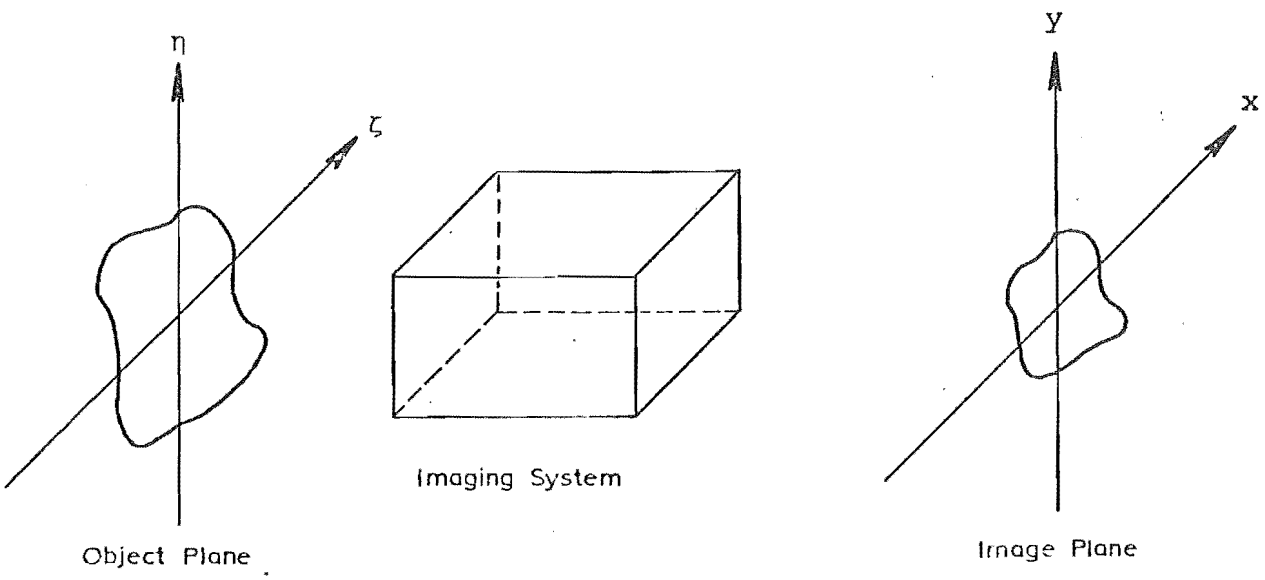

Figure 1.3 Image formation model.

For any general system, and for any input $f(\zeta,\eta)$, the output $g(x,y)$ is

$$g(x,y) = S\{f(\zeta,\eta)\}, \tag{1.2-1}$$

where $S\{\cdot\}$ is an operator acting on the input to produce the output. When the system is linear, an assumption which is realistic for many practical systems, the principle of superposition holds. That is, for all inputs $f_1(\zeta,\eta)$ and $f_2(\zeta,\eta)$ and for all constants a and b,

$$S\{af_1(\zeta,\eta) + bf_2(\zeta,\eta)\} = a\, S\{f_1(\zeta,\eta)\} + b\, S\{f_2(\zeta,\eta)\}. \tag{1.2-2}$$

Using the shifting properties of a delta function, any input can be considered to be a linear combination of weighted and displaced delta functions,

$$f(\zeta,\eta) = \int_{-\infty}^{+\infty}\int f(\zeta_1,\eta_1)\ \delta(\zeta-\zeta_1)\ \delta(\eta-\eta_1)\,d\zeta_1 d\eta_1. \tag{1.2-3}$$

The output of the system is therefore,

$$g(x,y) = S\{\int_{-\infty}^{+\infty}\int f(\zeta_1,\eta_1)\,\delta(x-\zeta_1)\,\delta(y-\eta_1)\,d\zeta_1 d\eta_1\} \tag{1.2-4}$$

When $f(\zeta_1,\eta_1)$ is considered to be a weighting function applied to the delta functions, the linearity property shown in equation (1.2-2) can be applied to bring the operator S within the integral

$$g(x,y) = \int_{-\infty}^{+\infty}\int f(\zeta_1,\eta_1)\,S\{\delta(x-\zeta_1)\,\delta(y-\ _1)\}\,d\zeta_1 d\eta_1\ . \tag{1.2-5}$$

The response of the system at output coordinates (x,y) to a delta function at input coordinates (ζ_1,η_1) is defined as

$$h(x,y;\zeta_1,\eta_1) = S\ \{\delta(x-\zeta_1)\ \delta(y-y_1)\}. \tag{1.2-6}$$

The output of the system is then

$$g(x,y) = \int_{-\infty}^{+\infty}\int f(\zeta,\eta)h(x,y;\zeta,\eta)d\zeta d\eta, \qquad (1.2\text{-}7)$$

where the subscripts have been dropped.

The system response to a delta function, equation (1.2-6), is called the point spread function (psf). In general, a point in the object plane does not image to a point in the image plane. The imaging system 'spreads' the point according to the psf. If the psf has the same shape over the image, i.e. it depends only on the difference between the variables and not on each variable independently, it is a spatially invariant point spread function (sipsf). When this is the case,

$$h(x,y;\zeta,\eta) = h(x-\zeta,y-\eta), \qquad (1.2\text{-}8)$$

and

$$g(x,y) = \int_{-\infty}^{+\infty}\int f(\zeta,\eta)\ h(x-\zeta,y-\eta)d\zeta d\eta \qquad (1.2\text{-}9)$$

This is a convolution relationship and shows that the psf of the system must be spatially invariant for deconvolution image processing techniques to be effective.

An alternative term to describe the above condition is isoplanatism. The so called 'isoplanatic patch' is used in astronomical imaging to specify the viewing angle over which the psf is spatially invariant (see §4.1.1).

1.2.2 Image Characterization

The object of interest can be characterized by a number of attributes such as reflectivity and size. However, the physical image is a distribution of

measurable physical properties. An array of detectors measures an electromagnetic flux which, when integrated over time, gives the intensity distribution of the object. A number of attributes can be used to describe the physical measurements.

(a) Spectral characteristics. The radiation received at the detector may be reflected by the scene (reflectivity as a function of wavelength) or may be generated within the scene (emissivity as a function of wavelength). The spectral characteristics give the relative radiant intensity of the object as a function of wavelength.

(b) Intensity. The detectors measure the radiation from the spatial distribution of image intensities. The intensity of a point in the image results in a flux field at the light sensitive surface of the detector. The dimensions of intensities may be given in radiometric terms, watts/steradian, or in photometric terms, lumens/steradian (Spiro 1974).

(c) Contrast. A measure which relates the range of intensities over the scene is the contrast. Booth and Schroeder (1977) give several methods for calculating contrast.

Contrast as modulation:

$$C_m = \frac{|L_t - L_b|}{L_t + L_b} = \frac{L_1 - L_2}{L_1 + L_2} = \frac{(L_1 - L_2)/2}{L_0} \qquad (1.2\text{-}10)$$

Contrast for dark targets ($L_t < L_b$):

$$C_d = \frac{2\ C_m}{1 + C_m} \qquad (1.2\text{-}11)$$

Contrast for light targets ($L_t > L_b$):

$$C_l = \frac{2\ C_m}{1 - C_m} \tag{1.2-12}$$

Contrast ratio:

$$C_r = \frac{1 + C_m}{1 - C_m} \tag{1.2-13}$$

Delta density:

$$\Delta D = \log_{10} \frac{1 + C_m}{1 - C_m} \tag{1.2-14}$$

where L_t = target luminance

L_b = background luminance

L_1 = maximum luminance

L_2 = minimum luminance

L_0 = average luminance = $(L_1 + L_2)/2$

(d) Dynamic Range. The ratio of intensities of the brightest part to the dimmest part can be characterized by the dynamic range. Dynamic range is usually defined as a logarithmic expression,

$$\text{Dynamic range} = 10 \log_{10} \frac{L_1}{L_2} \tag{1.2-15}$$

where L_1 and L_2 are the maximum and minimum luminances in the scene.

(e) Spatial frequency content. The concept of spatial frequency has proved to be useful in characterizing images. The Fraunhofer (far field) diffraction pattern in an observation plane (x,y) from a complex source distribution

in an aperture plane (ζ,η) is given by a Fourier transform relationship (see Figure 1.4).

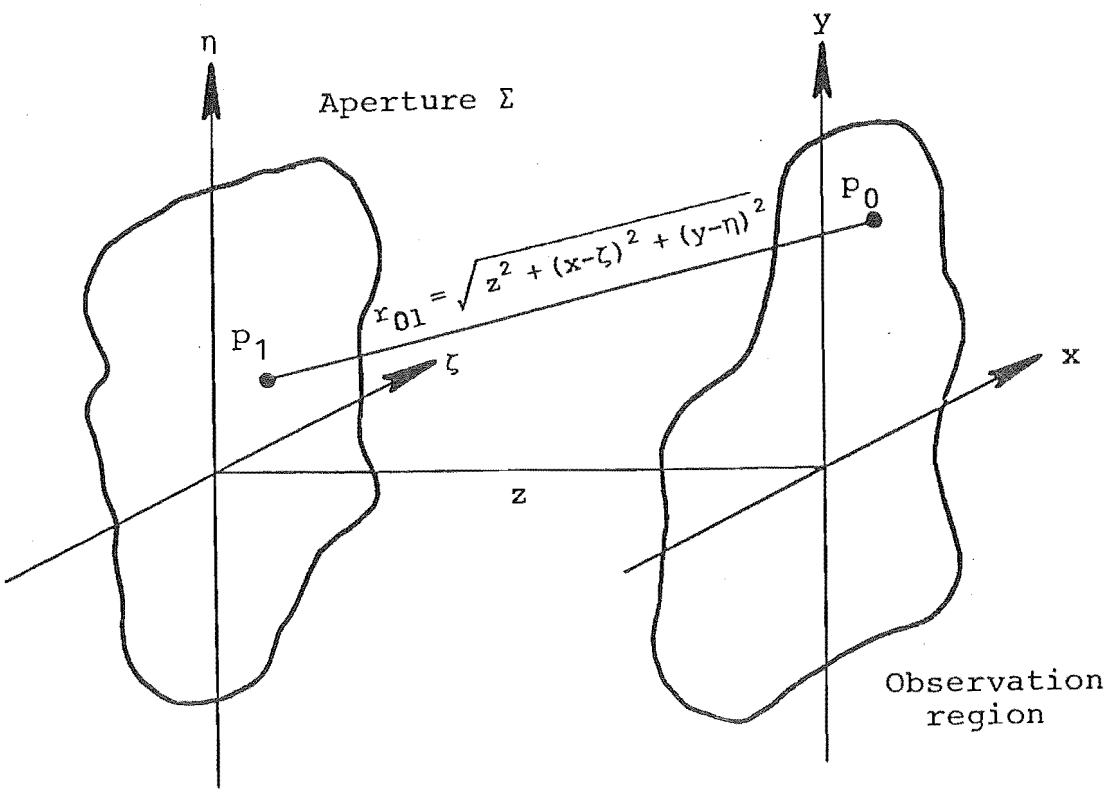

Figure 1.4 Diffraction geometry. (From Goodman 1968)

Following the development of Goodman (§4.1, 1968), the complex field distribution at a point (x,y) is given by the Huygens-Fresnel relationship:

$$U(x,y) = \frac{1}{j\lambda} \iint_{\Sigma} \frac{U(\zeta,\eta)}{r_{01}} \exp\,[j\,k\,r_{01}]\; d\zeta d\eta \qquad (1.2\text{-}15)$$

where λ is the mean wavelength,

$j = \sqrt{-1}$,

$k = \frac{2\pi}{\lambda}$,

Σ is the aperture, and

r_{01} is defined in Figure 1.4.

The integral can be written with infinite limits on the assumption that $U(\zeta,\eta)$ is zero outside the aperture Σ. It is further assumed that the distance between the aperture and the observation plane, z, is much greater than any linear dimension in either the aperture or the observation plane. These assumptions allow the substitution of z for r_{01} in the denominator of equation (1.2-15).

The Fresnel approximation for r_{01} uses the first two terms of a binomial expansion of the square root giving

$$r_{01} = z\sqrt{1 + \left(\frac{x-\zeta}{z}\right)^2 + \left(\frac{y-\eta}{z}\right)^2}$$

$$\simeq z\left[1 + \frac{1}{2}\left(\frac{x-\zeta}{z}\right)^2 + \frac{1}{2}\left(\frac{y-\eta}{z}\right)^2\right] \qquad (1.2\text{-}16)$$

The Fresnel approximation allows equation (1.2-15) to be written

$$U(x,y) = \frac{\exp[j\,k\,z]}{j\,\lambda\,z}\iint_{-\infty}^{\infty} U(\zeta,\eta)\exp\{\frac{j\,k}{2\,z}[(x-\zeta)^2 + (y-\eta)^2]\}\,d\zeta d\eta. \qquad (1.2\text{-}17)$$

Expanding the quadratic terms in the exponent yields

$$U(x,y) = \exp\,[j\,k\,z]\,\exp\left[\frac{j\,k}{2\,z}\,(x^2 + y^2)\right]\iint_{-\infty}^{\infty} U(\zeta,\eta)$$

$$\exp\left[\frac{j\,k}{2\,z}(-2\,x\,\zeta - 2\,y\,\eta + \zeta^2 + \eta^2)\right]\,d\zeta d\eta. \qquad (1.2\text{-}18)$$

The Fraunhofer assumption applies for the far field where

$$z >> \frac{k(\zeta^2 + \eta^2)_{max}}{2}. \qquad (1.2\text{-}19)$$

Therefore in the region of Fraunhofer diffraction

$$U(x,y) = \frac{\exp[j\,k\,z]}{j\,\lambda\,z} \exp\left[\frac{j\,k}{2\,z}\,(x^2+y^2)\right] \iint_{-\infty}^{\infty} U(\zeta,\eta)$$

$$\exp\left[-2\pi j\left(\frac{x}{\lambda z}\,\zeta + \frac{y}{\lambda z}\,\eta\right)\right] d\zeta\, d\eta. \qquad (1.2\text{-}20)$$

Except for the multiplicative factors preceding the integral which represent phase and magnitude scaling factors due to the geometry, the expression is a simple Fourier transform of the aperture distribution evaluated at frequencies

$$u = \frac{x}{\lambda z}\,, \qquad v = \frac{y}{\lambda z}\,. \qquad (1.2\text{-}21)$$

Therefore we can write

$$U(x,y) = K \iint_{-\infty}^{\infty} U(\zeta,\eta)\, \exp[-2\pi j(u\zeta + v\eta)]\, d\zeta\, d\eta \qquad (1.2\text{-}22)$$

where K is a complex constant.

As Shaw (1978) points out in his review of image evaluation methods, Luneberg (1944) and Duffieux (1946) showed the full advantages and implications of Fourier methods in optical image evaluation. A major advantage is that convolutions such as equation (1.2-9), can be transformed to become multiplications. This means that transfer functions for different components of the imaging system can be multiplied together to find the overall transfer function algebraically instead of solving multiple convolution integral equations.

1.2.3 Image Detectors

The conversion of an image into an analog signal is accomplished by a photoelectric or a photochemical mechanism.

Many textbooks explain the physics of the photoelectric effect (Holton and Roller 1958; Biberman and Nudelman 1971; Weidner and Sells 1975), and the characteristics of film (photochemistry) have been well described by many authors (Thompson 1966; Brown 1966; Thomas 1973; Dainty and Shaw 1974; Shaw 1978).

Solid state detectors are the prime interest here. Although photoelectric effect and photoemissive cathode devices are well understood and many devices are in use, e.g. television vidicon tubes (Chien and Snyder 1975), solid state sensors are becoming widely available and are suitable for many digital image processing applications. They can be made smaller and more robust because they do not require a vacuum or high accelerating voltages to operate. Fabricated with semiconductor technology, they can be mass produced and so are potentially less expensive than photocathode devices.

There are a number of important characteristics of solid state imaging devices.

(a) Quantum efficiency. In a photoelectric device, a photon is absorbed into the material of the device and an electron or a hole-electron pair is generated. These carriers then contribute to an electric current or charge which is proportional to the number of incident photons. Biberman and Nudelman (1971) define quantum efficiency as the ratio of the number of effective photons, i.e. those producing observable events, to the number of incident photons. This is a measure of the sensitivity of the device. Figure 1.5 plots the quantum efficiency as a

function of wavelength for several photoelectric devices.

(b) Sensitivity. The sensitivity of a solid state imaging array is defined as the minimum input flux which gives a detectable output. Sensitivity is therefore related to the noise performance and the responsivity or gain of the detector. Manufacturers such as Fairchild (1976) and Reticon (1977) usually give the responsivity, which gives the output signal (volts per microjoules per cm^2) and the saturation exposure (microjoules per cm^2). The spectral energy of the input flux must be known before a calculation can be made to find the sensitivity of the device (see §3.3.2).

(c) Spectal response. Figure 1.5 shows the quantum efficiency of a device as a function of wavelength of the incident radiation. This variability is known as the spectral responsivity.

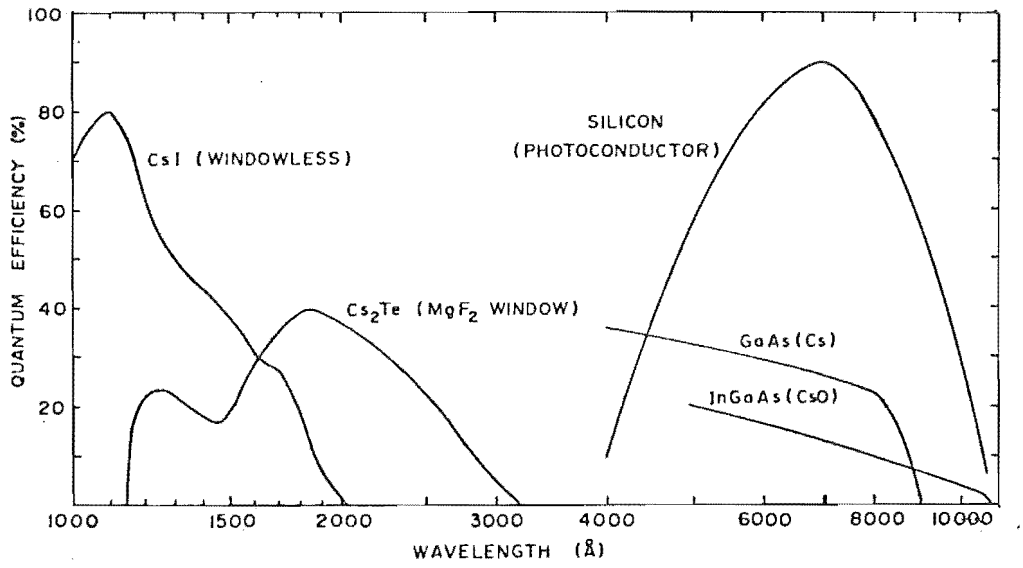

Figure 1.5 Quantum efficiency. (From Carruthers 1977)

(d) Noise. There are many noise mechanisms which operate in photoelectric devices. Among these are photon noise, shot noise and thermal noise (Dainty and Shaw 1974; Chien and Snyder 1975; Billingsley 1975). In addition, dark signal and fixed pattern noise act to obscure the desired signal. Taking into account all sources, the total noise can be considered to have two components,

$$V_T = V_{rms} + V_N \qquad (1.2\text{-}23)$$

where V_T is the total noise voltage, V_{rms} is the rms value and V_N is the fluctuating noise voltage.

(e) Dark signal. The dark signal is the component of the output signal which is not generated by incident radiation or by any readout process. The dark signal is measured in the absence of input radiation, hence its name. It is generally thermally generated and is a strong function of temperature, doubling every $7^{o}C$ (Amelio and Dyck 1975; Murphy 1977).

(f) Fixed pattern noise. Fixed pattern noise is relevant in array sensors and describes the fixed nature of defective picture elements (Amelio and Dyck 1975). In arrays such as the charge coupled device (see Chapter 3) elements can be defective by having too low or too high sensitivity. These are detected when the device is illuminated with a flat field and remain constant in space and relatively constant in time (Murphy 1979).

(g) Readout noise. In some array devices, the process of transferring charge from the storage sites generates noise. These noise mechanisms are usually

attributable to capacitive effects but also include the trapping of charge carriers in surface energy states for later release into other signal charge packets.

(h) Dynamic range. The dynamic range of a device is defined as the ratio of the output signal when an input causes saturation to the output signal with no input radiation. The dynamic range is expressed as a ratio or in decibles,

$$\text{Dynamic range} = 20 \log_{10} \frac{V_{SAT}}{V_{rms}} \qquad (1.2\text{-}24)$$

where V_{SAT} is the saturated output voltage and V_{rms} is the signal voltage output when no input is applied. It can be seen that the dynamic range is related to the average noise performance of the device.

(i) Signal-to-noise ratio. The noise performance of different devices is usually compared by the signal-to-noise ratio, which gives, for a *fixed illumination*, the signal available compared to all sources of *fluctuating* noise, V_N. The signal-to-noise ratio can be expressed in decibles,

$$\text{SNR} = 20 \log_{10} \frac{V_s}{V_N} \qquad (1.2\text{-}25)$$

where V_s and V_N are the signal and noise voltages.

(j) Detective quantum efficiency. The relative fluctuation in input and output signals is measured by the detective quantum efficiency (DQE). Consider (Shaw 1978) a detector which produces a mean output level R when exposed to an input of Q quanta. At this exposure level the gain of the detector is defined

$$g = \frac{dR}{dQ} \tag{1.2-26}$$

For any mean square fluctuation in the output $\overline{\Delta R^2}$, the mean square fluctuation at the input required to produce $\overline{\Delta R^2}$ is

$$\overline{\Delta Q_o}^2 = \frac{\overline{\Delta R^2}}{g^2} \quad . \tag{1.2-27}$$

DQE is defined as the ratio of actual mean square input fluctuation $\overline{\Delta Q^2}$ to the mean square output fluctuation referred to the input $\overline{\Delta Q_o}^2$,

$$DQE = \frac{\overline{\Delta Q^2}}{\overline{\Delta Q_o}^2} = \frac{g^2\ \overline{\Delta Q^2}}{\overline{\Delta R^2}} \quad . \tag{1.2-28}$$

If Poisson statistics are assumed for the input quanta,

$$\overline{\Delta Q^2} = Q \tag{1.2-29}$$

and

$$DQE = \frac{g^2\ Q}{\overline{\Delta R}^2} \quad . \tag{1.2-30}$$

For detectors where the signal-to-noise ratio is quantum limited, Dainty and Shaw (1974) show that DQE may be expressed as,

$$DQE = \frac{(\text{Output SNR})^2}{(\text{Input SNR})^2} \tag{1.2-31}$$

where (Output SNR) is the signal-to-noise ratio at the output of the detector and (Input SNR) is the signal-to-noise ratio at the input. It should be clear that DQE is always less than 1.0 and is usually expressed as a percent as shown in Figure 1.6.

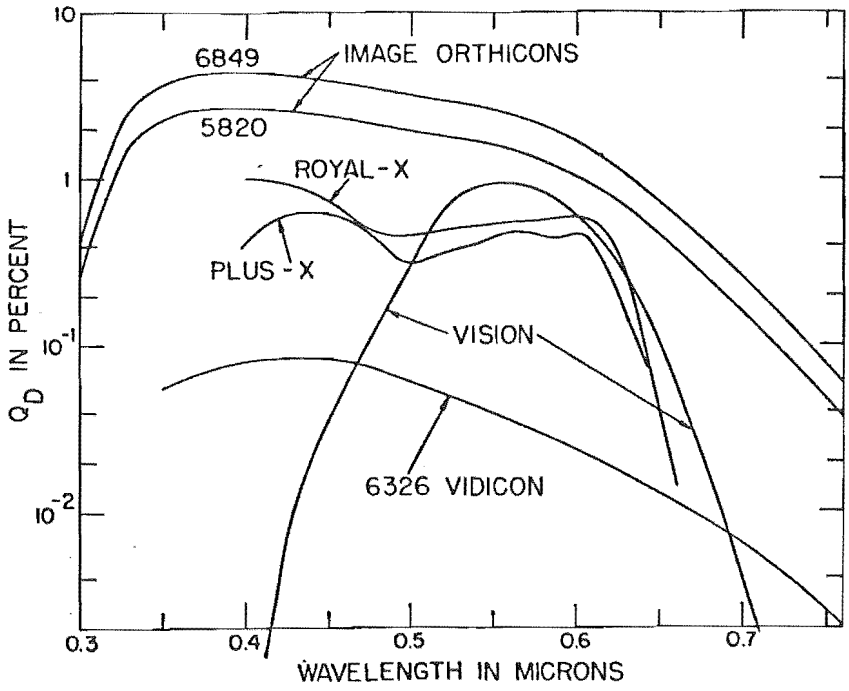

Figure 1.6 Detective quantum efficiency Q_D for various detectors. (From Jones 1957)

(k) Gamma. This term originally referred to the transfer characteristic of photographic film but is now used to define the characteristics of other transducers, e.g. CRT displays. In the photographic context, Figure 1.7 shows a curve of density as a function of log exposure. This curve is known as the H-D curve after Hurter and Driffield. Three regions are shown on the curve. The low density/ minimum exposure horizontal portion is called the gross fog level (Goodman, §7.2, 1968). The central portion shows the linear relationship between density and log exposure, and the maximum density/maximum exposure region is called the solarization region (Shore 1974). The slope of the middle portion of the curve is called the gamma, γ, and is defined

$$\gamma = \frac{\Delta D_F}{\Delta \log \text{exposure}} \qquad (1.2\text{-}32)$$

Gamma is a function of the type of film, exposure time, and the type and method of development.

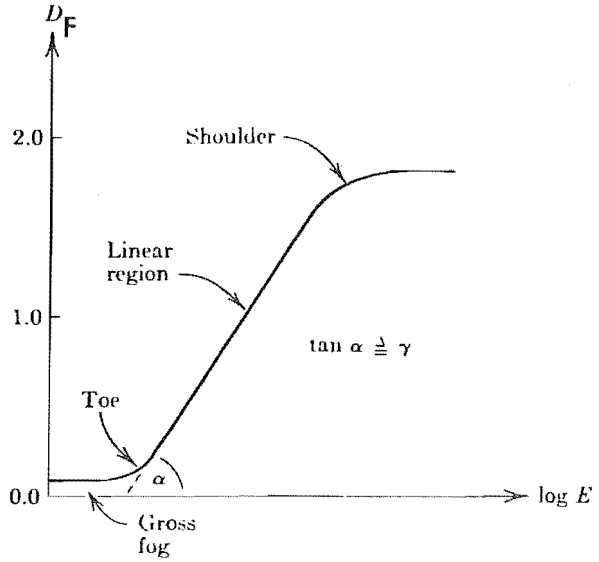

Figure 1.7 The Hurter-Driffield Curve. (From Goodman 1968)

(l) Linearity. Linearity is a term more often applied to photoelectric sensors than gamma. Linearity expresses the deviation away from a 1:1 relationship between the change in input radiation and the corresponding change in output signal. Manufacturers commonly define linearity as the maximum deviation from linear as a percentage of the full scale output value.

(m) Geometrical effects. The geometry of an imaging device specifies the accuracy with which the sensor records the spatial distribution of the two-dimensional image intensity. Geometrical effects include the fixed pattern noise described above, distortions and aberrations

introduced by the lens, and non-linear scanning mechanisms in scanning type sensors (Van Wie and Stein 1977).

(n) Modulation transfer function. The modulation transfer function (MTF) expresses the relative sensitivity of the device to spatial frequencies.

Following Dainty and Shaw (§6.2, 1974), consider a one-dimensional sinusoidal input distribution,

$$f(x) = a + b \cos(2\pi\omega x + \varepsilon) \qquad (1.2\text{-}33)$$

as shown in Figure 1.8 where ω is the one-dimensional spatial frequency and ε is a measure of phase.

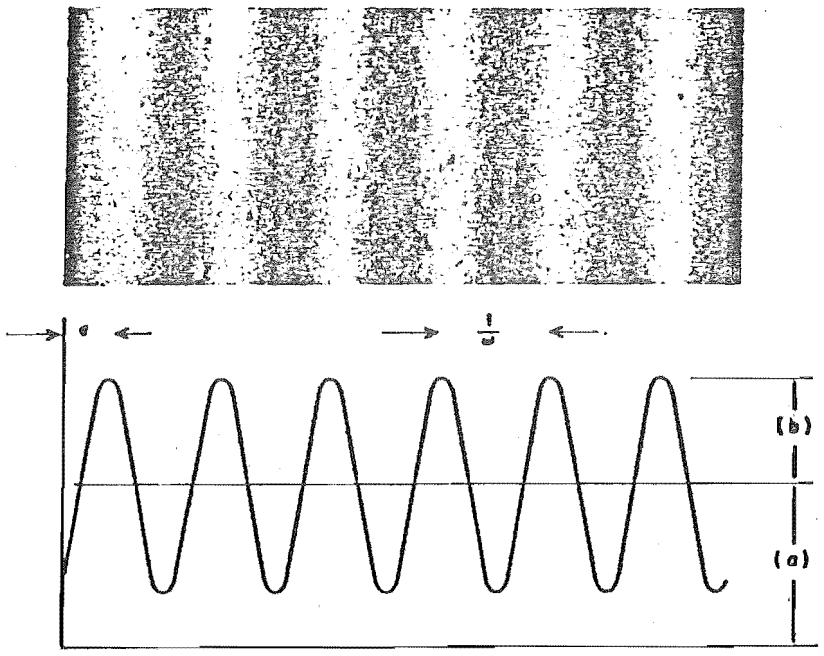

Figure 1.8 Sinusoidal input distribution. (From Dainty and Shaw 1974)

The input modulation is defined

$$M_{in} = \frac{f_{max} - f_{min}}{f_{max} + f_{min}} = \frac{b}{a} \quad . \qquad (1.2\text{-}34)$$

The convolution relationship of equation (1.2-9) for the output of an imaging system can be written

$$g(x,y) = \int_{-\infty}^{\infty}\int f(x-\zeta,\ y-\eta)\ h(\zeta,\eta)\ d\zeta\ d\eta$$

$$= \int_{-\infty}^{\infty}\int \{a + b\cos[2\pi\omega(x-\zeta) + \varepsilon]\}h(\zeta,\eta)d\zeta\ d\eta \qquad (1.2\text{-}35)$$

where $h(\zeta,\eta)$ is the spatially invariant psf. Integrating with respect to η gives

$$g(x) = \int_{-\infty}^{\infty} \{a + b\cos[2\pi\omega(x-\zeta) + \varepsilon]\}l(\zeta)d\zeta \qquad (1.2\text{-}36)$$

where $l(\zeta)$ is the line spread function. Using the expansion of cos(A-B) and normalizing the spread function such that its area is unity, equation (1.2-36) can be written as

$$g(x) = a + b\cos(2\pi\omega x + \varepsilon)\int_{-\infty}^{\infty} l(\zeta)\cos 2\pi\omega\zeta\ d\zeta$$

$$+ b\sin(2\pi\omega x + \varepsilon)\int_{-\infty}^{\infty} l(\zeta)\sin 2\pi\zeta\ d\zeta$$

$$= a + b\cos(2\pi\omega x + \varepsilon)\ C(\omega) + b\sin(2\pi\omega x + \varepsilon)S(\omega) \qquad (1.2\text{-}37)$$

where

$$C(\omega) - jS(\omega) = T(\omega) = \int_{-\infty}^{\infty} l(\zeta)\exp^{(-2\pi j\omega\zeta)}d\zeta \qquad (1.2\text{-}38)$$

The function $T(\omega)$ is called the optical transfer function (otf) and is the Fourier transform of the line spread function. The modulus $M(\omega)$ and the phase, $\Phi(\omega)$, of the otf are defined

$$M(\omega) = \sqrt{C^2(\omega) + S^2(\omega)}$$

$$\Phi(\omega) = \tan^{-1}\left[\frac{-S(\omega)}{C(\omega)}\right] \qquad (1.2\text{-}39)$$

and therefore

$$C(\omega) = M(\omega) \cos \Phi(\omega)$$

$$S(\omega) = -M(\omega) \sin \Phi(\omega) \qquad (1.2\text{-}40)$$

Equation (1.2-37) can be written

$$g(x) = a + M(\omega)\, b \cos(2\pi\omega x + \varepsilon + \phi(\omega)) \qquad (1.2\text{-}41)$$

Equation (1.2-41) shows that the output signal g(x) for a sinusoidal input is a sinusoid of the same frequency. The output modulation is defined

$$M_{out} = \frac{g_{max} - g_{min}}{g_{max} + g_{min}} = M(\omega)\ \frac{b}{a} \qquad (1.2\text{-}42)$$

Thus the ratio of output modulation to input modulation is equal to the modulus of the Fourier transform of the line spread function, $M(\omega)$.

In the more general case for two dimensions, the MTF of the system can be shown to be the modulus of the Fourier transform of the point spread function.

These attributes relate to the characterizing of image devices and are valid for the evaluation of any image sensor. Solid state imaging arrays, such as charge coupled devices, are being used in many new applications where images must be acquired, digitized and processed in real time. Chapter 3 considers the characteristics of one such device in terms of the attributes reviewed above.

1.2.4 Analog-to-digital Conversion

The imaging detectors convert radiation received from the source into an analog signal. The information must now be quantized and converted to a digital representation. If film is the conversion medium, the film transparency is scanned with a digitizer which measures the density of the film. This device is called a densitometer. See Shore (1974), Marcil (1974), and Dainty and Shaw (1974) for a review of densitometer techniques and instruments.

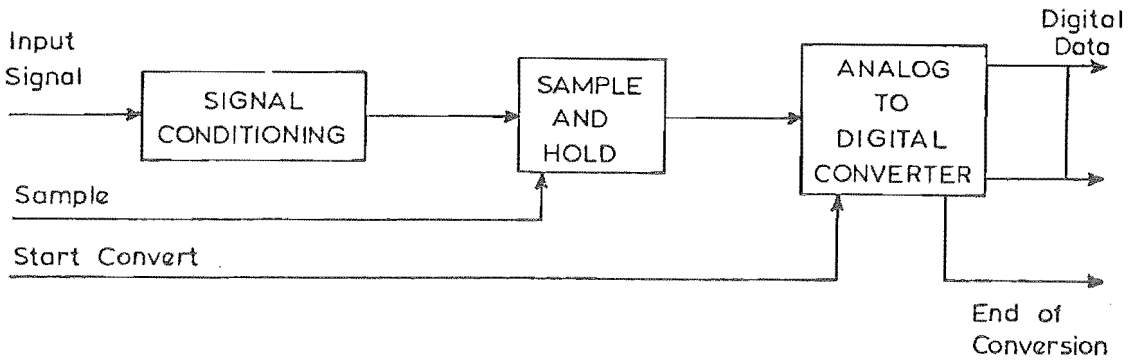

Figure 1.9 Analog-to-digital conversion.

The analog-to-digital conversion process used with photo-electrical devices is shown in Figure 1.9. The input signal from the sensor is first processed by a conditioning element. This provides buffering and isolation, amplifies the signal, and converts the polarity to that required by the sample-and-hold unit. The signal conditioning element also performs the important function of bandlimiting the input signal. If the signal is not bandlimited to one-half the

sampling frequency, aliasing occurs in the output data (Shannon 1963).

To specify an analog-to-digital converter for use in an imaging system, a number of operating parameters must be considered. Among these are:

(a) Accuracy. Absolute accuracy of a converter should not be confused with the specification of linearity or resolution. Absolute accuracy is affected by three types of errors. These are the inherent $\pm\frac{1}{2}$ least significant bit (LSB) digital error, analog errors due to circuit tolerances, and aperture error. Aperture error results from uncertainty in the input voltage during the conversion time. (See aperture time.) Relative accuracy is synonomous with linearity, and specifies the deviation in the output codes from a straight line drawn through zero and full scale. Accuracy specifications are given in the number of bits deviation, usually $\pm\frac{1}{2}$ least significant bit.

(b) Aperture time. This is the interval between the initiation of the conversion process, or a sample in the case of a sample-and-hold, and the output of the digital code. The aperture time determines the maximum error when sampling the analog voltage. For a signal of frequency f_M, with a maximum amplitude V_M, and with an aperture time of t_{AP}, the uncertainty in the input voltage ΔV can be shown to be

$$\Delta V = 2\pi V_M f_M t_{AP} . \qquad (1.2\text{-}41)$$

By choosing a n bit converter and setting the ratio $\Delta V/V_M$ equal to $1/2^n$, the aperture time required to sample a signal

with a maximum frequency component of f_M and with an error of 1 LSB is

$$t_{AP} = \frac{1}{2\pi f_M 2^n} \qquad (1.2\text{-}42)$$

(c) Conversion time. This is the total time required to complete a conversion, and generally establishes the upper frequency limit of a signal which can be converted without aliasing.

(d) Resolution. The smallest analog input voltage for which the converter will produce an output code is the resolution. For example, an eight bit converter has a resolution of 1 part in 256, or about 0.4% of the full scale value. Resolution and accuracy are often used interchangeably in data sheets, but in the strict sense, accuracy refers to the measured deviation from the straight line performance over the entire range of the operation of the converter and resolution refers to the smallest signal which can be digitized.

(e) Sample-and-hold. Often, the aperture time required to reduce the uncertainty in the input voltage to less than one least significant bit is far less than the conversion time required to satisfy the sampling rate from Shannon's theorem. When this is true, a sample-and-hold is used to sample the analog data and to hold it at a constant value for the analog-to-digital converter during the conversion time.

The required resolution and the upper frequency limit of the input signal are used to determine the specifications

of the analog-to-digital converter. For example, a resolution of 1 part in 1000 requires a 10 bit converter (n = 10). If the upper frequency component in the input signal is 1 MHz, the conversion time, given by Shannon's theorem, must be at most 0.5 microseconds and the aperture time must be 0.16 nanoseconds. In this case, a sample-and-hold with an aperture time of less than 0.16 ns and a 10 bit converter with a 2 MHz data rate would be specified.

In practice, A/D conversion systems have a number of other limitations. Departures from the ideal characteristics are defined by a number of secondary parameters including code skipping, gain accuracy, monotonicity, and slew rate. Useful references are Hnatek (1976) and Zuch (1979).

1.3 DIGITAL PROCESSING SYSTEM

The previous section describes the analysis of the input conversion system and considers the image attributes, the sensor characteristics, and the conversion from analog to digital information. This section now considers the digital image processing but is restricted to reviewing the *analysis* of image processing procedures in general. The reason for this is twofold. First, many excellent reviews of image processing procedures have been published (Stockham 1972; Andrews 1974; Huang 1975; McDonnell 1975; Andrews 1977; Andrews and Hunt 1977; Castleman 1979). Secondly, a digital image processing procedure can be analyzed to determine whether or not it is suitable for use in an interactive image processing manner. As discussed in §1.3.3,

this suitability can be expressed in terms of the time which an operator can wait for results and still be effective in processing images or solving problems. Therefore, we need not consider the many image processing algorithms in detail other than to specify their operating characteristics.

1.3.1 Image Processing Characterization

The analysis of the processing step in interactive image processing systems considers the effect of the processing on the image. The processor box (10) of Figure 1.2 indicates that the algorithm and the accuracy of the process must be considered.

(a) Algorithm. An important prerequisite for the development of an effective algorithm is a complete understanding of the problem to be solved. This helps ensure that the algorithm will perform as required and not produce unwanted results. Program design techniques such as top down design and structured programming (Ledgard 1975; McGowan and Kelly 1975) emphasize problem analysis and design before writing programs. Producing *efficient* algorithms, as Bentley (1979) points out, requires an insight into the way an algorithm works. Hopcroft (1974) and Weide (1977) survey methods of evaluating algorithms, and Knuth (1968, 1969, 1973) provides examples of many different algorithms. Unconventional approaches can produce highly efficient algorithm implementations. The 'brute force and ignorance' method can also be interminable. Bentley (1979) cites the example of a sorting problem requiring 138 hours of machine time for a naive comparison

algorithm and 4 seconds when a hashing technique is used.

In image processing applications, the use of look-up tables can significantly reduce the execution time of programs. However, one must balance the time required to calculate the index into the table, against the time to calculate the value itself. In assembler language programming, the use of in-line code (macros) instead of subroutine calls can speed up the operation. This also increases the size of the program but as Brooks (1975) points out, there is a memory space-time trade-off which is valid over a remarkably wide range. In general, for a given function, the larger the program, the faster it executes. An analysis of the accuracy with which calculations are made can sometimes lead to a significant increase in the execution speed. Integer arithmetic is faster than floating point arithmetic when performed in software, and so changing from a floating point mathematics package to an integer package will allow the program to operate faster.

(b) Accuracy. The computational accuracy affects not only the final representation of the image but the processing itself, because a requirement for high computational accuracy results in a requirement for a correspondingly large amount of storage for intermediate results. It also carries an attendant time penalty. As has been shown in §1.2.4, the dynamic range of the input signal determines the resolution of the analog-to-digital process and thus the minimum storage requirements for the image. The additional storage required by the processing

steps can be analyzed by considering how the image is represented in memory and what processing accuracy must be maintained. In general, the image is represented by a N_1 x N_2 array of numbers, where N_1 and N_2 are the dimensions in pixels of the image array. Each number is represented by n bits in the computer. All numbers are positive integers (because there are no negative intensities) and the number of bits, n, is determined by the resolution required by the specific imaging situation. Therefore, a N_1 x N_2 array of n bit digital words is required to represent the image in the computer.

Larger storage arrays are necessary when the digital representation must be kept as real or floating point numbers. Floating point numbers are generally required whenever processing involving the multiplication of numbers, such as in the Fourier transform or in correlation or convolution, is used. In this situation, each data point is represented by r + s + 2 bits, where r and s are the number of bits in the exponent and the mantissa respectively, and two extra bits are required for the sign of each. There are a number of floating point number schemes. One which we have found to be adequate in image processing uses six bits for the exponent and sixteen bits for the mantissa as shown in Figure 1.10.

A table of the accuracy (precision) and range of the fixed point (integer) and floating point (real) methods of representing numbers is given in Figure 1.11.

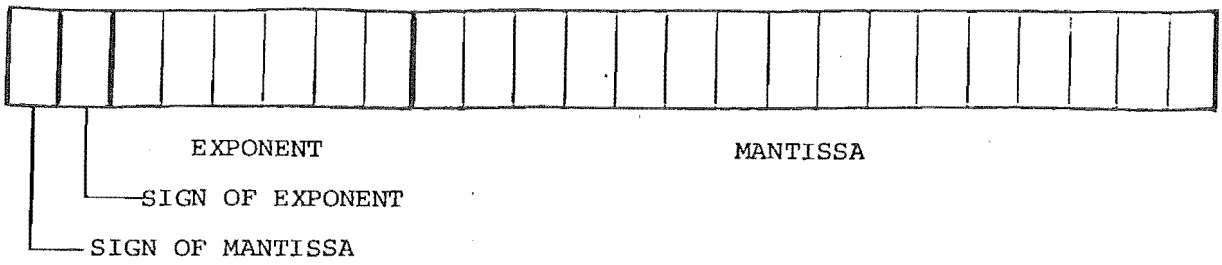

Figure 1.10 Floating point number representation.

Number representation	Number of bits	Accuracy	Range
Fixed point positive integer	n	$1/2^n$	$0 -- (2^n - 1)$
	8	1/256	0 -- 255
Fixed point two's complement	n	$1/2^n$	$-(2^{n-1}) -- (2^{n-1} - 1)$
	8	1/256	-128 -- +127
Floating point	exponent - r mantissa - s signs - 2	$1/2^s$	$\pm (0.5) \times 2^{-(2^r)}$ -- $(1 - (1/2^s)) \times 2^{2^{(r-1)}}$
	r - 6 s - 16	1/65,536	$\pm 0.5 \times 2^{-64}$ -- 0.999848×2^{63} = $\pm 5.42 \times 10^{-20}$ -- 9.2234517×10^{18}

Figure 1.11 Accuracy and range of fixed point and floating point number representations.

1.3.2 What is the Processing Time Limit for Interactive Image Processing?

An interactive processing procedure must be completed within some maximum elapsed time to allow effective user interaction (Shneiderman 1979). Comparisons of problem solving performances show the superiority of interactive (time-shared) systems over batch operations, especially where heuristic approaches to problem solving are used (Sackman 1968; Hansen 1976). The effect of system response time on the performance of users has been investigated and an attempt has been made in some cases to quantify the user's reaction, or 'feeling', toward the operation of the system when system response time has been altered (Goodman and Spence 1978). The man-machine interface has been investigated with the idea of improving certain parameters in the interface to improve the performance of the user. Walther and O'Neill (1974) and Miller (1977) conclude that various factors such as the output data rate and the flexibility of the command processor affect the performance of the user, and further careful research is needed to adequately define the man-machine interface.

The answer to the question posed above, however, requires an investigation of the psychology of problem solving. Miller (1968) summarizes these aspects of interactive computer problem solving, and a number of his findings which are relevant for interactive image processing are listed in Figure 1.12. Miller (1968) indicates that during a problem solving activity we become aware of response delays greater than 2 seconds and that delays

Topic	Response time	Comment - Image Processing Context
Human-human communication	2 sec	Silences greater than 4 seconds become embarrassing because a broken thread of communication is implied.
Response to control activity	< 0.1 sec	Feedback for key or switch movement.
Response to "System are you listening"	< 3 sec	Bootstrap load the system or sign-on in time-shared system.
Response to routine task request	< 2 sec	A simple processing routine such as sensor defect corrections.
Loading programs and data	15 sec - 1 minute	User spends time organizing notes.
Response to simple enquiry of listed information	2 sec	Displaying the processing menu.
Response to "System do you understand me?"	2-4 sec	If the user errors on input, he should be allowed to complete the entry before error message.
Response to complex inquiry in tabular form	4 sec	For complex tabular searches.
Response to program initiation	15 sec	Function of: - how long it took to write the program and to enter the data - number of additional runs or changes before selecting parameters - how anxious the user is to get back to other work.
Response to light pen entry of category for information	2 sec	Menu selection with light pen.
Graphic response from light pen	0.1 sec	Drawing lines on the display.

Figure 1.12 Typical response time in man-computer conversational transactions.

longer than this are inhibiting and become intolerable during creative activity. However, he also suggests that delays of up to 15 seconds are tolerable when the user recognizes that a complex activity is required of the computer. Furthermore, it seems likely that when dealing with complex problems such as image processing, an operator may need to think for periods greater than 2 seconds. Our own experience with image processing procedures described in §2.2 indicates that this is true. Therefore we propose that the result of an interactive image processing procedure should be available for viewing by the operator in less than fifteen seconds.

1.3.3 Analysis of Image Processing Time and Storage

The previous section has established that an image processing operator is capable of performing effective interactive processing tasks when the processing time is less than fifteen seconds. The processing time is defined as the elapsed time between initiating the process and viewing the final results, and includes the time required to load the program and data, execute the program, and transfer the data to the output display device. In this section the time required for loading picture data from bulk storage devices is analyzed. The processing times of several well known procedures are reviewed and storage times are given. The time to transfer a picture to a display device is considered. This typical sectionalization of a computer task into input-processing-output is done here because it is convenient to analyze the time for each section independently.

(a) Data input. The pictorial data is usually held in some type of bulk storage. In most image processing systems, the bulk storage medium is a disk unit. The fastest type of disk unit for retrieval of data is the fixed head disk which is commonly found on medium-to-large computer installations. By medium size, we mean those installations using at least a minicomputer.

Another popular type of disk storage, especially in smaller microcomputer based installations, is the floppy disk. Magnetic tape is also used in many instances. The storage of pictures on paper tape is almost unheard of except for very small images.

The storage requirement of the image may sometimes determine the type of bulk storage used. For example, with the large amount of data required for a single Landsat scene (30 megabytes), magnetic tape is invariably used.

A combination of storage devices may be used. When enough storage space is available on a relatively fast access device, such as a fixed head disk, part or the whole of the image may be transferred to the faster device from a slower device. This is particularly useful when several passes must be made through the data.

Figure 1.13 gives a comparative view of the storage capability and the speed of various types of storage devices.

(b) Processing time. The processing time of a computer is generally specified by the time the central processor unit takes to perform some representative instruction. In some cases, particularly in the competitive microcomputer field, the absolute shortest instruction is

Type of device	Storage capacity (bytes)	Average access time (ms)	Data transfer rate (Kbytes/s)*
Burroughs B6718 fixed head disk	20×10^6	23	345
Burroughs B6718 moving head disk pack	96×10^6	40	-
Digital Equipment Corp. RK05 disk pack	2.2×10^6	70	180
Digital Equipment Corp. RK07 disk pack	28×10^6	48	538
Winchester disk drive	11×10^6	50	648
IBM 3740 single density floppy disk	256,256	488	31.25
Double density floppy disk	512,512	488	62.5
SA 400 minifloppy	80,600	463	15.625
Magnetic tape, 9 track, 1600 bpi	38.4×10^6 per 1000'	**	72
Magnetic tape, 7 track, 800 bpi	11.5×10^6 per 1200'	**	96
MFE 450B digital cassette tape	366,000 per 300'	**	2-4
Digital cartridge tape	2.5×10^6	**	6
Paper tape	12,000 per 100'	**	70-1000 bytes/s (reading), 70-150 bytes/s (punching)
Cards	80 per card		1400 cpm (reading) 15 cpm (punching)

* 1 Kbytes = 1024 bytes.

** access time depends on the searching speed.

Figure 1.13 Storage capability and speed of storage devices.

specified. This tends to be misleading when attempting to evaluate image processing procedures. Most algorithms characteristically repeat some basic calculation or operation many times. For example, a Fast Fourier Transform (FFT) is characterized by the number of multiplications performed. Typically, these multiplications are performed using floating point arithmetic, and so an appropriate metric for the comparison of computers is the time taken to perform a floating point multiplication. Likewise, algorithms are measured by the number of real multiplications required. Figure 1.14, adapted from Hall (1972), Barnea and Silverman (1972), and Gaertner *et al.* (1976) shows a table of processing times for various image processing procedures. Processing time is in units of real multiplications, N is the image resolution, assuming an N x N image, and M x M is the size of filter used with the spatial filtering of Hall (1972) and Barnea and Silverman (1972).

(c) Processing storage. The storage for a single picture element in the computer depends on the accuracy that is required (§1.3.1). The processing steps usually require the entire image to be held in the memory of the computer, and therefore a N x N array of picture element values each with an accuracy of 1 part in 2^n requires n N^2 bits of storage. It is more common when specifying computer storage to give the storage in bytes, where a byte is equivalent to 8 bits. If b represents the number of bytes used to represent a single data point, then the storage required during execution of the various algorithms shown in Figure 1.14 can be given. The value of b is usually in

a) Two-dimensional Fourier Transform

$$t = 4 N^2 \log_2 N$$

b) Table Look-up Filters, Low Pass, High Pass and Bandpass Filters.

$$t = N^2 (4 + 8 \log_2 N)$$

c) Homomorphic Filters for Multiplicative Processes.

$$t = N^2 (12 + 8 \log_2 N)$$

d) Constrained Least-Squares Filter.

Iterative determination of $\hat{f}$, the estimated image.

$$t = N^2 (16 \log_2 N + 8.5) + p (4 \log_2 N + 6)$$

Iterative determination of $\hat{\gamma}$ which gives the estimated image.

$$t = N^2 (16 \log_2 N + 12.5) + p (4)$$

e) Wiener's Minimum Mean Square Error Filters.

$$t = N^2 (12 \log_2 N + 6)$$

f) Parametric Wiener Filters.

$$t = N^2 [(12 \log_2 N + 7.5) + p (4 \log_2 N + 6)]$$

g) Cole-Stockham's (Cole 1973) Homomorphic Filters.

$$t = N^2 (12 \log_2 + 6)$$

h) Aperiodic Convolution in the Spatial Domain.

$$t = N^2 M^2$$

i) Recursive Filter in the Spatial Domain.

$$t = (K^2 + L^2) N^2$$

t - Processing time expressed as the number of real multiplications to be performed.

N - Size of the image array (N x N).

p - Number of iterations to be performed to obtain the final filter. Observed to be between 3 and 12 (Gaertner 1976).

M - Size of convolution filter (M x M).

L - Feedback taps for recursive filter.

K - Feedforward taps for recursive filter.

Figure 1.14 Image processing times for representative procedures.

a) Two-dimensional Fourier Transforms.

$S = 2\ b\ N^2$ bytes

b) Table Look-up Filters.

$S = 3\ (2\ b\ N^2) = 6\ b\ N^2$ bytes

c) Homomorphic Filters for Multiplicative Processes.

$S = 4\ b\ N^2$ bytes

d) Constrained Least Squares Filters.

Iterative Determination of $\hat{f}$.

$S = 7.5\ b\ N$ bytes

Iterative determination of $\hat{\gamma}$.

$S = 6\ b\ N^2$ bytes

e) Wiener's Minimum Mean Square Error Filters.

$S = 5\ b\ N^2$ bytes

f) Parametric Wiener Filters.

$S = 7.5\ b\ N^2$

g) Cole-Stockham's Homomorphic Filters.

$S = 4\ b\ N^2$

h) Aperiodic Convolution in the Spatial Domain

$S = b\ N^2 + b\ M^2 + b\ (N + M)^2$

i) Recursive Filter in the Spatial Domain

$S = b\ N^2 + b\ (K + L)^2 + b\ (N + K + L)^2$

S - Storage area in bytes.
b - Number of bytes for each data point (1-4).
N - Size of image array (N x N).
M - Size of convolution filter (M x M).
L - Feedback taps for recursive filter.
K - Feedforward taps for recursive filter.

Figure 1.15 Image processing working storage requirements.

the range of 1, for a single byte integer to represent the picture element, to 4, for a floating point number representation.

Figure 1.15, again adapted from data given by Gaertner *et al.* (1976), shows the working storage requirements for various image processing algorithms.

(d) Data output. After the processing is finished, the data is output either to a display or back on to a bulk storage medium to await further processing. Output display devices are considered in §1.4, but the time requirements are considered here. The rate at which data may be transferred is the important parameter. In most systems this is limited by the speed at which the main storage memory can operate when transferring data to a television type video display. The basic unit in this operation is the memory cycle time which gives the time for a read or write cycle. Memory cycle times can be as low as 10 to 20 ns for very high speed memory, but a more typical time for semiconductor random access memory would be in the range of 100 to 250 ns. Call this time t_{cy}. The time to transfer data from the main processor memory to a display memory will be simply:

$$\text{Display transfer time} = N^2 \, t_{cy} \, .$$

This is the fastest time that is possible and is achievable only when using special direct memory access (DMA) techniques. For example, with a 256 x 256 display, and using memory with a cycle time of 250 ns, the display memory can be filled in 16 ms.

When direct memory access techniques are not used, the processor must transfer data from the working memory to the display memory. The time required to do this must include the processing time and may be 10 to 100 times the basic cycle time of the memory, depending on how many instructions have to be executed. In general, however, the total time required is much less than the 2 to 15 seconds limit determined in §1.3.2.

The transfer of data to bulk storage is governed by the rate at which data may be accepted by the device. Figure 1.13 gives data transfer rates for different types of storage devices. Data storage times can be longer than data retrieval times if the operating system checks that a storage operation has been performed correctly by re-reading the data. See Figure 2.10.

1.4 IMAGE DISPLAY

The display (11)-(15) of Figure 1.3, forms the last link in the image chain. The image must now be of an analog nature, and the necessary digital-to-analog conversion process is considered below. Display devices can be classed into two general categories. These are devices in which the display is of a transient nature, such as a video display with a continual refresh, and display devices which store the image for an extended time, such as a storage cathode ray tube. Hardcopy of the image is usually produced by a photographic process, but other techniques such as the production of images on thermo-sensitive or electrostatic paper are also used. However,

as Pucilowski and Schlam (1978) state, "...the perfect display for all applications not only does not exist, but is not on the horizon." It is appropriate to evaluate the parameters by which display devices and hard copy techniques may be compared, and to describe briefly some of these devices and techniques.

1.4.1 Digital-to-analog Conversion

The digital-to-analog (D/A) process is the reciprocal of the analog-to-digital process described in §1.2.4, and many of the same parameters of operation can be ascribed to the D/A process. There are, however, some additional characteristics of the D/A conversion process which should be mentioned.

(a) Accuracy. The absolute and relative accuracy and the linearity of digital-to-analog conversion is defined in the same way as for analog-to-digital conversion in §1.2.4.

(b) Resolution. Resolution is defined as the smallest input digital code for which an output analog level is produced.

(c) Settling time. The settling time is the time required for the converter output to settle within some specified error band. This error band may be defined as within $\pm\frac{1}{2}$ LSB or to within a specified percentage value of the final value. The converter used in the imaging system described in Chapter 2 has a settling time of 85 ns to within $\frac{1}{2}$ LSB.

(d) Glitches. A high speed D/A converter can have a very large spike at the output during the settling time. These 'glitches' are caused by asymmetrical switching times when the input bit patterns change state. For example, in logic circuits it is usual for switching times to be faster when switching from 1 to 0 than from 0 to 1. Therefore, when the input changes from 01111111 to 10000000 there is a momentary change to 00000000 between the starting and final values. This causes a glitch in the output which, even though of very short duration, can be visible on a display screen. Deglitching circuits (Hnatek 1976) can be used to reduce the effect of these asymmetrical switching transients.

1.4.2 Display Characteristics

The characteristics of the image have been described in §1.2.2 and the operating parameters of image detectors have been defined in §1.2.3. This section considers the parameters which describe the operation of display devices. In general, the display device should faithfully recreate the image, at least to the extent of recreating what the human viewer would perceive if the image processing chain were not present. The display exhibits characteristics such as dynamic range, contrast ratio, and luminance which relate to the image. In addition, a display has the operating characteristics of geometrical fidelity, flicker, resolution, and persistance which should be considered.

(a) Luminance. Luminance is the intensity of a surface measured in lamberts (Sowan 1968) or in lumens per steradian (Spiro 1974). Luminance is the brightness

perceived by the viewer, and decreases as the cosine of the angle of view from a perpendicular to the screen. Adequate luminance for a screen in a normally illuminated room is 25 to 50 millilamberts (Rouse 1975).

(b) Contrast ratio. As defined in §1.2.2, contrast ratio (C_r) expresses the relationship of the most, least, and average luminances in the scene. The contrast is an important parameter as it affects the ability of the human viewer to perceive spatial frequencies (Booth and Schroeder 1977, Gould 1968).

(c) Resolution. Resolution is a measure of the ability to recreate picture detail. Resolution may be stated in a number of ways, including the modulation transfer function, spot diameter, line width, or in spatial frequency lines per millimeter.

(d) Geometric fidelity. The fidelity with which the image is recreated on the display is dependent on the geometric fidelity of the display device. Factors which affect fidelity are spot distortion and non-linear scanning signals in raster scanning devices. Another source of distortion can be seen in storage displays. In this case, if a charge has been stored in one part of the display, the beam can be deflected by this charge when writing to another part of the screen.

(e) Flicker. Flicker is the sensation of image intermittence when the regeneration rate of the display is less than the critical fusion frequency. The critical fusion frequency is a function of the luminance, scanning

patterns, persistence of the phosphor, and ambient illumination levels (Rouse 1975).

(f) Persistence. When a cathode ray tube (CRT) display is used, the phospher material continues to radiate after the excitation is removed. The time of persistence is defined as the time between the removal of excitation and the time that the luminance has dropped to some fraction of its initial value.

1.4.3 Image Display Devices

There are few display devices commercially available which are suitable for interactive image processing work. An effective device must allow the operator to view the results of the processing step within the time limitations established in §1.3.2. Therefore, photographic reproduction techniques are eliminated. The television type refreshed display is one of the most popular devices used today. The ease with which full colour displays are generated contributes to this popularity, and many systems are offered with colour displays. New electronic devices, such as flat panel and electroluminescence displays, are being developed but do not generate gray scale images (Pucilowski and Schlam 1978). The direct view storage cathode ray tube (Priess 1978), commonly used in interactive graphics systems where a binary display is adequate, is sometimes used in imaging applications. A gray scale is generated using techniques similar to half-tone printing.

1.4.4 Hard Copy Techniques

The presently available methods for the generation of hard copy images are even less satisfactory than display methods. To date, most hard copy devices available are used in graphics systems where a binary (black and white) copy is produced. An inexpensive, fast, high resolution, hard copy device for gray scale images does not exist.

The most common techniques for producing hard copy of images use photographic methods. These produce images with better resolution and dynamic range than other methods, such as line printer overprinting. There are two techniques which use film as the hard copy medium. In the first, a computer controlled light beam is swept over a film plate. The intensity of the light beam is modulated by the computer to correspond to the intensity of the image. Commercial instruments, such as the Optronics C-4300 Colorwrite machine (McDonnell and Fowler 1979), produce high quality photographic films of digitized images. Colour reproductions are produced by successively writing to the film with three different colour beams. Positive transparencies or negatives for colour prints can be produced easily.

A similar film scanning method uses a CRT and photographic film. The film is placed in contact with the surface of the CRT, and a raster-scanned, z-modulated beam sweeps out the required image (Longshaw *et al.* 1976). This method is useful only for black and white images.

An alternative photographic method is to simply photograph the display monitor. This procedure means the photograph is limited to the same resolution and dynamic

range as the display device. Nevertheless, useful photographs can be produced, as demonstrated in Appendix C.

A method known as line printer overprinting can produce low resolution, low dynamic range images. A given intensity is produced at each pixel by successively over-printing with a sequence of selected characters. The useful dynamic range is generally limited to about 16:1, and the resolution is limited to the character spacing of the line printer. In general, this is not a satisfactory method.

1.5 CONCLUSION

This chapter has reviewed in detail the chain of procedures by which images are produced. The various links in the image chain have been described. The main aim has been to introduce terms and to define a regime of image processing which can be carried out interactively using relatively unsophisticated computing equipment. The total time required by a processing step allows the general division of image processing routines into those which can be performed interactively and those which may be better performed in a batch (or at least a walk-away-from-the-computer-and-do-something-else-for-awhile) mode. The next two chapters discuss in detail a complete microprocessor based interactive processing system, including its hardware and software. Some interactive image processing applications of the system are described.

CHAPTER 2

A MICROPROCESSOR BASED INTERACTIVE IMAGE PROCESSING SYSTEM

2.0 INTRODUCTION

In 1975 a project was started at the University of Canterbury to investigate the use of charge coupled device (CCD) imaging arrays in image processing systems. Our first use of the charge coupled device was in a system called the Fast Area Digitizing Scanner (FADS), reported by Ireland (1977). The FADS system incorporated an 'intelligent' block of memory using hardwired digital logic, and a charge coupled device installed in the focal plane of a 35 mm camera. A control system allowed an external computer, in this case the E.A.I. 590 Hybrid Computing System in the Electrical Engineering Department, University of Canterbury, to acquire data from the CCD camera. We soon realized that a microcomputer controlling the FADS memory, or an equivalent memory, would be more effective than the E.A.I. machine because it would allow a user to operate the imaging system independently without conflicting with other users of the Departmental system.

The microcomputer based system has become known as the University of Canterbury Image Processing System (UCIPS) and its first application was in the evaluation of the charge coupled device as an imaging array. The hardware was constructed so that the system was reasonably portable in order to test the premise that a microcomputer controlled

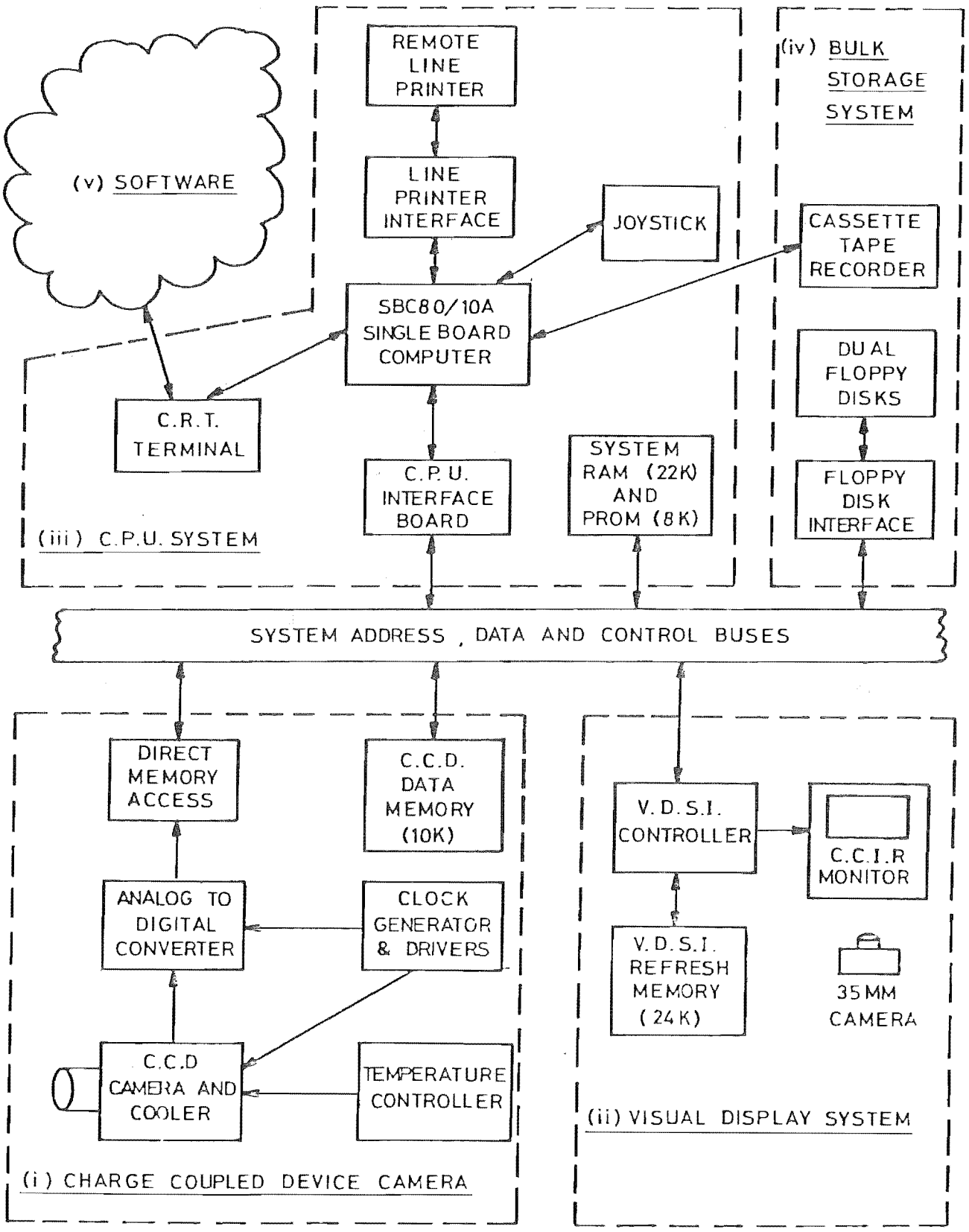

Figure 2.1 University of Canterbury Processing System (UCIPS).

solid state imaging system could be operated for remote sensing applications in a light aircraft (Hodgson *et al.* 1979). The system was successfully tested in flight trials in August 1979 (Hodgson *et al.* 1980).

It soon became clear that the imaging system was very useful in a stand-alone interactive mode of operation and as such had many potential applications. Several of these have been investigated (§2.3). This chapter describes the hardware and software which has proved to be so useful and versatile. It begins with a system overview and a description of the component parts. The flying system is described and examples of images obtained during the flight trials are given. The software developed for use in interactive image processing is described and a number of applications where the system has been used are given.

2.1 UNIVERSITY OF CANTERBURY IMAGE PROCESSING SYSTEM (UCIPS) OVERVIEW

Five major subsystems are identified in the system diagram (Figure 2.1). These are the CCD camera and its associated driving circuitry, direct memory access controller, and memory (i); the visual display store interrogator (VDSI) and CCIR standard television display (ii); the Intel 8080 microcomputer system with CRT terminal, graphics input joystick and fast line printer (iii); a bulk storage system consisting of a dual drive floppy disk and a digital cassette recorder (iv); and, finally, the software (v).

The architecture of the system is that of a standard computer with central address, data and control buses through which all devices communicate. In operation, a program which controls the capture and display of information from the CCD camera is loaded into memory from the floppy disk unit. The controlling program causes a signal to be sent to the direct memory access controller which in turn starts the capture of the next valid frame of data from the CCD camera. These data are placed in the CCD data memory from whence they are transferred to the visual display store interrogator (VDSI) refresh memory. The process is repeated at about six pictures per second until a key is depressed on the CRT console device. This freezes the last captured picture on the display, and the operator of the system then has an option of storing and/or processing the captured picture.

2.1.1 Charge Coupled Device Camera and Associated Circuitry (Figures 2.2, 2.3)

(a) CCD Camera and temperature controller. The CCD camera, associated drive circuitry, and analog-to-digital converter were developed and described by Ireland (1977). Three versions of the CCD camera have been made, two of which contain a Peltier effect cooling device. The CCD is mounted in the focal plane of the lens of each camera. The 3mm x 4mm format of the active area of the CCD makes it most suitable for 8 mm optics, but one camera has a universal mount which allows standard 35 mm screw thread lenses to be used. It also can be attached to a telescope. The thermo-electric cooling device allows the temperature of the CCD to

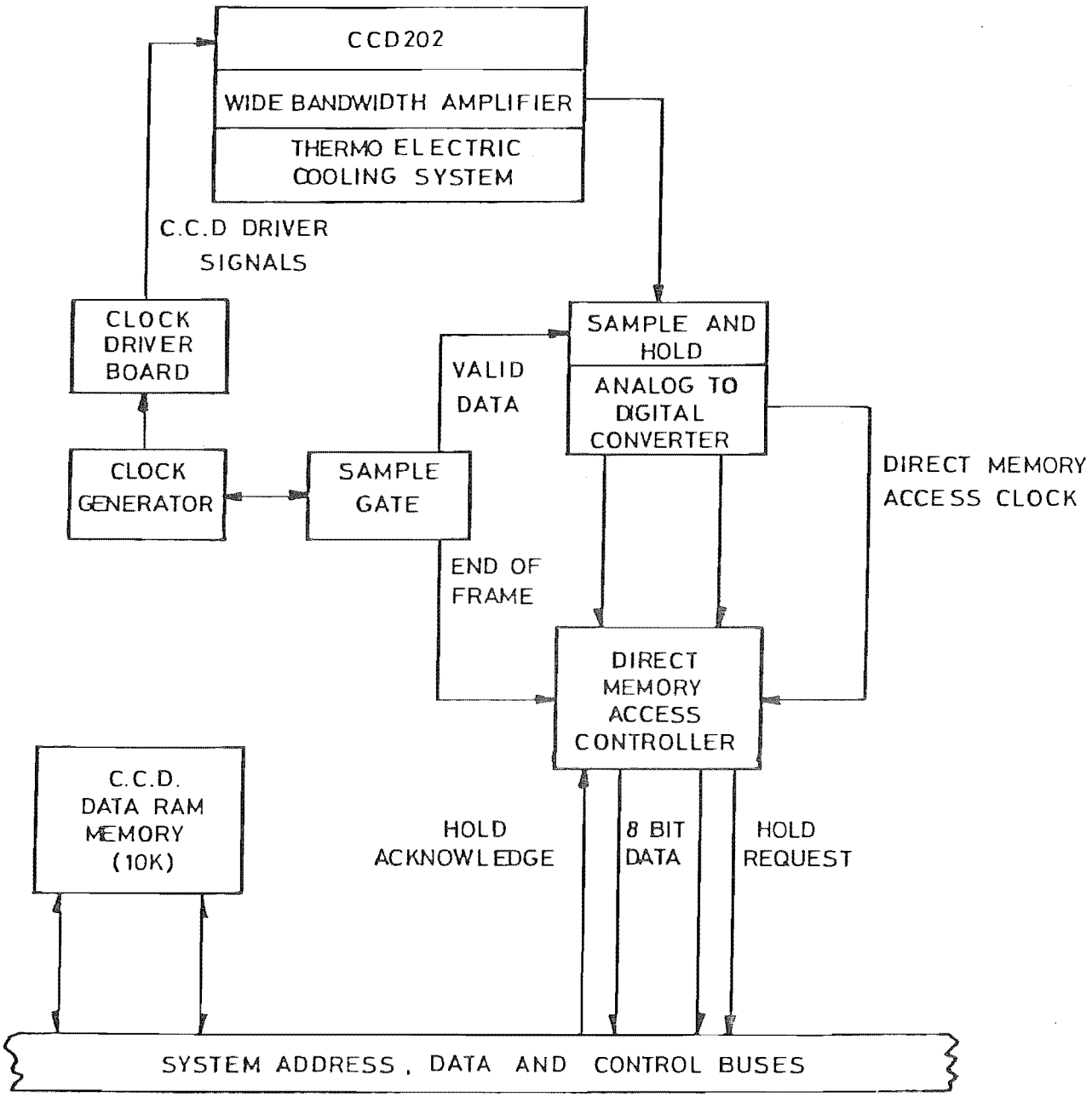

Figure 2.2 Charge coupled device camera system.

be controlled in the range of $-12^{o}C$ to $+30^{o}C$ (Hodgson 1979). The temperature controller is based on a design by Blackburn (1977) and adapted by Murphy (1979). One version of the CCD camera is shown in Figure 2.4. The CCD produces an output which is amplified by a wide bandwith amplifier before it is transmitted via coaxial cable to the analog-to-digital board.

(b) Clock generator and drivers. The clock generator circuitry is contained on two circuit boards which produce the required clocking signals for the CCD. These clocking signals are derived from digital logic circuits and are in the correct time sequence to clock the video out of the CCD. (See Appendix A for the CCD 202 specifications.) The clock generator boards also provide a signal which indicates when valid data is at the output of the CCD. This signal is used on the analog-to-digital board to actuate the sample-and-hold and to start an analog-to-digital conversion.

In addition to the requirement for the correct temporal relationship between the various CCD clocking signals, the level of each signal must be adjusted independently to obtain optimal operation of the CCD. A clock driver board allows each of the clocking signals to be adjusted between +15V and -15V.

(c) Analog-to-digital converter. The analog-to-digital board provides the sample-and-hold function and converts the analog signal from each pixel of the CCD into an eight bit digital data word. When conversion is completed, in one microsecond, the board generates a clock

signal for the direct memory access controller. This clock serves to indicate that the conversion of the data is complete and that the data may be transferred by the direct memory access controller into the memory. The analog-to digital converter is a ten bit converter, and in normal operation only the eight most significant digits are used. However, the eight least significant bits may be selected with a switch allowing the low level signal performance of the CCD to be evaluated.

(d) Direct Memory Access (DMA) controller. The direct memory access controller allows the data to be transferred directly from the analog-to-digital converter board into the CCD data memory at the rate it is clocked out of the CCD. This is necessary because the 1 MHz data rate is too high for the microcomputer to take the data directly. The DMA controller is initialized with an address in CCD data memory where the first byte of data is to be placed. It then receives a command from the microcomputer CPU to initiate a data request from the CCD. The DMA controller does so, putting the CPU into a hold state while the data is written directly from the analog-to-digital converter latches into the CCD data memory. The DMA controller receives a clock signal from the analog-to-digital converter board and uses this to generate the proper memory control signals and to advance a counter to the next memory location. An end-of-frame signal from the clock generator terminates the DMA operation and releases the CPU from its hold state.

Sensor: Fairchild CCD202B, 100 x 100 element charge coupled device.
Dynamic range - 300:1 at room temperature.
Saturation exposure - 0.4 $\mu J/cm^2$. Responsivity - 4.0 $V/\mu J\ cm^{-2}$.
(See Appendix A)

Thermoelectric Cooling Device: Cambion Model 3950-1. Heat pump capacity - 6.8 watts at a temperature differential of $0^{\circ}C$.
Maximum temperature differential - $54^{\circ}C$.

Temperature Transducer: Analog Devices AD590. Output - $1\mu A/K$ over $-55^{\circ}C$ to $+150^{\circ}C$.

CCD Video Amplifier: National Semiconductor LH0032 FET operational amplifier.
Unity gain bandwidth - 70 mHz. Slew rate - 500 $V/\mu s$.

Analog-to-Digital Converter: Datel ADCH101B. Resolution - 10 bits.
Conversion - Successive approximation, 100 ns. per bit.

Sample-and-Hold: Datel SHM-UH.
Aperture time - 200 ps. Acquisition time - 35 ns.
Output slew rate - 500 $V/\mu s$.

Figure 2.3 CCD Camera Technical Summary.

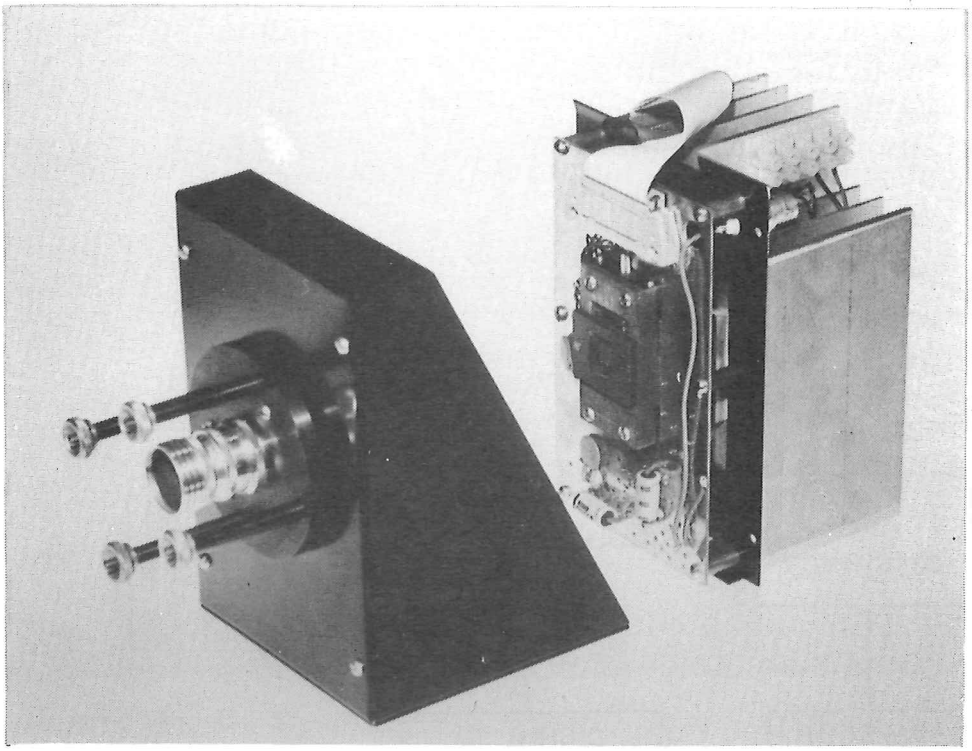

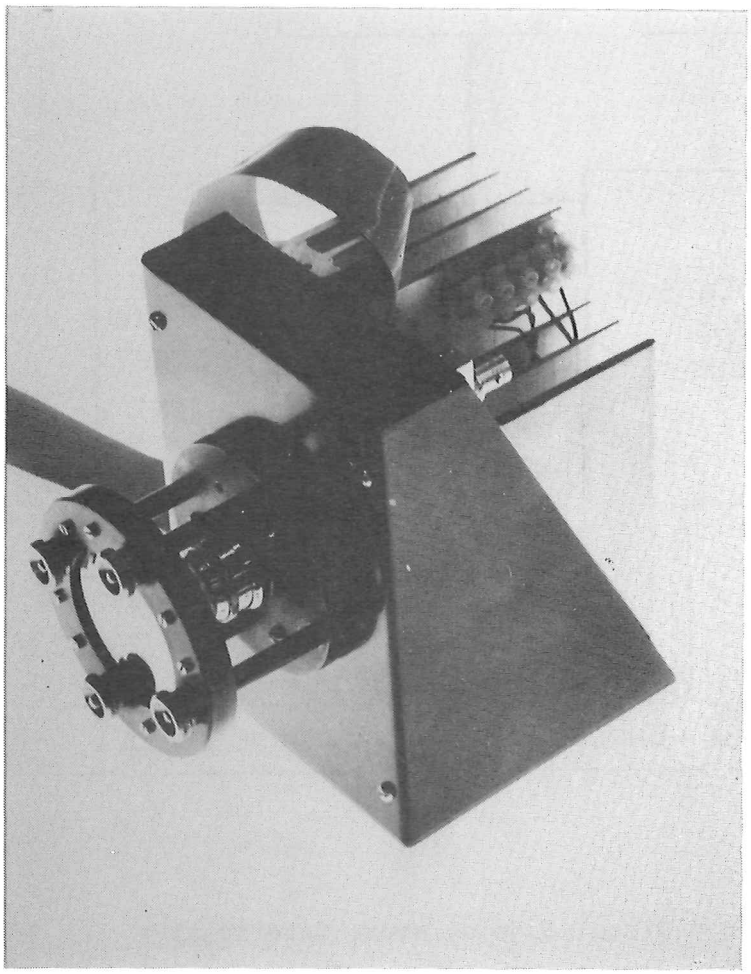

Figure 2.4 CCD camera.

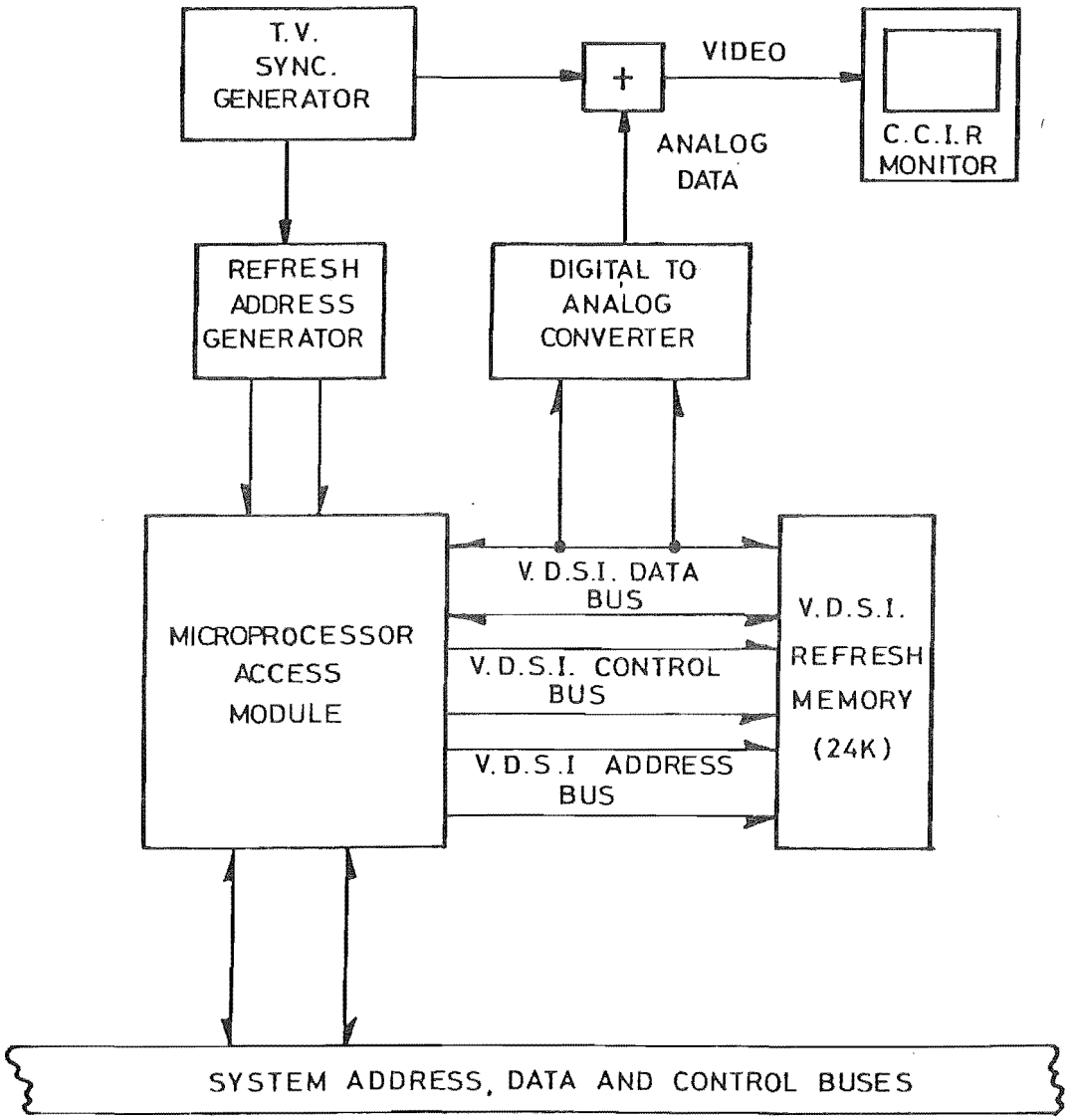

Figure 2.5 Visual display store interrogator.

(e) CCD Data memory. This is simply a section of memory that has been allocated by the software for use by the direct memory access controller. This memory can be any random access memory in the system that is not being used for another purpose although it must not be dynamic memory which requires refresh cycles. The memory boards are commercially produced and contain 8196 (8K) bytes of static random access memory. The microcomputer system memory is required to have an access time of at least 450 ns and is thus suitable for use as CCD data memory.

2.1.2 Visual Display System (Figures 2.5, 2.6)

(a) Visual display store interrogator (VDSI). Duncan (1978) developed the VDSI. It provides two basic functions. The first of these is to sequentially read data from the VDSI refresh memory and to convert these data bytes to a television compatible video signal. It accomplishes this task by generating the addresses and control signals required to read the data from the memory and at the same time generating synchronization signals for the CCIR standard 625 line video monitor. The digital data in the memory, eight bits per pixel, is converted to analog data by a digital-to-analog converter. This signal is then mixed with the synchronization signals to generate video for the television monitor.

The display format is chosen to match the sensor that is being used, and can be switched to display a centred picture of 128x128 or 100x100 pixels. The video is blanked outside the chosen display area except in an area of 16x100

pixels reserved at the bottom of the display for a title (see Figure 2.7). When generating the display, each line of CCD information is repeated as four lines on the television monitor. This serves to enlarge the display and, when coupled to the display timing in the horizontal direction, preserves the original 4x3 aspect ratio of the CCD imaging array.

The second basic function the VDSI controller performs is to control the access of the microcomputer to the memory dedicated to the display. In essence, two devices, the memory address generator for the refresh display and the microcomputer, must have access to the display memory. The microcomputer must have access to this memory to be able to change the picture that is being displayed. The controller has been organized so that the microcomputer has absolute priority of access over the display address generator. When this occurs, the display is automatically blanked. This necessary operational requirement gives rise to considerable degradation of the display when the microcomputer is changing information in the display area. No interference is seen under other normal microcomputer operations.

Twenty-four K bytes of fast refresh memory have been allocated to the VDSI memory space. This allows the storage of two complete images in memory. A starting address is programmed under software control into the VDSI address generator which allows either of the two images to be displayed.

Memory Allocation: 24,576 (24K) bytes, 250 ns access time, static random access memory.

Addressing Range: 65,536 (64K) bytes.

Digital-to-Analog Converter: Datel DAC-08BC. Resolution - 8 bits. Settling time - 85 ns.

Video Mixer: National Semiconductor LH0032. See Figure 2.3.

Video Amplifier: National Semiconductor LM310 voltage follower. Unity gain bandwidth - 20 MHz. Slew rate - 30 V/μs.

Video Monitor: Hitatchi 9", 625 line CCIR standard monitor.

Figure 2.6 Visual display system technical summary.

Figure 2.7 VDSI example output.

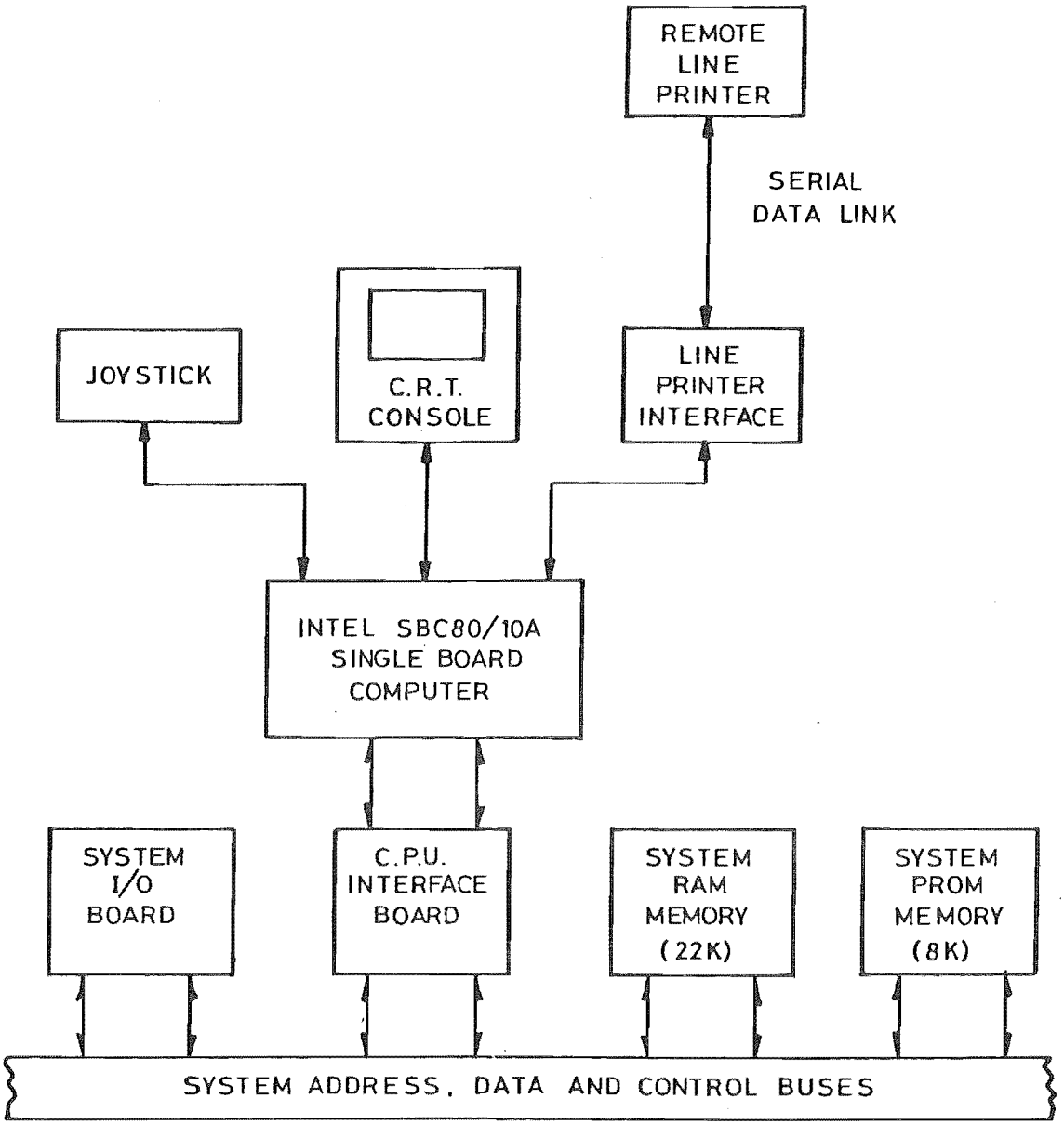

Figure 2.8 Central processor unit system.

(b) VDSI refresh memory. The memory which is used for the VDSI refresh memory is identical to all other random access memory in the system except that it must have an access time of 250 nanoseconds. Identical circuit boards with faster memory chips are used.

(c) Display hard copy. Hard copy of the display monitor is achieved by positioning a 35 mm camera in front of the screen. A special camera attachment has been constructed. Low quality hard copy can also be obtained by a line printer print-out. See Appendix C.

2.1.3 Central Processor Unit System Architecture (Figures 2.8, 2.9)

(a) Central processor unit. A commercially constructed single board computer (Intel SBC80/10A) was chosen as the central processor unit. It is a complete computer with random access memory, read only memory, and input/output ports. This processor board was designed and intended for use in dedicated applications, and some minor modifications were added to allow it to be used in a software development and general purpose imaging system application. These modifications include the selection of the communication rate of the CRT serial port and the facility to disable the on-board read only memory with a switch.

(b) Single board computer interface. The random access memory board described in §2.1.1(e) above, uses a different bus configuration than the single board computer. The single board computer interface, physically located on

the same board as the direct memory access controller, inverts the logic and provides the required drive circuitry for the address and data buses. The interface also provides logic to enable or disable the on-board read only memory through the action of a switch on the front panel of the system chassis.

(c) Cathode ray tube (CRT) console terminal. Communications with the operator of the imaging system are via a CRT display unit operating at 9600 Baud. This unit has a set of user programmable function keys which have proved to be very useful in image processing.

(d) Line printer interface. When a CRT is being used as the console device on an imaging system or software development system, provision must be made for the hard copy of programs and data. In the University of Canterbury system this requirement is met in a novel way. An interface has been constructed which connects the microcomputer to a remote line printer. The interface was developed by Camping (1979) and Savory (1979) and allows a number of microcomputer development systems to share a single line printer on a single coaxial line.

(e) Joystick. One of the input/output ports on the single board computer is used to interface a joystick to the system (Leonard 1979). This joystick allows the operator to identify any pixels displayed on the television monitor. The joystick device itself is a pair of orthogonal potentiometers and a multiplexing analog-to-digital converter. The device is driven by a program running in the micro-computer which determines the output of the A/D converter,

and flashes the appropriate pixel on the monitor.

(f) System RAM and PROM. The system random access memory has been described in 2.1.1(e). The system programmable read only memory (PROM) is a similar commercial board with up to 16,636 (16K) bytes of programmable read only memory.

(g) System input/output. An additional input/output capability has been added to the system by a simple I/O board. This board contains an additional 48 parallel I/O lines and a serial port with an RS232-C interface.

CPU Board: Intel SBC 80/10A single board computer. RAM - 1K bytes.
PROM - 4-8K bytes (enabled or disabled by a front panel switch).
I/O - 48 lines parallel bidirectional, RS232-C serial port.

CRT Console Device: Teleray 4016 programmable keyboard CRT terminal.
9600 Baud.

Line Printer: 40 column PR-40 printer plus access through a special interface to an Intel printer at a remote location.

System Memory: RAM - 57,344 (56K) bytes static with 24,576 (24K) bytes allocated to the refresh memory for the video display.
PROM - 8196 (8K) bytes 2708 type.

System I/O Board: Parallel - 48 lines. Serial - RS232-C.

Power Supply: National Semiconductor BLC665. Supplies 5V @ 30 A., -5V @ 1.75 A., +12V @ 4.5 A., -12V @ 1.75 A.

Figure 2.9 Central processor unit system technical summary

2.1.4 Bulk Storage System (Figure 2.10)

Any image processing system requires a storage device for images. The type of bulk storage chosen depends somewhat on the format of the input device being used. A very large input sensor, say 400x400 pixels will require much more storage than a smaller sensor such as the 100x100 array.

The University of Canterbury system uses two types of bulk storage. The most commonly used device is the dual floppy disk unit, but a digital cassette recorder is used with the Flying FADS described in §2.3.1 and is available for use as a general picture store.

(a) Dual floppy disk system. Figure 2.1 shows two single-density, single-sided disk drives. Each floppy diskette has 252,928 bytes available for storage and can store 21 pictures from the 100x100 CCD. In addition to serving as a bulk store for images, the floppy disk system allows the rapid development of software. An operating system with text editor and assembler allows the editing of text and the assembly of relocatable object files. A linker program links relocatable files together to produce an executable object file which the programmer can then run on the microcomputer. See §2.1.5.

(b) Digital cassette. A digital cassette was chosen as a storage device for the Flying FADS system (see §2.3.1). An operating system which allows the user to operate and to interact with the cassette tape in much the same fashion as with the floppy disk has been written by

Pairman (1980). The cassette tape system operates so that files which are programs to be loaded into memory and run as part of the image processing system may be accessed by typing in the name of the file. Files of images, on the other hand, are not named and the cassette drive must be positioned to the desired image before loading can occur. The cassette tape operating system has several commands to allow for rapid and easy positioning to any file on the tape. A digital cassette can store or retrieve a picture in six seconds and will store 30 pictures on a single side of a 100 metre cassette tape. Pictures may be recorded on both sides of the tape.

Dual Floppy Disk System: Icom FD400 Single density, single sided drives.
Storage capacity - 252,928 bytes per 8" IBM 3740 standard diskette.
Data transfer rate (writing) - 25 seconds for one picture (11,600 bytes).
Data transfer rate (reading) - 10 seconds for one picture.

Digital Cassette: MFE Model 450B. Recording density - 1600 fci., 20 inches/s., 2000 bytes/s., Storage capacity - 2.88×10^6 bits per 300 feet of ANSI/ECMA standard cassette.
Data transfer rate writing and reading - 6 seconds for one picture.

Figure 2.10 Bulk storage system technical summary.

2.1.5 Software

The software on an image processing system falls into two categories. The first, operating system software, includes programs which are necessary to interact with the

floppy disk storage system. The operating system also includes the software development tools to develop and debug a user's software. The second category is the user's image processing software. This software is dedicated to the manipulation and processing of images and is particular to the image processing requirements. In image processing applications, a software package which allows a choice of image processing routines is generally developed.

(a) Operating system software. There are three operating systems available for use on the University of Canterbury imaging system. The first is produced by the manufacturer of the floppy disk hardware, Icom FDOS III, the second is the CP/M operating system (Miller 1978, Stewart 1978), and the third is the University of California at San Diego (UCSD) PASCAL system (Bowles 1978). Each of these operating systems has an executive program which allows a user to access files stored on the floppy disk. These files may be programs, text files, or intermediate files which have been generated by editors or language translators and which will become executable files. There also may be data files which are accessed by other programs which the user may run. Images fall into this later category, and a suite of software routines is provided by the operating system to aid in their storage or retrieval.

The first two systems mentioned above, FDOS and CP/M, primarily support assembler language programming. Each has an editor and an assembler. The assembler in the FDOS system is rather more powerful in that it produces relocatable code and thus allows software to be written in

modular form. The system also includes a linker which links together the modules required to produce a complete program. The debugging facilities in the CP/M operating system are more powerful than those offered under FDOS because a symbolic debugging package is included. Programs developed under FDOS rely on the debugging facilities in the system monitor. Both FDOS and CP/M operating systems provide BASIC as a high level language for program development. In each system, a BASIC interpreter is provided.

The UCSD PASCAL operating system is dedicated to the PASCAL language described by Jensen and Wirth (1975). It is a high level language and the operating system supports program development in PASCAL with a screen oriented editor, a filer to control writing to and reading from the floppy disk, and a 'p-code' compiler and interpreter. The 'p-code' compiler produces a pseudo-machine language code which is then run by the interpreter resident in the microcomputer system. The execution of PASCAL language programs is similar to the operation of the BASIC interpreters available in FDOS and CP/M.

An additional component of the system software is the system monitor. A monitor is a supervisory program which provides basic input/output routines and debugging facilities. The monitor used on the University of Canterbury system is one adapted from the Intel Microcomputer Development System monitor. It has been extensively modified and includes additional debugging facilities in the form of trace and disassembly features (Wong 1979).

Appendix B gives a listing of the commands available in the University of Canterbury monitor. A number of other software packages, such as a floating point mathematics package, also are available for use in the system.

(b) User's software. User generated software is the most important part of the software on the image processing system. Here, a picture processing operating system has been developed. Not only does it allow us to interactively operate on a picture stored in the memory of the microcomputer, it also allows us to easily store and retrieve pictures on the floppy disk. It also loads and executes programs which may not be part of the basic picture processing facility. The following section is devoted to describing this software in detail.

2.2 INTERACTIVE IMAGE PROCESSING SOFTWARE

The main image processing software is a picture processing operating system because, like the floppy disk operating system, this software allows the operator to interact with the floppy disk both for loading and executing programs and for storing and retrieving images. A program called PIKKY has been written to accomplish these tasks.

PIKKY contains three basic modules. These are: (1) the command input and decoding section, (2) the floppy disk handling routines, and (3) the image processing routines inherent in the operating system. In addition, a suite of user generated processing routines has been developed. Many students who have worked on the imaging

system have contributed to this suite of software (Cady *et al.* 1979, Appendix C) and the number of routines available for interactive image processing is growing steadily. A fixed suite of routines is not sufficiently flexible to allow us to investigate different aspects of image processing. Therefore a very useful feature of the picture processing system is its capability to allow a large number of image processing routines to be run under its control. The number of routines that can be accessed is limited only by the storage capabilities of the floppy disks, a total of about one-half megabyte on the dual drive system. The size of any one processing routine is limited normally to about 12K bytes, exclusive of storage space for the images. For special processing routines, where the routines in PIKKY are not required, 32K bytes of memory are available. The processing power of PIKKY is therefore only limited by the imagination of the user, the cleverness of the programmer, and the speed limitations of the Intel 8080 central processor unit.

2.2.1 PIKKY - Picture Processing Operating System

PIKKY contains routines which input a command from the operator and decodes these commands to perform the required operation. When reading from or writing to the floppy disk is required, PIKKY contains a library of routines which can perform any interaction with the floppy disk storage. Finally, PIKKY contains a number of processing routines which can be used by the operator.

(a) PIKKY command input and decoding. All commands are entered into the picture processing system through an

ASCII serial keyboard. An # is displayed on the console crt as a prompt character, and commands are written in the form of a command line. Editing of the command line through the use of the rub-out (RO) key is permitted and line echo facilities are provided (CTL-R). The command line is terminated by a carriage return (CR) and is held in a text buffer in a specified and dedicated location in system random access memory. It is therefore available to other user generated software. Command decoding is achieved by matching the command string in the text buffer with a command table. The command table contains ASCII templates for each valid command with the starting address of the required routine following the template. Control is transferred to the required routine and returned to the command input processor when the routine is finished. If the command processor fails to find a match for the command line in the command table, it assumes that the command line specifies a processing routine found on the floppy disk unit. It then loads and executes the required routine. Parameters may be passed to any of the processing routines through the command line buffer.

(b) PIKKY floppy disk handling routines. All operations to and from the floppy disk units are handled by a set of routines supplied by the vendor of the system. These routines use a special section of memory to store 'system parameters' and thus communication between the picture processing operating system and the floppy disk interface software is easily accomplished.

The disk handling routines provide error messages

when a specified file is not found on the specified disk, a duplicate name exists, a media error has occurred, or a specified drive is not ready.

(c) Image processing routines in PIKKY. A number of image processing routines are available as standard options within the picture processing operating system. See Figure 2.11 and Appendix C. These routines form the basis for many image processing procedures, and may be accessed and executed in any order at the whim of the operator.

All processing which is done within the PIKKY routines occurs on one specific picture buffer. As mentioned in §2.12, the VDSI can display one of two picture buffers within its memory space. The PIKKY routines always operate on the picture buffer designated #1. Through the use of the P command the VDSI can be directed to display either picture buffer #1 or #2. Thus the operator can save an original of the picture to be processed in buffer #2, and perform some image processing operation on buffer #1. The two results can be compared by using the P command. A third buffer area is also available but is in normal system memory and must be transferred into the VDSI memory using the T command to be displayed.

2.2.2 External Image Processing Routines

One of the most powerful features of the interactive picture processing system is its facility to access and run any program which is stored in the floppy disk system. This means that picture processing is not limited to the basic

```
 INSTRUCTIONS (TYPE ANY CHARACTER TO CONTINUE)
G <ret>  - EXECUTE GPIK
SAVE,(FILENAME) <ret> - PUTS PICTURE ON DISK
LOAD,(FILENAME) <ret> - GETS PICTURE FROM DISK
M,X <ret> - MASK PICTURE BITWISE, AND-ING WITH X
I,X <ret> - INCREASE INTENSITY BY SHIFT LEFT X BITS
D,X <ret> - DECREASE INTENSITY BY SHIFT RIGHT X BITS
H <ret> - HISTOGRAM EQUALISATION
L,X,I,P,S,M <ret> - LINE PROFILE OF LINE X
   I,P,S,M - All Optional And In Any Order
   I - Super Impose Plot On Picture
   P - Leaves Plot As Points
   S - Scale
   M - Marker At Line Beins Investisated
R <ret> - RESTORE PICTURE
P <ret> - PICTURE CHANGE ROUTINE : 1,2 OR CR TO EXIT
T,A,B <ret> - MOVES PICTURE A TO POSITION OF PICTURE B (A,B=1,2 OR 3)
U <ret> or U,plist <ret> - ACCESS PREVIOUSLY LOADED USER MODULE
GO,XXXX  -  GO TO ADDRESS XXXXH
B <ret> - EXECUTE IN BATCH MODE
BD <ret> strins - BATCH DEFINE  strins FOR BATCH MODE
EXCH <ret> - EXCHANGE PICTURE A AND B
EXPND <ret> - LINEAR CONTRAST EXPANSION
E <ret> - EXIT TO THE MONITOR
F <ret> - RETURN TO FDOS
ON <ret> - TURN PIXEL FLASH MODE ON.
OFF <ret> - TURN PIXEL FLASH MODE OFF.
<ESC> - ACTIVATE FLASHING PIXEL FUNCTION KEYS.
        EXIT THIS MODE WITH ANOTHER <ESC>.  THE VALUE, ROW AND COLUMN
        ARE DISPLAYED.
SET,XX - SETS PIXEL VALUE
```

Figure 2.11 Image processing routines within PIKKY.

routines within PIKKY. Other software routines can be developed and run without requiring a new PIKKY with a new set of commands each time a new processing algorithm is to be tested.

There are two ways to access and execute a routine that is not within the basic repertoire of PIKKY. As mentioned above, if the command decoding section within PIKKY does not find a match in the internal command table, the command name is assumed to be a program which exits on the floppy disk. The command decoding module, through the use of the system parameter area of memory and the disk handler routines, loads the program from the floppy disk unit and executes it. If the program had already been loaded and was still in the memory, the U or the GO command in PIKKY will branch to the user routine.

The concept of external, or user generated, routines is very powerful. Many special purpose or trial routines can be developed and tried without interfering with the basic operation of the main picture processing system program. The only limitations on user generated routines are that they should start at a specific address, and at their termination should return to a specific address in PIKKY. Figure 2.12 gives a list, and Appendix C gives more formal details on a number of user generated routines which have been used.

ROUTINE	DESCRIPTION
TITLE	Write a title into a text display area below the picture.
WIPE	Blank the text display area.
AVG2, AVG3	Average out the defective pixels in each of two different CCD's.
EDGE	Set the three rows and columns around the periphery of the displayed picture to zero.
SLICE	Slice the picture into gray levels and show only those above or below a specified value.
DENSY	Plot the distribution of densities in the picture on the line printer or console.
SCALE	Fill the picture area with one of four different gray scales.
XOR	Exclusive OR the two picture areas.
L640	Transfer data to or from another computer in the Department.
FILTR	Spatial two-dimensional filter.
FIGS	Write text into the picture area starting at the location of the flashing pixel.
JOY	Operate the joystick as an input device.
FNUMS	Find the maximum in the picture and print its value and the values of its nearest eight neighbours on the console

Figure 2.12 Some user generated processing routines.

2.2.3 Evaluation of Image Processing Software

Interactive image processing has been defined in §1.1. Several metrics by which routines may be evaluated for their suitability in interactive image processing are defined in §1.3. The image processing routines within PIKKY and the user generated routines are interactive routines because that is the way we use them, and although we have not investigated thoroughly the limitations of using a microcomputer in image processing, we have performed complicated and useful processing in realistic interactive processing times.

Figure 2.13 shows a table giving the execution times and size of a number of useful image processing routines. The size of the routines does not include the image storage when the image is stored in the VDSI memory. Some routines, however, require extra storage space for intermediate results. The storage space required by these routines is shown in the table of Figure 2.13.

Most routines are executed in less than one second, much less than the operator's response time. The slice program has an execution time of nearly one and one-half minutes. This is the time taken to show 256 different pictures, each of which displays only those pixels above a threshold value. Note that all routines listed in Figure 2.13 have been written in assembler language which is faster and more compact than most high level languages. Also, note that Appendix C gives more detailed information on the operation of each routine.

Routine		Execution time (seconds)	Program size (bytes)
GPIK	Capture image from CCD	0.16	10,071
SAVE	Save image on floppy disk	20	29
LOAD	Load image from floppy disk	6	48
MASK	8 bit mask of each pixel	<1	23
INCREASE OR DECREASE	Intensity	<1	26
HISTOGRAM EQUALIZATION	Contrast expansion	<3	126
LINE PROFILE	Draw profile of intensity across a line	<1	448
TRANSFER FROM PICTURE 1 TO 2		<1	66
TITLE	Write a title on the display	<1	760
WIPE	Clear the title area	<1	27
AVG3	Compensate for CCD defects	<1	67
EDGE	Compensate for CCD edge defects	<1	100
SLICE	Display all pixels above a threshold value	1 min 24 sec for 256 levels	10,300
DENSY	Calculate and plot a histogram of pixel intensities	6	1100
SCALE	Gray scale test pattern	<1	150
XOR	Exclusive-OR two pictures	<1	23
FILTR	Two-dimensional spatial filter	12	500

Figure 2.13 Evaluation of assembler language image processing routines

2.3 APPLICATIONS OF THE UNIVERSITY OF CANTERBURY IMAGE PROCESSING SYSTEM

The initial application of the UCIPS was in the evaluation of the charge coupled imaging device. This work was performed by Murphy (1979) and some of his results are given in Chapter 3. The UCIPS was designed to be portable so that flight trials could be undertaken to test that a system could be used in a light aircraft to provide calibration for Landsat data. During this development, the system was found to be very useful in its own right as an image processing machine and a number of application areas, in addition to the Flying FADS, can be mentioned.

2.3.1 Flying FADS System

The Flying FADS system is so named because the earliest system using the CCD camera was known as the Fast Area Digitizing Scanner--FADS--(Ireland 1977). The UCIPS was developed as part of a research program which has as its aim the eventual construction of a system to provide local calibration of Landsat satellite imagery (Hodgson *et al.* 1979). In this application, a multispectral CCD camera system (Multi-FADS) is to be flown over selected test areas simultaneously with the overflight of the Landsat satellite. Data collected by the aircraft system would be used to calibrate the data obtained from the satellite. Flying FADS, a single channel test system based on UCIPS, has been the outcome of this hardware development to date (Hodgson *et al.* 1980; Pairman 1980).

The hardware in Flying FADS is shown in Figure 2.14

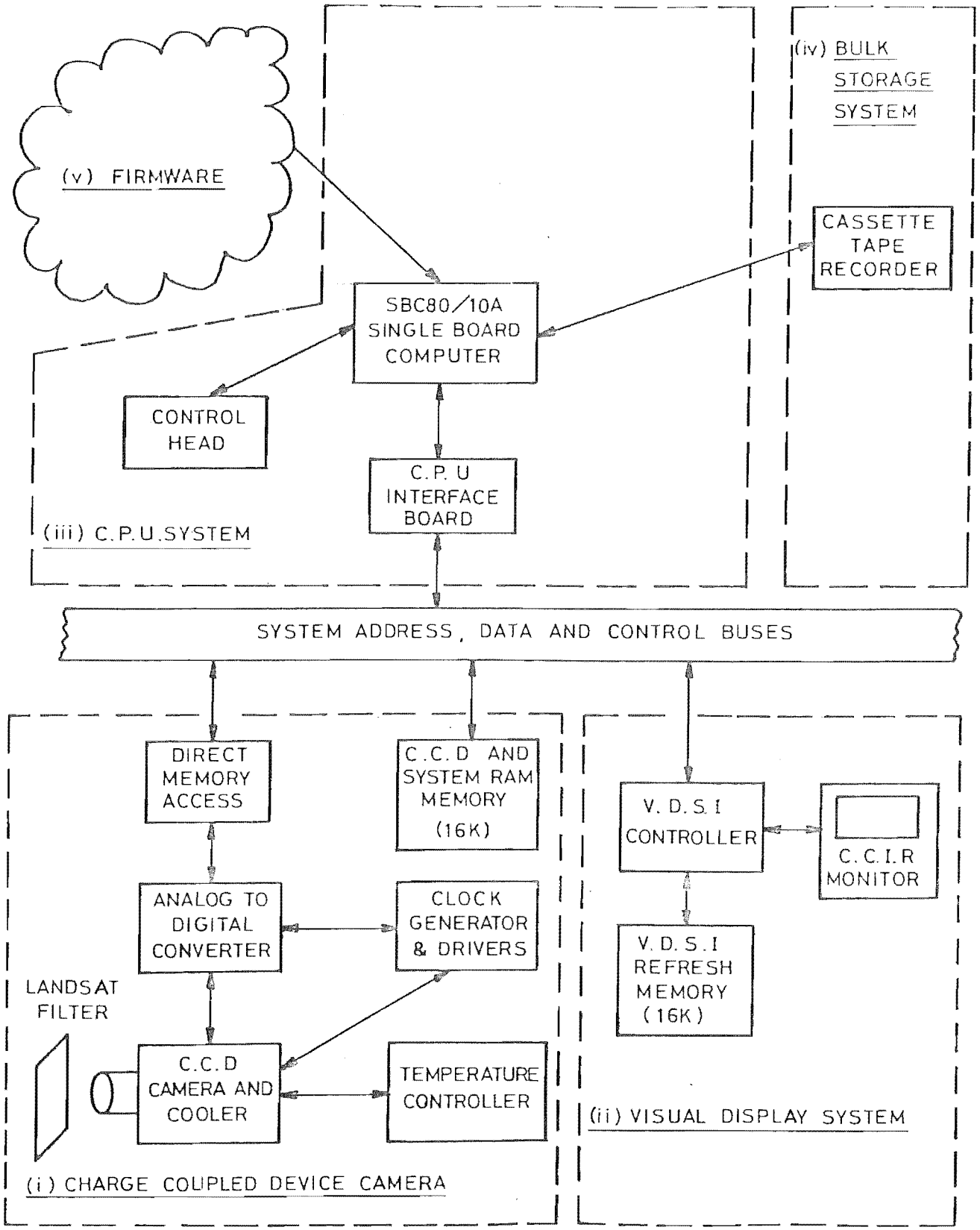

Figure 2.14 Flying FADS system.

and summarized in Figure 2.15. The hardware is essentially the same as that in Figure 2.1, except that equipment in the UCIPS not specifically needed in the flying version is deleted. Notice that the floppy disk storage unit (iv) has been replaced by a digital cassette recorder to reduce bulk and weight. Another major difference can be seen in the C.P.U. system (iii). The C.R.T. terminal and keyboard were considered too bulky and difficult to use in an aircraft, and Pairman (1980) designed a control head to provide operator input to control the system in flight. It controls all operations of the tape recorder, allows the selection of one of several modes of camera operation, and generates a run and survey code to identify each picture taken with the system. Figure 2.16 gives a summary of control head operations.

The initial flight trials of the system were held in August 1979, when the equipment was installed in an Aerocommander operated by New Zealand Aerial Mapping Services Ltd, Hastings, New Zealand. The equipment performed faultlessly and a number of photographs were taken, examples of which are given in Figure 2.17.

2.3.2 Evaluation of Image Processing Procedures

A project to investigate the *in vivo* detection of multiple pregnancies in sheep is being sponsored by the Auckland Industrial Development Division of the D.S.I.R. They hope that early detection will reduce the lambing morality rate. We were able to show, using a sample x-radiograph film, that digital edge enhancement techniques could provide an image which was superior to the original

Charge Coupled Device Camera:	See Figure 2.3
Spectral Band Responses:	Band 4 - 500-600 nm Band 5 - 600-700 nm Band 6 - 700-800 nm Band 7 - 800-1100 nm
Instantaneous Angular Field of View (IFOV):	0.35^{o} (included angle)
Angular Field Subtended by Image:	35^{o} (across track)
Linearity:	± 1% of F.S.D.
Dynamic Range:	1000:1 (100:1 acceptable)
Variation of Responsivity over Image Area:	2%
Thermal Range of Operation:	$-5^{o}C$ - $+35^{o}C$
Output Format:	8 bit digital
Power Supply:	24V aircraft supply
Power Consumption:	300 W
Weight:	25 kg
Display System:	VDSI with 16K bytes random access memory See Figure 2.6.
Central Processor System:	Same as given in Figure 2.8 except for console device, line printer and joystick.
Bulk Storage System:	MFE Model 450B digital cassette. See Figure 2.10.
Operator Control:	Control head operation. See Figure 2.16.

Figure 2.15 Flying FADS technical summary.

Cassette Recorder Function:	Record. Playback. Fast Forward or Fast Reverse (80/120 ips).
CCD Camera Function:	Intervalometer control. Internal timer control (6-30 s). Manual single shot.
Display Mode:	Continuous from CCD camera. Update only at time of storage.
Picture Identification:	Operator selection of run and survey identification codes. Automatic channel number and sequence numbers generated.

Figure 2.16 Control head operation summary.

(a) Picture taken with Hasselblad camera system

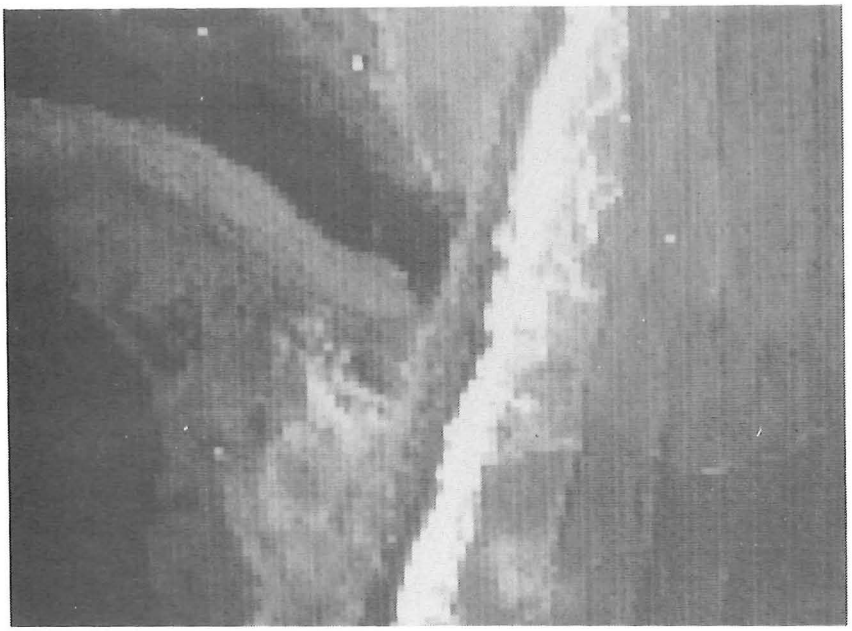

(b) Matching picture taken with CCD camera system

Figure 2.17 Images from flight trials of Flying FADS.

a. Original image.

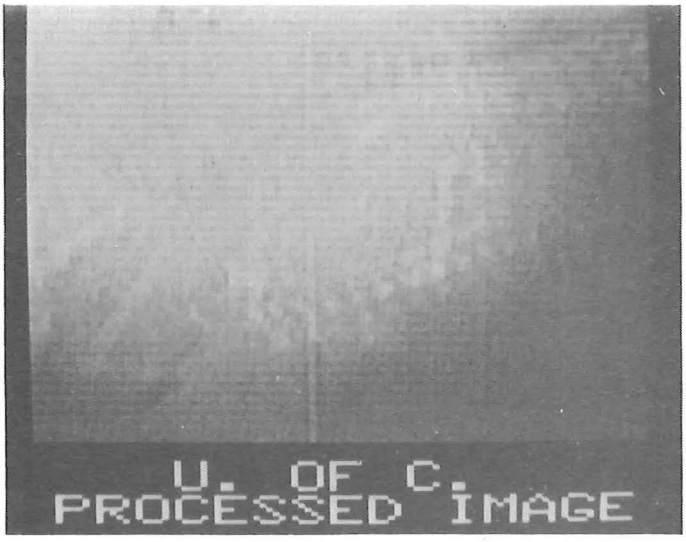

b. Edge enhanced image.

Figure 2.18 Edge enhancement for pregnant ewe evaluation.

and would allow an operator to determine the state of the ewe. Figure 2.18 shows an example of an image and its edge enhanced version.

2.3.3 Astronomical Imaging

Chapters 5 and 6 describe the use of the system in simulating attempts to image celestial bodies using large earthbound telescopes. The effect of a turbulent atmosphere (seeing) is described in Chapter 4, but in essence, seeing conditions can be shown to reduce the resolution of a large telescope (> 2 m or so) by a factor of 10 or more. This problem has been studied in the University of Canterbury Electrical Engineering Department Optical Laboratory. Before the development of the imaging system, simulated imaging and image processing had to be carried out optically using photographic techniques. This is a time consuming and laborious procedure. A major advantage of using the UCIPS in this application is that images are produced in real time. This allows rapid evaluation of image processing procedures and speeds up the development of different imaging algorithms. In addition, many of the digital processing techniques could not be performed optically.

2.3.4 Microscope Imaging

A microscope fitting allows the CCD camera to be attached to any standard microscope. Initial tests of this attachment with the system have shown that digital processing can be very effective in enhancing photo-micrographs. This use of the system has not been pursued but possible applications include the determination of

growth ring spacing in tree core samples and the calculation of open-to-closed area in very fine mesh screen. Each of these applications makes use of the precise physical construction of the CCD in making accurate measurements.

2.3.5 General Picture Digitization

The system is capable of digitizing photographic images. We have not done many because an accurate, even field illumination light source and a means to control the magnification and position of the photographic image are required. Nevertheless, the system could be easily set up to routinely do this if required.

2.4 CONCLUSION

The development of the University of Canterbury Image Processing System is continuing. The CCD202 imaging device described here is now obsolete and will be replaced by a larger charge coupled device array, the CCD211. This is a 190x244 element array similar in construction to the CCD202. The system hardware is being redesigned to allow this sensor to be used. When finished, up to eight sensors can be run simultaneously (Pairman 1980, Cree 1979). This development, known as 'MultiFADS' will allow true multi-spectral remote sensing imaging from a light aircraft.

CHAPTER 3

THE CHARGE COUPLED DEVICE IMAGING ARRAY

3.0 INTRODUCTION

Chapter 1 reviews interactive image processing by analyzing the image chain. Evaluation characteristics or parameters are given for each link in the chain. Chapter 2 describes an interactive image processing system which has proved useful. The charge coupled device (CCD) sensor used in the image processing system has a number of particular characteristics which have an impact on methods developed to evaluate the image processing procedures described in Chapter 5. A detailed understanding of the operating characteristics of the CCD is necessary to correctly interpret quantitative results. This chapter considers the operation of the Fairchild CCD202 imaging array.

3.1 SOLID STATE SELF SCANNED SENSORS

Semiconductor imaging devices are becoming widely available and are, in general, more suitable than photocathode devices for many digital image processing applications (Amelio; Gross 1975). Solid state devices have lower power requirements and increased quantum efficiency. They can be made smaller and more robust because their operation does not require a vacuum or high accelerating voltages. On the other hand, commercially

available semiconductor imaging devices have a lower resolution than photoemissive devices such as the television vidicon imaging tube. There are high resolution semiconductor devices, such as a 400x400 and a 800x800 pixel CCD array, that have been developed for use in spacecraft planetary imaging probes (Root 1976; Smith 1976). As the manufacturing technology improves, it is expected that these high resolution devices will become more readily available.

A solid state imaging sensor is an integrated structure containing:

(i) an array of sensing elements in which a photoelectric effect converts incident light to an electronic charge packet, and

(ii) a readout circuit which transfers the packet of charge from a collection site (a picture element -- pixel) to a measurement point.

There are several types of solid state imaging sensors commercially available. These include photodiode arrays (Reticon 1977; Sato *et al.* 1979), charge injection device (CID) arrays (General Electric 1977; Michon and Burke 1975, Michon *et al.* 1975) and charge coupled device arrays (CCD's). CCD arrays are more widely available with at least three manufacturers supplying devices (Fairchild, Texas Instrument and RCA). There have been a number of conferences and texts written on charge coupled device applications and theory [see CCD(1), CCD(2), CCD(3), CCD(4)].

Agajanian (1976) gives a comprehensive bibliography on charge coupled devices, and Murphy (1979) reviews the operation of the three basic type of imaging arrays.

The following discussion of charge generation and transfer is restricted to the CCD, because it is the device used in the UCIPS imaging system. It is also the most widely available solid state imaging device.

3.1.1 Charge Packet Generation

A cross-section of a typical cell of a CCD imaging array is shown during charge generation, or integration, in Figure 3.1a.

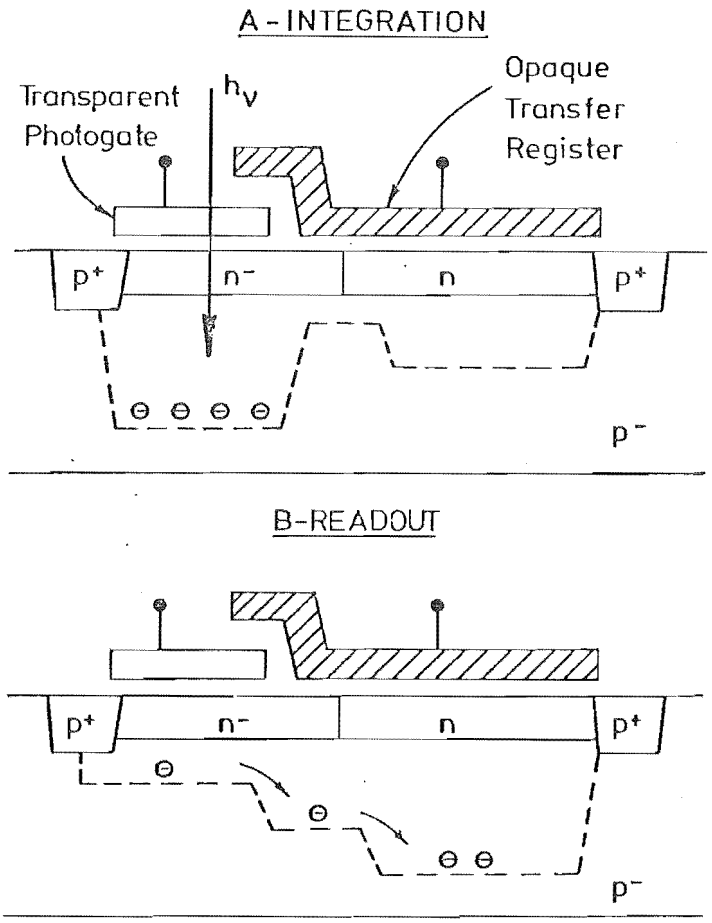

Figure 3.1 The unit cell of a CCD imaging device. (From Hodgson 1979.)

The incident light, hν, creates a hole-electron pair in the semiconductor material. Depending on the type of material, there will be an excess of either holes or electrons which will be free to move about in the material under the influence of an electric field, or by diffusion to an area of the material where the concentration of carriers is less dense. In an imaging device, these photoelectrically generated carriers are collected in a spatially quantized area formed by a semiconductor junction between two dissimilar semiconductor types or between a semiconductor and a conductor where a thin insulation layer separates two (metal-insulator-semiconductor, MIS). The Fermi energy levels of the different materials and the bias potential create a potential energy well in which the photocarriers (generally electrons) are collected. The amount of charge collected in the potential well per unit time is proportional to the incident light flux. It is also a function of many other factors, such as the area, the depth of the potential well, and the doping levels in the semiconductor material (Barbe 1975). It should be clear from the discussion of §1.2.3 that other considerations such as noise mechanisms, saturation effects, spectral characteristics and quantum efficiency are important in the operation and comparison of devices. These are considered in more detail in §3.2.

3.1.2 Charge Transfer

Charge transfer mechanisms in CCD arrays have been described in detail by Solomon, Barbe (1975), Sequin (1975) and Tanaka (1979). The process can be understood

from Figures 3.1 and 3.2.

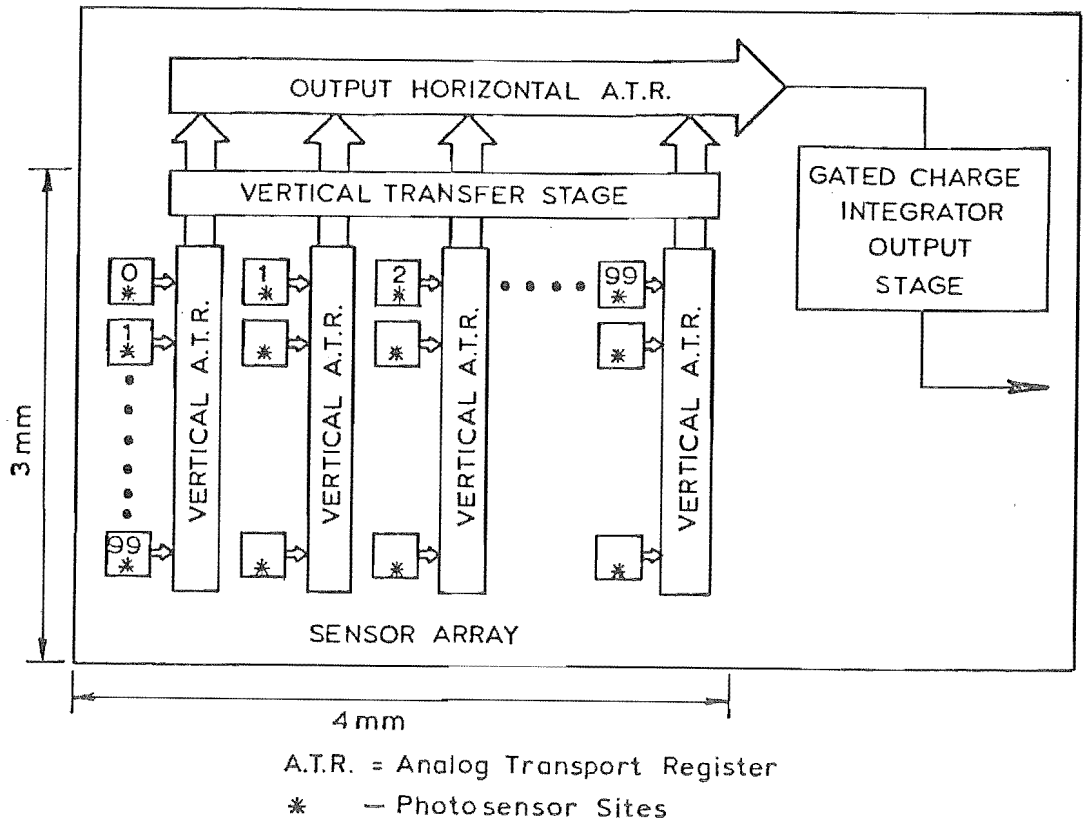

Figure 3.2 CCD chip 'real estate' plan.
(From Hodgson *et al.* 1980)

The charge packet generated under the transparent photogate electrode (Figure 3.1a) during integration is transferred to an adjacent register by changing the bias potentials of the electrodes. This 'tips' the charge from the photosite to the transfer, or transport, register. An area array, such as the CCD202, is shown in Figure 3.2. Each photosite, marked with *, in a column has an associated vertical analog transport register (ATR). The initial charge transfer, described above, is from the photosite into the adjacent vertical ATR. Bias potentials in alternate

storage locations in this ATR are then switched in turn, causing the charge to be shifted vertically to the output horizontal ATR. The output horizontal ATR shifts the charge packet to the gated charge integrator output stage. This type of device is known as an interline-transfer array. Information from the entire array of photosites is transferred out in two separate fields.

The clocking waveforms for the CCD202 are shown in Figure 3.3 and Appendix A.

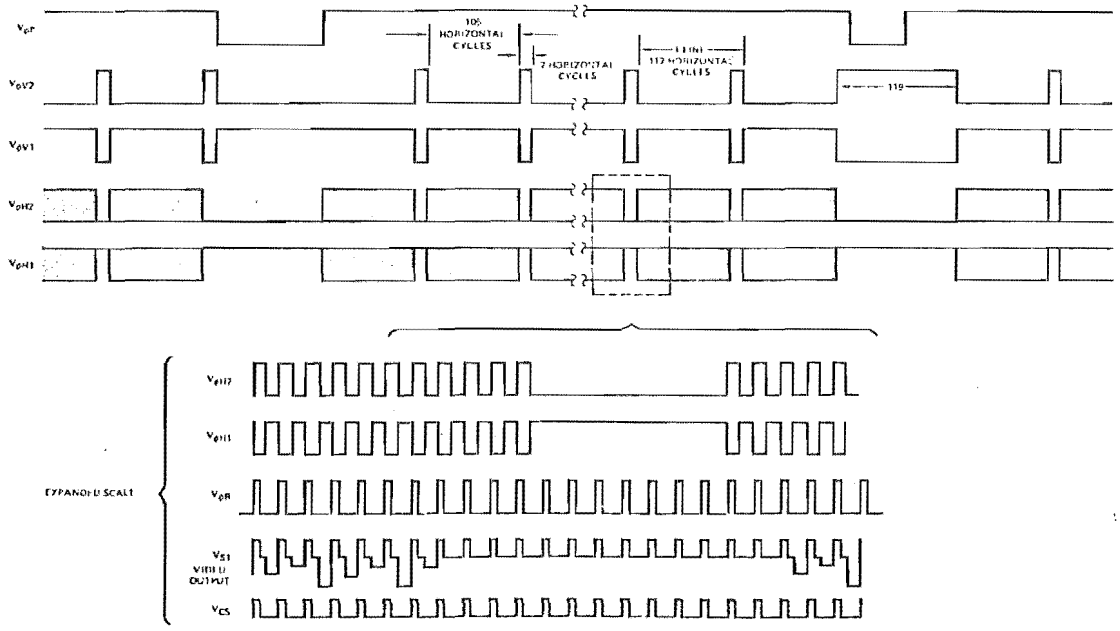

Figure 3.3 CCD clocking waveforms.

An interval of time h, the clock period of the waveform driving the output horizontal ATR, defines the rate at which analog data from the array is delivered to the output stage. The signal ϕ_H is the horizontal clocking waveform. The vertical ATR is clocked by ϕ_V with a time period of H, somewhat greater than 102h for the 100x100 element CCD202. More than 100 horizontal clock pulses are applied when each line is output to purge the horizontal ATR of excess charge left due to charge transfer inefficiencies. The photogate clock, ϕ_p, clocks the transfer of charge from the photosites to the vertical ATRs. It can be seen that first the even, and then the odd numbered photosites are transferred out of the array. While one field is being transferred, photosites in the other field are integrating charge. Thus the two fields in a frame are skewed by the time it takes for half of the photosites to be transferred to the output. This also defines the minimum integration time of the device.

3.2 CCD202 CHARACTERISTICS

The Fairchild CCD202 was the only commercially available solid state two-dimensional imaging array when the UCIPS project was started, but the device has proved to be adequate in the applications we have investigated. Folllowing the analysis made in §1.2.3, the major characteristics of the device are reviewed here.

3.2.1 Physical Architecture

Figure 3.2 gives a general view of the physical

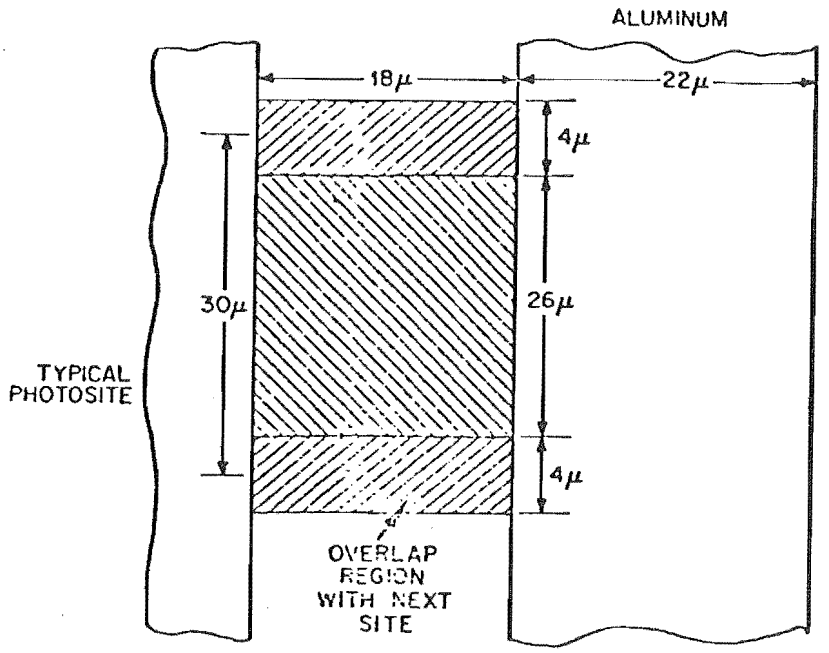

Figure 3.4a Photosite dimensions.

CLASSIFICATIONS – CCD202's are classified in terms of maximum number of image blemishes allowed and their position on the image format. The array is divided into three zones (see Figure), since blemishes near the periphery of the array are usually less objectionable than those near the center. The area of the array has a 4 x 3 aspect ratio. Zone 1 encompasses 16% of the photoelements, Zone 2,33% and Zone 3, 51%.

An image element is blemished if it shows a spurious output ≥ 10% of saturation. The output waveform of the array is analyzed under two conditions. (1) in the dark and (2) at 50% of the saturation level.

BLEMISH SPECIFICATION

CLASSES	ZONE 1	ZONE 2	ZONE 3	TOTAL
A TYPE	0	2	4	6
B TYPE	1	3	5	9

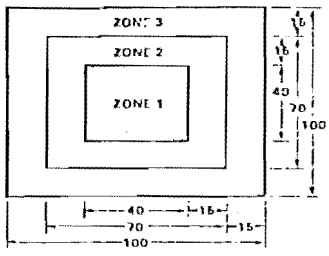

All dimensions in Elements

Figure 3.4b Blemish specification.

organization of the CCD array. The active area of the array is 3mm x 4mm and has 100 vertical columns of sensors separated by vertical analog transport registers. Each column has 100 sensor sites. Figure 3.4a shows the dimensions of each photosite. From this we see that the columns are contiguously sensitive to incident light, and the rows have sensitive areas separated by opaque transport register. Thus only 45% of the active area is sensitive to incident light flux. A blemish specification is given for the device and is defined in Figure 3.4b. All devices that have been used in the UCIPS have satisfied the B type specification.

3.2.2 Electrical Characteristics

A number of factors which characterize the operation of image sensors are defined in §1.2.3. These are now given for the CCD202 array.

(a) Quantum efficiency. This has not been measured for the CCD202 in our laboratory, and a specification is not given by the Fairchild data sheets (Appendix A). However, Gross (1975) reports the spectral responsivity for the CCD201, which is the precursor of the CCD202 and has the same construction. Figure 3.5 indicates that the quantum efficiency approaches 50%. This agrees with data given by Barbe (1975) for a similar 500x1 element array.

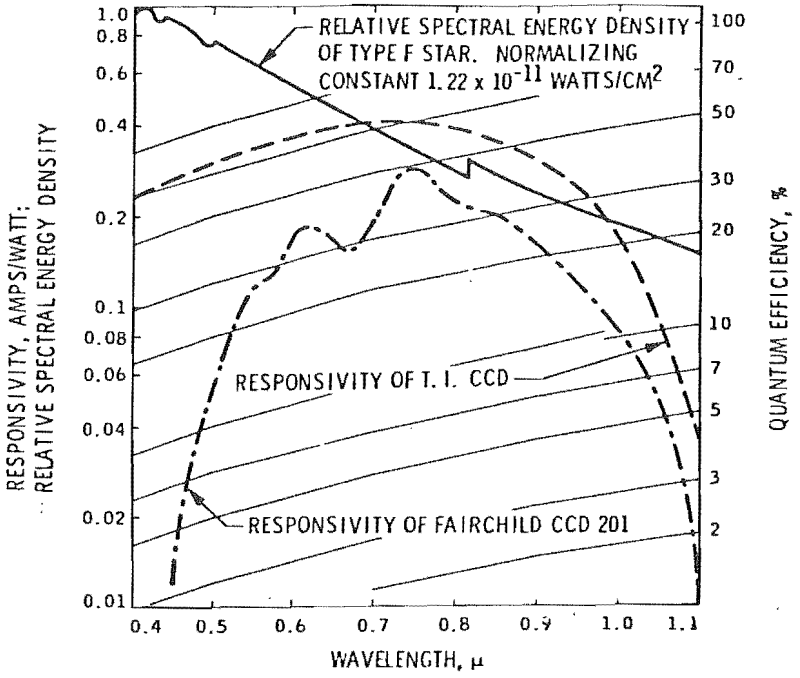

Figure 3.5 Quantum efficiency. (From Gross 1975).

(b) Sensitivity. The responsivity given by Fairchild (1976) is 4V/μJ cm^{-2} with a saturation exposure of 0.4μJ/cm^2 and an integration time of 6.6 ms. Assuming an 8 bit analog-to-digital converter, input radiation of 750 nm wavelength, and a quantum efficiency of 50%, approximately 6×10^4 photons are required to produce a one quantization level signal (see Appendix A). This value is confirmed by data given by Dyck and Jack (1974) in their analysis of the low light performance of the CCD201.

(c) Spectral response. The measured spectral response of the CCD is shown in Figure 3.6. The ripple in the response is caused by the spectral transmittance of the layers on top of the substrate and by multiple reflections within the layers. The refractive indices of the layers are not matched, resulting in a type of interference filter.

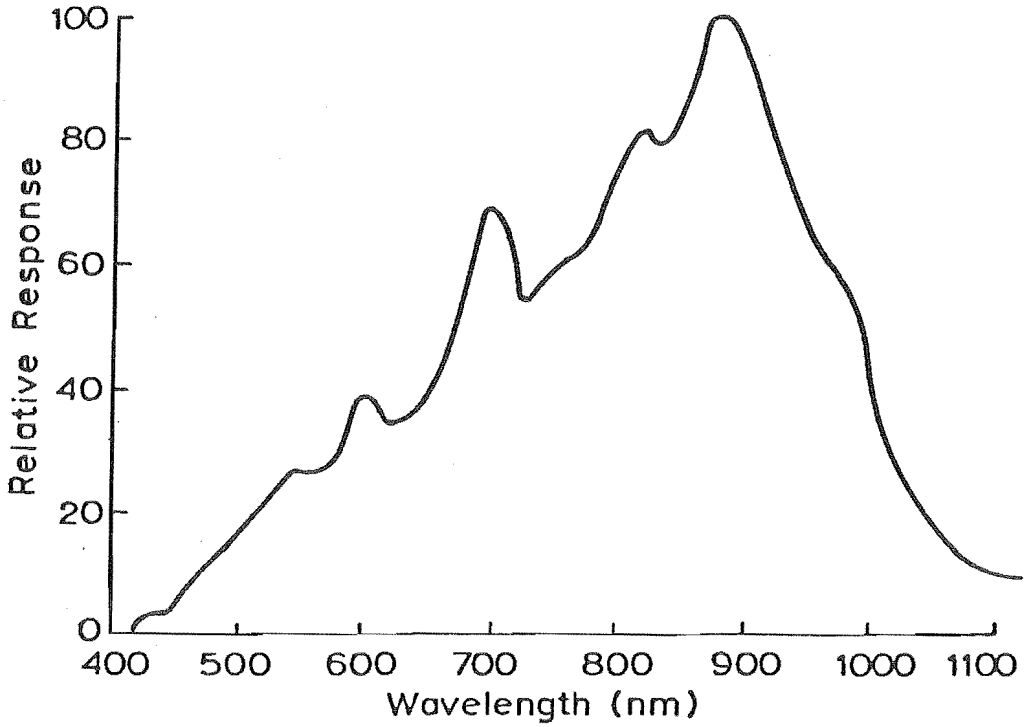

Figure 3.6 The measured spectral response of the CCD camera.

(d) Dynamic range. Murphy (1979) and Hodgson *et al.* (1979) report the experimental determination of the dynamic range at a temperature of 20°C and an integration time of 8 ms. Measurements were made using the 10 bit capability of the analog-to-digital converter (§2.1.1). A mean dark signal of 12.72 quantization levels was measured resulting in a dynamic range of 80:1. This is a factor of 3-4 lower than the specification from Fairchild (1976) and 3-4 higher than the analysis of Dyck and Jack (1974).

(e) Signal-to-noise ratio. Murphy's (1979) analysis of the signal-to-noise ratio is repeated here. The rms fluctuation in the output signal measured at 20°C and 8 ms integration time is given as a maximum of 1.1 quantization level with a mean value of 0.464 quantization level. The ratio of full scale signal-to-noise (§1.2.3) is then between 880:1 and 2086:1.

(f) Detective quantum efficiency. The DQE for the CCD202 has not been determined.

(g) Dark signal. The dark signal measured by Murphy (1979) was found to be 67.38 mV in a full scale value of 5V. This value halved with each temperature reduction of 7.05°C and was found to be stable over a time span of 36 days.

(h) Fixed pattern noise. The fixed pattern noise in the CCD imaging array is caused by a variation in sensitivity between pixels. This is manifested in the extrema by pixels which saturate very quickly (hot spots) and pixels which have no response at all (blemishes). The hot spots are easily determined by inspecting the CCD output when the light input is at a low level and the integration time is fairly long (>1s).

The extra-sensitive pixels show as bright spots on an otherwise dark display. This information is routinely used to eliminate artificially bright pixels from pictures. Pixels with no output can be detected in a similar manner but none has been noticed in the CCD202's inspected to date. Murphy (1979) measured the variation in sensitivity between pixels by using a uniform field and finding the mean and standard deviation of the output. A scaling constant for each pixel in the array was calculated and when applied to subsequent pictures the standard deviation of pixel values was reduced by a factor of 3.

(i) Readout noise. This is not a significant problem with the CCD202 because a compensation output which

contains the clocking signal is available to add in antiphase with the output video to remove clocking noise.

(j) Gamma and linearity. These quantities have not been measured for the CCD202 because a known light source has not been available to provide a calibrated input. Fairchild (1976) states that the gamma is approximately 1.0, but does not provide any linearity specifications. Figure 3.7 shows linearity measurements made by Dyck and Jack (1974).

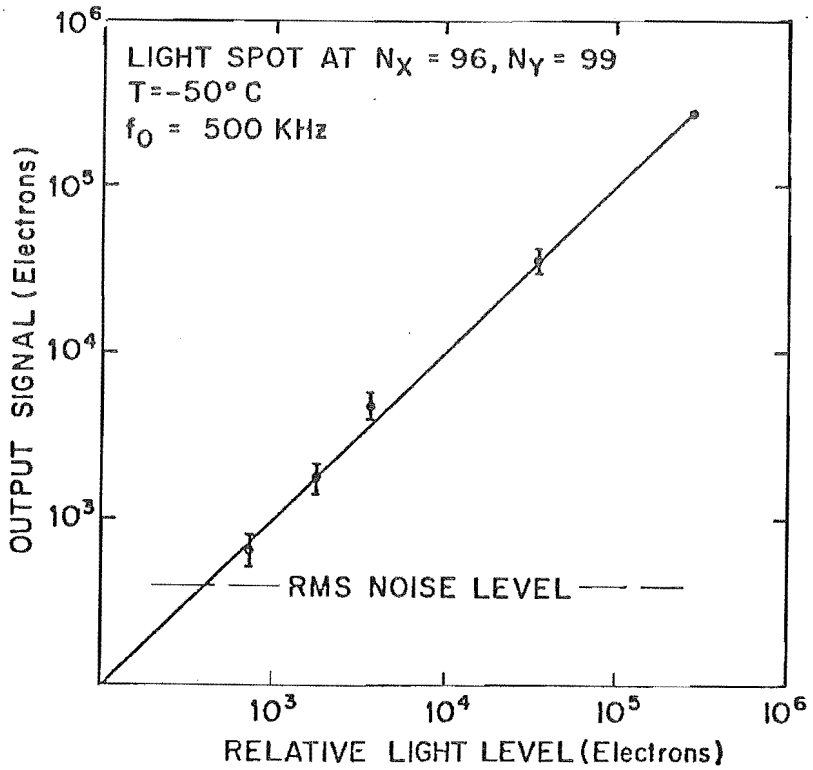

Figure 3.7 Output signal versus relative light level in elections. (From Dyck and Jack 1974).

(k) Modulation transfer function. An alternative expression for the MTF is the contrast transfer function (CTF). This is shown in Figure 3.8. It is primarily caused by the sampling of the image with pixels of finite size and spacing. This is known as the integration transfer function. Other factors which contribute to the CTF are the transfer inefficiency and diffusion transfer function (Barbe 1975). Campana and Barbe (1974) analyze the effect of the MTF on images.

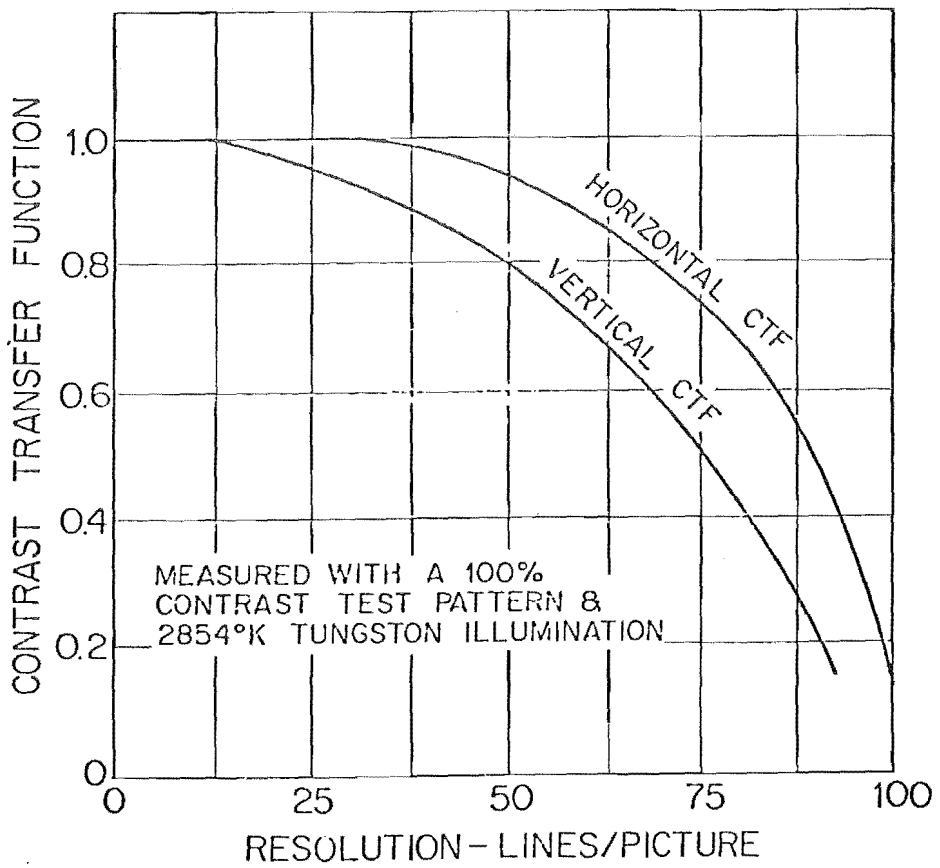

Figure 3.8 Modulation transfer function.

(1) Blooming. An additional characteristic not considered in §1.2.3 is that of blooming. When a storage location becomes saturated the charge can spill over into adjacent photosites. This is particularly evident in the vertical direction where the sensor sites are contiguous and not separated by transport registers as they are in the horizontal direction. Figure 3.9 shows the blooming characteristics of the CCD202. This tends to be a problem, particularly when long time integrations are performed, because the hot spots quickly saturate and spill charge over into adjacent photosites.

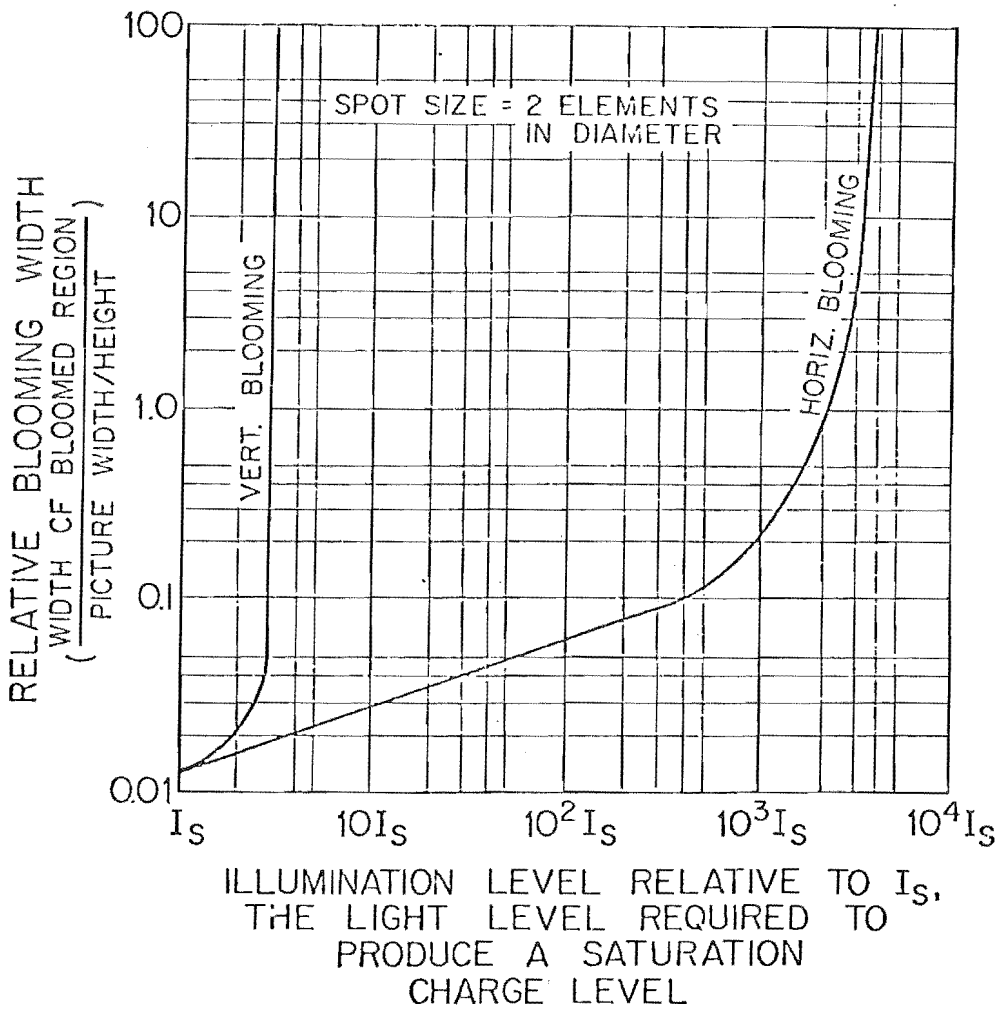

Figure 3.9 Blooming characteristics.

3.3 CONCLUSION

Specifications for the CCD202 have been given because they are relevant when evaluating the quantitative results presented in Chapter 5. Of especial importance is the physical construction of the device, which interposes opaque transport registers between vertical columns of sensors. This construction means that the geometry of the imaging system must be designed so that the image of an unresolvable object extends over more than one pixel if quantitative results are required. Even then, special techniques, such as moving the sensor between successive images and then forming an average, must be undertaken to reduce errors. Accurate geometrical measurements are also difficult to make unless the image is spread over several pixels. Gross (1975) gives an interpolation scheme which allows the measurement of image position on the array to an accuracy of 1/10 of an element. These factors must be taken into account when designing a system which uses the CCD202 or similar device.

CHAPTER 4

OPTICAL ASTRONOMICAL IMAGING

4.0 INTRODUCTION

In 1970 Labeyrie (1970) reported the use of a technique for obtaining diffraction limited resolution in large telescopes. This technique has become known as Speckle Interferometry (SI). Before that, high resolution measurements were restricted to determining the angular extent of objects by the use of the interferometric techniques of Michelson (Michelson and Pease 1920) and Hanbury Brown and Twiss (1956). The resolution of true images was limited to the resolution defined by the seeing conditions. Index of refraction fluctuations in the turbulent atmosphere (poor seeing) caused phase distortions severe enough to make the effective resolution of a large telescope used in the conventional sense many times the diffraction limited spot (the Airy disk). At optical wavelengths, spreading caused by these distortions could be of the order of a few seconds of arc, perhaps 100 times the size of the Airy disk of a 5 metre diameter telescope operating at a wavelength of 500 nm. Therefore, under normal time exposures (greater than one-half second or so), telescopes greater than 2 metres in diameter could resolve objects with no greater precision than their smaller counterparts, providing instead a greater light gathering ability and allowing fainter objects to be observed.

Labeyrie (1970) pointed out that very short time exposures (less than 10 ms) of celestial objects contain information on a scale near the diffraction, or Rayleigh limit. These very short time exposures effectively 'freeze' the turbulent atmosphere and result in an image which has a speckled appearance (see Figure 5.2). The speckled appearance is caused by the atmosphere creating random phases in the radiation from the star. Interference effects caused by the random phases generate the speckle, and Dainty (1975) shows that the statistics of astronomical speckle patterns are similar to those of laser speckle. The term (stellar) Speckle Interferometry (SI) is used here to describe the technique devised by Labeyrie to achieve diffraction limited information from speckled astronomical images.

As shown in §4.2, Labeyrie's process yields not an image but the autocorrelation of the object. This chapter reviews the methods used by Labeyrie and his successors to obtain diffraction limited resolution in poor seeing. The principles of high resolution imaging are briefly reviewed in §4.1, and the remainder of the chapter considers SI and extensions to SI.

4.1 HIGH RESOLUTION IN ASTRONOMY

Milner (1980) has produced an excellent review of the principles of high resolution astronomical imaging. A brief presentation of his work is given here.

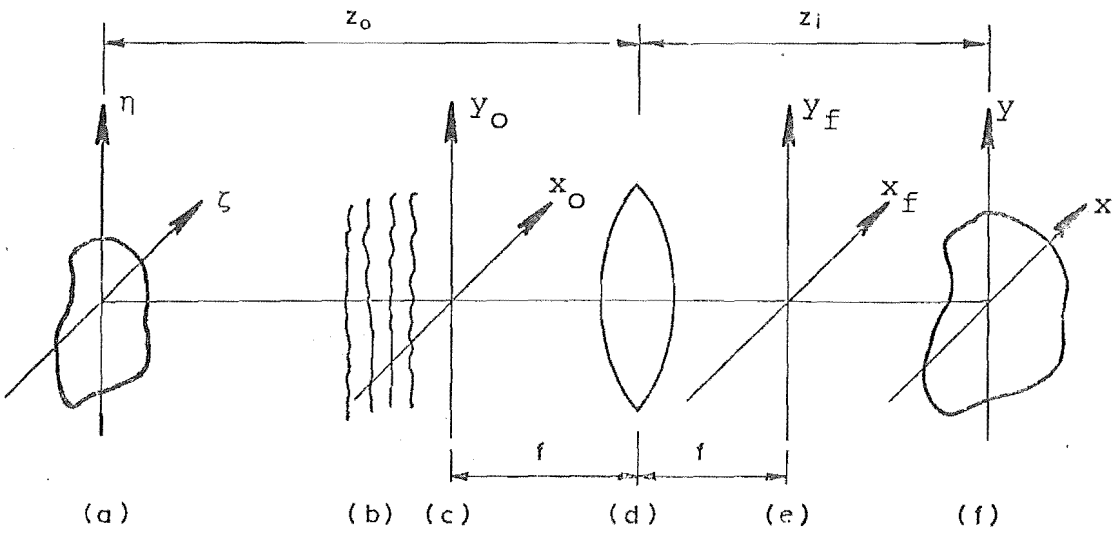

(a) Object plane.

(b) Turbulent media.

(c) Front focal plane.

(d) Lens (receptors).

(e) Rear focal plane.

(f) Image plane.

Figure 4.1 A simple astronomical imaging model.

4.1.1 Astronomical Imaging

The image formation model presented in Figure 1.3 is redrawn here (Figure 4.1) to show the components of the imaging system in the astronomical case. The model consists of the object plane, a randomly fluctuating medium, the lens or receptors, and the image plane. The radiation emitted or reflected by most celestial objects is spatially incoherent. The degree of spatial coherence is determined by considering the temporal correlation between radiating sources within the object having an angular separation of θ as seen by an observer in the image plane. If the correlation is zero for all finite θ, the object is spatially incoherent (Goodman, §6.1, 1968). When this condition applies, only the intensities of the radiating object are of a practical interest because the relative phase between any separated parts of the object is randomly changing (Born and Wolf, §7.1, 1970).

(a) The transmission function. The image produced by an imaging system is characterized at each wavelength by the transmission function. Let $o(\zeta,\eta)$ be the intensity of the radiating sources in the object plane. The average distribution of intensity in the image plane is

$$i(x,y,\lambda,t) = \frac{1}{t_{exp}} \int_0^{\infty} \iint_{-\infty}^{\infty} \int_0^{t_{exp}} o(\zeta,\eta)\ q(\zeta,x,\eta,y,t,\lambda)\, d\lambda\, d\zeta\, d\eta\, dt \qquad (4.1\text{-}1)$$

where t_{exp} is the time for a single exposure.

(b) Quasimonochromatic radiation. In astronomical imaging the bandwidth $\Delta\lambda$ of the received radiation is often

limited such that

$$\Delta\lambda << \bar{\lambda} \tag{4.1-2}$$

where $\bar{\lambda}$ is the mean wavelength of the radiation. Various prescriptions have been given (Dainty 1973; Labeyrie 1976; Schneiderman and Karo 1977; Karo and Schneiderman 1978) which indicate that the bandwidth must be limited so that the optical path difference is less than the coherence length (see §5.2.2). This gives a value for $\frac{\Delta\lambda}{\bar{\lambda}}$ in the range of 0.1 to 0.02. A simple calculation (Appendix F) based on the path differences in radiation measured at the centre and outside of a collector of diameter D, for a field of view θ, and with a mean wavelength $\bar{\lambda}$ confirms that

$$\frac{\Delta\lambda}{\bar{\lambda}} << \frac{4\bar{\lambda}}{D\theta} \tag{4.1-3}$$

When this condition has been met, the radiation is considered to be quasimonochromatic, and the transmission function may be evaluated at the mean wavelength $\bar{\lambda}$.

$$i(x,y,\lambda,t) = \frac{1}{t_{exp}} \iint_{-\infty}^{\infty} \int_{0}^{t_{exp}} o(\zeta,\eta)\ q(\zeta,x,\eta,y,t,\bar{\lambda})\, d\zeta\, d\eta\ dt. \tag{4.1-4}$$

(c) Exposure time. The time for one exposure, denoted by t_{exp}, is called the exposure time. If t_{exp} is short enough, the fluctuating medium is effectively motionless. Then the explicit time dependence in the transmission function may be discarded:

$$i(x,y) = \iint_{-\infty}^{\infty} o(\zeta,\eta)\ q(\zeta,x,\eta,y,\bar{\lambda})\ d\zeta\ d\eta \tag{4.1-5}$$

An implicit time dependence remains. Equation (4.1-5) is true only for exposures short enough that the atmosphere does not change. Over longer time periods the atmosphere does change and therefore successive short exposures separated by sufficient time will be different. In fact, all processing methods reviewed in this chapter require that each short time exposure be statistically independent of all others.

(d) Isoplanacity. The quasimonochromatic transmission function is usually called the point spread function (psf) of the imaging system (§1.2.1). The psf may be regarded as the intensity of the radiation in the image plane when the object is a point source. If the psf is independent of the position of the point source in the object plane during a single exposure, the resultant image is termed to be point spread invariant (psi). The region over which the point source in the object plane may be moved without changing the point spread function is called the isoplanatic region, or isoplanatic patch. For all object and image distributions that are contained within the isoplanatic region, and for quasimonochromatic radiation, it follows by definition that

$$q(\zeta,x,\eta,y,t,\bar{\lambda}) = q(\zeta - x,\ \eta - y,\ t). \qquad (4.1\text{-}6)$$

The distribution of radiation over the image plane due to a quasimonochromatic spatially incoherent distribution of radiating sources in the object plane, small enough to be within the isoplanatic region, is:

$$i(x,y,t) = \frac{1}{t_{exp}} \iint_{-\infty}^{\infty} \int_{0}^{t_{exp}} o(\zeta,\eta)\ q(\zeta-x,\ \eta-y,\ t)\ d\zeta\ d\eta\ dt \qquad (4.1\text{-}7)$$

This is a convolution integral, integrated over the exposure time, and when the exposure time is short enough (as in 4.1-5), (4.1-7) can be conveniently written in short hand form

$$i(x,y) = o(x,y) \ \theta\ q(x,y) \qquad (4.1\text{-}8)$$

where θ denotes convolution.

4.1.2 Diffraction Limited Imaging

The convolution expression in (4.1-8) gives the intensity distribution in the image plane when t_{exp} is short enough for the atmosphere to be effectively motionless. Milner (1980) notes that it is convenient to partition the psf q(x,y) into three parts:

$$q(x,y) = a(x,y) \ \theta\ b(x,y) \ \theta\ h(x,y) \qquad (4.1\text{-}9)$$

where a(x,y) is the psf due to the limited aperture of the receptor, b(x,y) is the psf due to any aberrations in the receptor, and h(x,y) is the psf due to the distorting media between the object and the receptor.

A(u,v), the transfer function of the receptor, is the Fourier transform of a(x,y) and it can be shown (Goodman §6.3, 1968) that for a circular aperture of diameter D

$$A(u,v) = \frac{2}{\pi} \cos^{-1}\left[\frac{(u^2+v^2)^{\frac{1}{2}}\,\bar{\lambda}}{D}\right] - \frac{(u^2+v^2)^{\frac{1}{2}}\,\bar{\lambda}}{D}\sqrt{1 - \frac{(u^2+v^2)\,\bar{\lambda}^2}{D^2}}$$

$$\text{for} \quad u^2 + v^2 \leq \left(\frac{D}{\bar{\lambda}}\right)^2$$

and

$$A(u,v) = 0 \quad \text{for} \quad u^2 + v^2 > \left(\frac{D}{\bar{\lambda}}\right)^2 \tag{4.1-10}$$

If only the effect of the limited aperture on the received image is considered, the image distribution may be defined as

$$e(x,y) = o(x,y) \circledast a(x,y) \ . \tag{4.1-11}$$

The Fourier transform of (4.1-11) is

$$E(u,v) = O(u,v)\, A(u,v) \tag{4.1-12}$$

and when (4.1-10) is substituted into (4.1-12), we see that the image formed with a limited aperture receptor contains no spatial frequencies above $D/\bar{\lambda}$. It is convenient to introduce a quantity $\hat{u}$ to define the range $(u^2 + v^2)^{\frac{1}{2}} < \hat{u}$ of spatial frequencies where A(u,v) has significant value, that is

$$\hat{u} \simeq \frac{D}{\bar{\lambda}} \tag{4.1-13}$$

This upper frequency limit is known as the diffraction limit.

The effect of aberrations with psf b(x,y) on the received image can be considered as above. The image intensity distribution is given by

$$g(x,y) = o(x,y) \circledast b(x,y) \tag{4.1-14}$$

and the Fourier transform of (4.1-14) is

$$G(u,v) = O(u,v)\, B(u,v) \ . \tag{4.1-15}$$

Goodman (§6.4, 1968) shows that the aberrations introduce a phase error into the wavefront passing through the receptor. The effect of this phase error is to lower the contrast of each spatial frequency component of image intensity. In general, although the absolute cut-off of B(u,v) remains constant, the reduction of the high spatial frequency content has a detrimental effect on image quality. Optical instruments are carefully designed to reduce aberrations, thus it is usual to say that a receptor is diffraction limited if it has no measurable aberrations other than those caused by its limited diameter.

4.1.3 Angular Resolution

The diffraction pattern of a uniformly illuminated circular aperture (Figure 4.2a) consists of a bright central disk, known as the Airy disk, surrounded by a series of concentric dark and light rings. This is the diffraction pattern which results from a point source. If two point source objects are viewed, they are said to be just resolvable when the centre of the bright central disk of one falls on the first dark ring of the other (Figure 4.2b). This is the Rayleigh criterion (Jenkins and White 1976), and the minimum angle of resolution is given by

$$\Theta = 1.22 \frac{\bar{\lambda}}{D} \qquad (4.1\text{-}16)$$

where Θ is the angular resolution in radians, $\bar{\lambda}$ is the mid-band wavelength of the received radiation, and D is the diameter of the receptor. Objects which are larger than a point source but smaller in angular extent than the angle given by (4.1-16) are considered to be unresolvable by the

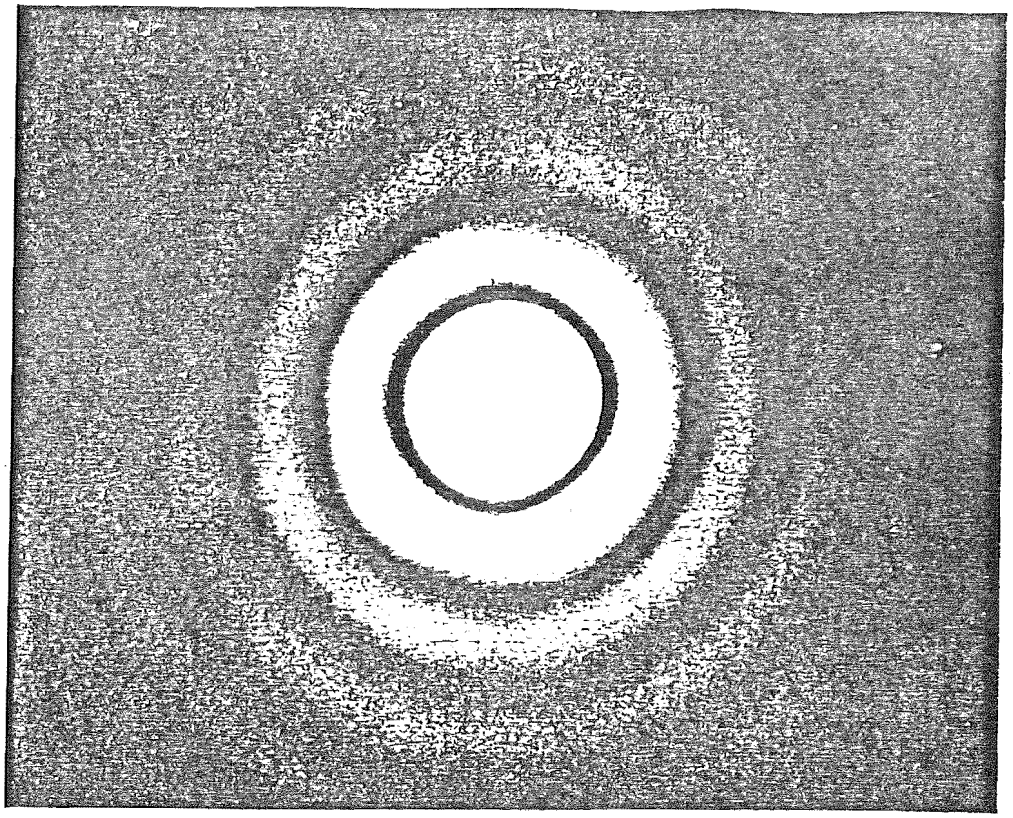

Figure 4.2a A diffraction pattern by a circular aperture.

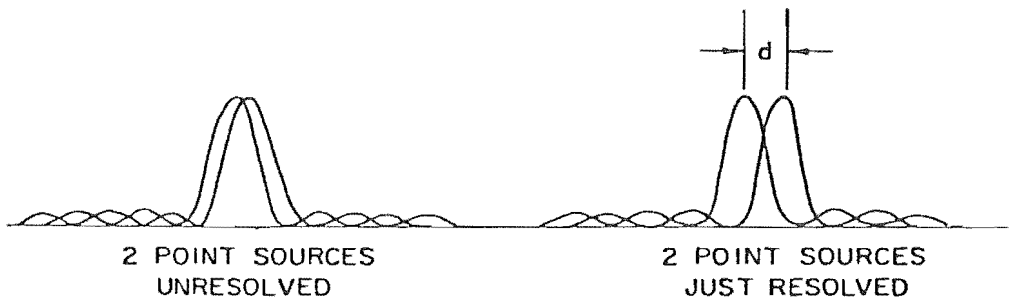

Figure 4.2b Diffraction image of two point sources.
(From Lehmann 1970)

instrument.

4.1.4 The Effect of the Atmosphere

The psf of the distorting media between the object and the receptor has been defined in (4.1-9). The fluctuations of index of refraction in the turbulent atmosphere account for the phase distortions in the plane wave from a celestial object. These produce speckle images in large telescopes when the conditions on exposure time and bandwidth are met. Strohbehn (1971) and Labeyrie (1976) have indicated that fluctuations in temperature cause most of the significant fluctuations in the index of refraction. The fluctuations of temperature are localized in what are known as turbules, and the sizes of these turbules that have most effect at optical wavelengths range between a millimetre to 100 metres at sea level. It is generally accepted for modelling purposes that the scale of the turbules in average seeing conditions is on the order of 10 cm (Labeyrie 1976). When the turbules are the same size or larger than the telescope, speckles are not produced. This is the reason that seeing is not a problem other than to cause image wander and size fluctuations in small (2 to 10 cm) telescopes. When the aperture of the telescope is very large, greater than about 1 metre, there may be several hundred to several thousand turbules, or seeing cells, across the aperture. Each of these turbules introduces a different random phase distortion and when a point source is viewed under these conditions, the Airy disk is destroyed. Elementary Fourier theory shows that the spread of the image is of the order of $\bar{\lambda}/r_o$, where r_o is the average correlation

scale of the incident wave (Fried 1966). The average correlation scale can also be interpreted as the average size of the seeing cell.

(a) Exposure time. The temporal parameter shown in equation (4.1-7) must be considered when imaging through the turbulent media. A short exposure is defined as an interval τ, short enough that the atmosphere is effectively motionless, or frozen. Under average seeing conditions τ is of the order of 5-40 milliseconds (Karo and Schneiderman 1978). It is this time limit that must be observed when forming a short exposure speckle image.

The atmosphere fluctuations are random with another characteristic time T. This is the minimum time interval to ensure statistical independence between successive short exposures. T is also referred to as the redistribution time of the atmosphere and is considered to be about one half second under average seeing conditions (Fried 1966). A long exposure image is one in which the exposure time is longer than T but still short enough that the statistics of the atmosphere are assumed to be stationary.

(b) Isoplanacity. Equation (4.1-7) is written for the case of quasimonochromatic spatially incoherent radiation, and for the condition of isoplanacity. Labeyrie (1976) indicates that the size of the isoplanatic patch is mainly dependent on the presence of turbulent layers at high altitude. The angular extent of the patch is generally considered to be of the order of 3 to 10 arc-seconds. Korff *et al.* (1975) have considered the theoretical aspects of isoplanacity assuming an atmosphere model, and

Nisenson and Stachnik (1978) and Lohmann and Weigelt (1979) have made measurements which verify this general view.

(c) Transmission function. To be able to write the transmission function in a more general form, it is convenient to define f(x,y) as the true image of the object resolved to the diffraction limit of the telescope including any system aberrations. Using (4.1-8) and (4.1-9),

$$f(x,y) = o(x,y) \,\theta\, a(x,y) \,\theta\, b(x,y) \qquad (4.1\text{-}17)$$

where a(x,y) is the psf due to the limited aperture of the receptor and b(x,y) is the psf due to any aberrations in the receptor. A long time exposure, given by (4.1-4), of an object viewed under the conditions of isoplanacity given by (4.1-6) reduces to

$$i(x,y,t) = \frac{1}{t_{exp}} \int_{-\infty}^{\infty} \int_{0}^{t_{exp}} f(\zeta,\eta)\; h(\zeta-x,\eta-y,t)\; d\zeta\, d\eta\, dt\,. \qquad (4.1\text{-}18)$$

where $h(\zeta-x,\eta-y,t)$ is the psf due to the turbulent atmosphere. The long time exposure image can also be written as the ensemble average of many short exposures,

$$\langle i(x,y)\rangle = \int_{-\infty}^{\infty} f(\zeta,\eta)\;\; \langle h(\zeta-x,\eta-y)\rangle\; d\zeta\; d\eta \qquad (4.1\text{-}19)$$

where $\langle\cdot\rangle$ denotes an ensemble average.

(d) Modulation transfer function. The modulation transfer function (MTF) for long and short exposures (Labeyrie 1976) has been experimentally determined (Gezarie *et al.* 1972; Dainty and Scaddan 1975; Karo and Schneiderman 1976) and theoretically studied (Hufnagel and Stanley 1964;

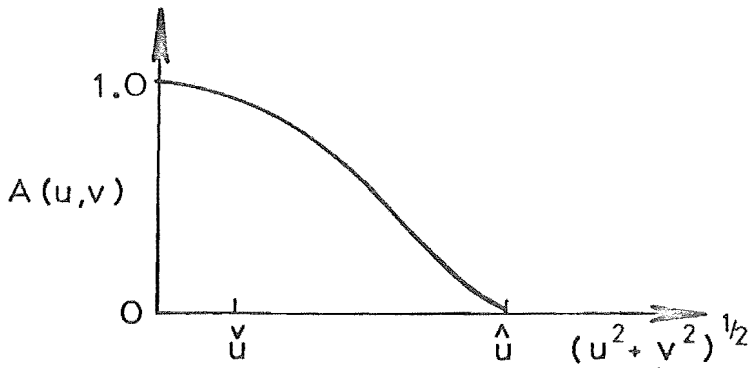

Figure 4.3a MTF of aperture of diameter D.

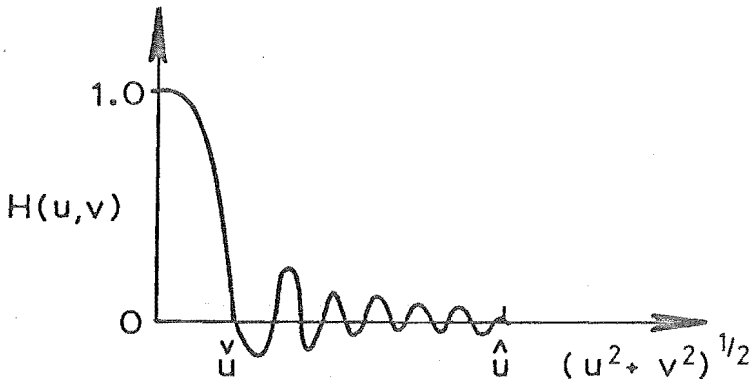

Figure 4.3b Short exposure MTF.

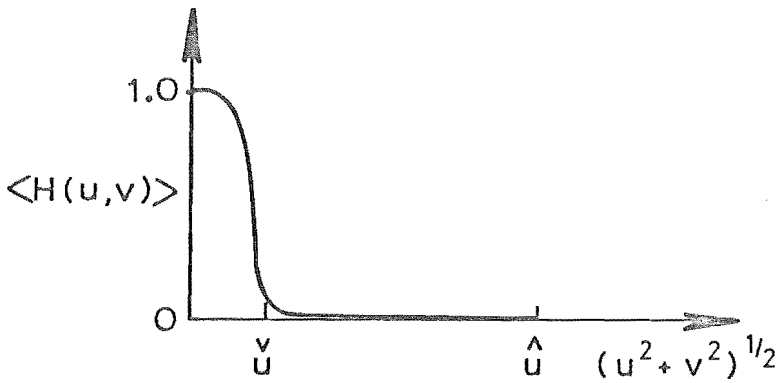

Figure 4.3c Long exposure MTF.

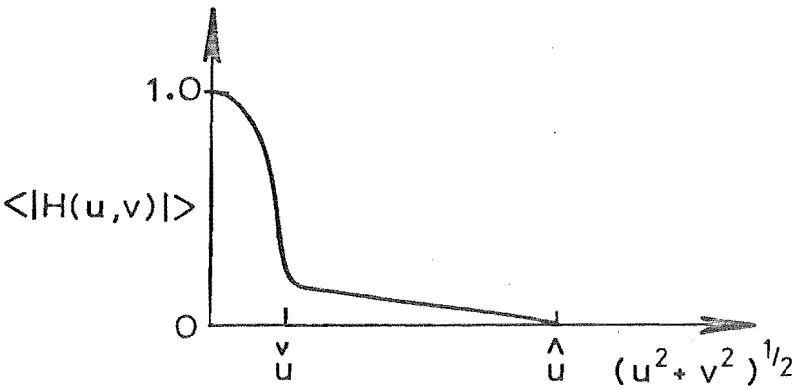

Figure 4.3d Mean square short exposure MTF.

Dainty 1973; Miller *et al.* 1973; Korff *et al.* 1975). The Fourier transform of (4.1-9) is the transfer function of the system psf

$$Q(u,v) = A(u,v)\ B(u,v)\ H(u,v) \qquad (4.1\text{-}20)$$

where A(u,v) and B(u,v) are the transfer functions of the limited aperture and the aberrations of the receptor, and H(u,v) is the transfer function of the atmosphere. Figure 4.3a shows the MTF for an aperture of diameter D, with a cut-off frequency of $\hat{u} = D/\bar{\lambda}$. Figure 4.3b is the modulation transfer function H(u,v) for a short exposure. The short exposure MTF features a central spike with surrounding feet extending out to and beyond the diffraction limit. The MTF for the long exposure case (Figure 4.3c) shows the frequency components above $\check{u}$ are cancelled in the averaging process. The upper frequency cut-off in the long exposure case is the *seeing limited* frequency and is given by

$$\check{u} = r_o/\bar{\lambda} \qquad (4.1\text{-}21)$$

where r_o is the average characteristic size of the seeing cells.

4.2 SPECKLE INTERFEROMETRY (Labeyrie)

A photographic exposure of an image of a point source formed by a large earthbound telescope is blurred unless the exposure is short enough to freeze the atmospherically induced phase distortions. If the bandwidth of the short exposure radiation satisfies the quasimonochromatic condition of (4.1-2), the resultant image is characterized by a speckled appearance. Speckle images have been

considered theoretically by Korff (1973), Dainty (1973, 1975) and Miller *et al.* (1973). They have shown that when typical turbulence models are used (Strohbehn 1971; Young 1974; Labeyrie 1976), the scale of the speckles is near the telescope resolution limit.

Starting from equation (4.1-18), the observed short exposure, narrow band image intensity is

$$i_n(x,y) = \int_{-\infty}^{\infty}\int f(\zeta,\eta)\, h_n(x-\zeta, y-\eta)\, d\zeta\, d\eta \qquad (4.2\text{-}1)$$

where $i_n(x,y)$ is the nth observed speckle image in a series of observation from 1 to N,

$f(\zeta,\eta)$ is the true image of the object resolved to the diffraction limit of the telescope, and

$h_n(x-\zeta, y-\eta)$ is the point spread function of the atmosphere at the time of the nth image.

The bandwidth of the radiation is limited to 10-70 nm (Karo and Schneiderman 1978)* and the exposure time is short enough that the atmosphere is motionless.

The convolution relationship (4.2-1) is conveniently written

$$i_n(x,y) = f(x,y) \circledast h_n(x,y). \qquad (4.2\text{-}2)$$

---

* Labeyrie (1970) reports that the "Temporal coherence requirements are fulfilled by using a 300 to 3000 Å bandpass filter..." It is suspected that this is a misprint because subsequent accounts reporting the use of the method indicate that a much narrower bandwidth is used, e.g. 250 Å by Gezari *et al.* (1972).

The Fourier transform of (4.2-2) yields

$$I_n(u,v) = F(u,v)\, H_n(u,v) \qquad (4.2\text{-}3)$$

where u,v are spatial frequencies in the x and y directions. The square of the magnitude of the Fourier transform is the power spectrum

$$|I_n(u,v)|^2 = |F(u,v)|^2 |H_n(u,v)|^2 \ . \qquad (4.2\text{-}4)$$

Labeyrie's method of processing requires that each speckle image be Fourier transformed, as in equation (4.2-3), and the power spectrum calculated. All phase information is lost in this process. A statistical average power spectrum is sought. As many individual power spectra as is convenient are combined to give the average power spectrum

$$|I(u,v)|^2 = \langle |I_n(u,v)|^2 \rangle = |F(u,v)|^2 \langle |H(u,v)|^2 \rangle \qquad (4.2\text{-}5)$$

where $\langle \cdot \rangle$ denotes an ensemble average.

$\langle |H(u,v)|^2 \rangle$ can be found by repeating the measurements when f(x,y) is a two dimensional delta function. This is achieved when the object is a single unresolvable star. This star, called the reference, is chosen to be as near the object star as possible. A series of reference observations are made shortly before or after the object measurements to ensure that the statistical properties of the atmosphere are nearly alike in each case. $\langle |H(u,v)|^2 \rangle$ can also be calculated from model equations developed by Korff (1973) and Dainty (1975). Dividing equation (4.2-5) by $\langle |H(u,v)|^2 \rangle$ yields $|F(u,v)|^2$. The inverse Fourier transform results in the autocorrelation,

ff(x,y), of the object:

$$f(x,y) \overset{\star}{\times} f(x,y) = ff(x,y) = \mathcal{F}^{-1} |F(u,v)|^2$$

$$= \int_{-\infty}^{\infty}\int f(x',y')\ f(x'+x,y'+y)\ dx'\ dy'$$

where $\overset{\star}{\times}$ denotes the correlation operator and $\mathcal{F}^{-1}$ the inverse Fourier transform. Therefore, Labeyrie's Speckle Interferometry technique gives the autocorrelation of the object which has proved useful for determining the diameters of resolvable stars and the separations of binary stars. This technique is now used routinely at a number of observatories (Gezari *et al.* 1972; Bonneau and Labeyrie 1973; Labeyrie 1974; Labeyrie *et al.* 1974; Beddoes *et al.* 1976; McAlister 1976, 1977a, 1977b, 1977c, 1978, 1979; Balega and Tikhonov 1977; Blazit *et al.* 1977; Hubard 1978; Morgan *et al.* 1978; Nisenson and Stachnik 1978; Scaddan *et al.* 1978; Schneiderman and Karo 1978; Weigelt 1978a; McAlister and Degioia 1979).

Figure 4.3d shows the transfer function for the Speckle Interferometry process. Squaring the amplitude spectra before averaging preserves the frequency information out to the diffraction limit. As has been noted, this operation destroys the phase and results in the auto-correlation of the object field when the inverse Fourier transform is computed.

The invention of Speckle Interferometry in 1970 marks the start of modern high resolution imaging techniques in astronomy. The processing has been performed both optically and digitally, and the technique is being used in

the infrared wavelengths (Selby *et al.* 1979). Because the process creates only the autocorrelation of the object, the technique is useful for centro-symmetric objects and objects for which the ambiguity caused by the lack of phase is not a problem. It has been used extensively to determine the separation of binary stars. For other objects, such as extended sources and clusters, the need exists for a technique which gives an image. The following sections deal with attempts to reconstruct real images from speckle images.

4.3 LARGE FIELD SPECKLE INTERFEROMETRY (Liu and Lohmann)

Liu and Lohmann (1973) (see also Lohmann and Weigelt 1975; Weigelt 1978) derive phase information from the long exposure image and use this information to help 'unravel' the autocorrelation produced by speckle interferometry. Using a single dimension, the nth short exposure speckle image (equation 4.2-1) can be written

$$i_n(x) = \int_{-\infty}^{\infty} F(u)\, H_n(u) \exp(2\pi jux)\, du \qquad (4.3\text{-}1)$$

where $F(u)$ and $H_n(u)$ are the Fourier transforms of the true diffraction limited image and the point spread function respectively, and the integral is the inverse Fourier transform. This image contains information out to the frequency determined by the aperture of the telescope, $\hat{u}$. A long time exposure image

$$i_L(x) = \int_{-\infty}^{\infty} F(u) \langle H(u) \rangle \exp(2\pi jux)\, du \qquad (4.3\text{-}2)$$

is deteriorated by the average point spread function $\langle H(u) \rangle$ but contains information up to the seeing limited frequency

$\check{u}$ as given by (4.1-20). It is the phase information associated with this image that Liu and Lohmann proposed to use to help resolve the autocorrelation generated ambiguity.

This technique is applicable for fields that contain a dark background interrupted by relatively small islands. One of these islands must be a point source, called the reference star, and the extent of the object field , including all the islands, must lie within the isoplanatic patch. If there are M islands in the object, one of which is the reference, the autocorrelation produced by Speckle Interferometry contains $M(M-1)+1$ islands. The problem is to determine which of these are the correct M islands. A long exposure of the M islands, if the seeing disk is not too large, can often show the number of objects plus the location of the reference object. A hard limited photograph of this long exposure is produced which has a transmissivity of one at the locations of the objects and zero elsewhere. This image is placed over the autocorrelation 'image' (a multiplication process when done with film) and the product of the hard limited image and the autocorrelation results in the true image of the object. Liu and Lohmann (1973) show that the reference star is required to reduce the probability of false peaks in the image as a result of the multiplication. They also suggest performing the processing twice with different stars chosen as the reference star. Comparing results of these two procedures allows the false peaks in each to be determined. Weigelt (1975) gives a method which varies the brightness of the reference star to help resolve

false peaks and to identify the correct star pattern. Weigelt (1975) reports model experiments which suggest that the width of objects that can be imaged with this technique may be 10 arcseconds in extent. Also, the effect of non-isoplanasy over this range is not great on the reconstructed object field. It seems clear from his results that it is necessary for the isolated islands of brightness to be far enough apart so that the seeing disk does not obscure more than one island. It is also necessary that the seeing be good enough to allow identification of the reference star.

4.4 SPECKLE HOLOGRAPHY (Bates, Gough and Napier)

Bates *et al.* (1973) note that the fringe visibility function obtained through Speckle Interferometry, given by

$$|F(u,v)|^2 = \frac{|I(u,v)|^2}{\langle |H(u,v)|^2 \rangle} \qquad (4.4\text{-}1)$$

where F(u,v), I(u,v) and H(u,v) are defined in §4.2, can, for certain classes of objects, be compared to a Fourier transform hologram. One can think of a Fraunhofer or Fourier hologram as the intensity of the combined complex visibility due to an object and a reference. When the separation between the object and the reference is greater than either of their extents, the object may be reconstructed if the hologram is illuminated by a beam similar to the original reference beam (Stroke 1969; Goodman 1968; Bates and Gough 1975). The correct relationship between the object and the reference permits the unique reconstruction of the object from the intensity of the complex visibility.

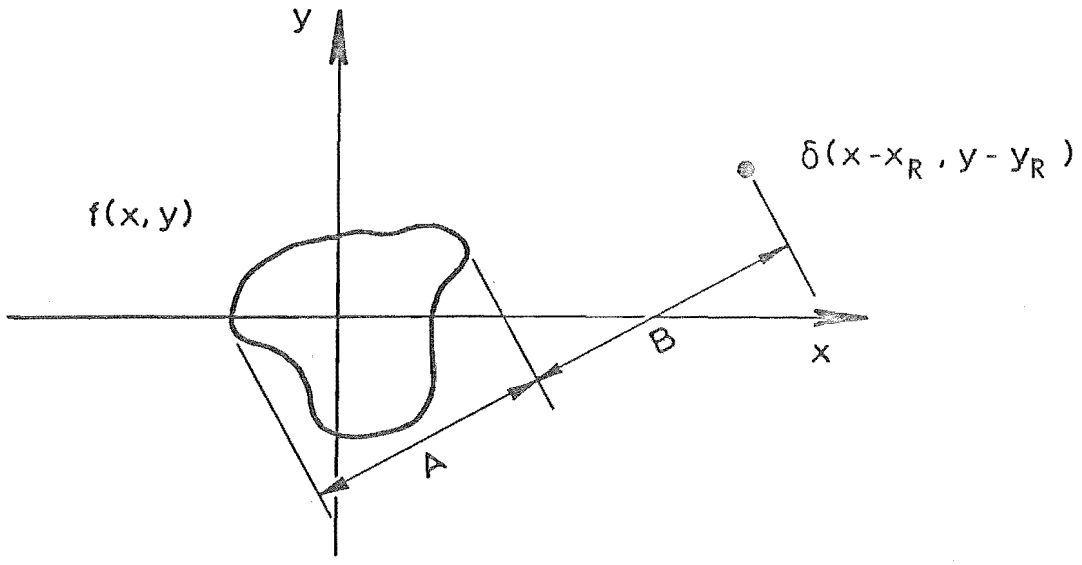

Figure 4.4a An object consisting of an extended point and a point source.

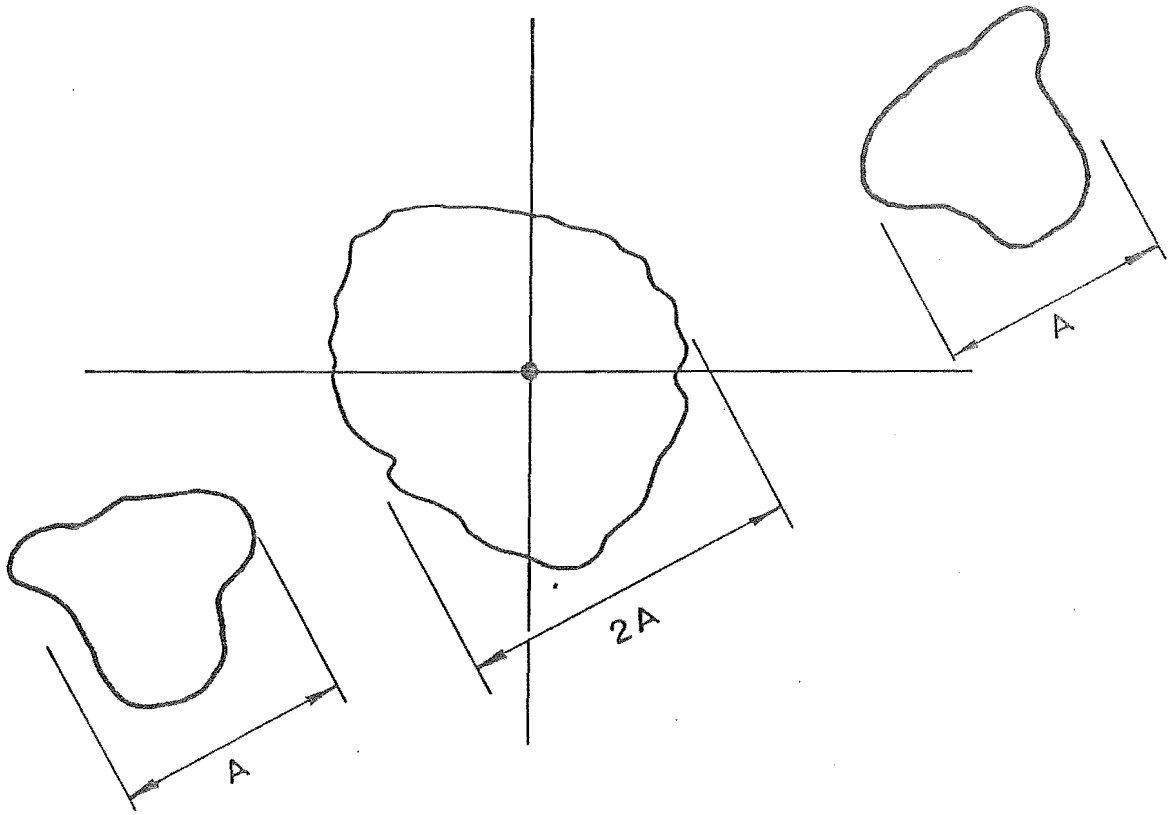

Figure 4.4b Speckle holography reconstruction.

To perform speckle holography, as shown by Gough and Bates (1974), the object, which may be an arbitrary extended object, and a point source reference must lie within the isoplanatic patch. The extended object is represented by $f(x,y)$ and the reference by $\delta(x-x_R, y-y_R)$, as shown in Figure 4.4a. A is the extent of $f(x,y)$ along the axis which bisects the two objects, and B is the mininum separation between them. The total object $f_T(x,y)$ can be written

$$f_T(x,y) = f(x,y) + \delta(x-x_R, y-y_R) \qquad (4.4\text{-}2)$$

The power spectrum (fringe visibility function) produced by Speckle Interferometry (equation 4.4-1) is Fourier transformed to give the autocorrelation written as

$$f_T f_T(x,y) = \delta(x,y) + ff(x,y) + f(x+x_R,\ y+y_R) + f(-x+x_R,\ -y+y_R) \qquad (4.4\text{-}3)$$

This is shown in Figure 4.4b where the central part contains the first two terms in (4.4-3), the third term is the true image, and the fourth term is the mirror of the true image. Provided that the separation between the object and the reference is greater than the extent of the object, the true image and the central autocorrelation terms are separated.

Gough and Bates (1974) have simulated the speckle holography process in an optical laboratory, and Weigelt (1978b) has reported results of speckle holography measurements of the stars Zeta Cancri and ADS 3358. These results confirm the validity of the optical simulations and the usefulness of the speckle holography technique in astronomical imaging.

Disadvantages of this method are that both the object of interest and the unresolvable point source reference must lie within the isoplanatic patch, and that the separation criterion established above must be met. This limits the number of astronomical objects for which the technique is useful.

4.5 KNOX AND THOMPSON ALGORITHM

Knox and Thompson (1974) propose that the phase required to reconstruct an image from speckle images can be obtained from the characteristics of the statistical auto-correlation of the speckle image transform. In the transform plane, in one dimension, the mean square image transform from Labeyrie's Speckle Interferometry is

$$\langle |I(u)| \rangle^2 = |F(u)|^2 \langle |H(u)|^2 \rangle \qquad (4.5\text{-}1)$$

where $I(u)$, $F(u)$, and $H(u)$ are the Fourier transforms of the nth speckle image, the true diffraction limited image, and the atmosphere point spread function at the time of the nth speckle image. The $\langle \cdot \rangle$ denote an average over an ensemble of N speckle images, and the n subscripts have been dropped. The statistical autocorrelation of the image transform is written

$$\langle I(u)\ I^*(u+\Delta) \rangle = F(u)\ F^*(u+\Delta)\ \langle H(u)\ H^*(u+\Delta) \rangle \qquad (4.5\text{-}2)$$

where Δ is a fixed, small displacement. When the separation is zero ($\Delta = 0$) equations (4.5-1) and (4.5-2) are identical and the phase information is lost. For a finite Δ the phase information is still present.

Following the development of Milner (1980), a new function L(u) is defined

$$L(u) = \frac{\langle I(u)\ I^*(u + \Delta)\rangle}{\langle H(u)\ H^*(u + \Delta)\rangle} \qquad (4.5\text{-}3)$$

The denominator in (4.5-3) must be greater than the random noise in the system for all spatial frequencies where the numerator is not zero. Knox and Thompson (1974) show that the denominator does have a significant value for all pairs of points u and u + Δ located anywhere along the u axis out to the diffraction limit of the telescope, providing Δ is less than the Fourier transform of the seeing disk. It follows from (4.5-1) and (4.5-2) that

$$L(u) = F(u)\ F^*(u + \Delta). \qquad (4.5\text{-}4)$$

L(u) is complex, and if only the phase term of (4.5-4) is considered,

$$\text{phase } L(u) = \text{phase } F(u) - \text{phase } F(u + \Delta) \qquad (4.5\text{-}5)$$

The phase of the true diffraction limited image at zero frequency is zero because the image is real, i.e.

$$\text{phase } F(0) = 0. \qquad (4.5\text{-}6)$$

So when u = 0,

$$\text{phase } F(\Delta) = -\text{phase } L(0) \qquad (4.5\text{-}7)$$

and it follows that for any non-negative integer i

$$\text{phase } F((i + 1)\Delta) = \text{phase } F(i\Delta) - \text{phase } L(i\Delta). \qquad (4.5\text{-}8)$$

This shows that the phase difference between two nearby points of the object transform can be determined by

measuring the complex correlation between those two points in the transform of the image photographs. The phase of F(u) can therefore be calculated at intervals of Δ, and the $|F(u)|$ can be determined by Labeyrie's Speckle Interferometry. In principle, F(u) can then be determined from a set of speckle images.

The Knox-Thompson method suffers from a sensitivity to noise (Ehn and Nisenson 1975). Any real imaging system will have noise in the signal which causes errors when calculating the phase differences (Miller 1977). If the phase difference calculations were independent, the errors caused by noise would tend to cancel. However, the phase difference between any two points is not independent of the other phase differences and so errors tend to accumulate rather than cancel. For this reason, the higher spatial frequencies, which are important to the reconstruction of detail in the image, have errors in their phases. Procedures for reducing the cumulative effects of errors are being investigated (Knox 1976; Nisenson and Stachnik 1979) but these have not been reported to be successful. Stachnik *et al.* (1977) report the use of the method in the reconstruction of solar surface features but no other reports of its use with real astronomical data have been made.

4.6 LYNDS, WORDEN AND HARVEY METHOD

Lynds *et al.* (1976) were the first to have reconstructed an image of an extended object from speckle images. They resolved an image of Alpha Orionis (Betelgeuse)

which shows surface structure in the form of limb darkening.

It is convenient to think of a speckle image of an extended object as a collection of independent, distorted, diffraction limited images superimposed in image space. Providing the object is within the isoplanatic patch, each speckle is considered to be the true diffraction limited image convolved with the average speckle due to a point source with additive noise. Thus, a speckle image can be written

$$i(x,y) = \Delta(x,y) \circledast g(x,y) + N \qquad (4.6\text{-}1)$$

where $\Delta(x,y)$ is a sum of delta functions positioned at the centre of the speckles, $g(x,y)$ represents the true diffraction limited image convolved with the average speckle due to an unresolvable object, and N is the background noise. $\Delta(x,y)$ can be defined:

$$\Delta(x,y) = \sum_{k=1}^{K} s_k \, \delta(x - x_k, \, y - y_k) \qquad (4.6\text{-}2)$$

where s_k and (x_k,y_k) are the intensity and position in image space of the kth speckle. In practice the speckle image is not a collection of widely separated bright speckles. However, a few speckles are usually significantly brighter than the others and if these can be identified, the rest can be considered as background noise. Lynds *et al.* (1976) form an estimate of $\Delta(x,y)$ by computing the Fourier transform of $i(x,y)$, low pass filtering it, and computing the inverse transform. This discriminates against the background noise and the less bright speckles, producing a number of easily identifiable bright spots whose centres are the positions of

the delta functions in $\hat{\Delta}(x,y)$, an estimate of $\Delta(x,y)$. This estimate can be written

$$\hat{\Delta}(x,y) = \sum_{l=1}^{L} s_l \, \delta(x - x_l, \, y - y_l) \qquad (4.6\text{-}3)$$

where s_l and (x_l,y_l) are the intensity and coordinates in image space of the lth speckle, and $L \leq K$. The speckle image can then be written

$$i(x,y) = \hat{\Delta}(x,y) \, \theta \, g(x,y) + \tilde{N} \qquad (4.6\text{-}4)$$

where $\tilde{N}$ consists of the less bright speckles plus the background noise from (4.6-1).

The cross-correlation of $\hat{\Delta}(x,y)$ with $i(x,y)$ produces a *correlated image* (Bates and Milner 1978, 1979). The correlated image $\hat{g}(x,y)$ is the average of the bright speckles identified in a single speckle image centered at the origin of correlation space. This term is surrounded by cross-correlation terms located away from the centre. The spacing of these cross-correlation terms depends on the spacing of the delta functions in $\hat{\Delta}(x,y)$. The average of the bright speckles, $\hat{g}(x,y)$, is an estimate of the true image, $f(x,y)$, convolved with the average speckle due to a point source. Lynds *et al.* (1976) performed this process over many statistically independent short exposures, and averaged many correlated images to get a better estimate of the distorted image $\langle\hat{g}(x,y)\rangle$. When the process is repeated with an unresolvable object (as in SI), the average speckle due to a point source is found and an inverse filtering procedure, such as Wiener filtering, can be used to recover the diffraction limited image $f(x,y)$.

McDonnell and Bates (1976) observe that since the speckles of an extended object like Betelgeuse are larger than the speckles of an unresolvable object, an uncertainty exists in determining their centres when forming $\hat{\Delta}(x,y)$. They define a function which represents the distribution of errors in the estimates of the centres of the speckles. This function is combined with the psf of an unresolvable object to form a composite psf. An estimate of this composite psf is derived from the average of a number of the LWH estimates of $\hat{g}(x,y)$. The average correlated image is then Weiner filtered by this composite psf. McDonnell and Bates (1976) claim that the image of Betelgeuse obtained in this way has less distortion and more surface structure than the result achieved by Lynds *et al.* (1976).

The Lynds, Worden and Harvey method has been used by Wilkerson and Worden (1977) in further studies of Alpha Orionis to verify the results of the original paper. Their data, taken two years after that of Lynds *et al.* (1976), show no change in the radius and do not reveal any statistically significant surface structure. Worden (1975, 1976), and Welter and Worden (1979) use the method to determine the angular diameter of other supergiant stars. In each of these cases, the angular diameter of the stellar disk is only a few resolution elements. Worden *et al.* (1976) indicate that the method is useful only for objects up to about 3-5 Airy disks in diameter because for larger objects the speckles tend to overlap. Bright speckles then become difficult to identify in the speckle image.

4.7 SPECKLE MASKING (Weigelt)

The speckle masking technique (Weigelt 1977) reconstructs real images from speckle images of double stars where one star is brighter than the other. Two part objects where one object is unresolvable can also be reconstructed by this technique. The method makes use of the instantaneous point spread function to reconstruct the phase of the object. As in speckle holography, a reference is used to reconstruct the phase, but the speckle masking method differs in that the reference is produced synthetically by the preprocessing method explained below.

When double stars are to be imaged by Weigelt's method, two pieces of *a priori* information are needed. These are: (i) the separation and (ii) the relative brightness of the two stars. Speckle Interferometry (§4.2) gives this information. The first step in the speckle masking process is to non-linearly preprocess each speckle image to give two new images. One of these, depending on the relative brightness of the two stars, contains two spatially separated parts: (i) the speckle image of the double star, and (ii) a distribution which is the instantaneous point spread function. The preprocessing step which converts the speckle image into the two new images can be performed using several different methods described by Weigelt (1977). One is illustrated here.

The object, resolved to the diffraction limit of the telescope, is a binary star given by

$$f(x,y) = A\,\delta(x,y) + B\,\delta(x - x_o, y - y_o) \qquad (4.7\text{-}1)$$

where A and B are the brightness of the two stars, and (x_o, y_o) is the position of the second star in image space. The first is located at the origin. The nth speckle image is the true resolved image convolved with the psf of the atmosphere at the time of the nth image,

$$i_n(x,y) = f(x,y) \circledast h_n(x,y) \qquad (4.7\text{-}2)$$

Equation (4.7-2) can be written (in the single dimension)

$$i_n(x) = A\, h_n(x) + B\, h_n(x - x_o) \qquad (4.7\text{-}3)$$

A new speckle image $s_n^-(x)$ is found by shifting $i_n(x)$ an amount x_R (where x_R is large compared to x_o) and adding to it the difference between $i_n(x)$ and $i_n(x - x_o)$.

$$s_n^-(x) = \begin{cases} [i_n(x - x_R) + (i_n(x) - i_n(x - x_o))] & \text{for } [\ldots] \geq 0 \\ 0 & \text{for } [\ldots] < 0 \end{cases} \qquad (4.7\text{-}4)$$

The second new speckle image is

$$s_n^+(x) = \begin{cases} [i_n(x - x_R) + (i_n(x) - i_n(x + x_o))] & \text{for } [\ldots] \geq 0 \\ 0 & \text{for } [\ldots] < 0 \end{cases} \qquad (4.7\text{-}5)$$

Note that if the value in $[\,\cdot\,]$ is negative, the $s_n^{\pm}$ are set to zero. The $i_n(x - x_R)$ in equations (4.7-4, 4.7-5) are the unchanged object speckle image, and the rest are approximately the instantaneous point spread functions of the atmosphere at t_n, the time of the nth speckle image.

By substituting (4.7-3) into (4.7-4) and (4.7-5)

we obtain

$$s_n^-(x) = \begin{cases} [i_n(x - x_R) + (A\, h_n(x) + B\, h_n(x - x_o) \\ \quad - A\, h_n(x - x_o) - B\, h_n(x - 2x_o))], & \text{if } [\ldots] \geq 0 \\ 0, & \text{if } [\ldots] < 0 \end{cases} \tag{4.7-6}$$

$$s_n^+(x) = \begin{cases} [i_n(x - x_R) + (A\, h_n(x) + B\, h_n(x - x_o) \\ \quad - A\, h_n(x + x_o) - B\, h_n(x))], & \text{if } [\ldots] \geq 0 \\ 0, & \text{if } [\ldots] < 0 \end{cases} \tag{4.7.7}$$

If A > B:

$$s_n^-(x) \simeq i_n(x - x_R) + A\, h_n(x), \quad s_n^+ \text{ useless} \tag{4.7-8}$$

If B > A:

$$s_n^+(x) \simeq i_n(x - x_R) + B\, h_n(x - x_o), \quad s_n^- \text{ useless} \tag{4.7-9}$$

Equation (4.7-8) shows that when A > B, the term $B\, h_n(x - x_o)$ in equation (4.7-6) is destroyed by the term $A\, h_n(x - x_o)$. The desired term $A\, h_n(x)$ is reduced by the term $B\, h_n(x - 2x_o)$ and so the approximation for $s_n^-(x)$ holds. The function $s_n^+(x)$, equation (4.7-7), is useless because no cancelling of terms occurs. A dual relationship holds for B > A between equation (4.7-7) and (4.7-6) to give (4.7-9). In any event, one of the processes will produce the desired two component speckle image, now called $s_n(x)$. If there is no *a priori* information about the brightness of the two stars, the image reconstruction procedure must be carried out twice, first with the functions s_n^- and then with s_n^+. One class of

functions yields a good image of a double star, and the other a poor image with three stars. The process described above is repeated for a number of speckle images $i_n(x)$ and from the derived functions $s_n(x)$ the image of the double star can be reconstructed.

The derived functions $s_n(x)$ are Fourier transformed and the average power spectra calculated

$$\begin{aligned} &\langle |\mathcal{F}\,[s_n(x)]|^2\rangle \simeq \langle |\mathcal{F}\,[i_n(x-x_R) + A\,h_n(x)]|^2\rangle \\ &= \langle |\mathcal{F}\,[f(x-x_R) \ominus h_n(x) + A\,h_n(x)]|^2\rangle \\ &= \langle |\mathcal{F}\,[f(x-x_R) \ominus h_n(x) + A\ \delta(x) \ominus h_n(x)]|^2\rangle \\ &= \langle |\mathcal{F}\,[(f(x-x_R) + A\,\delta(x)) \ominus h_n(x)]|^2\rangle \\ &= |\mathcal{F}\,[f(x-x_R) + A\,\delta(x)]|^2\ \langle |\mathcal{F}\,[h_n(x)]|^2\rangle \end{aligned} \tag{4.7-10}$$

where $\mathcal{F}$ denotes the Fourier transform and $\ominus$ convolution. The ensemble average MTF of the atmosphere, $\langle |\mathcal{F}[h_n(x)]|^2\rangle$, is found by conventional Speckle Interferometry (§4.2). Equation (4.7-10) is divided by this quantity and the inverse Fourier transform is calculated to find the autocorrelation.

$$\begin{aligned} &[f(x-x_R) + A\,\delta(x)] \mathbin{\text{⋋}} [f(x-x_R) + A\,\delta(x)] \\ &= ff(x) + A^2\,\delta(x) + A\,f(x-x_R) + A\,f(-x-x_R) \end{aligned} \tag{4.7-11}$$

where ⋋ is the correlation operator. The first two terms in (4.7-11) are the autocorrelation of the object and a bright central spike. The next two terms are the object and its mirror image displaced the distance x_R from the centre.

The translation x_R must be sufficiently large to allow the image to be separated from the central terms.

Weigelt (1977) obtains good results when simulating the speckle masking technique, however, no reports have been made of its practical use.

4.8 AUTOCORRELATION, CROSS-CORRELATION SUBTRACTION (Worden)

Worden *et al.* (1977) have proposed a method to determine the autocorrelation of an object which does not require an independent estimate of the mean square atmosphere or a reference star. The method produces an autocorrelation because no phase information is used in the reconstruction. Welter and Worden (1978) and Fante (1979) have shown that the method destroys frequency information below the seeing limited frequency. This limits the application of the method to objects smaller than the seeing disk. Angular diameter information can be reconstructed, however, on objects substantially larger than the diffraction limit.

The simple viewpoint of Lynds *et al.* (1976) that the speckle image can be considered to be the convolution of the diffraction limited image and a field of delta functions is followed. In the single dimension, the nth speckle image is written

$$i_n(x) = f(x) \ominus \Delta(x) \qquad (4.8\text{-}1)$$

where $f(x)$ is the diffraction limited image, and $\Delta(x)$ a field of delta functions at the centres of the speckles in $i_n(x)$. $\Delta(x)$ is written

$$\Delta(x) = \sum_k s_k \, \delta(x - x_k) \qquad (4.8\text{-}2)$$

where s_k is the intensity of the kth speckle, and x_k is its position in image space. (Note that subscripts n on the k have been dropped.) The Fourier transform of (4.8-1) is

$$I_n(u) = F(u) \, \overline{\Delta}(u) \qquad (4.8\text{-}3)$$

and the autocorrelation of the speckle image is

$$i_n(x) \mathbin{\not\star} i_n(x) = i_n i_n(x) = \mathcal{F}^{-1}[I_n(u) \, I_n(-u)] \qquad (4.8\text{-}4)$$

where $\not\star$ denotes the correlation operator, and $\mathcal{F}^{-1}$ the inverse Fourier transform. Substituting (4.8-3) into (4.8-4)

$$i_n i_n(x) = \mathcal{F}^{-1}[F(u) \, \overline{\Delta}(u) \, F(-u) \, \overline{\Delta}(-u)]. \qquad (4.8\text{-}5)$$

Note that the function $\Delta(x)$ has non-zero values only at $x = x_k$, thus

$$\overline{\Delta}(u) = \mathcal{F}[\Delta(x)] = \mathcal{F}\left[\sum_k s_k \, \delta(x - x_k)\right]$$

$$= \sum_k s_k \exp(-2\pi j \, x_k \, u) \qquad (4.8\text{-}6)$$

Therefore,

$$\overline{\Delta}(u) \, \overline{\Delta}(-u) = \sum_k s_k \exp(-2\pi j \, x_k \, u) \sum_k s_k \exp(2\pi j \, x_k \, u)$$

$$= \sum_k s_k^2 + \sum_n \sum_{m \neq n} s_n \, s_m \exp[-2\pi j (x_n - x_m) u] \qquad (4.8\text{-}7)$$

By the substitution of (4.8-7) into (4.8-5),

$$ii(x) = F^{-1}\left[F(u)\ F(-u)\left(\sum_k s_k^2 + \sum_n \sum_{m\neq n} s_n\, s_m \cdot \exp[-2\pi j(x_n - x_m)u]\right)\right]$$

$$= F^{-1}\left[\sum_k s_k^2\ F(u)F(-u)\right] + F^{-1}\left(F(u)\ F(-u)\cdot \sum_n \sum_{m\neq n} s_n\, s_m \exp[-2\pi j\ (x_n - x_m)u]\right)$$

$$= \sum_k s_k^2\ ff(x) + F^{-1}\left[F(u)\ F(-u) \sum_n \sum_{m\neq n} s_n\, s_m \cdot \exp[-2\pi j(x_n - x_m)u]\right] \qquad (4.8\text{-}8)$$

The first term in (4.8-8) is the autocorrelation of the diffraction limited image multiplied by a constant. The second term can be shown to be closely approximated by the mean cross-correlation between two frames separated sufficiently in time so that the psf in each is uncorrelated.

Consider the cross-correlation of two speckle images,

$$i_n(x) \ \text{⋋}\ i_n'(x) = F^{-1}\left[F(u)\ F(-u)\ \bar{\Delta}\ (u)\ \bar{\Delta}'\ (u)\right]$$

$$= F^{-1}\left[F(u)\ F(-u) \sum_k s_k \exp(-2\pi j\ x_k\ u) \sum_{k'} s_{k'} \exp(2\pi j\ x_{k'}, u)\right]$$

$$= F^{-1}\left[F(u)\ F(-u) \sum_k \sum_{k'} s_k\, s_{k'}, \exp[-2\pi j(x_k - x_{k'},)]u\right] \qquad (4.8\text{-}9)$$

The similarity between (4.8-9) and the second term of (4.8-8) is obvious. Worden *et al.* (1977) make the reasonable assumptions that: (i) on the average the locations of individual speckles in a single frame are uncorrelated, and (ii) the mean character of the atmosphere psf is well defined when averaged over a number of speckle images on a time frame of seconds. These are the same assumptions implicit in all speckle interferometric techniques. When this is true, (4.8-9) should give a value approximately equal to the second term in (4.8-8). Thus Worden *et al.* (1977) assert that the object correlation is

$$f(x) \not\times f(x) \simeq \langle i(x) \not\times i(x) \rangle - \langle i(x) \not\times i'(x) \rangle \qquad (4.8\text{-}10)$$

Welter and Worden (1978) have provided a more rigorous proof of this method using a more complete speckle model than the simplistic model of Lynds *et al.* (1976). They also have shown that it is necessary to carefully normalize and centre speckle frames before applying the autocorrelation, cross-correlation subtraction method.

Worden *et al.* (1977) and Worden and Stein (1979) have presented results of using the technique on the asteroids Vesta and Pallas. In these cases, the sizes of the objects are of the order of the seeing disk and the slightly larger than expected angular diameter measurements have been attributed to the fact that the method destroys information below the seeing limited frequency (Fante 1979).

4.9 BATES AND MILNER SPECKLE MASK AND CORRELATION PROCESSING

Bates and Milner (1978, 1979) have developed two processing techniques which they called *speckle mask processing* (not to be confused with Weigelt's speckle masking §4.7) and *correlation processing*. The speckle mask processing is an extension of the idea of Lynds *et al.* (1976; §4.6), that the speckles in a speckle image are distorted versions of the true image resolved to the diffraction limit of the telescope. Speckle mask processing is extended by applying techniques developed by x-ray crystallographers for Patterson map analysis (Lipson and Cochran 1966). Baldwin and Warner (1976) recognized that if one star in a cluster is appreciably brighter than the others, the autocorrelation is dominated by cross-correlations of this star with the others. The information derived from speckle mask processing is used with this idea to perform correlation processing.

Bates and Milner (1979) reason that most celestial objects of interest are apt to be unresolvable rather than resolvable objects as treated by Lynds *et al.* (1976). Further, if the object of interest is a cluster of stars, where the extent of the cluster is resolvable but the individual stars within the cluster are unresolvable, the diffraction limited image is a collection of Airy disks. The essential information in any such image can be represented by an array of delta functions, the relative positions and intensities of which correspond to the relative positions and intensities of the Airy disks. Invoking the viewpoint of Lynds *et al.* (1976) that a speckle

is a distorted version of the diffraction limited image, it must be true that the speckle image of a star cluster contains speckles in the same relative positions and intensities as the diffraction limited object. Furthermore, if one of the stars in the cluster is appreciably brighter than the others, the brightest speckles are likely to correspond to the brightest star.

A speckle mask is formed by finding the bright speckles in a speckle image. This produces an array of delta functions where the intensities and the positions correspond to the intensities and positions of the bright speckles. This is equivalent to $\hat{\Delta}(x,y)$ equation (4.6-3). This speckle mask is cross-correlated with the speckle image, either optically (Bates *et al.* 1978), or, more preferably, using digital techniques (Bates and Milner 1979). This cross-correlation generates a correlated image, as in Lynds *et al.* (1976), which is a distorted version of the desired star cluster. In general, a few of the stars in the cluster are usually recognizable, and this is called the *basic star pattern.* The signal-to-noise ratio in the basic star pattern can be enhanced by averaging a number of correlated images formed from statistically independent speckle images. Bates and Milner (1978) report, however, that faint stars can seldom be recovered using this method. Correlation processing as described below is then used to recover the faint stars.

The basic star pattern produced by the speckle masking method as described above is recognized to have distortion in the relative intensities and positions of the

recognized stars. However, the key point is that a (partial) true image has been reconstructed which shows some of the stars in the cluster. This information is then used with the autocorrelation produced by conventional Speckle Interferometry. The autocorrelation provides accurate relative positions and intensities. The basic star pattern is used to resolve the ambiguity in position due to the loss of phase in the SI technique, a process called *correlation processing*.

Correlation processing is in essence a pattern recognition exercise. The basic star pattern generated by the speckle masking method is used to search the autocorrelation for matching patterns. When a matching pattern is found, the distortions in the positions and the intensities of the basic star pattern can be corrected. In addition, stars not recovered by the speckle masking method are recovered each time a matching pattern is found in the autocorrelation. The position of the new star in the cluster is given by the centre of correlation space, and the intensity is derived by computing the auto-correlation value from the basic (corrected) star pattern.

Bates and Milner (1978, 1979) report several simulations of the speckle mask processing method and correlation processing. These methods have not yet been used with real astronomical data.

4.10 FIENUP ALGORITHM

Fienup (1978, 1979) describes an algorithm in which the image of a real, non-negative object is reconstructed

from Fourier modulus data. The technique is to find a Fourier transform pair

$$G(u,v) = \mathcal{F}[g(x,y)] \qquad (4.10\text{-}1)$$

that satisfies all known constraints that

(i) in the Fourier domain $|G(u,v)|$ equals the measured Fourier modulus, and

(ii) in the object domain $g(x,y)$ be non-negative.

An auxiliary object domain constraint, which may be applied to help in finding solutions, is that the diameter of the object is one-half the diameter of the autocorrelation. Fienup's algorithm, which is iterative and relies only on the constraints mentioned above, is a modification of an iterative super-resolution technique by Gerchberg and Saxton (1972) and Gerchberg (1974). The Gerchberg and Saxton (1972) approach is known as an error energy reduction method and is illustrated in Figure 4.5a.

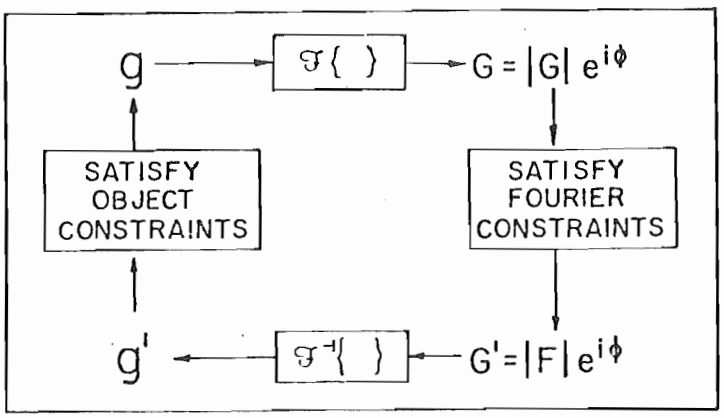

Figure 4.5a Block diagram of error reduction approach. (From Fienup 1979)

With this approach, one iteratively transforms back and forth between object and Fourier domains, satisfying the constraints in each domain before returning to the other domain. In the Fourier domain, G'(u,v) is found by replacing the modulus of G(u,v) by the measured modulus |F(u,v)| obtained by SI. In the object domain, g(x,y) is formed by forcing g'(x,y) to be zero where it violates object domain restraints.

The mean-squared error at each iteration can be defined in the Fourier domain by

$$E_F = \frac{\int_{\infty}^{\infty}\int [|G(u,v)| - |F(u,v)|]^2 \, du \, dv}{\int_{-\infty}^{\infty}\int |F(u,v)|^2 \, du \, dv} \qquad (4.10\text{-}2)$$

and in the object domain by

$$E_O^2 = \frac{\int\int_{\gamma_E} [g'(x,y)]^2 \, dx \, dy}{\int_{-\infty}^{\infty}\int [g'(x,y)]^2 \, dx \, dy} \qquad (4.10\text{-}3)$$

where γ_E includes all points at which g'(x,y) violates the constraints. Gerchberg and Saxton (1972) show that the mean-squared error can only decrease or at least not increase at each iteration. Fienup (1978, 1979) notes that while the mean-squared error decreases rapidly at first, it decreases extremely slowly for later iterations, and he proposes the input-output concept shown in Figure 4.5b to speed up the convergence.

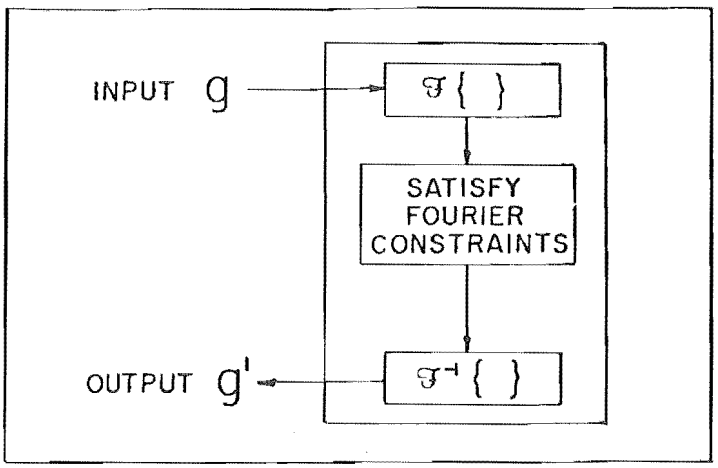

Figure 4.5b Block diagram for the input-output concept. (From Fienup 1979)

In this case, instead of using the output of the previous iteration (limited by the object constraints) as the input for the next iteration, the operator manipulates the input in such a way to force the ouput to be non-negative. A useful method of choosing the next input is given by

$$g_{k+1}(x,y) = \begin{cases} g'_k(x,y), & (x,y) \notin \gamma_E \\ g_k(x,y) - \psi\, g'_k(x,y), & (x,y) \in \gamma_E \end{cases} \qquad (4.10\text{-}4)$$

where γ_E is defined as in (4.10-3) and ψ is a constant. It is noted that changing the method of choosing $g_{k+1}(x,y)$ every few iterations works better than using only one stragegy.

Fienup (1978, 1979) gives results of using the method with and without noise in simulated speckle data and the results of a blind test where simulated Fourier modulus data was supplied by another research organization. His results, which contain remarkable similarities to the original object also contain significant differences. This is particularly evident where two reconstructions have been performed from

the same Fourier modulus data.

The major objection to this type of reconstruction is that although the object found satisfies all constraints, there is no guarantee of its uniqueness. This is shown in the object reconstructed from noisy data. Fienup (1978, 1979) does not claim that his solutions are unique for this case but does point out that the reconstructed images do share a number of common features and correlate well with the original object. To be able to adequately show that the algorithm does not suffer from the question of the uniqueness of the result, a large number of reconstructions of the same Fourier modulus data, perhaps by different people, should be averaged and then the mean-square error criteria evaluated. This has not yet been done.

4.11 CLEAN (Högbom)

In this section a method developed for processing brightness distributions produced by synthetic aperture techniques in radio astronomy is described. Although this process, CLEAN (Högbom 1974), has not been reported to have been used in the processing of optical astronomical data, it is described here as a prelude to its use in the procedures described in Chapter 6. Högbom (1974) and Schwartz (1978) describe the use of CLEAN in removing the effect of sidelobes in the synthesized beam from the data. In the jargon of radio astronomy, CLEAN is used to subtractively de-convolve a 'dirty map' of the brightness distribution to produce a 'clean map'. The dirty map is the measured brightness distribution and is equal to the

true brightness distribution convolved with the 'dirty beam' containing sidelobes. This can be written

$$DM = f(x,y) \circledcirc DB \qquad (4.11\text{-}1)$$

where DM is the dirty map, f(x,y) is the true brightness distribution, and DB is the dirty beam with sidelobes. The convolution operation is denoted by $\circledcirc$.

When the similarity between equation (4.11-1) and (4.2-2) is noted, the description of CLEAN can be given in terms of its analogy in optical image processing. The measured image, i(x,y) is the convolution of the diffraction limited image f(x,y) with the point spread function of the atmosphere h(x,y). Therefore, the analogy exists between the measured image and the dirty map, the true diffraction limited image and the true synthesized brightness distribution, and the point spread function of the atmosphere and the dirty synthetic beam.

Högbom (1974) shows that CLEAN does not work when the source is very complex. The expected distribution must be a relatively sparce array of bright points in a dark background. As noted in §4.9, when the object of interest is a collection of unresolvable point sources, the diffraction limited image is a collection of Airy disks. The essential information in any such image is an array of delta functions, with relative positions and intensities corresponding to the relative positions and intensities of the Airy disks. When this array is convolved with the psf of the atmosphere, the measured image is the result.

The CLEAN procedure can be described in a few simple steps.

(i) Find the image $i(x,y)$ and the point spread function $h(x,y)$.

(ii) Subtract over the whole image a point spread function pattern which is centered at the point where $i(x,y)$ has its maximum value I_o. The maximum in the point spread function is normalized to ρI_o. The fraction ρ is called the loop gain. This step is represented by

$$i'(x,y) = i(x,y) - \alpha\, h(x - x_o,\ y - y_o) \qquad (4.11\text{-}2)$$

where $i'(x,y)$ is the image remaining, and α a scaling factor so that the intensity of the brightest point in $h(x,y) = \rho I_o$. The (x_o,y_o) is the shift required to move the brightest point in $h(x,y)$ to the position of the brightest point $i(x,y)$.

(iii) Repeat step (ii), each time replacing $i(x,y)$ with $i'(x,y)$ generated in the previous iteration. Stop the iterations when the current value of I_o is no longer significant with respect to the general noise level of the image.

(iv) Add to the final remaining image all those components that were removed in step (ii), but do this in the form of the ideal image, generally as delta functions, at the appropriate positions and intensities.

Each individual iteration will represent a correct interpretation if the value I_o did in fact contain a contribution with an amplitude of at least $\rho\ I_o$ from some real object. The process can be visualized as one in which

a ceiling is lowered through the I_o while continuously shaving off all that protrudes above the ceiling along with any 'sidelobes' of the point spread function. The best choice for the loop gain ρ is one that is very small. However, Högbom (1974) indicates that for typical sparse bright sources generally reconstructed by synthetic aperture radio telescopes, a value of $\rho = \frac{1}{2}$ is reasonable. A value of $\rho = 1$ can be used in the simplest cases.

The procedure outlined above can be visualized in a single dimension as shown in Figure 4.6. Figure 4.6a shows the unresolvable real image f(x,y) consisting of two delta functions, and 4.6b the point spread function of the system h(x,y). The convolution of f(x,y) with h(x,y) is shown in 4.6c. The dotted shape in 4.6c is the proportion of the point spread function which is subtracted from the image i(x,y). The result, i'(x,y), is shown in 4.6d with the second subtractive element shown dotted. Four iterations are performed and the result of adding the amounts subtracted, as delta functions, to the final remainder is shown in Figure 4.6g. Note that CLEAN is a subtractive deconvolution procedure and therefore generally limited in application to objects which are isolated. This type of deconvolution is contrasted by the more conventional deconvolution procedures (e.g. Weiner filtering) which are multiplicative and do not have this object domain constraint.

The CLEAN procedure has been discussed here as a technique to be used in processing images obtained in optical astronomy. An obvious difficulty exists which prevents its use in 'normal' speckle image processing.

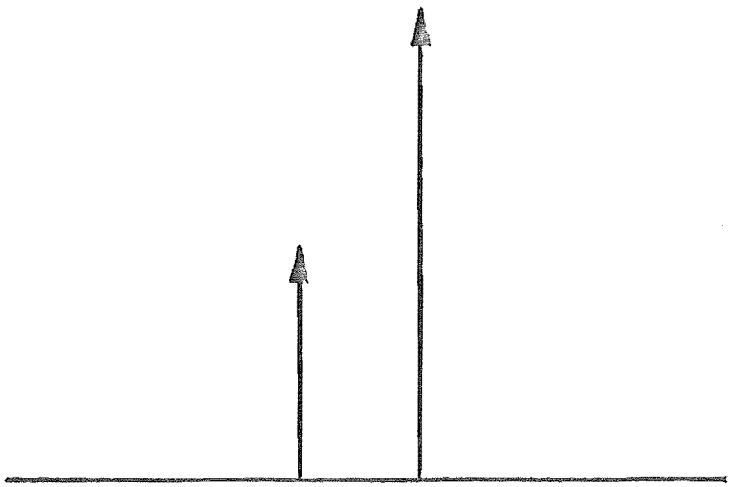

Figure 4.6a Unresolvable image f(x,y).

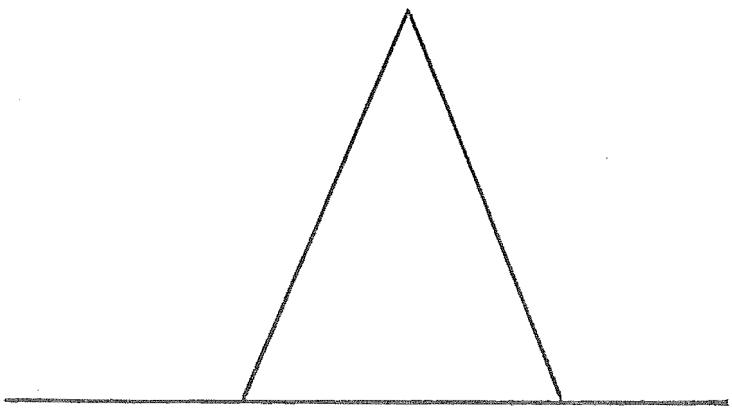

Figure 4.6b Point spread function h(x,y).

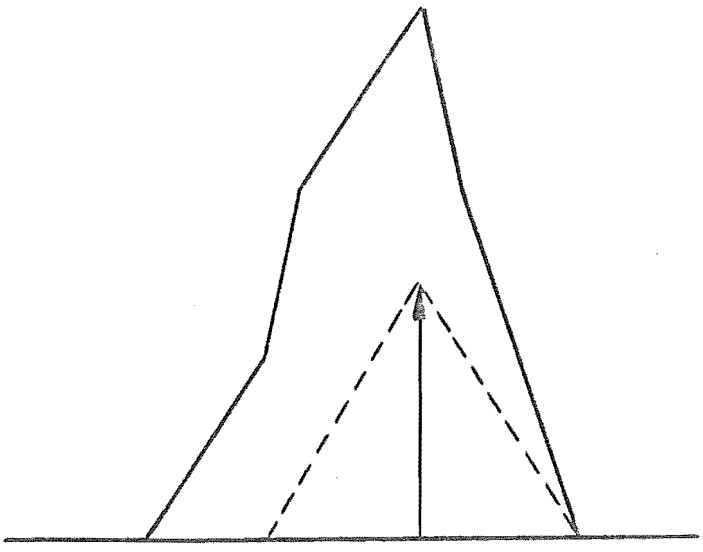

Figure 4.6c Measured image i(x,y).

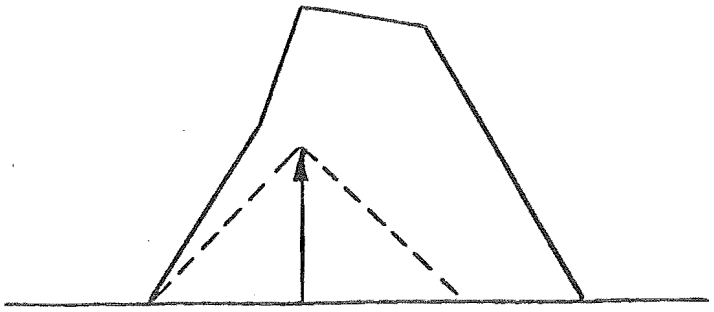

Figure 4.6d Image after one CLEAN subtraction.

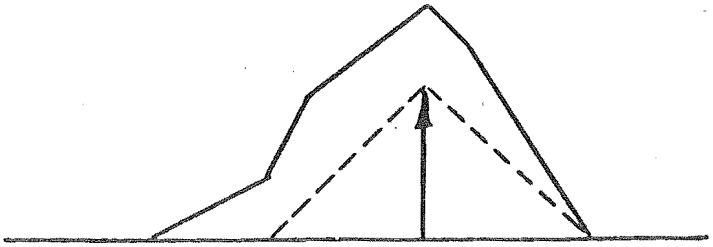

Figure 4.6e Image after two CLEAN subtractions.

Figure 4.6f Image after three CLEAN operations.

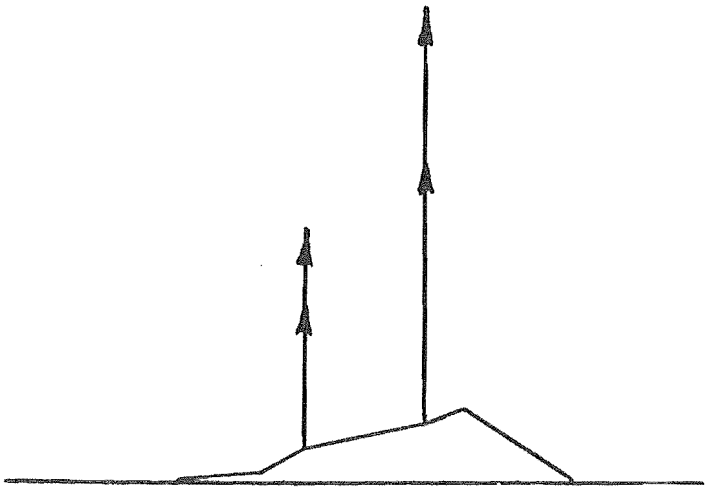

Figure 4.6g Image after four CLEAN operations with the clean beams added to the residue.

As we have demonstrated in §4.1, speckle images are formed by the tubulent atmosphere, and the instantaneous point spread function is not known. If it were, normal deconvolution or inverse filtering could be carried out. In Chapter 5, however, we describe a method of speckle processing which allows the CLEAN procedure to be used to subtractively deconvolve an image using an average point spread function. Results obtained using CLEAN are presented in Chapter 6.

4.12 A STOCHASTIC IMAGE RESTORATION PROCEDURE (Bates)

Bates (1976) presents a method for restoring an image which has been distorted by a multiplicative process. This method is a precursor of the shift and add process described in Chapter 5. It artificially produces a series of 'speckle' images distorted by random phases. Bates (1976) suggests that when an image is distorted by some physical process, the effect of the distortion is least where the intensity of the image is greatest. Therefore, by keying on the brightest point in a number of images and performing a suitable averaging process, the effective distortion can perhaps be reduced.

The stochastic restoration procedure can be described as follows. Consider an image i(x,y) which is multiplicatively distorted,

$$i(x,y) = f(x,y) \circledast h(x,y) \qquad (4.12\text{-}1)$$

where f(x,y) is the true undistorted image and h(x,y) is the psf of the distortion process. The Fourier transforms

of these quantities are I(u,v), F(u,v) and H(u,v). Providing H(u,v) is a member of an ensemble of random processes and that the actual intensity and position in image space of the ideal image is unimportant, a stochastic restoration procedure is suggested. To perform this procedure, I(u,v) is calculated, if it is not already given, and multiplied by $G_m(u,v)$, a member of an ensemble of random processes which is thought to be of the same class as H(u,v). The inverse FT is taken and the image is normalized so that the brightest point is unity, and then shifted to the centre of image space. This process is repeated, with other members of $G_m(u,v)$, and an average of all the images so produced is computed. Image domain restraints are applied to set the real part of the image to zero wherever it is negative. This image is denoted $\bar{i}_1(x,y)$. The process is repeated to produce an image $\bar{i}_2(x,y)$. A final image is produced from the summation of $\bar{i}_1(x,y)$ and $\bar{i}_2(x,y)$ when $\bar{i}_1(x,y)$ and $\bar{i}_2(x,y)$ are sufficiently alike, to within some threshold, and to zero when the values are sufficiently different. Bates (1976) indicates that this non-linear method of processing has defeated attempts to establish a mathematical analysis but that a computer simulation of the technique has produced encouraging results.

The analogy between this process and the production of normal speckle images is clear. Whereas Bates (1976) takes one distorted image and produces a number of distorted images by introducing a random phase artificially, speckle images are produced naturally by the turbulent atmosphere. If it is true that the brightest point in any image

corresponds to the brightest point in the object, and if the brightest point suffers least in the distorting process, a similar procedure should work in reconstructing real images from speckle images. This procedure is described in Chapter 5.

4.13 OTHER PROCESSING METHODS

Various methods for extracting diffraction limited information from a telescope operating under turbulent seeing conditions have been described in the previous sections. Some of these generate the autocorrelation of the object from which the diameter of a single object or the spacing of multiple objects can be measured. Others produce real images. Some other existing techniques which produce measurements of angular diameters are mentioned briefly here, along with methods which have been proposed to produce images.

(a) Michelson Interferometry. Michelson made the first measurements of the angular diameter of a star in 1920 when he reported that the angular diameter of Betelgeuse was 47×10^{-3} seconds of arc (Michelson and Pease 1921). An interesting historical review by DeVorkin (1975) and comments by Hanbury Brown (1974) relate the work that leads up to Michelson's first successful measurement. Much earlier work had been done. Galileo made the first attempt at measuring the angular diameter of a star by suspending a fine string and measuring the distance at which he had to stand so that the string occulted the image of the first magnitude star

Vega. He reached the conclusion that the angular diameter was about 5 seconds of arc, a value about 1500 times too large. Newton made a theoretical attempt to calculate the angular size of a first magnitude star. His calculations, based on the hypothesis that the sun is a body similar to the fixed stars and the assumption that if it were removed a suitable distance it would appear as a first magnitude star, gave an angular diameter of 2×10^{-3} seconds of arc, a value about two thirds of the currently accepted value for Vega. Michelson's interferometry work was preceded by Fizeau who, in 1868, proposed the interferometric method for circumventing the limitations of the atmosphere and the instrument. Stephan attempted to implement Fizeau's ideas in 1873-1874 but the measurements were unsuccessful. Michelson did some initial testing of his ideas in 1890 but it was not until 1920 that a successful instrument was made. The original Michelson stellar interferometer, described in many standard texts, made measurements of the angular diameters of six giant stars but attempts to make a larger instrument failed, due to atmospheric scintillations and the difficulty in maintaining correct instrument alignment (Hanbury Brown 1974).

(b) The Intensity Interferometer. A major difficulty in the construction of a Michelson interferometer is the requirement that the total differences in the two optical paths of the instrument must be less than the coherence length of the illuminating light. Mechanical tolerances therefore limit the size of the instrument.

Hanbury Brown (1974) describes the development of the intensity interferometer which he first proposed in 1954 (Hanbury Brown and Twiss 1954). This device worked at radio wavelengths, and its success encouraged their proposal for an intensity interferometer to work in the optical wavelengths (Hanbury Brown and Twiss 1956). The intensity interferometer relaxes the requirement of the Michelson interferometer that the path differences be kept within strict tolerances by replacing the optical interference paths with electrical signals. Photoelectric detectors are placed at each of the two telescopes, and the signals from these are combined electrically to produce the correlation between them. Measurement of this correlation gives the angular diameter of the object. Hanbury Brown (1974) gives a complete analysis of the intensity interferometer as well as providing an interesting history of its development.

(c) Phase Flipping. Lohmann and Weigelt (1978) proposed a method which they call *phase flipping*. They state that for certain simple objects the loss of phase in Speckle Interferometry is not important because the phase can be guessed. The object is assumed to be centro-symmetric and this assumption, together with the reality of the object intensity, causes the Fourier transform of the object to be real. The centre value of the object Fourier transform, shown in Figure 4.7a, is always positive and the phase is zero. At higher frequencies the Fourier transform may be negative, indicating the phase is π. The parts with phase π are separated from the parts with phase zero by dark bands.

Therefore a strategy is adopted which flips the phase between zero and π at each dark band. This approach is not reliable since a phase equal to zero everywhere cannot be excluded. This is unlikely because it would require a discontinuous gradient in the Fourier transform as shown by the dotted lines in 4.7b.

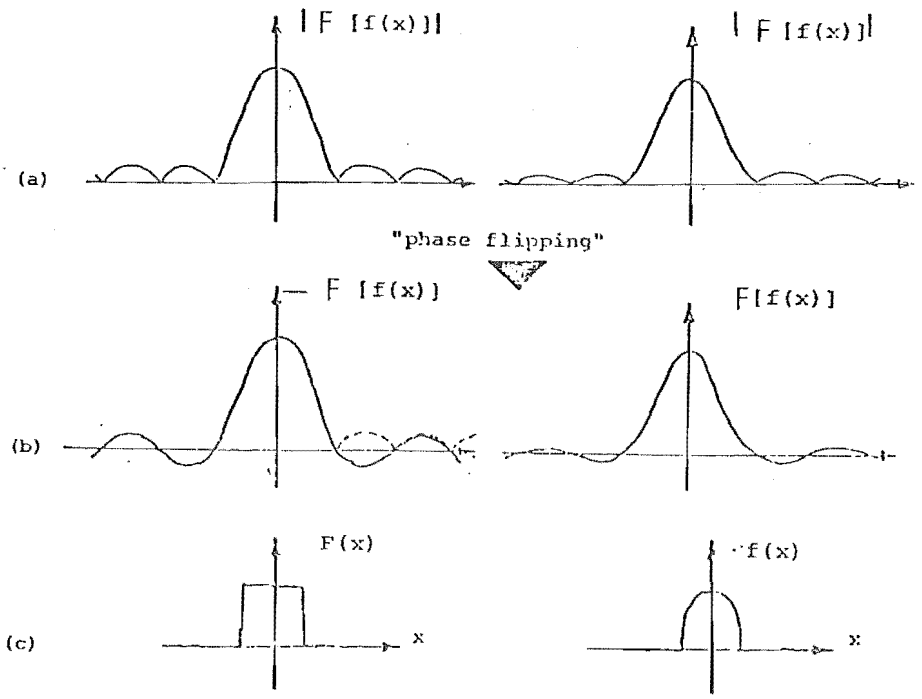

Figure 4.7 Illustration of phase flipping.
(From Lohman and Weigelt 1978)

(d) Stellar Interferometry with a Prominent Variable.

Bates and Milner (1979) point out that if Speckle Interferometry is performed for a cluster of stars which contains a prominent variable, a direct analogy can be made between the crystallographic technique of isomorphic replacement and the comparison of the autocorrelations made when the variable is at its maximum and minimum intensities. Rogers (1979) analyzes the simplification of the autocorrelation which takes place in this circumstance. Each of the auto-

correlations will contain cross-correlation terms which do not change plus a set which do change because of the variable. If the two autocorrelations are subtracted, a simplification of the autocorrelation results and the analysis is simpler. Rogers (1979) cautions against the danger of subtracting two signals to obtain a wanted pattern. Unless the signal-to-noise ratio in each signal is very high, the signal-to-noise ratio in the difference signal easily becomes unacceptable.

4.14 DISCUSSION AND CONCLUSION

High resolution imaging methods used in optical astronomy have been reviewed in this chapter. With the exception of Michelson interferometry, intensity interferometry, and CLEAN, all methods have been derived from Labeyrie's Speckle Interferometry. His remarkable observation that the mean square image transform of a short exposure speckle image contains information out beyond the seeing limited frequency has led to a number of methods which provide real images of celestial objects. Of the methods which produce images, only speckle holography (§4.4), the Knox-Thompson method (§4.5) and the Lynds, Worden and Harvey method (§4.6) have been reported to have been used in practice. There seem to be several reasons for this. Large field speckle interferometry (§4.3) and speckle masking (§4.7) require complicated optical processing, and a significant amount of *a priori* information about the object is needed. The Feinup algorithm (§4.10) suffers from disquiet about the uniqueness of the result. Speckle mask

and correlation processing (§4.9) has only recently been introduced. The method of Knox-Thompson has been used to reconstruct solar features, but, except in very special cases, it seems to be too sensitive to noise to be useful in practice.

Chapter 5 introduces a new speckle image processing method called *speckle shift and add*. This is an extremely simple processing method which can be done in real time using simple computing equipment. The results obtained with it are distinctly promising for it appears that the method is applicable for processing speckle images of faint objects as well as extended objects.

CHAPTER 5

A NEW METHOD TO RECONSTRUCT DIFFRACTION LIMITED IMAGES

5.0 INTRODUCTION

A new procedure for forming nearly diffraction limited images of objects viewed through a turbulent media has been developed using the image processing system described in Chapter 2 plus elements of the imaging methods presented in Chapter 4. Astronomical imaging simulations have been carried out on an optical bench using techniques similar to those described by Gough and Bates (1974) and Milner (1980). The results of these simulations are discussed in Chapter 6.

The new method of processing, called *speckle shift and add*, is an adaptation of the stochastic image restoration procedure (Bates 1976) described in §4.12 and similar to the processing method of Lynds *et al.* (1976, §4.6). For the purposes of the discussion below, let us define *a speckle* as a nearly diffraction limited, distorted version of the true diffraction limited image. A speckle of a single unresolvable object is a single spot in image space about the size of the diffraction limited spot. A *speckle image* is defined as a collection of independent, randomly distorted speckles superimposed in image space. A speckle image of a cluster of stars, one of which is brighter than all the others, is a collection of independent, distorted, nearly diffraction limited images superimposed in image

space. Providing the object is within the isoplanatic patch, distorted images of each star in the cluster will maintain their correct geometrical relationship with each other but their relative amplitudes will be distorted. When an average is taken, either over the ensemble of speckles in a single speckle image or over an ensemble of statistically independent speckle images, amplitude distortions are reduced. The speckle image of the star cluster with a bright star will contain bright spots, and if the difference in intensities between the two brightest stars is high enough, and the distortions in the amplitudes are not too severe, the brightest spot in a speckle image is likely to be produced by the brightest star in the cluster. The brightest spot will have associated with it, at the correct positions in image space, less bright spots corresponding to the dimmer stars. The simulations of speckle mask processing by Bates and Milner (1978, 1979, §4.9) and the imaging performed by Lynds *et al.* (1976, § 4.6) and Worden *et al.* (1977, §4.8) have shown this to be a valid representation.

In this chapter the implementation of the speckle shift and add process is described and the methods used to test its application in astronomical imaging by simulation are given. Chapter 6 follows with the results of the simulations performed. Note that terms relating to 'brightness' and to 'intensity' are used interchangeably even though brightness is a photometric concept, and intensity is found by a radiometric measurement.

5.1 SPECKLE SHIFT AND ADD PROCESSING

In speckle shift and add processing, all of the speckle images in a series are recorded. The brightest point in each image is found and the whole image is *shifted* without rotation so that this brightest point is in the centre of image space. This shifted speckle image is then *added* to all previous shifted speckle images. The process is repeated for a large number (as many as is convenient) of statistically independent speckle images. A *processed image* is thereby formed which is the average of the shifted-and-added speckle images. This processed image is shown below to be the convolution of the true diffraction limited image and an *average* diffraction limited point spread function.

It is convenient to analyze the *shift and add* processing method in terms of one-dimensional images. All the results are immediately applicable in two dimensions. The nth speckle image is

$$i_n(x) = \int_{-\infty}^{\infty} f(\zeta)\ h_n(x-\zeta)\ d\zeta \qquad (5.1\text{-}1)$$

where $f(\alpha)$ is the true diffraction limited image and $h_n(\alpha)$ is the point spread function of the atmosphere at the time that the nth speckle image is recorded. The position of the brightest point in the speckle image is denoted by a_n, and the speckle image is shifted so that the brightest point is in the centre of image space. This is written as

$$i_n(x-a_n) = \int_{-\infty}^{\infty} f(\zeta)\ h_n(x-\zeta-a_n)\ d\zeta. \qquad (5.1\text{-}2)$$

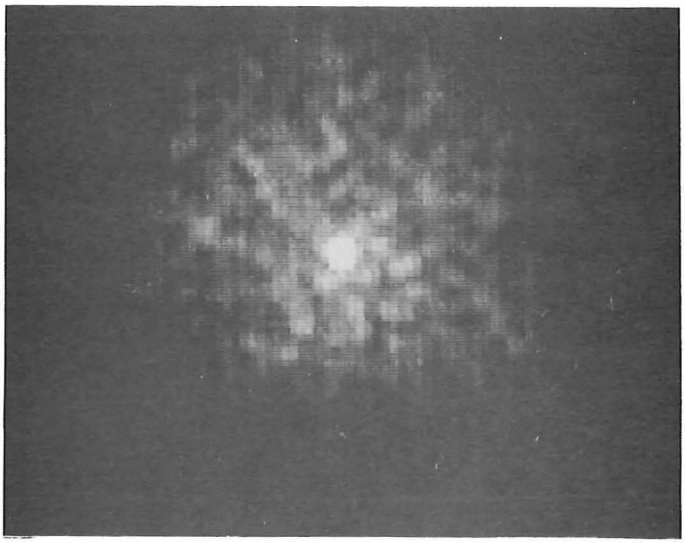

Figure 5.1 Point spread function of shift and add process.

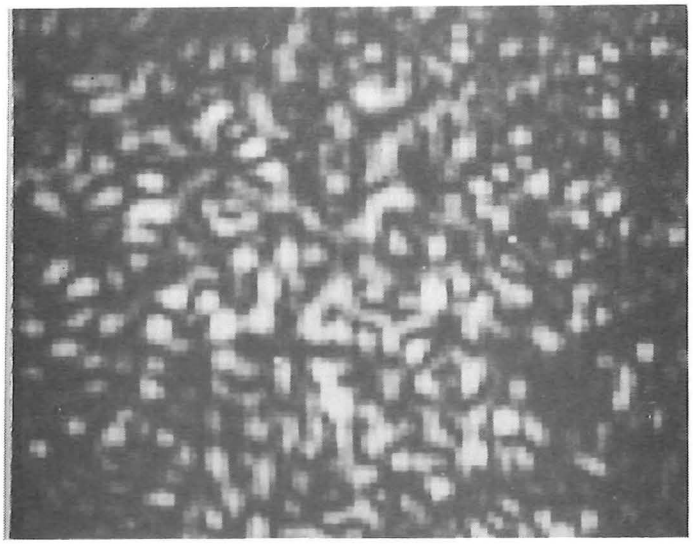

Figure 5.2 Simulated speckle image.

When N speckle images are shifted, added, and averaged, the processed image that results is

$$p(x) = \frac{1}{N} \sum_{n=1}^{N} i_n(x - a_n) = \frac{1}{N} \sum_{n=1}^{N} \int_{-\infty}^{\infty} f(\zeta)\, h_n(x - \zeta - a_n)\, d\zeta$$

$$= \int_{-\infty}^{\infty} f(\zeta) \left[\frac{1}{N} \sum_{n=1}^{N} h_n(x - \zeta - a_n) \right] d\zeta. \qquad (5.1\text{-}3)$$

Equation (5.1-3) can be written

$$p(x) = \int_{-\infty}^{\infty} f(\zeta)\, \hat{h}(x - \zeta)\, d\zeta = f(x) \ominus \hat{h}(x). \qquad (5.1\text{-}4)$$

This shows that the processed image p(x) is the convolution of the true diffraction limited image f(x) with a point spread function $\hat{h}(x)$. The psf $\hat{h}(x)$ is the average of N shifted and added, diffraction limited point spread functions and is observed to be nearly diffraction limited (Figure 5.1). The intensities in a speckle image of a single unresolvable object are Rayleigh distributed, and speckles are formed which are the size of the diffraction limited spot (Labeyrie 1976). The contrast of a speckle is high in those images where there is enough light (see Figure 5.2). This means that each bright speckle is isolated from its neighbour by an intervening dark area. Therefore, when the brightest speckle is shifted into the centre and added to previous bright speckles, the diffraction limited spot is reinforced and the less bright speckles, randomly positioned in each speckle image, are reduced to a general 'fog' in the background. This is clearly shown in Figure 5.1.

Speckle shift and add processing has several advantages over the speckle mask and correlation processing methods of Bates and Milner (1978, 1979, §4.9) and the processing method of Lynds *et al.*(1976, §4.6). In each of these latter methods, the speckle image must contain a number of identifiable bright speckles. Through the use of the correlation 'mask', all bright speckles in a single speckle image are superimposed, averaging the distortions in each. The correlated image from this process is an average over the ensemble of speckles in a single speckle image. An average of many correlated images formed from statistically independent speckle images can improve the signal-to-noise ratio of the process. The speckle shift and add process generates a processed image, which is an average of the brightest speckle over an ensemble of statistically independent speckle images. This image is similar to the 'correlated' image of Lynds *et al.*(1976, §4.6). The processing is much the same as speckle mask processing but requires only one speckle from each speckle image. Therefore, the speckle shift and add method can be used in situations where the stars are very faint, and only a very few speckles are present in each recorded speckle image.

Speckle shift and add processing can be performed with a wider bandwidth than normal speckle interferometry (Bates and Cady 1980). In conventional speckle interferometry the bandwidth must be narrow enough to maintain coherence over the entire seeing disk (Karo and Schneiderman 1978). This restriction is relaxed for shift and add processing because only the information around the

brightest spot is required to produce an image. Therefore the bandwidth must be only narrow enough to maintain coherency across the extent of the object itself. A wider bandwidth assists in the detection of faint objects by allowing more light to be transmitted to the detector.

Another advantage of the shift and add method is that the processing algorithm is very simple. No pattern recognition procedures (as in correlation processing, §4.9) or Fourier transformations (as in the Lynds, Worden and Harvey method, §4.6) are required. Simple computing equipment such as the microprocessor based system described in Chapter 2 can be used to produce a diffraction limited image in nearly real time. High speed, special purpose hardware to perform the algorithm could be easily constructed.

5.2 EXPERIMENTAL PROCEDURES

The speckle shift and add processing algorithm described in the previous section has been implemented on the University of Canterbury Image Processing System. Speckle images were produced using an optical simulation technique. Speckle image simulations are described by several authors including Liu and Lohmann (1973), Gough and Bates (1974), Schneiderman *et al.* (1977), Karo and Schneiderman (1979) and Milner (1980). The particular technique used here is a modification of that reported by Gough and Bates (1974) and Milner (1980).

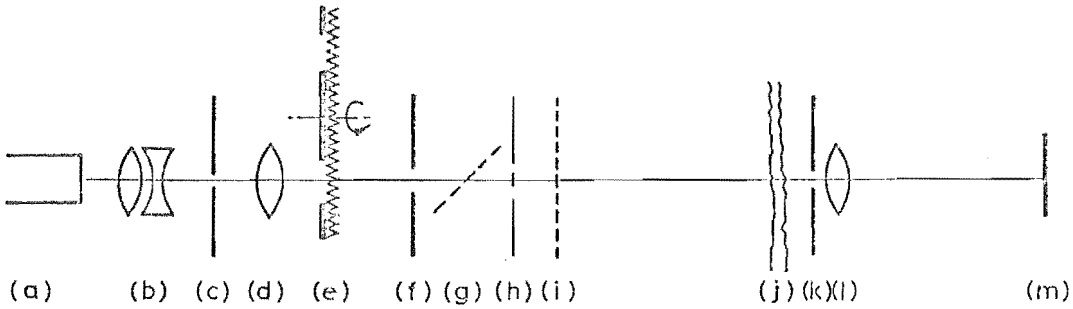

(a) 3.5 mW, 632.8 mm, He - Ne Laser. (Spectra-Physics Model 135).

(b) x20 Microscope Objective lens.

(c) 25 μm pinhole.

(d) Collimating lens (f = 95 mm).

(e) Rotating mylar disk diffuser.

(f) 11 mm diameter spatial filter.

(g) Mirror used with wide band light source only.

(h) Object mask.

(i) 100 nm filter used with wide band light source only.

(j) Model atmosphere.

(k) 2.75 mm diameter telescope aperture.

(l) Telescope objective lens (f = 308 mm).

(m) Image plane.

Figure 5.3 Optical instruments to simulate astronomical imaging.

5.2.1 The Optical Laboratory

The simulation of astronomical imaging was performed in the Optical Laboratory of the Electrical Engineering Department. The surface of the optical table in the laboratory is a 4" thick slab of polished granite optically aligned to be flat and level. The concrete base for this table has been formed into the foundation of the building. On top of the concrete base is a 1" thick slab of rubber, several layers of concrete blocks, another 1" thick layer of rubber, and finally the granite slab. The combination of concrete and rubber gives a table which is stable and has a low natural frequency of vibration. A cast iron precision optics bench is placed on the table to hold optical instruments in alignment. The arrangement of the optical apparatus to simulate astronomical imaging is shown in Figure 5.3.

A Helium-Neon laser (a) is used as the light source for narrow band simulations. The source used for wide band simulations is described in §6.4. The light from the laser is focused by the microscope objective (b) to a point at the 25 μm pinhole (c). The pinhole lies in the front focal plane of the collimating lens (d) which produces a beam of parallel light. A crumpled 0.05 mm thick mylar disk rotating at approximately 250 rpm is at (e), and produces spatially incoherent light. This beam, filtered by the circular aperture (f), then passes through the object mask (h). The object mask is cut from a 125 μm thick brass sheet. For star clusters, a pattern of holes 0.3 mm in diameter is drilled in the brass sheet. This acts as the object plane,

and emits quasimonochromatic, spatially incoherent light to simulate an astronomical object. The radiation from the object passes through the model atmosphere (j), the telescope aperture (k), the telescope objective lens (l) and is detected at the image plane (m) by the CCD camera.

The model atmosphere (j) must produce random phase pertubations in the incoming wavefront. To simulate the turbulent atmosphere, it should have hundreds to thousands of seeing cells across the aperture of the telescope (see § 4.1.4). Labeyrie (1976) points out that atmospheric seeing does not have to be exactly reproduced to achieve realistic speckle patterns. Results obtained with the many schemes that have been tried confirm that this is true. Gough and Bates (1974) and Weigelt (1975, 1977) used shower glass, Schneiderman *et al.* (1975) used lacquer sprayed grass plates, Karo and Schneiderman (1979) produced a random phase with glass film plates, and Parry *et al.* (1977) used a 2 kW bar heater to generate a real turbulent atmosphere. The atmosphere used here is a disk of perspex which has been lightly singed by a gas torch to cause buckling and small bubbles in the plastic. This forms seeing cells which are small enough to generate realistic speckles as shown in Figure 5.2. Continuously changing speckle images are produced for the shift and add processing by slowly rotating the perspex disk. The rotational speed is governed by two factors. It must rotate slowly enough so that the atmosphere is effectively stationary during the exposure time of the CCD camera (approximately 0.1 seconds for faint speckle images). It must also rotate fast enough so that by

the time processing is completed (approximately 4 seconds) the atmosphere is sufficiently different so that it can produce a statistically independent different speckle image. This allows the exposure time criteria established in §4.1.4 to be satisfied.

The image of an unresolvable stellar disk at the surface of the CCD detector should be spread over several pixels if quantitative measurements are to be made (§3.2.1). The angle subtended by a simulated star is determined by the physical layout of the simulation. The resolution of the system is determined by the telescope aperture. The distance from the object plane (h) to the telescope objective lens (l) is 2360 mm. Therefore, the angle subtended by a simulated star 0.3 mm in diameter is 26 arcseconds. The telescope aperture (k) is 2.75 mm in diameter, giving an angular resolution of 59 arcseconds. The optics of the simulation spreads the image of the stellar object over an area of approximately 9 pixels at the CCD (m). When the aperture of the telescope is enlarged to values greater than 7 mm, the 0.3 mm stellar disk is resolvable by the system. In this case, the size of the image of the star is 40 μm, which is approximately the size of one pixel in the CCD array.

5.2.2 Spatial Incoherency

The parallel beam of laser light produced by the optical apparatus (a) - (g) must be spatially incoherent to allow the simulation of two different stellar radiators. The light emitted by the laser has a high degree of temporal and spatial coherence. Consider a point source of light

emitting an infinitely long monochromatic wave train having spherical or plane wavefronts. Under ideal conditions, the phase difference between any two points along the ray does not change with time. Equivalent to this, the phase difference measured at any point in space at the beginning and end of a fixed interval Δt does not change with time. This is perfect temporal coherence. Spatial coherence is determined by measuring the phase difference between two points normal to the ray direction as a function of time. Complete time independence gives perfect spatial coherence. A real source of light is not perfectly monochromatic and does not have perfect spatial and temporal coherence. A real source has a finite bandwidth $\Delta\nu$, and a coherence time

$$\Delta t = \frac{1}{\Delta\nu} . \qquad (5.2\text{-}1)$$

The distance light travels in this time is called the coherence length, given by

$$L_c = c\,\Delta t = \frac{c}{\Delta\nu} \qquad (5.2\text{-}2)$$

Jenkins and White (1976) show that a more accurate equation for coherence length takes into account the doppler broading of the spectra and gives

$$L_c = \frac{0.32\ c}{\Delta\nu} \qquad \text{for low pressure discharges} \qquad (5.2\text{-}3)$$

$$L_c = \frac{0.11\ c}{\Delta\nu} \qquad \text{for high pressure discharges} \qquad (5.2\text{-}4)$$

The bandwidth of the He-Ne laser used in the simulations is 2×10^9 Hz giving a coherence time of 5×10^{-10} and a coherence length of 4.8 cm by equation (5.2-3).

The rotating mylar disk at (e) reduces the spatial coherence of the laser beam during the integration time of the CCD detector. Spatial incoherence was verified by placing the CCD detector at position (j) in Figure 5.3 and using a binary star pattern at (h). Without the mylar disk, interference fringes could be seen on the television display. When the mylar disk was rotating at approximately 250 rpm, no fringes were seen at the minimum integration time of the CCD (approximately 0.01 seconds).

5.2.3 Relative Intensities of the Stars

The relative intensities of the stars in the object pattern were measured to evaluate the distortions produced by the shift and add processing. The simulated atmosphere was removed and a 1.5 mm diameter aperture was used at the telescope objective lens. This reduced the intensity of the image at the CCD, avoiding saturation of the sensor. It also spread the image over several pixels, allowing more accurate measurements to be made (§3.2.1). The shift and add process was performed without the atmosphere, and the CCD camera was moved slightly between each iteration of the process. This ensured that the images of the stars were averaged over a number of pixels and reduced the effects of any fixed pattern variations in sensitivity. The sum of the brightest pixel and its eight nearest neighbours in each of the resultant star images was calculated. The ratio of these sums was taken to be the relative intensity of the stars (see Figure 5.4a).

a1	a2	a3
a4	a5	a6
a7	a8	a9

Brighter Star

b1	b2	b3
b4	b5	b6
b7	b8	b9

Dimmer Star

$$R_I = \frac{\sum_{n=1}^{9} a_n}{\sum_{m=1}^{9} b_m} \qquad (5.2\text{-}5)$$

where the a_n denotes the pixels in the brighter star, and b_m the dimmer.

Figure 5.4a Calculation of relative intensities of two stars.

This procedure was verified by using a narrow beam photometer to measure the intensities of the stars at the object mask (h). The correlation of these results is shown in Figure 5.4b.

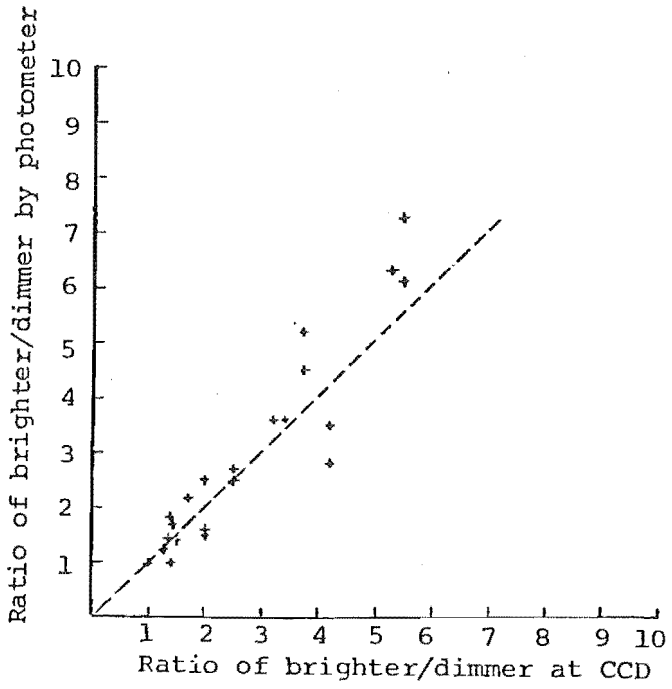

Figure 5.4b Verification of relative intensities.

An additional calculation must be performed to find the relative intensities of the stars after the shift and add processing. As shown in Figure 5.1, the image of a star rises above a general background intensity caused by averaging the randomly positioned less bright speckles. This background level must be subtracted from the absolute intensities before calculating the relative intensities as shown in equation (5.2-5). The method for finding the average background level is demonstrated by considering a 5 x 5 pixel array around the brightest point in any star, as in Figure 5.5. The background is found by averaging the pixels labelled 1,5,6,10,16,20,21 and 25. It is felt that these corner pixels would be far enough away from the centre of the stellar image (for the aperture generally used) so that the effect of the psf would be minimal. The results have been satisfactory.

1	2	3	4	5
6	7	8	9	10
11	12	13	14	15
16	17	18	19	20
21	22	23	24	25

Figure 5.5 5 x 5 pixel array around the brightest point in a star image.

5.2.4 Shift and Add Algorithm Implementation

The shift and add algorithm has been implemented in assembly language code for the Intel 8080 microprocessor used in the UCIPS. A structure diagram and program operating instructions are given in Appendix D.

The shift and add algorithm is very simple. However, the microprocessor system forces some limitations on its implementation. The major restriction is that there is limited storage area available for data arrays. The total memory available in the system for data and program storage is 57,344 (56K) bytes. In order to monitor the processing, both the processed image and the speckle image should be available for viewing. Three 10,000 byte buffers are required to capture and display these images. One of the buffers is used by the direct memory access controller to store the data from the CCD. These data are in two separate fields which are then interlaced and transferred to one of the refresh display buffers in the VDSI. The other display buffer contains the processed picture. The operator can select either of these pictures for display on the television monitor at anytime during the process. Roughly 26K bytes of memory remain for program storage and for an accumulating array for the processed picture. This limits the accumulating array to 16 bits per pixel, or 20,000 bytes in total. Therefore the number of iterations before overflow occurs in the 16 bits per pixel accumulating array is limited. In practice, with the light levels present in the simulation, and the number of iterations performed, this has not been a significant limitation.

The processed image, given by equation (5.1-4) is the *average* of the shifted and summed speckle images. Since division is a time consuming operation when done in software on a microprocessor, an equivalent operation which results in a pleasing display of the processed image with no loss of information has been used. The VDSI converts 8 bit data in the refresh memory to video for the television monitor. Larger numbers make brighter pixels on the display. To have a bright display, the processed picture is multiplied by two (arithmetic left shifts) until the brightest pixel contains a 1 in the most significant bit position. The most significant eight bits from each shifted 16 bit accumulated pixel is then transferred to the processed image display buffer.

The shift and add program allows the operator to select a range of speckle images to be included in the summation for the processed image. The average value of 32 pixels in the centre of image space is calculated and compared with limits set by the operator at the beginning of the program. The lower limit eliminates speckle images which are judged to be too dim to contain useful speckles, and the upper limit eliminates those with bright spots which are formed when the perspex disk atmosphere is too 'thin' to generate good speckle images. Speckle images are automatically rejected if any pixel in the image has a value of 255_{10}, indicating saturation of the sensor.

The shift and add algorithm implemented on the 8080 microprocessor operates very nearly in real time. The redistribution time of the earth's atmosphere, usually taken

to be about 1 second (§4.1.4), means that the process should take no longer than 1 second to be considered real time. The process as it has been implemented takes approximately 4 seconds.

5.3 CONCLUSION

Speckle shift and add processing has been simple to implement on the microcomputer. Care was taken to develop techniques which allowed reasonably accurate quantitative results to be obtained from the simulations reported in Chapter 6. The technique is beautifully simple and an array sensor combined with any microcomputer will allow on-line, real time acquisition of nearly diffraction limited images.

CHAPTER 6

EXPERIMENTAL RESULTS OF SHIFT AND ADD PROCESSING

6.0 INTRODUCTION

A wide range of stellar objects has been simulated using the experimental techniques outlined in Chapter 5. Both unresolvable and resolvable objects have been used. Single unresolvable stars have allowed the determination of the point spread function of the process. Binary stars and stellar clusters comprised of unresolvable stars have been used to test the effectiveness and accuracy of the processing. Extended objects, many resolution elements in extent, have been used to demonstrate that the method can reconstruct extended images.

The stellar object mask has been illuminated with very narrow band laser light and with wide band light (Bates and Cady 1980). In each of these cases an almost diffraction limited image was obtained. In addition, severe telescope aberrations have been simulated by defocussing the instrument. Again, a nearly diffraction limited image was reconstructed.

This chapter presents experimental results which show the effectiveness and accuracy of shift and add processing. Errors are analyzed and difficulties encountered in making the measurements are discussed. Chapter 7 follows with a general discussion of further work, and recommendations for the effective use of the shift and add process in

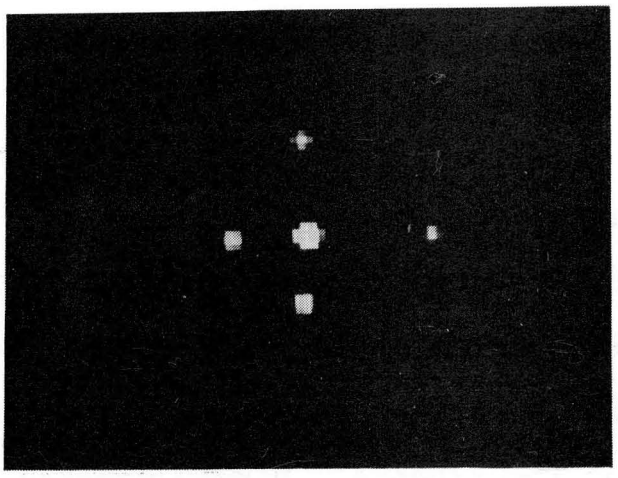

a. Perfect seeing.

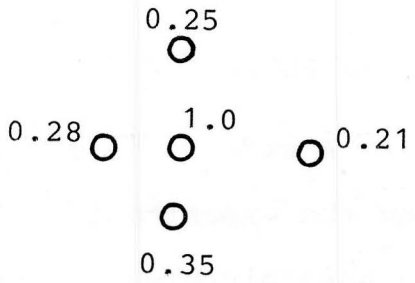

b. Relative intensities of a.

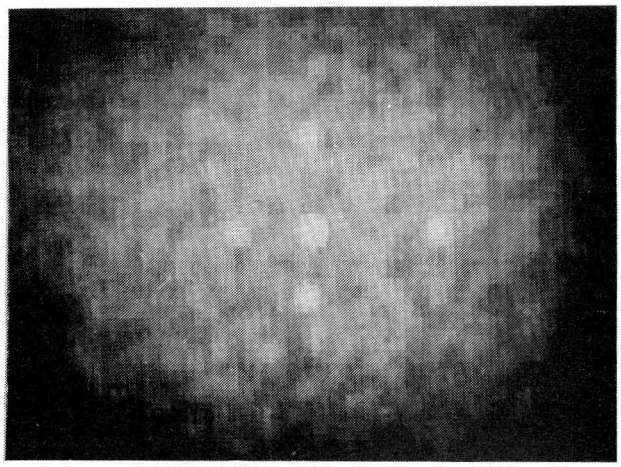

c. Processed image.

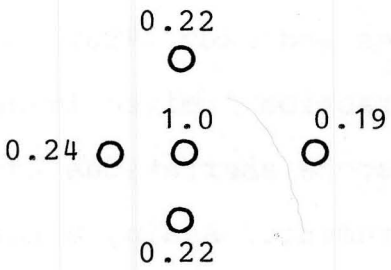

d. Relative intensities of c.

Figure 6.1 Star cluster imaging.

astronomical imaging. Appendix E lists the experimental conditions present for each of the results reported in this chapter, and Appendix F gives sample calculations.

6.1 IMAGING STAR CLUSTERS

A star cluster is a group of unresolvable stars. The extent of the stellar cluster, however, is resolvable by the instrument. In the images shown in Figure 6.1, a resolution element is approximately 3 mm. A five star cluster imaged when the seeing is perfect is shown in Figure 6.1a. The intensities of each star relative to the brightest (normalized to 1.0) are shown in Figure 6.1b. The processed image after 128 iterations of shift and add is shown in Figures 6.1c and 6.1d. The relative intensities for the stars under perfect seeing, and for the processed image, have been calculated as shown in §5.2.3 and Appendix F. The processed image correctly reconstructs the positions of the stars in the cluster, and the relative intensities show good agreement with the original.

6.2 POINT SPREAD FUNCTION FOR SHIFT AND ADD

The point spread function for the shift and add process is found by using a single unresolvable star. The psf for 128 iterations is shown in Figure 6.2a. Figure 6.2b demonstrates the shape of the psf showing the central diffraction limited spike rising out of the background fog. This psf is used with the CLEAN process described in §6.8. Notice that the psf is about three pixels wide, corresponding well to the line profile of a single star imaged without

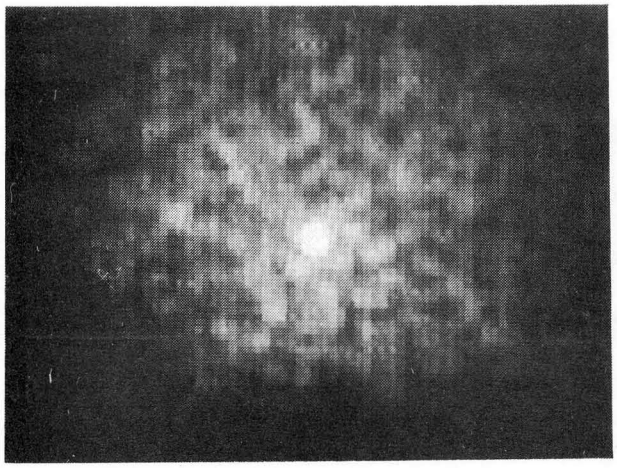

a. Point spread function of shift and add process.

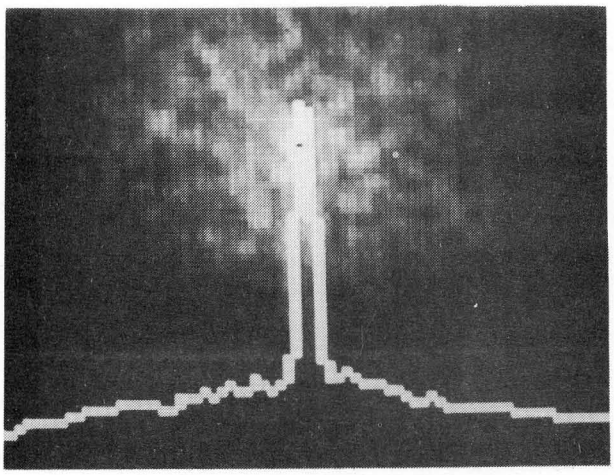

b. Intensity of horizontal line through the brightest point.

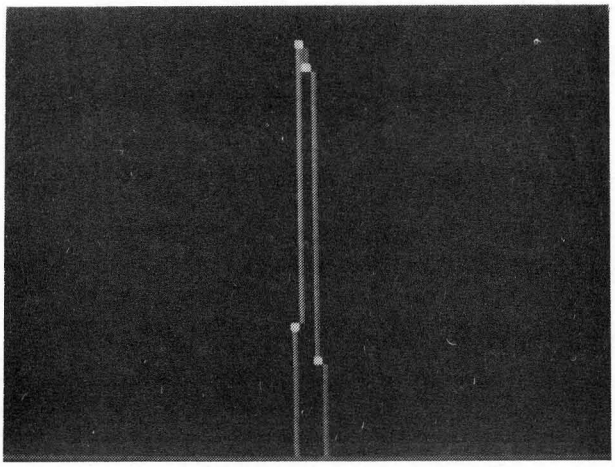

c. Original single star with perfect seeing.

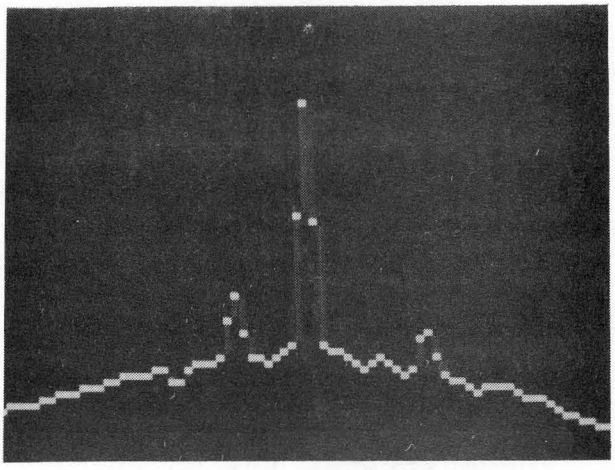

d. Intensity of the horizontal line through the brightest star of Figure 6.1c.

Figure 6.2 Point spread function of shift and add process.

the atmosphere (see Figure 6.2c). Figure 6.2d shows that the intensity along the horizontal line containing the brightest star in the star cluster of Figure 6.1 has the same general shape as the psf.

6.3 CALIBRATION OF SHIFT AND ADD PROCESSING

The accuracy with which the processing reconstructs the positions of the stars is shown in Figure 6.1. The point spread function of the process is given in Figure 6.2. In addition to these important characteristics, the affect of the processing on the relative intensity ratios of pairs of stars has been determined.

6.3.1 Relative Intensities

A series of measurements was made to investigate the ability of the shift and add processing to correctly reconstruct the true relative intensities of the stars. The relative intensities of the stars imaged without the atmosphere were measured before and after 128 iterations of the processing were performed. A binary star and a triple star pattern were used in two tests. The results of the first, using a binary star pattern, are shown in Figure 6.3a. The relative intensities of the two stars were found for a range of intensity ratios. The ideal relationship between relative intensities before and after processing is shown as a dotted line. There are several points of interest in this result. The first is the dynamic range of the process. After 128 iterations, two star images could be clearly seen for intensity ratios up to about 14:1. This corresponds to a stellar magnitude difference of nearly 3.

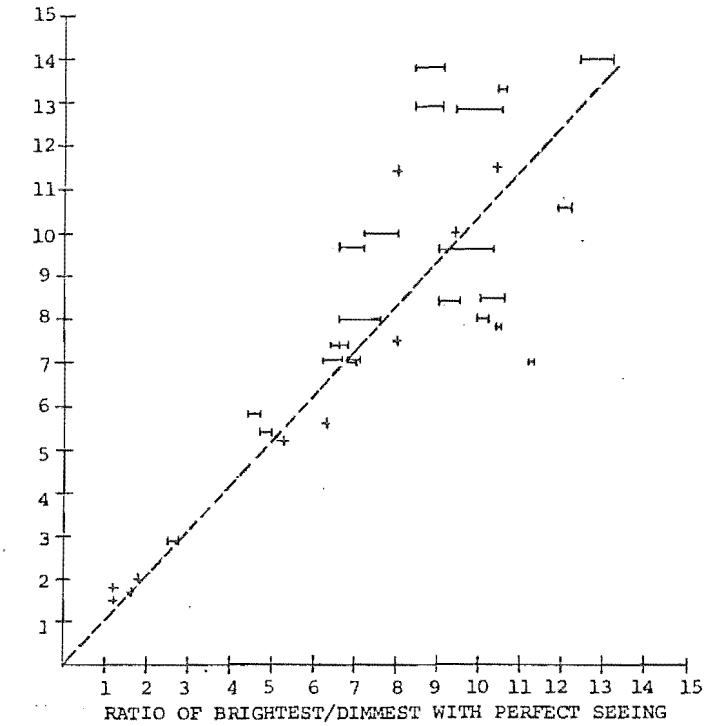

a. Binary star pattern

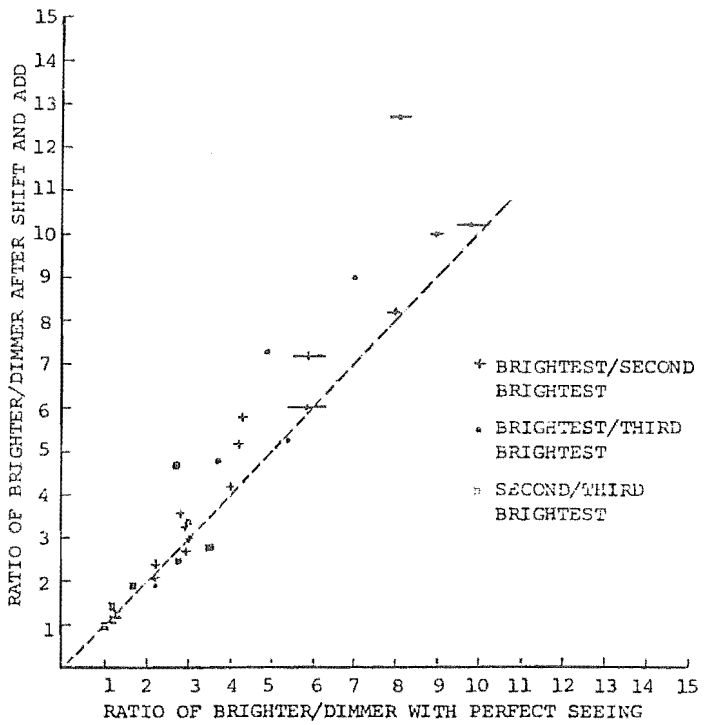

b. Triple star pattern.

Figure 6.3 The effect of shift and add processing on the relative intensities of the stars.

There is, however, considerable spread about the ideal curve for relative intensities greater than about 8:1. The horizontal bars drawn for some points in Figure 6.3a indicate the extreme values of the relative intensity ratios for perfect seeing when measured immediately before and after the shift and add processing. The simulation of high relative intensity ratios, where one star is considerably brighter than the other, was very sensitive to physical changes in the experimental apparatus. Any drift in the equipment during the processing caused changes in the ratios. The general trend is evident and good agreement is found for ratios below about 8:1. The position of the stars is accurate to the resolution of the CCD.

The second test was performed with a triple star pattern. The relative intensities between each of the three pairs of stars were calculated, both under perfect seeing and after the shift and add processing. The results are shown in Figure 6.3b. Good agreement is again demonstrated for relative intensity ratios less than about 8:1 for any of the star pairs.

6.3.2 Ghost Stars.

The behaviour of the process when the intensity ratios were less than about 2:1 was investigated. In this case, one expects that due to random distortion of the intensities, some of the time the less bright of the two stars produces the brightest spot in the speckle image. When shifted into the centre, the 'speckle' from the truly most intense star will contribute to the processed image in a position we call the *ghost* position. This is clearly evident

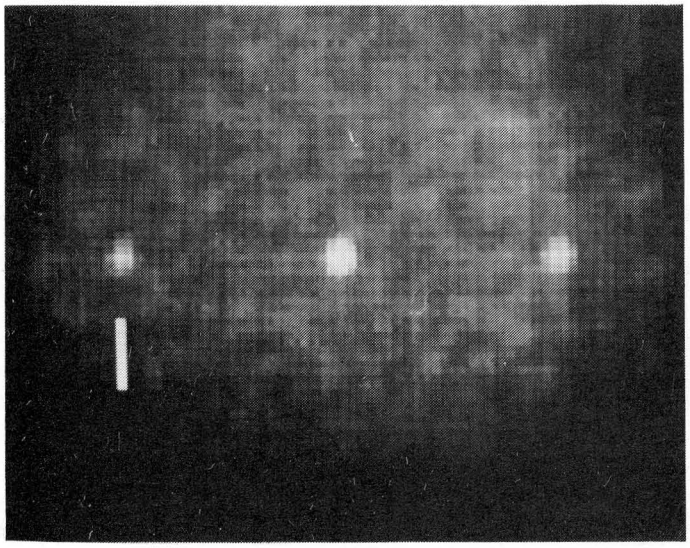

Figure 6.4a Ghost star image.

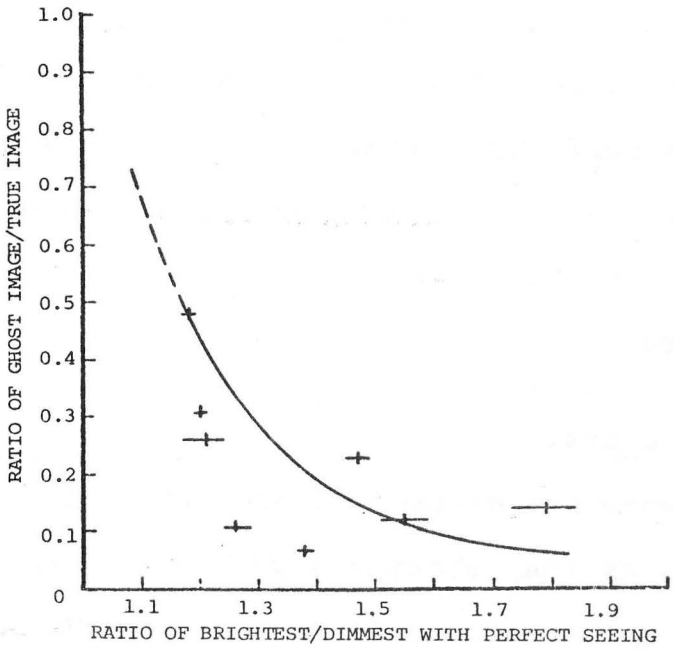

b. Intensity ratio between the ghost star and the true second brightest star.

Figure 6.4 Ghost star patterns.

in Figure 6.4a, where the original intensity ratios under perfect seeing were 1.3:1. The vertical line in 6.4a indicates the ghost position. The statistics of the intensities in the speckle image around the brightest point have not been investigated, but it seems reasonable to expect that speckles will sometimes add up in a 'wrong' way and create the ghost image. This must depend to a large extent on the seeing conditions and on the complexity of the cluster. With more stars, a more complex speckle image is produced and speckles are more likely to overlap in the wrong place. Quantitative work has not been done, but in simulations of clusters such as that shown in Figure 6.1, the ratio between the brightest and the next brightest must be larger than in the case of simple binary stars to avoid the ghost image. Figure 6.4b shows the ratio of the intensity of the ghost star to the intensity of the true second brightest star as a function of the relative intensities of the two stars found under perfect seeing. This shows, at least for binary stars and for the atmospheric conditions of the simulation, that when the ratio is above about 2:1, no ghost star is discernible.

6.4 THE SIMULATION OF WIDE BAND SPECKLE IMAGING

Bates and Cady (1980) report the effect of bandwidth on the shift and add process. Normally, in Labeyrie's SI (§4.2), the bandwidth is limited to 10-70 nm. This satisfies the quasimonochromatic condition of equation (4.1-2) and allows the coherent formation of speckles across the extent of the seeing disk. A good signal-to-noise ratio

can then be achieved from a single speckle image. In contrast, the shift and add process requires only the information around the brightest point. The bandwidth may be broader because coherency is required only over the extent of the object, which is usually much smaller than the seeing disk. Consequently, fainter objects may be imaged with the shift and add process. A series of experiments were performed to establish that the process is effective with wide band radiation.

Referring to Figure 5.3, a mirror was placed at (g) to allow a wide band light source to illuminate the star pattern (h). A 100 nm bandwidth Landsat filter (band 5, 600-700 nm) was used at (i) to produce wide band filtered light. The wide band source was a quartz halogen spotlight, and the spectral emissivity of the spotlight and the filter combination are shown in Figure 6.5. The single element simulated telescope lens (l) was retained for this experiment, and dispersion effects of the atmosphere and the lens were not considered. A 9.5 mm diameter aperture (k) was used to provide enough light so that the CCD integration time could be reduced to a reasonable value. The 0.3 mm diameter star disk was just resolvable by the instrument and the Airy disk was approximately the size of one pixel. With this aperture, quantitative measurements of the relative intensities are likely to be in error, and so only the positional accuracy of the reconstruction is reported here.

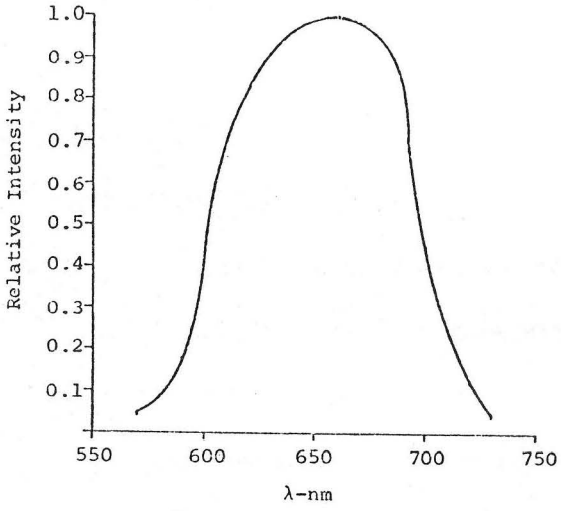

Figure 6.5 Spectral emissivity of wide band source and Landsat filter.

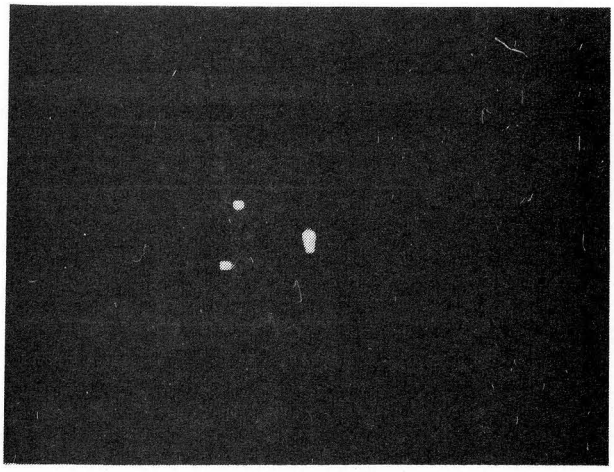

Figure 6.6a Diffraction limited star cluster with perfect seeing.

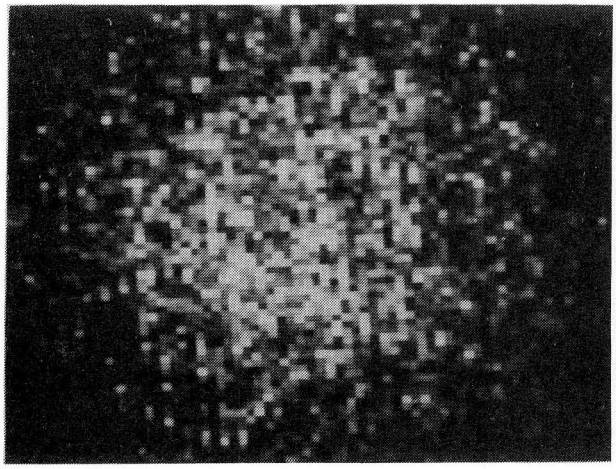

Figure 6.6b Speckle image from narrow band (laser) source.

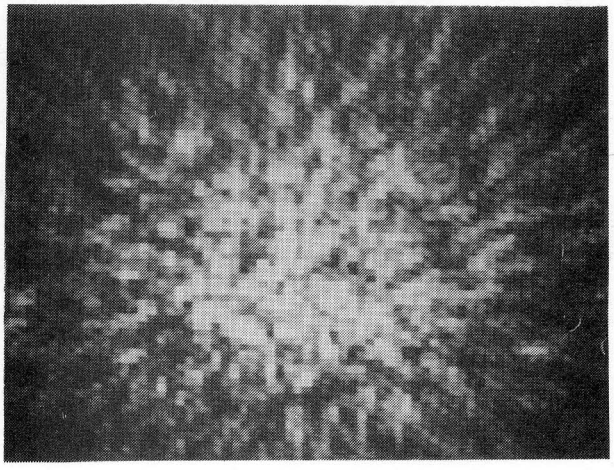

Figure 6.6c Speckle image from wide band source.

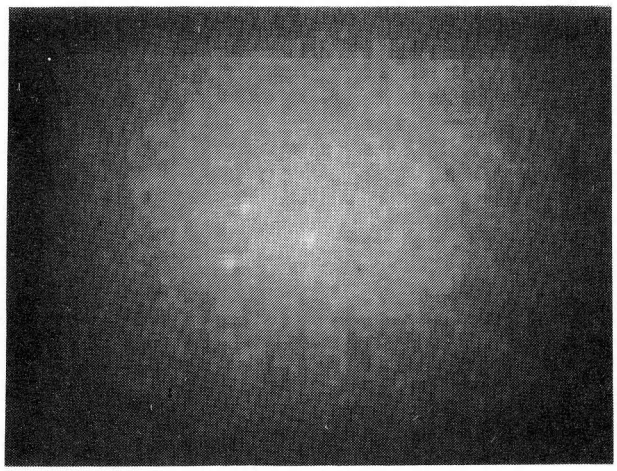

Figure 6.6d Processed image from narrow band source.

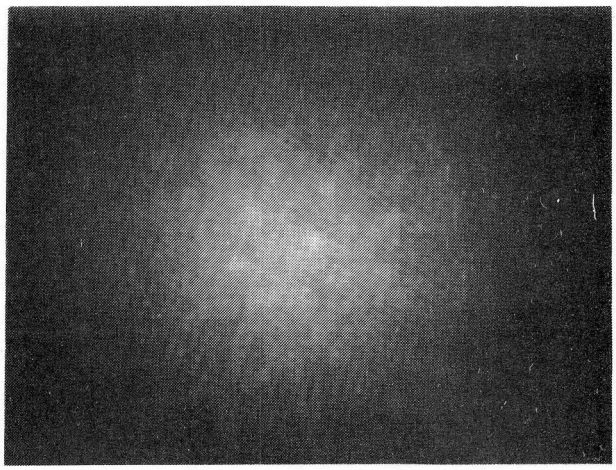

Figure 6.6e Processed image from wide band source.

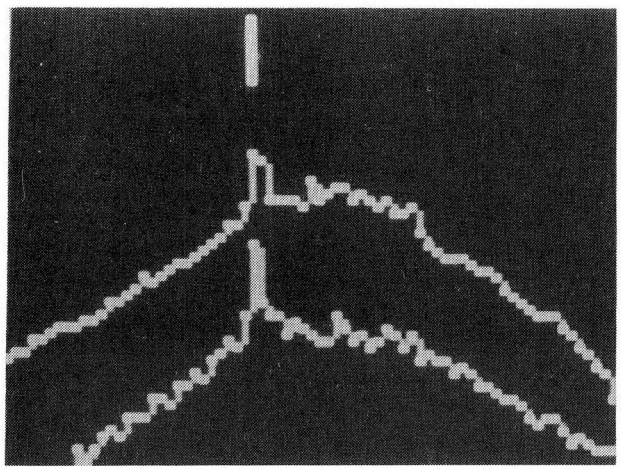

Figure 6.6f Intensity of the line through the lower left star of 6.6d (lower) and 6.6e (upper).

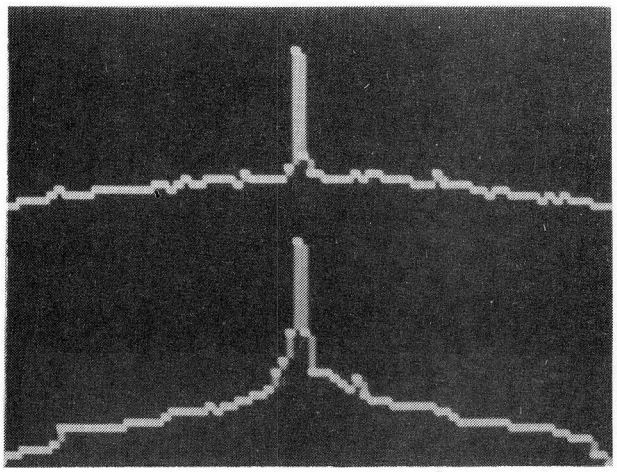

Figure 6.6g Point spread functions for narrow band (upper) and wide band (lower).

6.4.1 Wide Band Speckle Results

The diffraction limited image of a three star cluster imaged under perfect seeing with the laser source is shown in Figure 6.6a. Typical speckle images generated by a fixed atmosphere with the narrow band (laser) and the wide band source are shown in Figures 6.6b and 6.6c. As expected, the wide band speckle image is blurred, compared with the narrow band image, except for a narrow region in the centre. This is enough for the shift and add processing when the sharp central region contains the brightest point. It is expected, however, that the blurred region may contain the brightest point some of the time. This tends to reduce the contrast of the processed image. Figures 6.6d and 6.6e show the processed images for narrow band and wide band light. A recognizable version of the true image can be distinguished in each, although the photographic reproduction process does not contain the detail which can be seen on the television monitor. Figure 6.6f shows graphically the difference in contrast of the two images. The upper curve is a plot of the intensity across a horizontal line through the lower, left star in the wide band processed image of Figure 6.6e. The lower curve is the intensity of the corresponding line in the narrow band processed image of Figure 6.6d. As expected, the contrast in the wide band case is reduced but the star is clearly seen above the vertical bar.

A slight spreading of the star in the wide band case is also present, indicating that the average size of the speckles for wide band is somewhat larger than for narrow

band radiation. This is also shown in Figure 6.6g which plots the point spread functions for the narrow band (lower curve) and the wide band cases.

6.5 SHIFT AND ADD PROCESSING IN THE PRESENCE OF SEVERE ABERRATIONS

The work reported in the previous sections has assumed that telescope aberrations are negligible. In §4.1.2 it is shown that aberrations normally reduce the contrast at high spatial frequencies and cause blurring of the image. However, an analysis by Korff *et al.* (1972) shows that poor instruments preserve spatial frequency information out to the diffraction limit when forming speckle images. Dainty (1973) proposes that a poor instrument can be made to resolve objects to the diffraction limit by ensuring that the seeing conditions are bad enough. He suggests the introduction of random phase perturbations when seeing conditions are too good! Dainty (1977) indicates that the distortion due to seeing must be worse than that due to the instrument. Karo and Schneiderman (1977) give measurements of the lens-atmosphere MTF which provide practical confirmation of Korff's and Dainty's conjectures. Roddier *et al.* (1978) confirm their results theoretically. In each of these analyses, speckle interferometry is implied and the question of resolving diffraction limited *images* with aberrated telescopes is left unanswered.

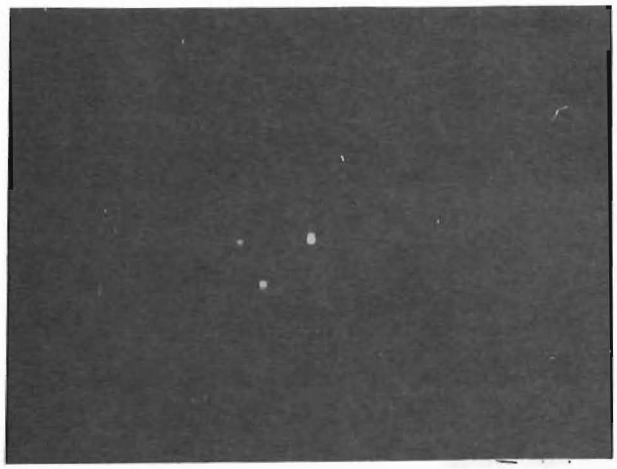

a. Triple star cluster with perfect seeing and focussed instrument.

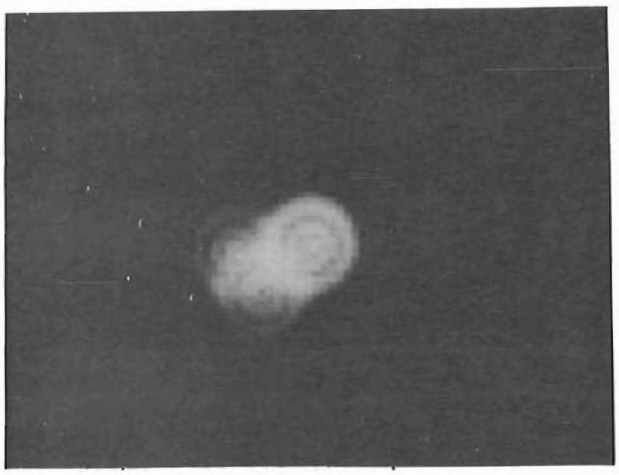

b. Triple star cluster with perfect seeing and 4.7λ defocus.

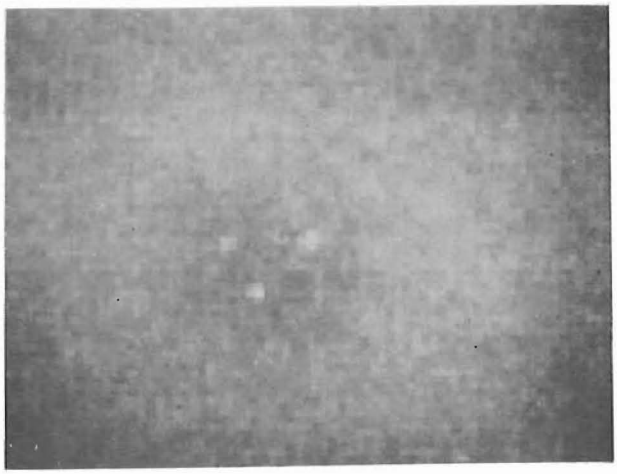

c. Processed image with 4.7λ defocus.

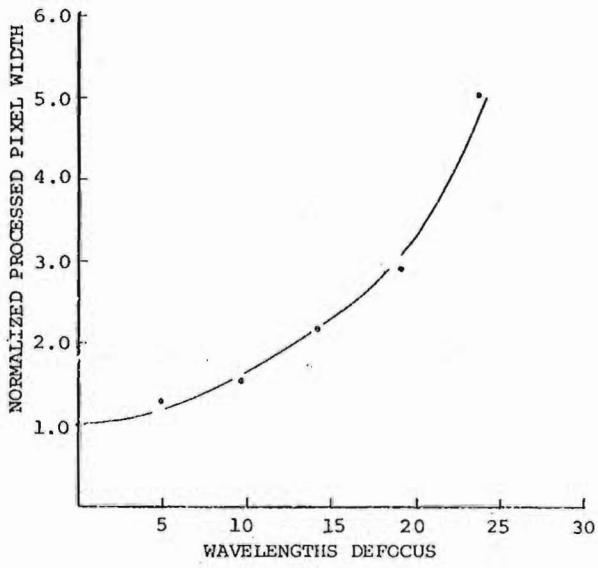

d. Size of the processed image as a function of defocus.

Figure 6.7 Speckle Shift and Add processing with a defocussed telescope.

6.5.1 Results of Imaging with a Defocussed Instrument

It has been experimentally confirmed that nearly diffraction limited images can be resolved when the seeing conditions are worse than the aberrations caused by the instrument. Using narrow band light and defocussing the simulated telescope, the following results were obtained. Figure 6.7a shows the simulated cluster of three stars under perfect seeing conditions and with a focussed telescope. The aperture was selected so that the stellar disk was the size of one pixel in the CCD. Figure 6.7b shows the same cluster when the instrument has been defocussed by 4.7λ. The amount of defocus is the path length difference between a ray from the edge and one through the centre of the aperture. λ = 632.8 nm. Figure 6.7c, the processed image after 128 iterations, shows the cluster resolved to nearly the diffraction limit with the individual stars in their correct relative positions, taking into account the scale change produced by the movement of the CCD sensor away from the lens. Very severe defocus is required before the processed image shows spreading due to a loss of high spatial frequency information in the speckle image. Figure 6.7d shows the result of experiments to determine the amount of defocus that can be tolerated under the seeing conditions pertaining in our simulations. (See Appendix F for sample calculations.) When 25λ defocus is approached, the image becomes considerably blurred. Although not shown here, at this point the Airy disk of the defocussed image under perfect seeing was about the size of the seeing disk found

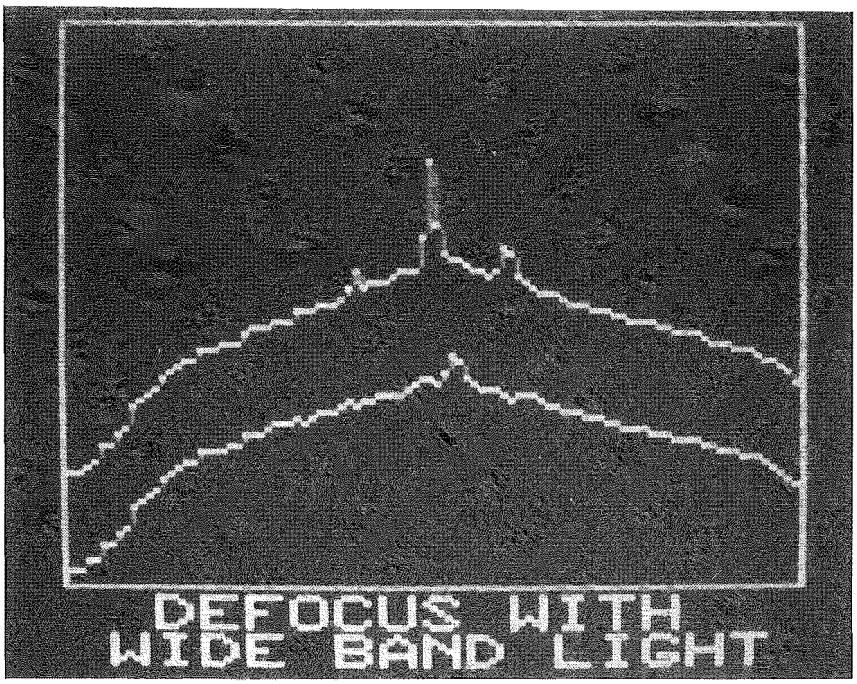

Figure 6.8 Imaging with wide band radiation and a defocussed telescope.

when the atmosphere was in place and the telescope was in focus.

6.6 SHIFT AND ADD PROCESSING WITH WIDE BAND RADIATION AND SEVERE ABERRATIONS

The limiting magnitude of a star which can be imaged by speckle interferometry is determined by the detector used in the system. For a given detector with a given noise performance during the integration time of the measurement, fainter objects can be detected by increasing either the bandwidth of the system or the size of the telescope. Shift and add processing has been shown to work with wide band radiation (§6.4). Large, high quality, low aberration telescopes are very expensive, but the previous section has shown that the shift and add process can produce images even in the presence of severe aberrations. The combination of these two results allows the use of wide band radiation with telescopes that have been manufactured with relaxed specifications and should therefore be less expensive.

A simulation using the wide band source and a defocussed instrument has been performed. As expected, the contrast in the image is very low but the three star pattern can be seen for 9.4λ defocus with wide band radiation. Figure 6.8 shows a plot of the intensity of the processed image along a line containing the brightest and second brightest star. Below it, the line containing the third brightest star is plotted. The contrast is very low, but even in this extreme case of wide band radiation and defocus an image can be reconstructed.

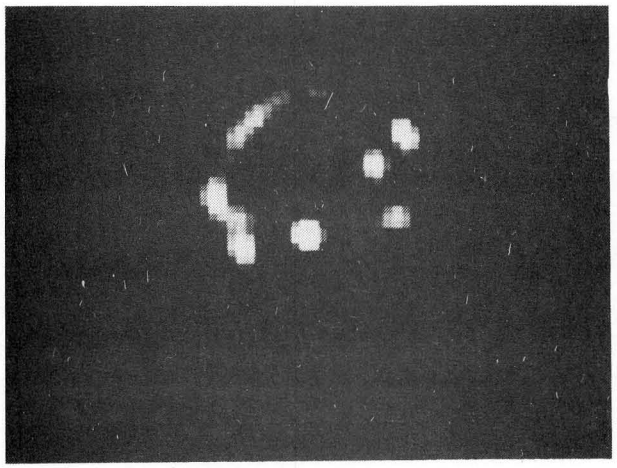

a. Extended object with perfect seeing.

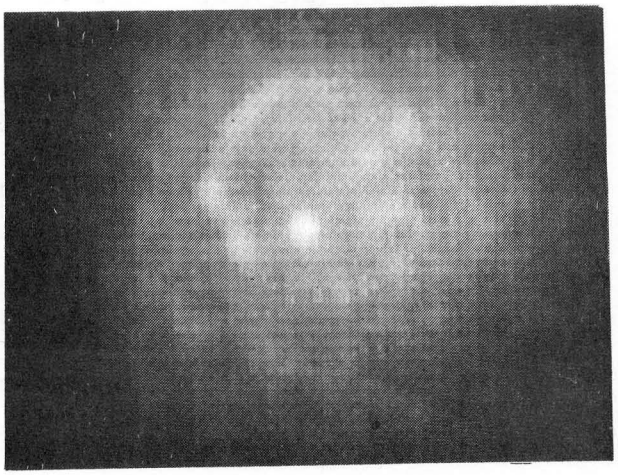

b. Processed image of extended object.

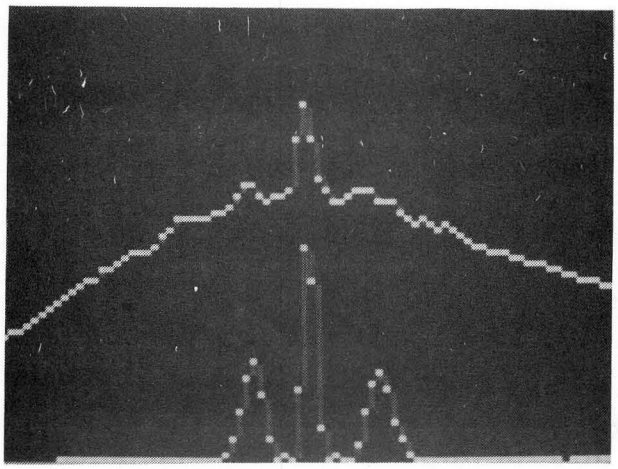

c. Line intensities through the central portion of a (lower) and b.

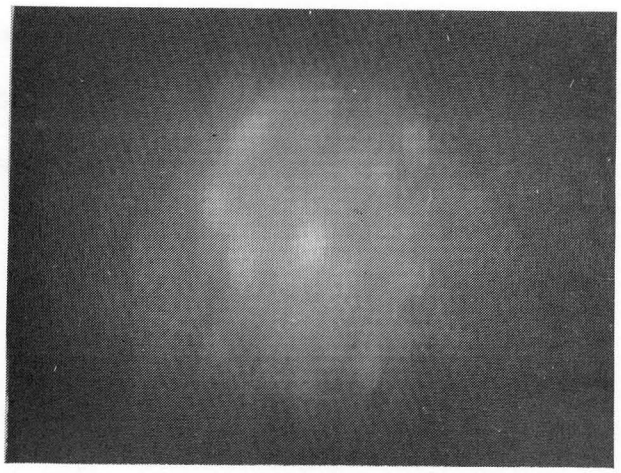

d. Processed image of extended object with 9.4λ defocus.

Figure 6.9 Imaging an extended object.

6.7 IMAGING AN EXTENDED OBJECT

Lynds *et al.* (1976) were the first to form an image of an extended object and their method has been used subsequently to image other extended objects (§4.6). To perform their method, a number of bright speckles must be identifiable in a single speckle image. The cross-correlation of the 'speckle mask' with the speckle image averages the distortions in each individual speckle. In each of the cases where the method has been used, the object was only a few resolution elements in extent. As Worden *et al.* (1976) points out, the individual speckles tend to become larger and overlap as the object becomes larger. Worden *et al.* (1976) claim that the object should be no more than 3-5 Airy disk diameters in extent for their method to be effective.

This requirement limiting the extent of the object is relaxed for shift and add processing. Providing the object has a bright point which on the average produces the brightest point in a speckle image, a processed image of an extended object many resolution elements in extent may be formed. Figure 6.9a shows an extended object when the seeing is perfect in narrow band radiation. The aperture creates an Airy disk three pixels in extent. The central bright point is roughly twice the intensity of the next brightest point in the object. Figure 6.9b shows the processed image after 128 iterations of shift and add. The contrast of the processed image is low but the line intensities plotted in Figure 6.9c for a horizontal line through the central portion of Figures 6.9a and 6.9b show

that relative intensity information is present in the processed image.

6.7.1 Imaging an Extended Object with a Defocussed Instrument

Confirmation of the results of §6.5 for an aberrated instrument with an extended object are presented in Figure 6.9d. Again, the extended object is clearly shown in the processed image with an attendant scale change due to changing the position of the CCD detector.

6.7.2 An Extended Object with Wide Band Light

An attempt was made to perform the processing of an extended object with wide band light. A satisfactory result was not obtained. The light intensity was low, requiring a longer integration with an increase in the CCD dark signal. Speckles were not bright enough, relative to this dark signal, to be seen. It should also be noted that the imaging of the extended object was performed with a small aperture to spread the Airy disk over several pixels. This was done to avoid the problem of the open/closed ratio of the active area in the CCD chip mentioned in §3.2.1. When a larger aperture was used, the contrast in the processed image was reduced even further because at times the speckles in the speckle image would not be detected by the CCD. In the previous wide band and defocussed results, this reduction in the contrast and the apparent increased distortion in the relative intensities of the processed image were accepted in order to be able to accurately measure the size of the processed image.

6.8 USE OF THE METHOD CLEAN

A method for improving a degraded image by subtractively deconvolving the point spread function of the system is presented in §4.11. This method, called CLEAN, has been used in the processing of sparsely populated brightness distributions generated by synthetic aperture radio astronomy. The procedure is used here to improve the images generated by shift and add processing.

The CLEAN procedure is implemented as described in §4.11. The point spread function used to characterize the shift and add process is that shown in Figures 6.2a and 6.2b. This psf array is centered on the brightest point in the image to be CLEANed (the *dirty* array) and a fractional part of the psf is subtracted. A *clean* array is initialized to zero, and a *clean beam* is added at the same relative position as the centre of the bright spot in the dirty array. In the examples given below, two forms of clean beam have been used. For objects which are isolated, unresolvable point sources, the clean beam is a single pixel wide. CLEAN is also applied to extended objects, and in this case the clean beam is a scaled array as shown in Figure 6.10. The extended beam is an approximation of the psf shown in Figure 6.2.

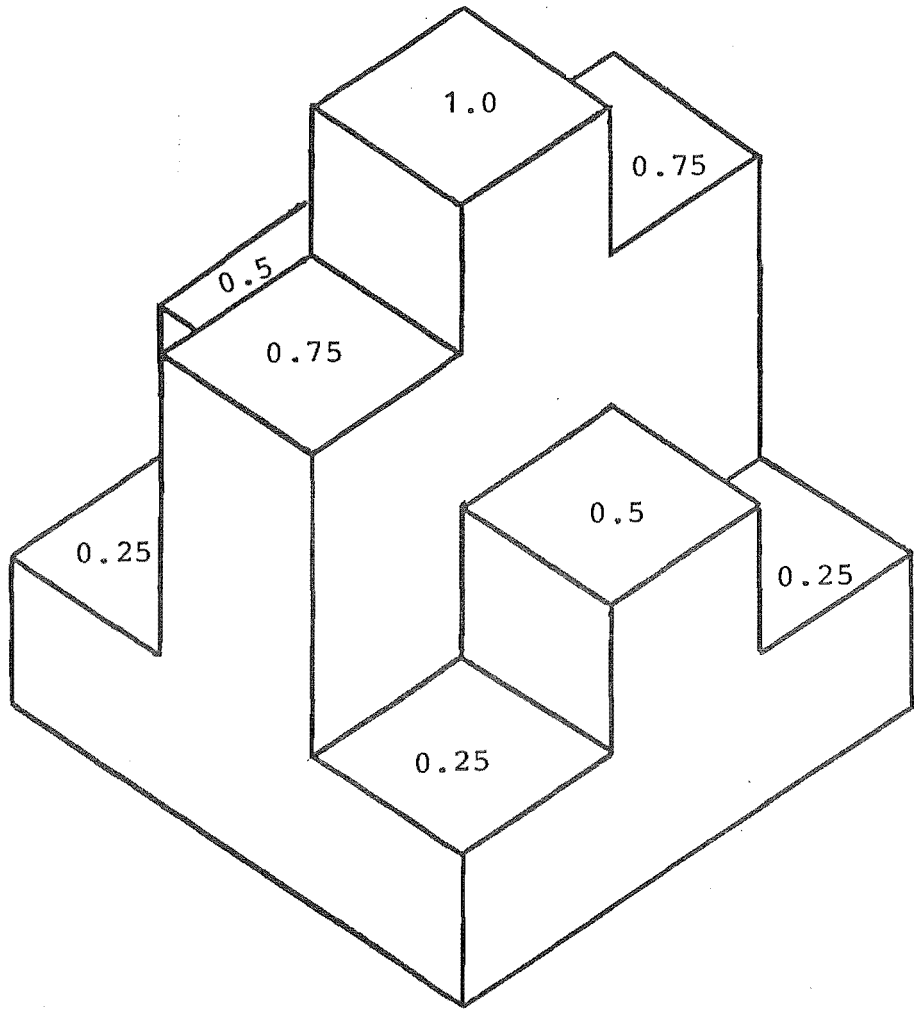

Figure 6.10 Extended clean beam.

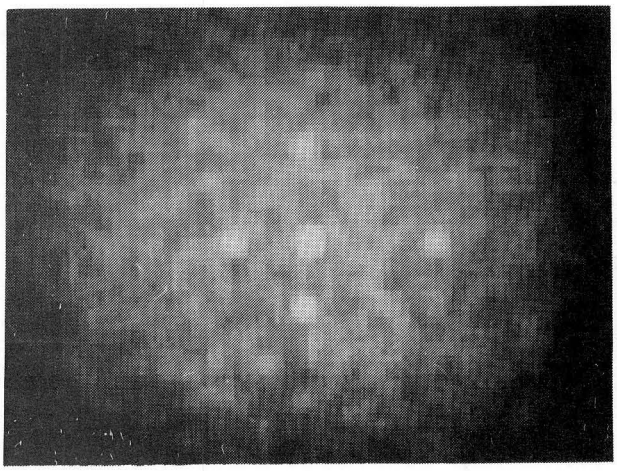

a. Five star cluster processed image before CLEAN.

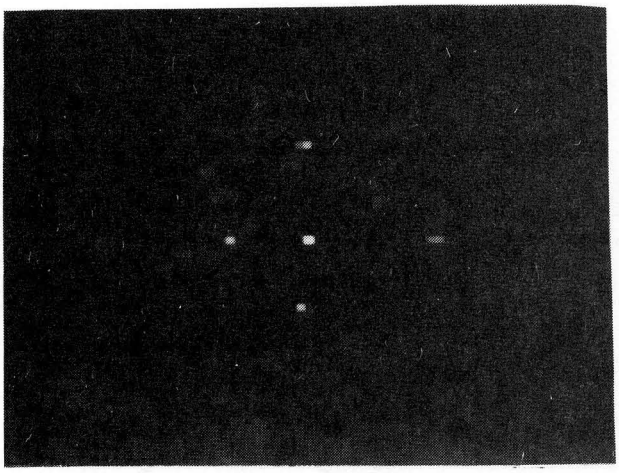

b. Five star cluster after CLEAN.

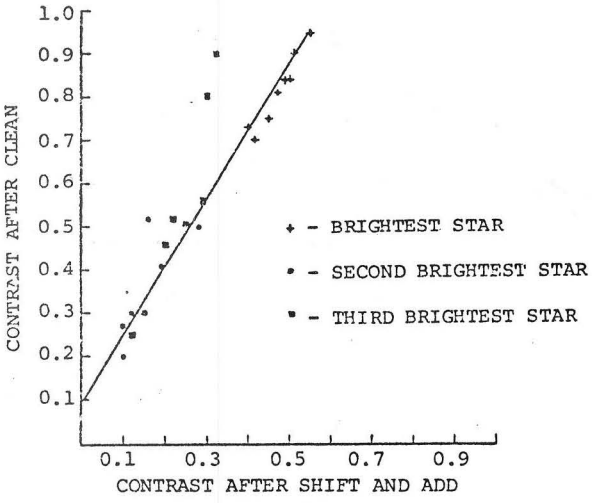

c. Contrast improvement of CLEAN.

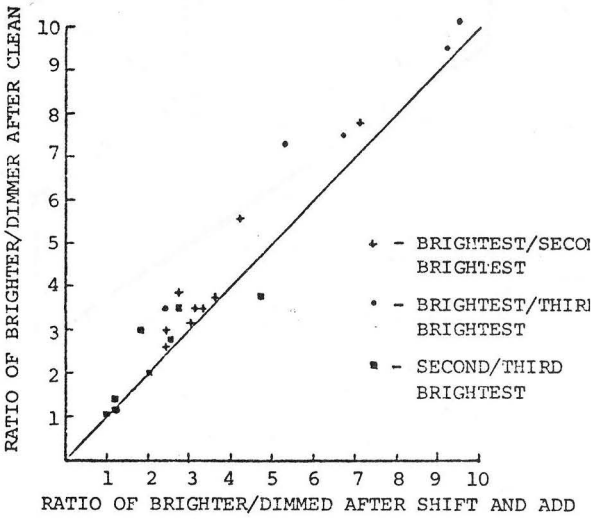

d. Affect of CLEAN on relative intensities.

Figure 6.11 CLEANing shift and add processed images.

6.8.1 CLEAN with Star Clusters

The use of CLEAN with the five star cluster of Figure 6.1 is shown in Figure 6.11. The shift and add processed image (Figure 6.1c) is repeated here in Figure 6.11a. The five star cluster image after the CLEAN operation is shown in 6.11b. Comparison of these results shows that the CLEAN procedure has reduced the background level and increased the contrast of the image. Using equation (1.2-10) to define the contrast of the star, the affect of CLEAN on contrast is shown in Figure 6.11c. (See Appendix F for sample calculations.) Figure 6.11d shows that CLEAN does not have a significant effect on the relative intensities of the processed image.

6.8.2 CLEAN with an Extended Object

CLEAN has proved to be useful in extracting information from extended objects imaged by shift and add. An extended clean beam, shown in Figure 6.10, is used to construct the clean array. This is done to restore diffraction limited information in the image. A single pixel clean beam, as used in the previous example, is truly valid only for infinite resolution or when the object is known to be an unresolvable point.

CLEAN was applied to the processed image of the extended object shown in §6.7. Figures 6.12a and 6.12b show the image formed under perfect seeing and the resultant shift and add processed image. The image of the extended object after CLEANing is shown in Figure 6.12c. Structure which is visible in the original is also clearly seen in the CLEANed image.

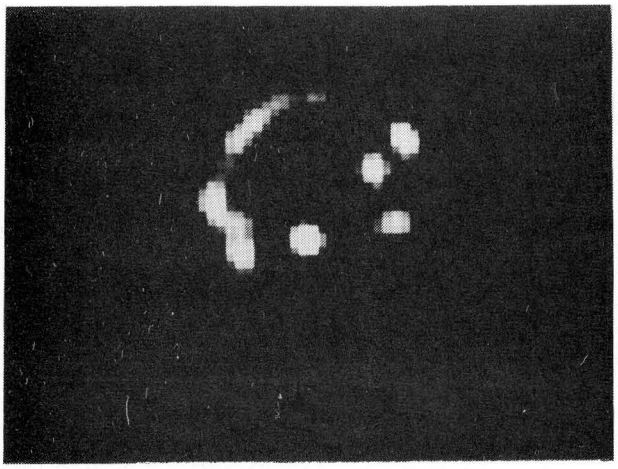

a. Extended object with perfect seeing.

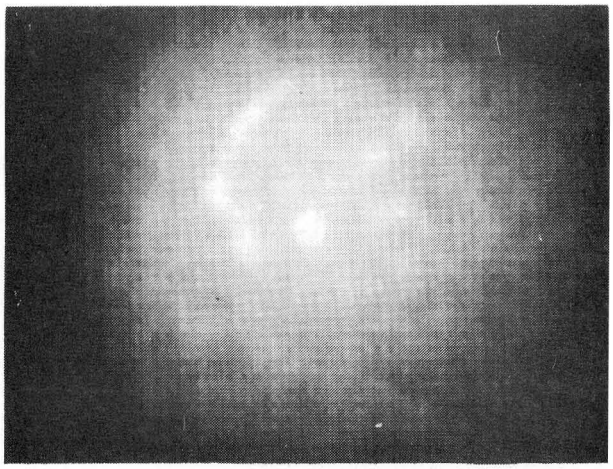

b. Extended object processed image before CLEAN.

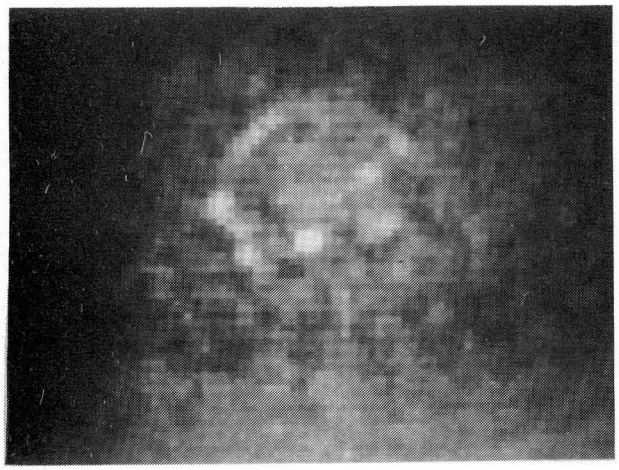

c. Extended object after CLEAN.

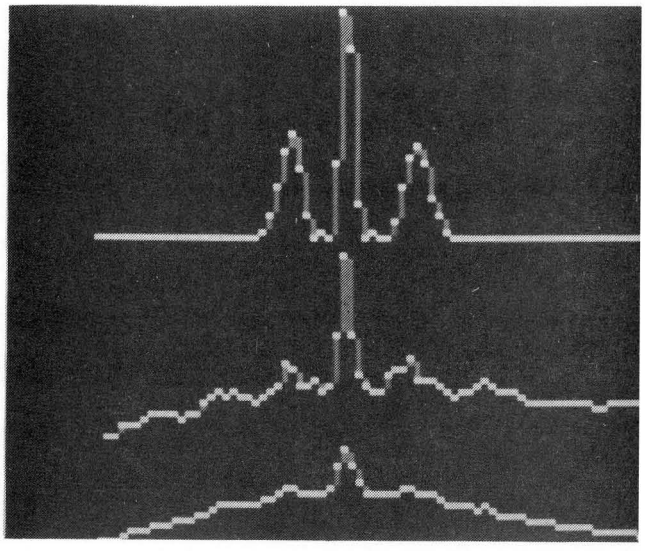

d. Line intensities through a (top), b (bottom), and c (middle).

Figure 6.12 CLEANing extended object images.

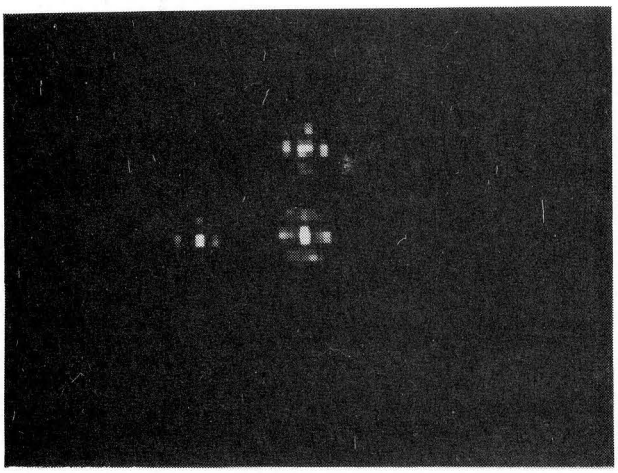

a. Image formed under perfect seeing.

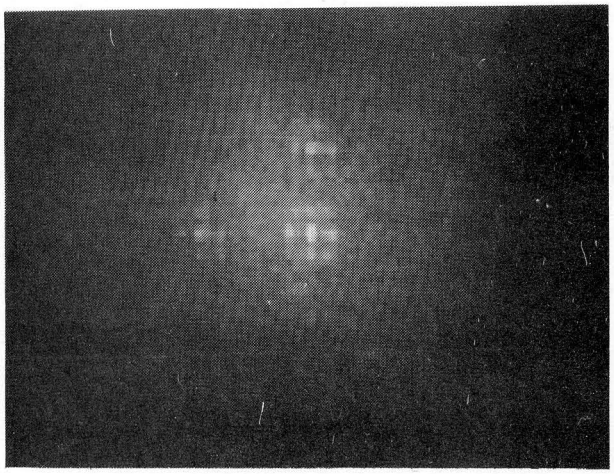

b. Shift and add processed image.

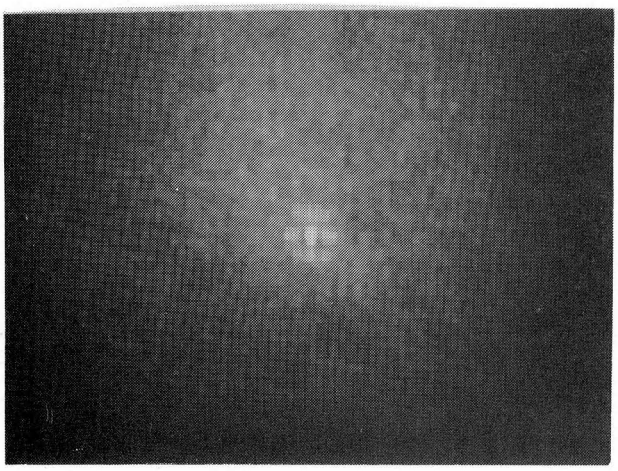

c. Point spread function.

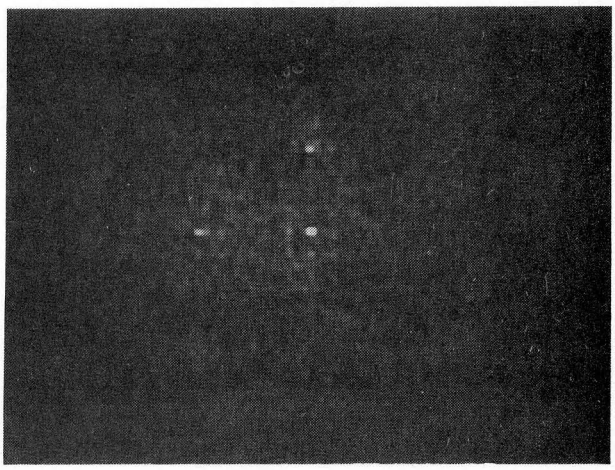

d. Shift and add image after CLEAN.

Figure 6.13 Imaging with a multiple aperture.

Plots of the intensities along a line through the central portion of 6.12a (top), 6.12b (bottom) and 6.12c (middle) are shown in Figure 6.12d. This further confirms the effect of CLEAN on image contrast.

6.9 IMAGING WITH A MULTIPLE APERTURE

The single aperture at (k) in Figure 5.3 was replaced by a 6.35 mm diameter main aperture and an additional multiple aperture mask. This consisted of a number of randomly positioned 1.4 mm diameter holes. The main aperture diameter was limited so that the size of the Airy disk was approximately the size of one CCD pixel. Labeyrie (1976) shows speckle images that are produced when multiple apertures (in this case with regular spacing) are used. Frequency components corresponding to the maximum spacing in the pupil plane generate nearly diffraction limited images. All frequencies are not present, and the image of an unresolvable object under perfect seeing conditions contains sidelobes as shown in Figure 6.13a. The shift and add process reconstructs images with sidelobes as shown in Figure 6.13b. The point spread function, found by using a single star, is shown in 6.13c and also contains sidelobes. This situation has a direct analogy in synthetic aperture radioastronomy mentioned in §4.11 where CLEAN is used to eliminate the sidelobes of the 'dirty' beam. CLEAN processing is effective here also. Figure 6.13d shows the image after the CLEAN method has been used. The intensity of the sidelobes is reduced and contrast of the image is increased.

6.10 OTHER SHIFT AND ADD CHARACTERISTICS AND RESULTS

The previous sections have reported the main results that have been achieved in simulations of astronomical imaging and shift and add processing. Other points regarding the processing which either have not been investigated thoroughly or for which the results agree well with work done by others are mentioned briefly here.

6.10.1 Contrast Improvement by Increasing the Number of Iterations of Shift and Add

This characteristic has not been investigated quantitatively or thoroughly. At least one set of measurements were taken of a star pattern where the intensity ratios were constant over the period of measurement. Results were taken for 64, 128, 256, 512 and 1024 iterations of the process. The contrast of the stars in the processed image, calculated by equation (1.2-10), did not improve over these measurements. This seems a reasonable result because the contrast of the processed image should be a stronger function of the contrast of the speckle image than of the number of iterations of the process. More experimentation is required to confirm this hypothesis.

6.10.2 Background Noise

Fluctuations in the intensity of the background 'fog' are caused either by insufficient averaging or by images which are not statistically independent. The background fluctuations have been observed to diminish as the number of iterations have increased. This tends to verify that the images used in the process are statistically independent.

6.10.3 Other Extended Objects

The process has been applied to extended objects other than that shown in §6.7. Providing there is a bright spot, at least the outline of the object and usually detail such as other bright spots can be seen in the processed image. The limitations of the shift and add process in reconstructing extended objects have not been explored, but it seems that contrast is very much reduced when imaging these objects.

6.11 DISCUSSION OF RESULTS

Shift and add processing has been shown to be effective for imaging clusters of stars and extended objects. The process works with wide band radiation and with severe instrument aberrations. Simulating astronomical imaging and performing quantitative measurements was straightforward after a method was found to determine the relative intensities of the stars without the presence of the atmosphere. However, a major limitation on performing quantitative radiometric measurements is the structure of the CCD sensor. With only 45% of the image area capable of

detecting photons, much information falls into the 'cracks' and is not measured. Using a small aperture to spread the image of an unresolvable object over a number of pixels improved the measurement reliability. Another factor which contributed to uncertainty in the results was the physical instability of the optical apparatus. Any changes in the position of any item in the simulation, for example shifting the star pattern to set a new relative intensity ratio, could result in drift in the ratio over the period of measurement. This drift was random but it was felt that measurements made with perfect seeing before and after a shift and add processing run would indicate the extremes of the drift. The extremes have been plotted as horizontal bars in Figures 6.3a and 6.3b. The quantitative results presented in §6.1 and §6.3 show good positional accuracy but considerable spread in the relative intensities. It would be difficult, given the simulation techniques used, to determine how much of this spread is caused by the shift and add process, how much by the sensor itself, and how much by drift in the apparatus during the period of measurement.

A larger aperture (9.5 mm, see Appendix E) was used to achieve the wide band speckle imaging results reported in §6.4 The larger aperture was necessary because the intensity of the wide band source was lower than the laser source. The speckles produced in this case were roughly the size of the CCD pixel. Therefore, quantitative measurements of relative intensities were not taken. In addition, because the light intensity was lower, even

with the larger aperture, the CCD integration was increased with an attendant increase in CCD dark current. This reduced the contrast of the speckles, resulting in a lower contrast in the processed image. A further degradation of the speckle image was caused by the single element lens and by not correcting for dispersion in the atmosphere. This would be done in any real system utilizing the method. Nevertheless, the results of §6.4 do show, at least qualitatively, that nearly diffraction limited images can be achieved in a system using a wider bandwidth than that used in normal speckle interferometry.

The larger aperture (9.5 mm) was also used when performing the defocus tests given in §6.5. In this case, the laser source was used and so speckles were bright and had high contrast. The larger aperture was used so that the diffraction limited image was about one pixel in extent. Thus the effect of defocus on the size of the processed image could be measured easily.

The reconstruction of the extended object was a pleasant surprise. Previous experimental results by Worden *et al.* (1976), seem to indicate that the maximum size of an object which could be reconstructed using the method of Lynds *et al.* (1976) was in the order of 3-5 Airy disks in diameter. This restriction does not apply in the shift and add processing. The object simulated, Figure 6.9a, has rather marked intensity variations over its extent. It also has a single bright point which is about 2 times brighter than any other point in the object. This may belong to a limited class of objects for which the method will work.

More experimentation must be done to determine the limits of the shift and add process when imaging extended objects.

CHAPTER 7

CONCLUSIONS AND SUGGESTIONS FOR FURTHER RESEARCH

7.0 INTRODUCTION

Shift and add is a processing method which can be applied in many imaging situations. In the astronomical application described in the previous chapters, the image is distorted by random phase perturbations in the atmosphere. The application of shift and add when the image is distorted by systematic phase distortion seems possible as shown by the results of §6.5. When aberrations are severe enough that diffraction limited resolution is unobtainable, it may be possible to introduce random phase distortion into the instrument (i.e. give it a seeing problem), and then use the shift and add process to reconstruct a diffraction limited image. This could be applicable in the construction of very large optical telescopes.

7.1 FURTHER SHIFT AND ADD PROCESSING EXPERIMENTAL WORK

The shift and add process is not fully understood and there are a number of interesting characteristics which deserve further investigation. These are discussed briefly here.

7.1.1 Extended Objects

The limitations of the method in restoring the overall shape and intensity distribution of an extended object should be determined. Thus far, only very simple extended objects have been imaged. For shift and add to restore details within an extended object, the details must have high contrast. Low contrast information is obscured by the background fog in the processed image. It may be possible to form a series of processed images, each generated from a number of speckle images. Each of these could be inverse filtered with an average point spread function and then averaged to form a composite processed image which may preserve details within an extended object. This is similar to the method of Lynds *et al.* (1976, §4.6) which averages many correlated images to form a better estimate of the distorted image.

7.1.2 Aberrations

The effect of aberrations in the system were simulated by defocussing the simulated telescope (§6.5). Other types of aberrations are now being investigated by a colleague. A sheet of glass has been introduced into the optical path between the lens (l) and the image plane (m) of Figure 5.3. With perfect seeing conditions, two images are formed of each point source in the object. Early results indicate that shift and add processing removes this type of aberration as well as defocus.

7.1.3 Wide Band Simulations

The wide band simulations described in §6.4 were not

entirely satisfactory because the intensity of the source was much less than that of the laser. A longer CCD integration time was necessary which increased the level of dark noise obscuring the signal. In addition, no correction was made for dispersion in either the perspex atmosphere or the single element lens. It would be instructive to apply dispersion correction techniques and to use a multi-element lens in the simulation. The upper limit on bandwidth could then be investigated. Preliminary tests made with white light indicated that good results may be obtainable even with very wide band radiation.

7.1.4 Ghosts

A ghost star in the processed image, shown in §6.3.2, occurs when the relative intensities of the two brightest stars in a cluster are very nearly alike. This raises questions about the statistics of the intensities around the brightest point in the speckle image. As pointed out in §6.3.2, random processes which create the speckle image can sometimes make the less bright of two stars apparently brighter. The ghost image is the result. It may be possible to correct the relative intensities of the processed image when this happens. To do this, one should know more about the distribution of intensities around the brightest point. It is suspected that this distribution is a function of the distance from the brightest point, the relative intensities of the two stars, and the seeing conditions. A series of careful tests must be performed to determine these relationships. Ghost stars may not be a frequent occurrence when the method is applied to the imaging of stellar

clusters, but it is important to understand the mechanism by which they are formed when attempting to interpret the results of imaging an extended object.

7.1.5 Inverse Filtering

The only filtering operation that has been performed on shift and add processed images is the subtractive deconvolution CLEAN technique described in §6.8. Multiplicative inverse filtering, such as Weiner filtering, requires that the image and an estimate of the point spread function be Fourier transformed. The fast Fourier transform (FFT) is generally used. The filtering process is carried out in the frequency domain, and the result is inverse transformed to give the filtered image. The FFT requires $4N^2 \log_2 N$ multiplications for a N x N image array and therefore takes considerable time on a microcomputer. (We have estimated 1½ hours to perform the FFT on a single image using the UCIPS.) However, we will soon be able to transfer shift and add processed images to a high speed computer so the FFT can be performed rapidly. When this is done, the effect of inverse filtering on the image could be evaluated. An investigation into the point spread function of the process could be made and the effect of CLEAN could be compared with inverse filtering.

7.1.6 Solar Speckle Shift and Add

Astronomers continue to investigate the surface structure of the sun (Harvey and Breckinridge 1973; Harvey and Schwartschild 1975; Aime and Roddier 1977; Aime and Ricort 1978; Ricort and Aime 1979; Stachnik *et al.* 1979).

Seeing conditions are worse during the daytime than at night. In solar observations, the points of interest are often dark in a field of light, just the reciprocal of the stellar imaging situation. It would seem possible that, providing the distribution of intensities in a speckle image is gaussian, as indicated by Dainty (1975) and Labeyrie (1976), dark speckles may correspond to the dark points in the solar surface. This has yet to be investigated but could be simulated in the optical laboratory described in §5.2.1. If such a simulation gave encouraging results, the first practical application of shift and add processing could be in this area.

7.2 PRACTICAL APPLICATION OF THE SHIFT AND ADD METHOD

It is with some trepidation that I recommend the application of shift and add in astronomical applications. As an Electrical Engineer and not an Astronomer, I can only infer from reading journals what operating procedures are used in high resolution optical astronomy. Nevertheless, local astronomers agree that the simulated speckle images (Figure 5.2) are realistic when compared with previously published speckle images. Methods developed using similar simulation techniques have been verified in practice. The speckle holography technique (Bates *et al.* 1973, §4.4) has been used by Weigelt (1978b) to form images of stars. Therefore, I am confident that the simulations reported here are realistic and that results should relate well to the real astronomical imaging situation.

7.2.1 Implementation

It is hoped that the shift and add method will prove to be useful for routine observations. The processing is simple enough to be performed in real time as the observation program is proceeding. The ability to interact with the measurements and to see results while observations are being made are invaluable aids to a greater understanding of the processes involved. In this application, an array sensor, digitizer, and on-line computing equipment such as the UCIPS described in Chapter 2 are required. However, for the first application of the method, pre-recorded data will no doubt be used so the processing will be performed after the observations have been taken. This has the disadvantage that real time information feedback is not possible, but the advantage that the investigator can select the 'best' images and so achieve a better signal-to-noise ratio than with the more automatic on-line process. In addition, having pre-recorded data means that other processing techniques may be tried in conjunction with shift and add. For example, Labeyrie's SI produces an accurate amplitude of the Fourier transform of the object. When this is combined with the phase information retrieved by shift and add, an improved image may be obtained.

We look now at the practical implementation of the shift and add technique which involves a choice of sensor, computational facilities, and data storage.

(a) Choice of sensor. We have shown that a device like the CCD202 or the larger CCD211 with its opaque transport registers interposed between active photosites

has definite drawbacks. The overall quantum efficiency is lowered and, unless the image of an unresolvable source is spread over several pixels, accurate radiometric measurements can not be made. Other sensors which do not have this deficiency have been constructed. The 400 x 400 element array described by Smith (1976) is a backside illuminated CCD, and thus exhibits a better quantum efficiency because the entire area of the sensor is active. It is not known if these devices are commercially available. Fairchild has proposed a version of their 488 x 380 element sensor especially constructed for astronomical imaging. In this device the transport register strips are eliminated so that the active area of the device increases from 45% to 100% (King 1979). At the very low light levels pertaining in most astronomical applications, the sensor must be cooled to a very low temperature to reduce noise in the device. Marcus *et al.* (1979) describe the application of a CCD211 which is cooled to liquid nitrogen temperatures. Very low noise levels (20 electrons rms) are achieved. Campbell (1977) and Davis and Latham (1979) describe similar installations using photodiode arrays.

(b) Computational facilities. It is hard to imagine the shift and add method being performed by any means other than digitally. Optical techniques are most surely ruled out by the difficulty in finding the brightest point in a speckle image and performing the shifting and adding accurately enough to reconstruct an image. When performed digitally, however, the process is very simple and straightforward. An on-line microcomputer based system

has proved to be nearly fast enough to perform the calculations required within the redistribution time of the atmosphere. The system described in Chapter 2, with its real time video monitor display, provides an effective, low cost, on-line system suitable for the shift and add process when the resolution of the imaging array is limited to 100 x 100 or at most 128 x 128 elements. In applications where larger arrays are used, consideration must be given to using a faster processor. The new 16 bit microprocessors, such as the Intel 8086, are capable of increasing the computational speed by a factor of 10 and should be suitable for most reasonable size applications, say up to 400 x 400 elements.

(c) Data storage. It would be useful to record the speckle images which are used to generate the shift and add processed image. Other processing methods, described in Chapter 4, could then use the data. Data storage requirements become difficult to meet when high resolution (>128 x 128) real time image capture is required. However, even the prototype system for the Landsat calibration instrument described in §2.3.1 (Flying FADS) is capable of storing 100 x 100 element pictures in roughly 6 seconds. The proposed design for the multi-channel device will have at least four times this data storage rate. It should be possible to store a speckle image, even with the higher resolution arrays, in about the same time as it takes to process it. If direct memory access techniques are used, the storage and the processing can take place simultaneously with only a small increase (probably less than 50%) over the

time taken to process the image alone.

7.2.2 Optical Instruments

The results shown in §6.4 for wide band speckle imaging and in §6.5 for imaging in the presence of severe aberrations are significant. They show that very high quality optical instruments and very narrow band radiation are not necessary when forming diffraction limited images of faint stellar objects. Large telescopes can be made more cheaply because the specifications can be relaxed. In addition, as shown by the results of the multiple aperture simulation of §6.9, arrays of telescopes can be used to record diffraction limited images. It also seems feasible to make use of synthetic aperture techniques to build and operate a long thin array of telescopes. Providing the aberrations in such a system do not cause image spreading greater than that caused by the seeing, the shift and add technique should be able to resolve nearly diffraction limited images.

7.2.3 Shift and Add with Other Techniques

Labeyrie's conventional Speckle Interferometry (SI) (§4.2) produces the modulus of the Fourier transform of the object intensity distribution $|F(u,v)|$ but all phase information is lost. $|F(u,v)|$ is accurately known and could be used with the phase information retrieved by the shift and add method. This may result in a diffraction limited image which is more accurate than the original shift and add processed image. The following processing procedure is suggested:

(i) Record a series of speckle images of a stellar object and a point source reference as would be done in normal SI.

(ii) Perform shift and add to form a processed image $p(x,y)$ and SI to form $|F(u,v)|$ of the object. Similar calculations using the speckle images produced by the reference star are performed to find the shift and add psf $\hat{h}(x,y)$ and the modulus of the average system otf $\langle|H(u,v)|\rangle$.

(iii) Form an estimate of $F(u,v)$ and of $H(u,v)$ by using the accurate amplitude information from SI and the phase of the transforms of $p(x,y)$ and $\hat{h}(x,y)$.

(iv) Perform an inverse filtering operation on the estimate of $F(u,v)$ with the estimate of $H(u,v)$ and then inverse transform to find an estimate of $f(x,y)$.

It is reasonable to expect this procedure to work when the stellar object is a star cluster. The relative intensities of the stars in the cluster should be more accurate than those found by the shift and add process alone. Optical simulations can be performed to determine the effect of this procedure for an extended object.

When a stellar cluster is the object of interest, an alternative procedure is suggested. The correlation processing of Bates and Milner (1978, 1979, §4.9) makes use of the autocorrelation information from SI to correct the intensities and relative positions of stars found by speckle mask processing. Forming the autocorrelation of the processed image $p(x,y)$ should allow matching patterns

to be found easily, and allow corrections to be made to the relative intensities found by shift and add.

The phase found in the processed shift and add image may be used with the modulus information from SI for the starting point in the Feinup algorithm (§4.10). By using an estimate of the actual phase of the object instead of any random phase, more credence may be given to the final result. This may be tested using data generated by optical simulations.

7.3 CONCLUSION

Speckle shift and add processing has been tested fairly comprehensively in the Optical Laboratory. Because the process is not completely understood, testing is continuing. However, it should be tried with real astronomical data. It is simple enough to be performed on-line while observations are being made, so that it is an easily acquired extension to an astronomer's armoury of data collection techniques.

REFERENCES

Agajanian, A.H. (1976) "A bibliography on charge coupled devices," Solid State Technology, May 1976, pp. 48-54.

Aime, C.; Kadiri, S.; Ricort, G.; Roddier, C.; Vernin, J. (1979) "Measurements of stellar speckle interferometry lens-atmosphere modulation transfer function," Optica Acta. Vol. 26, No. 5, pp. 575-581.

Aime, C.; Ricort, G. (1978) "One-dimensional speckle interferometry of the solar granulation," Astrophys. J. Vol. 221, pp. 362-367.

Aime, C.; Roddier, F. (1977) "One-dimensional stellar and solar speckle interferometry," Opt. Commun. Vol. 21, No. 3, pp. 435-438.

Aitchison, M.S. (1978) "A visual display terminal and serial data interface for an image processing microcomputer," Electrical Engineering Third Professional Year Project Report, University of Canterbury, Christchurch, N.Z.

Amelio, G.F. The Impact of Large CCD Image Sensing Arrays. Mountain View, Calif.: Fairchild Semi. Components Grp.

Amelio, G.F.; Dyck, R.H. (1975) "Fixed pattern noise and cooled photosensor arrays," Proceedings of the NATO Advanced Study Institute on Solid State Imaging, Louvain-la-Neuve, Belgium, September 1975, pp. 114-122.

Andrews, H.C. (1974) "Digital image restoration: a survey," Computer. Vol. 7, No. 5, pp. 36-45.

Andrews, H.C. (1977) "A potpourri of mathematical techniques applied to image science," Symposium on Current Mathematical Problems in Image Science, Monterey, Calif., N. Hollywood, Calif.: Western Periodicals, pp. 71-77.

Andrews, H.C.; Hunt, B.R. (1977) Digital Image Restoration. Englewood Cliffs, N.J.: Prentice-Hall.

Baldwin, J.E.; Warner, P.J. (1976) "Aperture synthesis without phase measurements," Mon. Not. R. astr. Soc. Vol. 175, pp. 345-353.

Baldwin, J.E.; Warner, P.J. (1978) "Phaseless aperture synthesis," Mon. Not. R. astr. Soc. Vol. 182, pp. 411-422.

Balega, Yv.; Tikonov, N.A. (1977) "Speckle interferometry of some bright stars with the 6-meter telescope," Sov. Astron. Lett. Vol. 3, pp 272-273.

Barbe, D.F. (1975) "Image devices using the charge coupled concept," Proc. IEEE. Vol. 63, No. 1, pp.38-67.

Barnea, D.I.; Silverman, H.F. (1972) "A class of algorithms for fast digital image registration," IEEE Trans. Computers. Vol. C-21, No. 2, pp. 179-186.

Bates, R.H.T. (1976) "A stochastic image restoration procedure," Opt. Commun. Vol. 19, No. 2, pp. 240-244.

Bates, R.H.T.; Cady, F.M. (1980) "Towards true imaging by wideband speckle interferometry," Opt. Commun. Vol. 32, No. 3, pp. 365-369.

Bates, R.H.T.; Gough, P.T. (1975) "New outlook on processing radiation received from objects viewed through randomly fluctuating media," IEEE Trans. Comp. Vol. C-24, pp. 449-459.

Bates, R.H.T.; Gough, P.T.; Napier, P.J. (1973) "Speckle interferometry gives holograms of multiple star systems," Astron. & Astrophys. Vol. 22, pp. 319-320.

Bates, R.H.T.; Lewitt, R.M.; Peters, T.M.; Smith, P.R. (1975) "Image reconstruction from incomplete projections," Image Processing for 2-D and 3-D Reconstruction from Projections: Theory and Practice in Medicine and the Physical Sciences, Topical Meeting, Aug. 4-7, 1975, Stanford University, pp. WA2-1-WA2-4.

Bates, R.H.T.; McDonnell, M.J.; Gough, P.T. (1977) "Imaging through randomly fluctuating media," Proc. IEEE. Vol. 65, No. 1, pp. 138-141.

Bates, R.H.T.; Milner, M.O. (1978) True Imaging of Star Clusters by Extensions of Speckle Interferometry. Research Report, Electrical Engineering Department, University of Canterbury, Christchurch, N.Z.

Bates, R.H.T.; Milner, M.O. (1979) "Towards imaging of star clusters by speckle interferometry," Image Formation from Coherence Functions in Astronomy, C. Van Schooneveld (ed.), Dordreght, Holland: D. Reidel Publishing Co., pp. 187-193.

Bates, R.H.T.; Milner, M.O.; Lund, G.I.; Seagar, A.O. (1978) "Towards high resolution imaging by speckle interferometry," Opt. Commun. Vol. 26, No. 1, pp. 22-26.

Bauer, M.E. (1976) "Technological basis and applications of remote sensing of the earth's resources," IEEE Trans. Geoscience Electronics. Vol. GE-14, No. 1, pp. 3-9.

Beddoes, D.R.; Dainty, J.C.; Morgan, B.L.; Scaddan, R.J. (1976) "Speckle interferometry on the 2.5 m Isaac Newton telescope," J. Opt. Soc. Am., Vol. 66, No. 11, pp. 1247-1251.

Bentley, J.L. (1979) "An introduction to algorithm design," IEEE Computer. Vol. 12, No. 2, pp. 66-78.

Bernstein, R. (1976) "Digital image processing of earth observation sensor data," IBM J. Res. Develop., Jan. 1976, pp. 40-57.

Biberman, L.M.; Nudelman, S. (1971) Photoelectronic Imaging Devices, Vol. 1: Physical Processes and Methods of Analysis. Vol. 2: Devices and their Evaluation. New York-London: Plenum Press.

Billingsley, F.C. (1975) "Noise considerations in digital image processing hardware," Picture Processing and Digital Filtering. Ed. T.S. Huang. Berlin: Springer-Verlag, Ch. 6.

Blackburn, P.A. (1977) "Cooling a charge coupled device, used in a scanning system, by Peltier effect cooling techniques," Electrical Engineering Third Professional Year Project Report, University of Canterbury, Christchurch, N.Z.

Blazit, A.; Bonneau, D.; Koechlin, L.; Labeyrie, A. (1977) "The digital speckle interferometer: preliminary results on 59 stars and 3C 273*," Astrophys. J. Vol. 214, pp. L79-L84.

Bonneau, D.; Labeyrie, A. (1973) "Speckle interferometry: color dependent limb darkening evidence on Alpha and Omicron Ceti," Astrophys. J. Vol. 181, pp. L1-L4.

Booth, J.M.; Schroeder, J.B. (1977) "Design considerations for digital image processing systems," Computer. Vol. 10, No. 8, pp. 15-20.

Born, M.; Wolf, E. (1976) Principles of Optics, 4th Ed. London: Pergamon Press.

Bowles, K.L. (1978) "UCSD Pascal: a (nearly) machine independent software system," Byte. May 1978.

Brooks, F.P. (1975) The Mythical Man-Month. Reading, Mass.: Addison-Wesley.

Brown, F.M. (ed.) (1966) Photographic Systems for Engineers. Boston: Farnsworth Press, Ch. 10.

Cady, F.M.; Bates, R.H.T. (1980) "Speckle processing gives diffraction limited true images from severely aberrated instruments," Optics Letters, to be published.

Cady, F.M.; Hodgson, R.M.; Ireland, A.J.; Duncan, G.A. (1979) "A CCD based image processing system," NZIE Proc. Tech. Groups. Vol. 4, No. 2E (ETG), NZIE Annual Conference, Hamilton, N.Z., 1978.

Cady, F.M.; Pairman, D.; Hodgson, R.M. (1979) "PIKKY - a floppy disk based interactive picture processing operating system," Presented at NELCON 79, Aug. 29-31, 1979, Christchurch, N.Z.

Campana, S.B.; Barbe, D.F. (1974) "Tradeoffs between aliasing and MTF," Proc. Intl. Conf. Technology and Applications of Charge Coupled Devices, Univ. of Edinburgh, pp. 168-176.

Campbell, B. (1977) "The DDO diode array spectrometer," Publications of the Astronomical Society of the Pacific. Vol. 89, pp. 728-732.

Camping, S.J.; Savory, M.A. (1979) "Multiplexing a line printer to several micro-development systems," Electrical Engineering Third Professional Year Project Report, University of Canterbury, Christchurch, N.Z.

Capece, R.P. (1978) "Tackling the very large-scale problems of VLSI: a special report," Electronics. Nov. 23, 1978, pp. 111-125.

Carruthers, G.R. (1977) "Electronic imaging for space science and applications," Astronautics & Aeronautics. October 1977, pp. 56-68.

Castleman, K.R. (1979) Digital Image Processing. Englewood Cliffs, N.J.: Prentice-Hall.

CCD(1) NATO Advanced Study Institute on Solid State Imaging, Louvain-la-Neuve, Belgium, Sept. 3-12, 1975. Netherlands: Hordhoff, 1975.

CCD(2) Proceeding Conference on Charge-coupled Device Technology and Applications. Nov. 30 - Dec. 2, 1976. Pasadena, CA: Jet Propulsion Laboratory JPL SP 43-40.

CCD(3) Proceedings International Conference on Technology and Applications of Charge Coupled Devices. Univ. of Edinburgh, Sept. 25-27, 1974. Edinburgh: Univ. of Edinburgh, 1974.

CCD(4) Symposium on Charge-coupled Device Technology for Scientific Imaging Applications, Pasadena, CA., May 6-7, 1975. Pasadena, CA: Jet Propulsion Laboratory JPL SP 43-21.

Chien, R.T.; Synder, W. (1975) "Hardware for visual image processing," IEEE Trans. Circuits and Systems. Vol. CAS-22, No. 6, pp. 541-555.

Cole, E.R. (1973) The Removal of Unknown Image Blurs by Homomorphic Filtering. Ph.D. dissertation, Dept. of Electrical Engineering, Univ. of Utah, Salt Lake City, Utah.

Cree, R.A. (1979) "A dual port memory system," Electrical Engineering Third Professional Year Project Report, University of Canterbury, Christchurch, N.Z.

Dainty, J.C. (1973) "Diffraction-limited imaging of stellar objects using telescopes of low optical quality," Opt. Commun. Vol. 7, No. 2, pp. 129-134.

Dainty, J.C. (1975) Laser Speckle and Related Phenomena. Topics in Applied Physics. Vol. 9. Berlin: Springer-Verlag.

Dainty, J.C. (1977) "Telescope requirements for stellar interferometry," Proc. ESO Conf. Optical Telescopes of the Future. Geneva: Dec. 1977, pp. 43-46.

Dainty, J.C.; Scaddan, R.J. (1975) "Measurements of the atmospheric transfer function at Mauna Kea, Hawaii," Mon. Not. R. astr. Soc. Vol. 170, pp. 519-532.

Dainty, J.C.; Shaw, R. (1974) Image Science. London: Academic Press.

Davis, M.; Latham, D.W. (1979) "Photon counting Reticon detector," SPIE Conference Instrumentation in Astronomy - III, Jan. 29 - Feb. 1. 1979.

Devorkin, D.H. (1975) "Michelson and the problem of stellar diameters," Jrnl. for the History of Astronomy, Vol. 6, pp. 1-18.

Duffieux, P.M. (1970) Private Publication (see also the Fourier Transform and its Applications in Optics (Parts: Masson)).

Duncan, G.A. (1978) Sensor Evaluation and the Design of a Display for an Image Processing System. Master of Electrical Engineering Report, University of Canterbury, Christchurch, N.Z.

Dyck, R.H.; Jack, M.D. (1974) "Low light level performance of a charge-coupled area imaging device," Proc. Intl. Conf. Technology and Applications of Charge Coupled Devices, Univ. of Edinburgh, 25-27 Sept. 1974, pp. 154-161.

Ehn, D.G.; Nisenson, P. (1975) "Astronomical speckle imaging," J. Opt. Soc. Am. Vol. 65, No. 10, p. 1196.

Fairchild (1976) CCD202 Specifications. Mountain View, CA: Fairchild Camera and Instrument Corp.

Fante, R.L. (1979) "Comments on a method for processing stellar speckle data," J. Opt. Soc. Am. Vol. 69, No. 10, pp. 1394-1396.

Fienup, J.R. (1978) "Space object imaging through the turbulent atmosphere," Applications of Digital Image Processing, SPIE Vol. 149, pp. 72-81.

Fienup, J.R. (1979) "Space object imaging through the turbulent atmosphere," Optical Engineering. Vol. 18, No. 5, pp. 529-534.

Fried, D.L. (1966) "Optical resolution through a randomly inhomogeneous medium for very long and very short exposures," J. Opt. Soc. Am. Vol. 56, No. 10, pp. 1372-1379.

Gabriel, W.P. (1979) "Intervalometer," 1979 N.Z. Electronics Review. Vol. 12, p. 15.

Gaertner, W.W.; Reddi, S.S.; Retter, C.T.; Singh, I.M. (1977) "Computational complexity and parallelism of image processing algorithms," Symposium on Current Mathematical Problems in Image Science, Monterey, Calif., Nov. 1976, N. Hollywood, Calif.: Western Periodicals, pp. 224-228.

Gault, W.A. (1976) "Acquisition, transformation and analysis of airborne interferograms from the Michelson interferometer previously developed by York University, and investigation of imaging arrays for this interferometer," Toronto, Canada: Center for Research in Experimental Space Science, York University, March 1976.

General Electric (1977) TN2500 Solid State Camera Specifications. Syracuse, N.Y.: General Electric Co.

Gerchberg, R.W. (1974) "Super-resolution through error energy reduction," Optica Acta. Vol. 21, No. 9, pp. 709-720.

Gerchberg, R.W.; Saxton, W.O. (1972) "A practical algorithm for the determination of phase from image and diffraction plane pictures," Optik. Vol. 35, No. 2, pp. 237-246.

Gezari, D.Y.; Labeyrie, A.; Stachnik, R.V. (1972) "Speckle interferometry: diffraction limited measurements of nine stars with the 200-inch telescope," Astrophys. J. Vol. 173, pp. L1-L5.

Goodman, J.W. (1968) Introduction to Fourier Optics. New York: McGraw-Hill.

Goodman, T.; Spence, R. (1978) "The effect of system response time on interactive computer aided problem solving," Computer Graphics. Vol. 12, No. 3, pp. 100-104.

Gough, P.T.; Bates, R.H.T. (1974) "Speckle holography," Optica Acta. Vol. 21, No. 3, pp. 243-254.

Gould, J.D. (1968) "Visual factors in the design of computer-controlled CRT displays," Human Factors. Vol. 10, No. 4, pp. 359-376.

Green, W.B. (1977) "Computer image processing - the Viking experience," IEEE Trans. Consumer Electronics. Vol. CE-23, No. 3, pp. 281-289.

Gross, W.C. (1975) "CCD star trackers," Symposium on Charge-coupled Device Technology for Scientific Imaging Applications, Pasadena, CA., May 6-7, 1975, Pasadena, CA: Jet Propulsion Laboratory JPL SP 43-21.

Hall, E.L. (1972) "A comparison of computations for spatial frequency filtering," Proc. IEEE. Vol. 60, No. 7, pp. 887-891.

Hanbury Brown, R. (1974) The Intensity Interferometer. London: Taylor & Francis Ltd.

Hanbury Brown, R.; Twiss, R.Q. (1954) "A new type of interferometer for use in radio astronomy," Phil. Mag. Vol. 45, p. 663.

Hanbury Brown, R.; Twiss, R.Q. (1956) "A test of a new type of stellar interferometer on Sirius," Nature. Vol. 178, p. 1046.

Hansen, J.V. (1976) "Man-machine communication: an experimental analysis of heuristic problem-solving under on-line and batch processing conditions," IEEE Trans. Systems, Man, and Cybernetics. Vol. SMC-6, No. 11, pp. 746-752.

Harvey, J.W.; Breckinridge, J.B. (1973) "Solar speckle interferometry," Astrophys. J. Vol. 182, pp. L137-L139.

Harvey, J.W.; Schwartschild, M. (1975) "Photoelectric speckle interferometry of the solar granulation," Astrophys J. Vol. 196, pp. 221-226.

Hnatek, E.R. (1976) A User's Handbook of D/A and A/D Converters. New York: John Wiley & Sons.

Hodgson, R.M. (1979) "Charge transfer devices and their use," New Zealand Engineering. Vol. 34, No. 11, pp. 246-249.

Hodgson, R.M.; Cady, F.M.; Murphy, J.K.N. (1979) "The development of a multispectral scanner to be flown in a light aircraft," Proc. Landsat 79, 1st Australasian Landsat Conference, May 22-25, 1979, Sydney, Australia.

Hodgson, R.M.; Cady, F.M.; Pairman, D. (1980) "Remote sensing from light aircraft using solid state arrays," Photogrammetric Engineering & Remote Sensing.

Högbom, J.A. (1974) "Aperture synthesis with a non-regular distribution of interferometer baselines," Astron. Astrophys. Suppl. Vol. 15, pp. 417-426.

Holton, G.; Roller, D.H.D. (1958) Foundations of Modern Physical Science. Reading, Mass: Addison-Wesley.

Hopcroft, J.E. (1974) "Complexity of computer computations," Proc. IFIP Congress 74. Vol. 3, Amsterdam, The Netherlands: North Holland Publishing Co., pp. 620-626.

Huang, T.S. (ed.) (1975) Picture Processing and Digital Filtering. Berlin: Springer-Verlag, p. 12.

Hubard, G.; Reed, M.; Strittmatter, P.; Hege, K. (1979) "Digital speckle interferometry to measure the angular diameters of faint objects," I.A.U. Colloquium No. 50, Ed. J. Davis and W.J. Tango, Sydney: Chatterton Astronomy Department, School of Physics, University of Sydney, pp. 28-1-28-8.

Hufnagel, R.E.; Stanley, N.R. (1964) "Modulation transfer function associated with image transmission through turbulent media," J. Opt. Soc. Am. Vol. 54, pp. 52-61.

Ireland, A.J. (1977) A Solid State Fast Area Digitising Scanner. Master of Electrical Engineering Report, University of Canterbury, Christchurch, N.Z.

Jenkins, F.A.; White, H.E. (1976) Fundamentals of Optics, 4th ed. New York: McGraw-Hill.

Jensen, K.; Wirth, N. (1975) Pascal User Manual and Report 2nd ed. New York: Springer-Verlag.

Jones, R.C. (1959) "Quantum efficiency of detectors for visible and infrared radiation," Adv. Electronics and Electron Physics. Vol. 11, pp. 87-183.

Karo, D.P.; Schneiderman, A.M. (1976) "Speckle interferometry lens-atmosphere MTF measurements," J. Opt. Soc. Am. Vol. 66, No. 11, pp. 1252-1256.

Karo, D.P.; Schneiderman, A.M. (1977) "Speckle interferometry with severely aberrated telescopes," J. Opt. Soc. Am. Vol. 67, No. 9, pp. 1277-1278.

Karo, D.P.; Schneiderman, A.M. ((1978) "Speckle interferometry at finite spectral bandwidths and exposure times," J. Opt. Soc. Am. Vol. 68, No. 4, pp. 480-485.

Karo, D.P.; Schneiderman, A.M. (1979) "Laboratory simulation of stellar speckle interferometry," Applied Optics. Vol. 18, No. 6, pp. 828-833.

King, A.R. (1979) Letter to Astronomers from Fairchild Camera and Instrument Corp. May 29, 1979.

Knox, K.T. (1976) "Image retrieval from astronomical speckle patterns," J. Opt. Soc. Am. Vol. 66, No. 11, pp. 1236-1239.

Knox, K.T.; Thompson, B.J. (1974) "Recovery of images from atmospherically degraded short-exposure photographs," Astrophys. J. Vol. 193, pp. L45-L48.

Knuth, D.E. The Art of Computer Programming, Vol. I: Fundamental Algorithms (1968), Vol. II: Seminumerical algorithms (1969), Vol. III: Sorting and Searching (1973). Reading, Mass: Addison-Wesley.

Korff, D. (1973) "Analysis of a method for obtaining near-diffraction-limited information in the presence of atmospheric turbulence," J. Opt. Soc. Am. Vol. 63, No. 8, pp. 971-980.

Korff, D.; Dryden, G.; Miller, M.G. (1972) "Information retrieval from atmospheric induced speckle patterns," Opt. Commun. Vol. 5, No. 3, pp. 187-192.

Korff, D.; Dryden, G.; Leavitt, R.P. (1975) "Isoplanicity: the translation invariance of the atmospheric Green's function," J. Opt. Soc. Am. Vol. 65, No. 11, pp. 1321-1330.

Labeyrie, A. (1970) "Attainment of diffraction limited resolution in large telescopes by Fourier analysing speckle patterns in star images," Astron. & Astrophys. Vol. 6, pp. 85-87.

Labeyrie, A. (1974) "Observations interferometriques au Mont Palomar," Nouv. Rev. Optique. Vol. 5, pp. 141-151.

Labeyrie, A. (1976) "High resoltuion techniques in optical astronomy," Progress in Optics, ed. E. Wolf. Vol. XIV, Amsterdam, North-Holland, pp. 46-87.

Labeyrie, A.; Bonneau, D.; Stachnik, R.V.; Gezari, D.Y. (1974) "Speckle interferometry III: High resolution measurements on twelve close binary systems," Astrophys. J. Vol. 194, pp. L147-L151.

Ledgard, H.F. (1975) Programming proverbs for Fortran Programmers. New Jersey: Hayden Book Co.

Lehmann, M. (1970) Holography Technique and Practice. London: Focal, p. 34.

Lehmann, M. (1974) "The optical laboratory," Coherent Optical Processing. Vol. 52, San Diego, CA: Proc. Soc. Photo-opt. Instrum. Engr., pp. 23-26.

Leonard, J. (1979) "A graphics input device for an image processing system," Electrical Engineering Third Professional Year Project Report, University of Canterbury, Christchurch, N.Z.

Lewitt, R.M.; Bates, R.H.T. (1978a) "Image reconstruction from projections: I: General theoretical considerations," Optik. Vol. 50, No. 1, pp. 19-33.

Lewitt, R.M.; Bates, R.H.T. (1978b) "Image reconstruction from projections: III: Projection completion methods (theory)," Optik. Vol. 50, No. 3, pp. 189-204.

Lewitt, R.M.; Bates, R.H.T. (1978c) "Image reconstruction from projections: IV: Projection completion methods (computational methods)," Optik. Vol. 50, No. 4, pp. 269-278.

Lewitt, R.M.; Bates, R.H.T.; Peters, T.M. (1978) "Image reconstruction from projections: II: Modified back-projection methods," Optik. Vol. 50, No. 2, pp. 85-109.

Lipson, H.; Cochran, W. (1966) The Determination of Crystal Structures. London: G. Bell & Sons.

Liu, C.Y.C.; Lohmann, A.W. (1973) "High resolution image formation through the turbulent atmosphere," Opt. Commun. Vol. 8, No. 4, pp. 372-377.

Lohmann, A.W.; Weigelt, G.P. (1975) "Large field speckle interferometry," Technical Digest, Topical Meeting on Imaging in Astronomy. Cambridge, Mass: 1975, pp. THC3-1-THC3-4.

Lohmann, A.W.; Weigelt, G.P. (1978) "Image reconstruction from astronomical speckle interferograms," Proc. Optical Telescopes of the Future. Geneva: ESO Conference, February 1978, pp. 479-494.

Lohmann, A.W.; Weigelt, G.P. (1979) "Astronomical speckle interferometry: measurements of isoplanicity and of temporal correlation," Optik. Vol. 53, No. 3, pp. 167-180.

Longshaw, T.G.; Viljoen, R.P.; Hodson, M.C. (1976) "Photographic display of Landsat-1 CCT images for improved geological definition," IEEE Trans. Geoscience Electronics. Vol. GE-14, No. 1, pp. 66-78.

Luneberg, R.K. (1964) Lecture Notes (see also the Mathematical Theory of Optics (University of California Press, 1964)).

Lynds, C.R.; Worden, S.P.; Harvey, J.W. (1976) "Digital image reconstruction applied to Alpha Orionis," The Astroph. J. Vol. 207, pp. 174-180.

Marcil, G.S. (1974) "Microdensitometer data acquisition," Acquisition & Analysis of Pictorial Data. The Modern Science of Imagery, Proc. of the SPIE. Vol. 48, August 19-20, 1974, San Diego, CA., pp. 23-33.

Marcus, S.; Nelson, R.; Lynds, R. (1979) "Preliminary evaluation of a Fairchild CCD-211 and a new camera system," SPIE Conference Instrumentation in Astronomy - III, Jan. 29 - Feb. 1, 1979.

Masursky, H. *et al.* (1976) "Planetary imaging: past, present, and future," IEEE T.O. Geoscience Electronics. Vol. GE-14, No. 3, pp. 122-134.

McAlister, H.A. (1976) "Speckle interferometry of Eta Orionis," Publ. Astr. Soc. Pac. Vol. 88, pp. 957-959.

McAlister, H.A. (1977a) "Speckle interferometry of the Hyades spectroscopic binary 51 Tauri," Astrophys. J. Vol. 212, pp. 459-461.

McAlister, H.A. (1977b) "Speckle interferometric measurements of binary stars I," Astrophys. J. Vol. 215, pp. 159-165.

McAlister, H.A. (1977c) "Binary star speckle interferometry," Sky and Telescope. May 1977, pp. 346-350.

McAlister, H.A. (1978) "Speckle interferometric measurements of binary stars II," Astrophys. J. Vol. 225, No. 3, pp. 932-938.

McAlister, H.A. (1979) "Speckle interferometric measurements of binary stars IV," Astrophys J. Vol. 230, pp. 497-501.

McAlister, H.A.; Degioia, K.A. (1979) "Speckle interferometric measurements of binary stars III," Astrophys. J. Vol. 228, pp. 493-496.

McCarthy, D.W.; Low, F.J.; Howell, R. (1977) "Angular measurements of Alpha Orionis, Vy Canis Majoris and IRC+10216 at 8.3, 10.2 and 11 micrometers," Astrophys. J. Vol. 214, pp. L85-L89.

McCord, T.B.; Bosel, J.P. (1975) "Potential usefulness of CCD imagers in astronomy," Symposium on Charge-coupled Device Technology for Scientific Imaging Applications, Pasadena, CA., May 6-7, 1975, Pasadena, CA: Jet Propulsion Laboratory JPL SP 43-21.

McDonnell, M.J. (1975) Nonrecursive Digital Image Restoration. Ph.D. dissertation. Dept. of Electrical Engineering, University of Canterbury, Christchurch, N.Z.

McDonnell, M.J.; Bates, R.H.T. (1978) "Digital restoration of an image of Betelgeuse," Astrophys. J. Vol. 208, pp. 443-452.

McDonnell, M.J.; Fowler, A.D.W. (1979) "Landsat digital image processing in New Zealand," Proc. Landsat 79, 1st. Australasian Landsat Conference, May 22-25, 1979, Sydney, Australia.

McGowan, C.L.; Kelly, J.R. (1975) Top Down Structured Programming Techniques. New York: Petrocelli/Charter.

Mersereau, R.M.; Oppenhein, A.V. (1974) "Digital reconstruction of multidimensional signals from their projections," Proc. IEEE. Vol. 62, No. 10, pp. 1319-1338.

Michelson, M.G.; Pease, F.G. (1921) "Measurement of the diameter of Alpha Orionis with the interferometer," Astrophys. J. Vol. 53, pp. 249-259.

Michon, G.J.; Burke, H.K. (1975) "Charge injection devices for solid state imaging," Proceedings of the NATO Advanced Study Institute on Solid State Imaging, Louvain-laNeuve, Belgium, Sept. 3-12, 1975, pp. 447-461.

Michon, G.J.; Burke, H.K.; Brown, D.M. (1975) "Recent developments in CID imaging," Symposium on Charge-coupled Device Technology for Scientific Imaging Applications, Pasadena, CA., May 6-7, 1975, Pasadena, CA: Jet Propulsion Laboratory JPL SP 43-21.

Michon, G.J.; Burke, H.K.; Ghezzo, M.; Brown, D.M. (1975) "A high density CID imager with non-destructive readout capability," Technical Digest, Topical Meeting on Imaging in Astronomy. Cambridge, Mass: 1975, FB4-1-FB4-4.

Miller, A.R. (1978) "CP/M: an 8080 disk operating system with editor, assembler, and debugger," Interface Age. July 1978, pp. 156-162.

Miller, L.H. (1977) "A study in man-machine interaction," Joint Computer Conference. Vol. 46, June 13-16, 1977, AFIPS Conference Proceedings, pp. 409-421.

Miller, M.G. (1977) "Noise considerations in stellar speckle interferometry," J. Opt. Soc. Am. Vol. 67, No. 9, pp. 1176-1184.

Miller, M.G.; Schneidermqn, A.M.; Kellen, P.F. (1973) "Comparison of methods for processing short exposure data from large telescopes," Astrophys. J. Vol. 186, L91-L93.

Miller, R.B. (1968) "Response time in man-computer conversational transactions," Joint Computer Conference. Vol. 33, Dec. 9-11, 1968, AFIPS Conference Proceedings, pp. 267-277.

Milner, M.O. (1980) Error Correction in Images and Imaging Instruments. Ph.D. dissertation, Dept. of Electrical Engineering, University of Canterbury, Christchurch, N.Z.

Mizner, W. (1979) Reader's Digest. November 1979, p. 67.

Morgan, B.L.; Beddoes, D.R.; Scadden, R.J.; Dainty, J.C. (1978) "Observations of binary stars by speckle interferometry," Mon. Not. R. astr. Soc. Vol. 183, pp. 701-710.

Murphy, J.K.N. (1979) Solid State Imaging Arrays for Remote Sensing. Master of Electrical Engineering Report. University of Canterbury, Christchurch, N.Z.

Nisenson, P.; Stachnik, R.V. (1978) "Measurements of atmospheric isoplanatism using speckle interferometry," J. Opt. Soc. Am. Vol. 68, No. 2, pp. 169-175.

Nisenson, P.; Stachnik, R.V. (1979) "Restoration of turbulence degraded images - a review," I.A.U. Colloquium No. 50, ed. J. Davis and W.J. Tango, Sydney: Chatterton Astronomy Department, School of Physics, University of Sydney. pp. 34-1-34-14.

Pairman, D. (1978) Hardware and Software Development for an Image Processing System. Electrical Engineering Third Professional Year Project Report, University of Canterbury, Christchurch, N.Z.

Pairman, D. (1980) Hardware and Software Developments for an Airborne Multispectral Scanning System. Master of Electrical Engineering Report, University of Canterbury, Christchurch, N.Z.

Parry, G.; Pusey, P.N.; Jakeman, E.; McWhirter, J.G. (1977) "Focussing by a random phase screen," Opt. Commun. Vol. 22, No. 2, pp. 195-201.

Peters, T.M. (1973) Image Reconstruction from Projections. Ph.D. dissertation, Dept. of Electrical Engineering, University of Canterbury, Christchurch, N.Z.

Preiss, R. (1977) "Storage CRT display terminals: evolution and trends," IEEE Computer. Vol. 11, No. 11, pp. 20-26.

Pucilowski, J.J.; Schlam, E. (1978) "Emerging display devices," IEEE Trans. Electron Devices, Vol. ED-25, No. 2, pp. 167-171.

Reticon (1977) Reticon RA100x100 Specification. Sunnyvale, CA: Reticon Corp.

Richardson, D.E. (1978) "Spy satellites - somebody could be watching you," Electronics & Power, Aug. 1978, pp. 573-578.

Ricort, G.; Aime, C. (1979) "Solar seeing and the statistical properties of the photospheric solar granulation," Astron. & Astrophys. Vol. 76, pp. 324-335.

Roddier, F.; Ricort, G.; Roddier, C. (1978) "Defocussing effects in astronomical speckle interferometry," Opt. Commun. Vol. 24, No. 3, pp. 281-284.

Rogers, G.L. (1979) "The stellar interferometry of a star cluster with a prominent variable," Opt. Commun. Vol. 30, No. 1, pp. 1-4.

Root, G. (1976) "Testing thinned, backside illuminated CCD area image sensors," Proceedings Conference on Charge-coupled Device Technology and Applications. Nov. 30 - Dec. 2, 1976, JPL SP 43-40, pp. 63-71.

Rouse, W.B. (1975) "Design of man-computer interfaces for on-line interactive systems," Proc. IEEE. Vol. 63, No. 6, pp. 847-857.

Sackman, H. (1968) "Time-sharing versus batch processing: the experimental evidence," Joint Computer Conference. Vol. 32, April 30 - May 2, 1968, AFIPS Conference Proceedings, pp. 1-10.

Scaddan, R.J.; Morgan, B.L.; Dainty, J.C. (1979) "Diffraction-limited observations of binary star systems," I.A.U. Colloquium No. 50, ed. J. Davis and W.J. Tango, Sydney: Chatterton Astronomy Department, School of Physics, University of Sydney, pp. 27-1-27-10.

Schneiderman, A.M.; Karo, D.P. (1977) "How to build a speckle interferometer," Optical Engineering, Vol. 16, No. 1, pp. 72-79.

Schneiderman, A.M.; Karo, D.P. (1978) "Measurements of RO with speckle interferometry," J. Opt. Soc. Am. Vol. 68, pp. 348-351.

Schneiderman, A.M.; Karo, D.P. (1979) "Imaging in the presence of random wave aberration," J. Opt. Soc. Am. Vol. 69, No. 5, pp. 717-724.

Schneiderman, A.M.; Kellen, P.F.; Miller, M.G. (1975) "Laboratory-simulated speckle interferometry," J. Opt. Soc. Am. Vol. 65, No. 11, pp. 1287-1291.

Schwartz, U.J. (1978) "Mathematical-statistical description of the iterative beam removing technique (method CLEAN)," Astron. & Astrophys. Vol. 65, pp. 345-356.

Selby, M.J.; Wade, R.; Magro, C.S. (1979) "Speckle interferometry in the near infra-red," Mon. Not. R. astr. Soc. Vol. 187, pp. 553-566.

Sequin, C.H. (1975) "Introduction to charge-coupled devices," NATO Advanced Study Institute on Solid State Imaging, Louvain-la-Neuve, Belgium, Sept. 3-12, 1975, Netherlands: Nordhoff, pp. 233-259.

Shannon, C.E.; Weaver, W. (1963) The Mathematical Theory of Communication. The University of Illinois Press.

Shaw, R. (1978) "Evaluating the efficiency of imaging processes," Rep. Prog. Phys. Vol. 41, pp. 1102-1155.

Shepard, M. (1977) "Distributed computing power: a key to productivity," Computer. Vol. 10, No. 11, pp. 66-74.

Shneiderman, B. (1979) "Human factors experiments in designing interactive systems," IEEE Computer. Vol. 12, No. 12, pp. 9-19.

Shore, S.H. (1974) "An overview of sensitometry and densitometry for the macro and micro conditions," Acquisition & Analysis of Pictorial Data. The Modern Science of Imagery, Proc. of the SPIE. Vol. 48, August 19-20, 1974, San Diego, CA., pp. 2-16.

Smith, B.A. (1976) "Astronomical imaging applications for CCDS," Proceedings Conference on Charge-coupled Device Technology and Applications. Nov. 30 - Dec. 2, 1976, JPL SP 43-40, pp. 135-138.

Solomon, A.L. Parallel-transfer-register Charged Coupled Imaging Devices. Palo Alto, Calif.: Fairchild Instr. and Camera Corp.

Sowan, F.A. (1968) "Light units in SI," Mullard Technical Communications. No. 95, pp. 182-184.

Spiro, I.J. (1974) "Symbols-units and nomenclature for radiometry and photometry - an update," Acquisition & Analysis of Pictorial Data. The Modern Science of Imagery, Proc. of the SPIE. Vol. 48, August 19-20, 1974, San Diego, CA., pp. 34-37.

Stachnik, R.V.; Nisenson, P.; Ehn, D.C.; Hudgin, R.H.; Schriff, V.E. (1977) "Speckle image reconstruction of solar features," Nature. Vol. 266, pp. 149-151.

Stewart, J.F. (1978) "CP/M primer," Kilobaud. April 1978, pp. 30-34.

Stockham, T.G. (1972) "Image processing in the context of a visual model," Proc. IEEE. Vol. 60, No. 7, pp. 828-842.

Stockman, T.G. (1977) "The role of psychophysics in the mathematics of image science," Symposium on Current Mathematical Problems in Image Science, Monterey, Calif. Nov. 1976. N. Hollywood, Calif.: Western Periodicals, pp. 57-66.

Strickland, R.N.; Bennet, J.C.; Anderson, A.P. (1978) "Retrieval of diffraction-limited images from below the threshold of recognition by superdirective data processing," Microwaves, Optics and Acoustics. Vol. 2, No. 3, pp. 85-90.

Strohbein, J.W. (1971) "Optical propagation through the turbulent atmosphere," Progress in Optics. Vol. 9, pp. 75-122.

Tanaka, S.C. (1979) "Coping with charge transfer inefficiency affecting modulation transfer function (MTF) of charge-coupled devices (CCD)," Optical Engr. Vol. 18, No. 5, pp. 504-512.

Thomas, W. (ed.) (1973) SPSE Handbook of Photographic Science and Engineering. New York: John Wiley & Sons. Ch. 8.

Thompson, M. (ed.) (1966) Manual of Photogrammetry, 3rd ed. Falls Church, VA: American Society of Photogrammetry, Ch. 6.

Tomiyasu, K. (1978) "Tutorial review of synthetic-aperture radar (SAR) with applications to imaging of the ocean surface," Proc. IEEE. Vol. 66, No. 5, pp. 563-583.

Van Wie, P.; Stein, M. (1977) "A Landsat digital image rectification system," IEEE Trans. Geoscience Electronics. Vol. GE-15, No. 3, pp. 130-137.

Voss, M.A. (1977) "Image processing componentry," Electrical Engineering Third Professional Year Project Report, University of Canterbury, Christchurch, N.Z.

Walker, J.G. (1979) "Optimum exposure time and filter bandwidth in speckle interferometry," I.A.U. Colloquium No. 50, ed. J. Davis and W.J. Tango, Sydney: Chatterton Astronomy Department, School of Physics, University of Sydney, pp. 25-1-25-24.

Walther, G.H.; O'Neill, H.F. (1974) "On-line user-computer interface - the effects of interface flexibility, terminal type, and experience on performance," Joint Computer Conference. Vol. 43, May 6-10, 1974, AFIPS Conference Proceedings, pp. 379-384.

Weide, B. (1977) "A survey of analysis techniques for discrete algorithms," Computing Surveys. Vol. 9, No. 4, pp. 291-313.

Weidner, R.T.; Sells, R.L. (1975) Elementary Physics: Classical and Modern. Boston: Allyn and Bacon, Inc., Ch. 36.

Weigelt, G.P. (1975) "Large field speckle interferometry," Optik. Vol. 43, No. 2, pp. 111-120.

Weigelt, G.P. (1977) "Modified astronomical speckle interferometry 'speckle masking'," Opt. Commun. Vol. 21, No. 1, pp. 55-59.

Weigelt, G.P. (1978a) "Speckle interferometry measurements of 12 binary stars," Astron. & Astrophys. Vol. 68, pp. L5-L6.

Weigelt, G.P. (1978b) "Speckle holography measurements of the stars Zeta Cancri and ADS3358," Applied Optics. Vol. 17, pp. 2660-2662.

Welter, G.L.; Worden, S.P. "The angular diameters of supergiant stars from speckle interferometry."

Welter, G.L.; Worden, S.P. (1978) "A method for processing stellar speckle interferometry data," J. Opt. Soc. Am. Vol. 68, No. 9, pp. 1271-1275.

Wensley, N. (1977) "Control terminal for an imaging system," Electrical Engineering Third Professional Year Project Report, University of Canterbury, Christchurch, N.Z.

Wilkerson, M.; Worden, S.P. (1977) "Further speckle interferometric studies of Alpha Orionis," The Astron. J. Vol. 82, No. 8, pp. 642-645.

Wilson, S.J. (1979) "Reticon linear diode array investigation," Electrical Engineering Third Professional Year Project Report, University of Canterbury, Christchurch, N.Z.

Wong, G. (1979) "Trace, a software debugging package," Electrical Engineering Third Professional Year Project Report, University of Canterbury, Christchurch, N.Z.

Worden, S.P. (1975) "The angular diameter of Alpha Herculis A," Astrophys. J. Vol. 201, pp. L69-L70.

Worden, S.P. (1976) "Digital analysis of speckle photographs: the angular diameter of Arcturus," Pub. Astr. Soc. Pac. Vol. 88, No. 521, pp. 69-72.

Worden, S.P. (1977) "Astronomical image reconstruction," Vistas in Astronomy. Vol. 20, pp. 301-318.

Worden, S.P.; Lynds, C.R.; Harvey, J.W. (1976) "Reconstructed images of Alpha Orionis using stellar speckle interferometry," J. Opt. Soc. Am. Vol. 66, No. 11, pp. 1243-1246.

Worden, S.P.; Stein, M.K. (1979) "Angular diameter of the asteroids Vesta and Pallas determined from speckle observations," Astron. J. Vol. 84, No. 1, pp. 140-142.

Worden, S.P.; Stein, M.K.; Schmidt, G.D.; Angel, J.R.P. (1977) "The angular diameter of Vesta from speckle interferometry," Icarus. Vol. 32, pp. 450-457.

Young, A.T. (1974) "Seeing: its cause and cure," The Astroph. J. Vol. 189, pp. 587-604.

Zuch, E. (ed.) (1979) Data Acquisition and Conversion Handbook. Mansfield, MA: Datel-Intersil Inc.

CCD202

100×100 ELEMENT AREA IMAGE SENSOR

CHARGE COUPLED DEVICE

GENERAL DESCRIPTION – The CCD202 is a solid state area image sensor organized in an array of 100 horizontal lines by 100 vertical columns. The 10,000 image sensing elements are 18 μm horizontally and 30 μm vertically and are located on 40 μm horizontal centers and 30 μm vertical centers. The dimensions of the image sensing area are 4 mm by 3 mm.

The X-Y format of the array was selected to provide a 4 x 3 image aspect ratio. The highly precise location of the photosites allows precise identification of each component of the image signal. This feature allows the device to be used in applications requiring precise dimensional measurement. The device is also intended to be used in video cameras that require low power, small size, high sensitivity and high reliability.

The CCD202 is an improved version of the CCD201 100 x 100 Area Image Sensor. The device is manufactured using Fairchild buried channel charge coupled device technology and is packaged in a 24-pin hermetic DIP with an optical glass window.

- 10,000 IMAGE SENSING ELEMENTS ON A SINGLE CHIP
- NO LAG, NO GEOMETRIC DISTORTION
- GAMMA CHARACTERISTIC OF APPROXIMATELY 1.0
- ON-CHIP PREAMPLIFIER PROVIDING TYPICALLY 1.0 V OF VIDEO SIGNAL
- HIGH DYNAMIC RANGE: TYPICALLY 300:1
- WIDE RANGE OF VIDEO DATA RATE UP TO 500 FRAMES/s
- LOW POWER DISSIPATION: TYPICALLY 75 mW
- HIGH RELIABILITY
- 24-PIN HERMETIC PACKAGE WITH AN OPTICAL GLASS WINDOW

BLOCK DIAGRAM

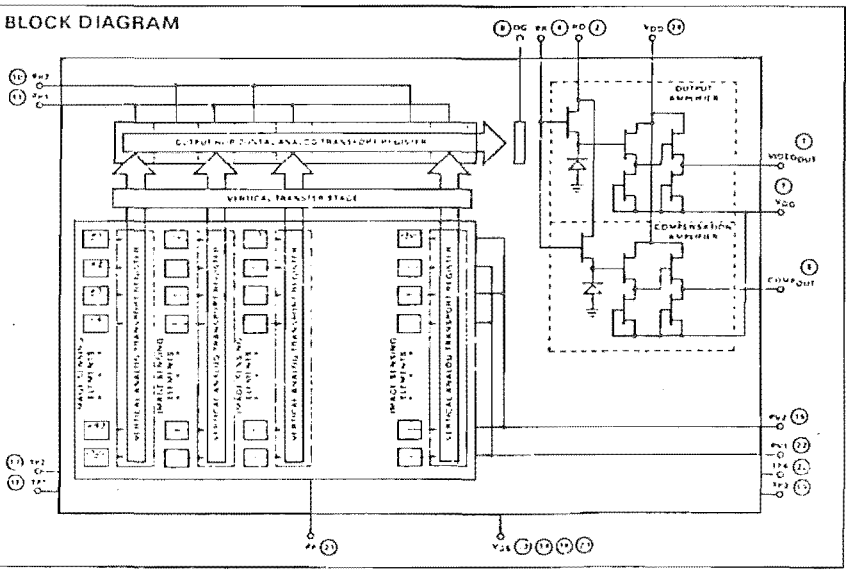

CONNECTION DIAGRAM
DIP (TOP VIEW)

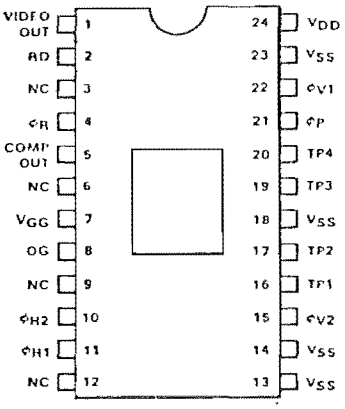

PIN NAMES	
$VIDEO_{OUT}$	Video Output
$COMP_{OUT}$	Compensation Output
ϕ_P	Photogate Clock
ϕ_{V1},ϕ_{V2}	Vertical Analog Transport Register Clocks
ϕ_{H1},ϕ_{H2}	Horizontal Analog Transport Output Register Clocks
ϕ_R	Reset Clock
RD	Reset Drain
OG	Output Gate
V_{DD}	Output Drain D.C. Supply
V_{GG}	Signal Ground
V_{SS}	Substrate Ground
NC	No Connection
TP1 – TP4	Test Points

FAIRCHILD CHARGE COUPLED DEVICE • CCD202

ABSOLUTE MAXIMUM RATINGS

Operating Temperature	−25°C to +55°C
Storage Temperature	−25°C to +100°C
Pins 1, 2, 5, 16, 24	−0.6 V to +15 V
Pins 4, 8, 10, 11, 15, 17, 19, 20, 21, 22	−10 V to +15 V
Pins 7, 13, 14, 18, 23	V_{SS} = 0 V

Caution: The device has limited built-in gate protection. Static charge build-up should be minimized.

FUNCTIONAL DESCRIPTION – The CCD202 consists of the following subsections as illustrated in the Block Diagram.

1. 10,000 image sensing elements in a 100 x 100 array.
2. 100 columns of 50 element 2-phase vertical analog transport registers.
3. A 102 element 2-phase horizontal analog output shift register charge coupled to the output of each of the 100 column shift registers.
4. A two-stage gated charge integrator which detects and converts the charges delivered from the horizontal analog transport register to the output terminal $VIDEO_{OUT}$ (pin 1).

Light energy incident on the image sensor elements generates a packet of electrons at each sensing element. Electrical clocking of the photogate, the vertical analog transport registers, and the horizontal analog output register sequentially deliver the charge packets to the preamplifier. Detailed descriptions of the functional subsections follows.

Image Sensing Elements – Image photons pass through a transparent polycrystalline silicon gate structure and are absorbed in the single crystal silicon producing hole-electron pairs. The resulting photoelectrons are collected in the photosites during the HIGH state of the photogate. The amount of charge accumulated is a linear function of the incident illumination intensity and of the integration period. The output signal voltage ranges from a thermally generated bacground level in the absence of illumination to a maximum at saturation.

Vertical Analog Transport Registers – At the end of an integration period, the charge packets are transferred out of the array in two sequential fields of 50 lines each. When the photogate voltage is lowered, alternate lines of charge packets are transferred to their corresponding sites in the vertical registers (*i.e.*, the odd numbered photoelements in the block diagram). Clocking of the vertical register at ϕ_{V1} and ϕ_{V2} delivers the charge packets from the 100 vertical registers to the horizontal analog transport register through a vertical transfer stage. A minimum of 51 vertical transfers (51 clock cycles on ϕ_{V1} and ϕ_{V2}) are required to transport each field of charge packets out of the vertical registers. Subsequent to the removal of one field a second field cycle is initiated to receive the information from photosites corresponding to the other field (*i.e.*, the even numbered photoelement rows). Clocking of the register transports these charge packets in a similar fashion to the output.

Horizontal Analog Output Transport Register – The horizontal output register is a 102 element 2-phase register that receives the charge packets from the vertical transport registers line by line. As each row of information is received from the vertical registers it is serially moved to the output amplifier by the horizontal clocks ϕ_{H1} and ϕ_{H2}. A minimum of 102 horizontal clock pulses are required to complete transfer of one row of information to the on chip amplifier.

A Two-Stage Gated Charge Integrator – Charge packets are transported to a pre-charged diode whose potential changes linearly in response to the quantity of the signal charge delivered. This potential is applied to the gate of the first stage of a two-stage n-channel MOS amplifier producing a signal output at $VIDEO_{OUT}$ (pin 1). A reset transistor, driven by a reset clock (ϕR), recharges the charge-detector diode capacitance before the arrival of each new signal charge packet from the transport registers. The output of the CCD202 is a series of video levels corresponding to the optical information. The $VIDEO_{OUT}$ pin provides a typical saturation voltage of 1.0 V. Present in the output waveform are reset clock coupling pulses from the clock ϕ_R. Also provided at the output is a signal ($COMP_{OUT}$, pin 5) which can be used to cancel any ϕ_R clock coupling in $VIDEO_{OUT}$ by differential amplification. (See timing diagram).

PHOTOSITE DIMENSIONS

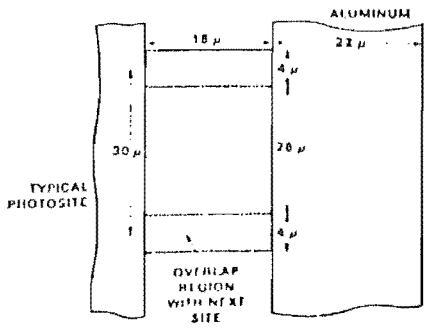

TEST LOAD CONFIGURATION

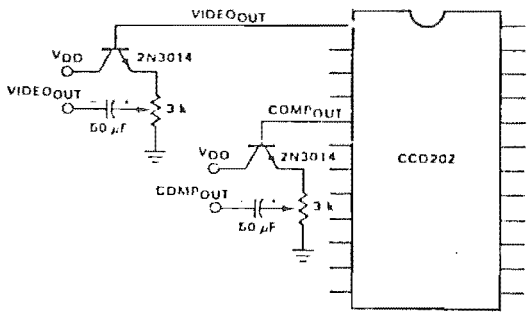

FAIRCHILD CHARGE COUPLED DEVICE • CCD202

DC CHARACTERISTICS: T_A = 25°C

SYMBOL	PARAMETER	RANGE			UNITS	CONDITIONS
		MIN	TYP	MAX		
V_{RD}	Reset Drain Voltage	5.0	10	15.5	V	
V_{DD}	Output Drain D.C. Supply	14.5	15	15.5	V	
V_{OG}	Output Gate Voltage	−1.0	0	+1.0	V	Note 1
V_{SS}	Substrate Ground		0		V	Clock Return Line
V_{GG}	Signal Ground		0		V	Signal Return Line
TP1	Test Point 1	10	15	15.5	V	Can be Tied to V_{DD}
TP2	Test Point 2		0		V	Ground to V_{SS}
TP3	Test Point 3					Connect to ϕ_{H2}
TP4	Test Point 4					Connect to ϕ_{H1}
$C_{\phi P}$	Photogate Clock Capacitance		1500		pF	With respect to V_{SS}. All Other Terminals Gnd.
$C_{\phi V1}$.$C_{\phi V2}$	Vertical Clocks Capacitance		1000		pF	With respect to V_{SS}. All Other Terminals Gnd.
$C_{\phi H1}$.$C_{\phi H2}$	Horizontal Clocks Capacitance		35		pF	With respect to V_{SS}. All Other Terminals Gnd.
$C_{\phi R}$	Reset Clock Capacitance		5.0		pF	With respect to V_{SS}. All Other Terminals Gnd.
R_{OUT}	Output Resistance		700		Ω	

CLOCK CHARACTERISTICS: T_A = 25°C

SYMBOL	PARAMETER	RANGE			UNITS	CONDITIONS
		MIN	TYP	MAX		
$V_{\phi PL}$	Photogate Clock LOW		0		V	
$V_{\phi PH}$	Photogate Clock HIGH	4.0	6.0	12	V	Note 2
$V_{\phi RL}$	Reset Clock LOW		0.0		V	
$V_{\phi RH}$	Reset Clock HIGH	4.0	10	12	V	Note 2
$V_{\phi H1L}$.$V_{\phi H2L}$	Horizontal Analog Transport Register Clock LOW		0		V	
$V_{\phi H1H}$.$V_{\phi H2H}$	Horizontal Analog Transport Register Clock HIGH	4.0	9.0	12	V	Note 2
$V_{\phi V1L}$.$V_{\phi V2L}$	Vertical Analog Transport Register Clock LOW		0		V	
$V_{\phi V1H}$.$V_{\phi V2H}$	Vertical Analog Transport Register Clock HIGH	4.0	6.0	12	V	Note 2
$f_{\phi H1}$.$f_{\phi H2}$	Horizontal Analog Transport Register Clock Frequency	0.1	2.0	6.0	MHz	
$f_{\phi V1}$.$f_{\phi V2}$	Vertical Analog Transport Register Clock Frequency	0.001	0.02	0.06	MHz	
$f_{\phi R}$	Reset Clock Frequency (Video Data Rate)	0.1	2.0	6.0	MHz	

AC CHARACTERISTICS: T_A = 25°C, $f_{\phi H1}$ = $f_{\phi H2}$ = 2 MHz, t_{INT} = 6.6 ms (see Note 8); Light source is 2854°K Tungsten illumination with a Corning 1-75 I.R. cutoff filter.

SYMBOL	PARAMETER	RANGE			UNITS	CONDITIONS
		MIN	TYP	MAX		
DR	Dynamic Range	200	300			Note 3
SE	Saturation Exposure	0.3	0.4		$\mu J/cm^2$	Note 4
V_{sat}	Saturation Output Voltage	0.8	1.6		V	Note 5
R	Responsivity		4.0		$V/\mu J\ cm^{-2}$	
S	Shading		±2.0	±10	% of V_{sat}	Note 6
V_D	Average Peak Dark Voltage		0.08		V	Note 7

FAIRCHILD CHARGE COUPLED DEVICE • CCD202

NOTES:

1. Adjustment in the range of −1.0 V to +1.0 V is required for optimum performance.
2. Adjustment in the range of 4.0 V to 12 V is required for optimum performance.
3. Measured by adjusting incident illumination to the signal saturation point, then attenuating the incident light with a neutral density filter of density N.D. = 2.3 (which corresponds to a reduction in incident light of 200 times). The resultant off chip video signal should be ≥ 4 $mV_{p\text{-}p}$.
4. 1 $\mu J/cm^2$ = 0.02 fcs at 2854°K
   1 fcs = 50 $\mu J/cm^2$ at 2854°K
5. Saturation output voltage (V_{sat}) is measured by reading the output signal voltage ($VIDEO_{OUT}$) obtained when the illumination level is adjusted just below the point where the output signal starts to flatten. The saturation voltage includes the signal plus dark pedestal but not the clock transients which are present in the unprocessed video. (See Timing Diagram)
6. Shading is measured at 50% of saturation with uniform illumination by observing the variations in photoelements amplitude across a particular line (as shown in the Timing Diagram) or field. The first and last three bits of a line and first and last three rows of a field are excluded from the measurement.
7. Average dark signal is the video output obtained from the device in the dark. In making the measurement care must be taken to distinguish between the dark signal and the normally present clock transients. The value stated is the average of the peak values from all photosites.
8. The minimum integration time (t_{INT}) is equal to $t_{INT} = 2 \times 52 (102\ t_h + 2\ \mu s)$
   $= (1.0608 \times 10^7/f_{\phi H} + 0.208)$ ms

   Example: If $f_{\phi H} = 2$ MHz, then $t_{INT} = 1.0608 \times 10^7/2 \times 10^6 + 0.208 = 5.548$ ms and $f_{\phi FRAME} = 180$ Hz.

TYPICAL ELECTRICAL CHARACTERISTICS

SPECTRAL RESPONSE

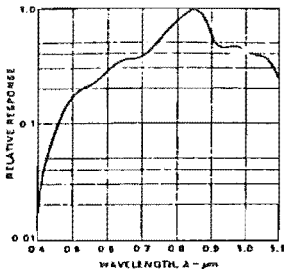

AVERAGE PEAK DARK VOLTAGE VERSUS TEMPERATURE

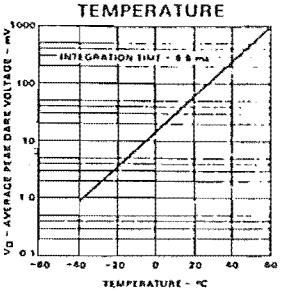

CONTRAST TRANSFER FUNCTION

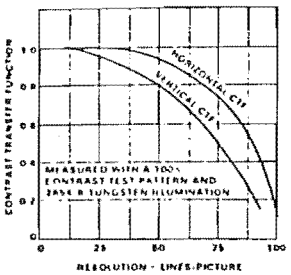

BLOOMING CHARACTERISTICS

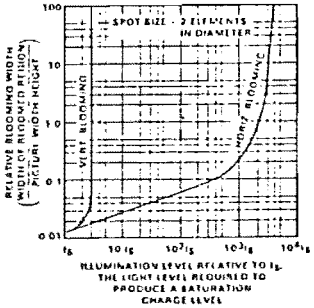

TIMING DIAGRAM DRIVE SIGNALS

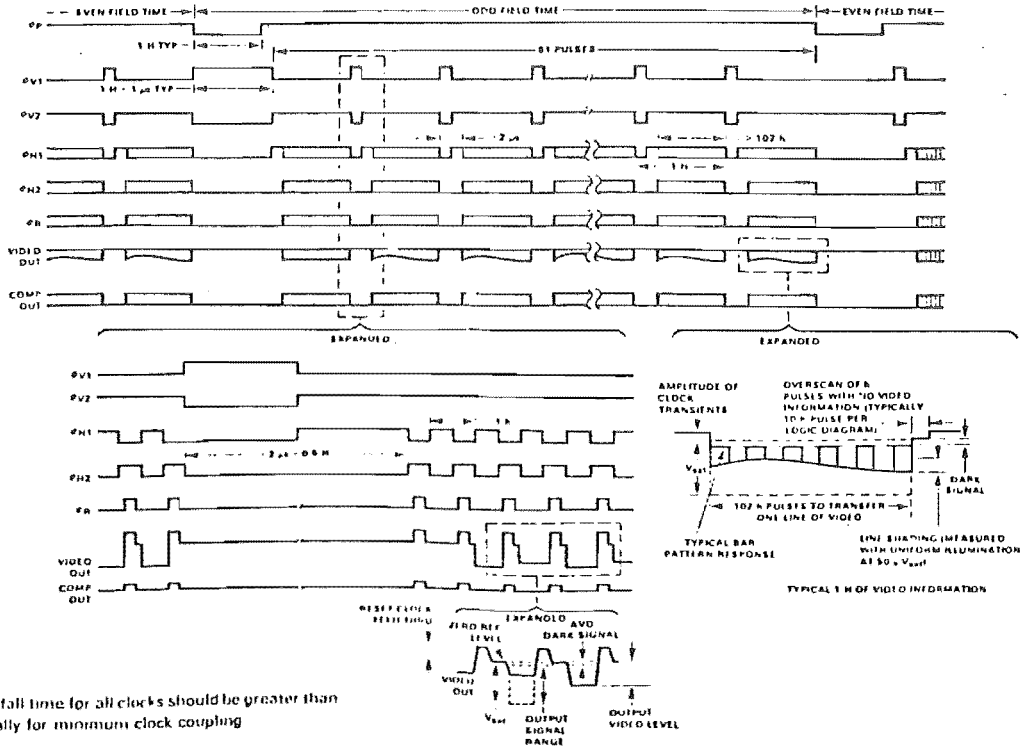

All rise and fall time for all clocks should be greater than 15 ns typically for minimum clock coupling

CCD202 DRIVE CIRCUITRY

The drive electronics described here can be used over a fairly wide frequency range (0.1 MHz – 6.0 MHz video data rate). Figure 1 shows the necessary logic for generating the waveforms required by the CCD202. Figure 2 shows a discrete driver stage and Figure 3 shows a typical sweep circuit.

The *master clock* in Figure 1 operates at four times the horizontal frequency rate. It covers the frequency range from 0.4 MHz to 24 MHz for a $f_{\phi H}$ range of 0.1 MHz to 6.0 MHz. The output of the master clock goes to a *frequency divider* via a buffer stage, T4D. The divider provides outputs at $f_{\phi H}$ and 2 $f_{\phi H}$ rates.

The $f_{\phi H}$ waveforms are shifted by the master clock pulse within the *phase shifter* section. This shift places the 2 $f_{\phi H}$ waveform inside the leading and falling edges of the $f_{\phi H}$ waveforms. The outputs of the phase shifter are complementary square waves.

The *phase control logic* establishes the necessary control over the output waveforms at the ends of lines and fields. Here the $f_{\phi H}$ and 2 $f_{\phi H}$ waveforms are gated by control signals V_{OFF} and $H_{INHIBIT}$, two waveforms derived from the low frequency logic section. The $H_{INHIBIT}$ logic holds the high frequency output waveforms in a fixed state while the next row of data from the vertical registers is being transferred to the horizontal register of the CCD202. $H_{INHIBIT}$ goes LOW at the beginning of the vertical shift time and remains LOW for 16 $f_{\phi H}$ clock periods. It then returns HIGH for 112 $f_{\phi H}$ periods.

The V_{OFF} waveform overrides the $H_{INHIBIT}$ control to give the special shape shown associated with the $f_{\phi H1}$ inhibit interval. V_{OFF} goes LOW at the end of the vertical transfer time for eight horizontal clock periods. It is a 50% duty cycle waveform except during the field transfer time where it is gated off for one complete horizontal line time.

One output taken from the phase shifter section is fed through a buffer amplifier to the low frequency logic. This, in effect, becomes the clock for the low frequency section.

The low frequency logic contains a frequency dividing network which divides down the clock input to produce the vertical and photogate pulses for the CCD202. Additional outputs available from this circuitry are the timing pulses necessary for generating an interlaced display and those required for blanking.

The *line counter* section establishes the duration of a horizontal line. In this design, 128 h counts are permitted. When the terminal count is reached by T12, the line start flip-flop T7B is toggled. This enables gate T14A, which allows the next clock pulse to set horizontal inhibit flip-flop T9B and vertical control flip-flop T9A.

The *field counter* divides the terminal count of the line counter down further to generate the pulse rates required at field and frame rates. This circuit produces a pulse for every 52 input pulses. Thus, there are 52 $f_{\phi V}$ pulses for every field for this design.

The *vertical logic* section produces the $f_{\phi V1}$ and $f_{\phi V2}$ waveforms. The vertical control flip-flop T9A is set at the end of each line and at the end of even fields, but not at the end of odd fields. This condition is created by gating out the line start pulse by T14C with the mixed field and frame control signal from T1D. T9A is reset after eight counts of T11 by control gate T14D. At the end of a field the count will be 128 plus eight, for a total of 136 before T9A is reset.

The *photogate logic* produces the $f_{\phi P}$ waveform. The field control flip-flop T10A is set by the terminal count from the field counter and reset by the terminal count of the line counter. Thus the $f_{\phi P}$ pulse duration will be one line time.

The *frame control logic* contains a flip-flop T10B which toggles with each terminal count pulse from the field counter. Its output is a 50% duty cycle pulse at the frame fequency. One output can be used as input to an interlace circuit.

All drive pulses required by the CCD202 are coupled from the logic circuits via driver circuits. The driver outputs are voltage variable over the range of −10 V to +10 V. Rise and fall times of 20 ns are achievable with these circuits. A typical driver configuration is shown in Figure 2.

The sweep circuit illustrated in Figure 3 will provide two linear ramps corresponding in time to the line and field scanning rates of the CCD202. The vertical and horizontal sweep blanking pulses, in combination with the interlace signal, control the sweep duration, blanking and base line offset required for interlace field scanning.

For both sweeps, linear ramp generation is accomplished by using a Fairchild μA740 FET input operational amplifier with a capacitor in its feedback loop. With the μA740 supplying constant current to the capacitor, the only non-linearity will be due to leakage paths across the amplifier. Two possible leakage paths exist: those due to the capacitor and those due to the clamp transistor; both should be selected for low leakage.

Horizontal sweep blanking is accomplished using both vertical and horizontal blanking pulses which control the output of T30A. Each time the output of T30A goes HIGH, clamp transistor T31 turns on providing a discharge path across C1 and amplifier T28, returning the output level to zero. Upon completion of the blanking period, T31 turns off and capacitor C1 starts to recharge at a linear rate. Rate of charge across C1 is controlled by horizontal width control R1.

Vertical sweep generation is accomplished by amplifier T32 and controlled by clamp transistor T33 in the same manner as for the horizontal sweep. Vertical sweep charge rate is controlled by height adjustment R2. The positive going linear sawtooth from the output of T32 is mixed at the summing junction of amplifier T35 with the dc voltage from R3, the vertical base line adjustment, and a 50% duty cycle square wave from R4, the interlace adjustment control.

R3 is adjusted to cause amplifier T25 to produce a linear negative going sawtooth with base line at a positive 1.01 V when interlace signal from R4 is LOW (even field). When the interlace signal is HIGH, R4 is adjusted so that the base line of the sawtooth is 1.0 V positive (odd field). The vertical height adjustment R2 is then adjusted to give a 1.0 V amplitude negative going sawtooth sweep voltage with properly interlaced sweep.

FAIRCHILD CHARGE COUPLED DEVICE • CCD202

ORDER INFORMATION – The CCD202 as described in this data sheet can be ordered in its various classes as a standard device. The CCD202 has on chip a charge injection port where analog information can be fed to an input horizontal analog transport register in series form. This register is similar to the output register and is situated at the bottom of the block diagram on page 1. This information is then clocked in parallel through the vertical column registers to the output horizontal analog transport register which is then clocked in series and provides at the output a line by line reproduction of the electrical input information. The device is thus organized in a series-parallel-series (SPS) configuration. It can be used in conjunction with an imaging array for frame to frame comparison type of applications. For further information concerning S.P.S. operation refer to the CCD351 data sheet.

Standard CCD202 devices are not tested to have their input registers operational. To order a CCD202 in its various forms order the corresponding device types outlined in the table below.

DESCRIPTION	DEVICE TYPE
Standard CCD202, Class A Blemish Classification	CD202ADC
Standard CCD202, Class B Blemish Classification	CD202BDC

Also available are printed circuit boards that contain all the necessary clock, logic, drivers, amplifiers and sweep circuits to operate the CCD202. For further information regarding these PC boards, contact your nearest Fairchild sales office.

CLASSIFICATIONS – CCD202's are classified in terms of maximum number of image blemishes allowed and their position on the image format. The array is divided into three zones (see Figure), since blemishes near the periphery of the array are usually less objectionable than those near the center. The area of the array has a 4 x 3 aspect ratio. Zone 1 encompasses 16% of the photoelements, Zone 2, 33% and Zone 3, 51%.

An image element is blemished if it shows a spurious output ≥ 10% of saturation. The output waveform of the array is analyzed under two conditions. (1) in the dark and (2) at 50% of the saturation level.

BLEMISH SPECIFICATION

CLASSES	ZONE 1	ZONE 2	ZONE 3	TOTAL
A TYPE	0	2	4	6
B TYPE	1	3	5	9

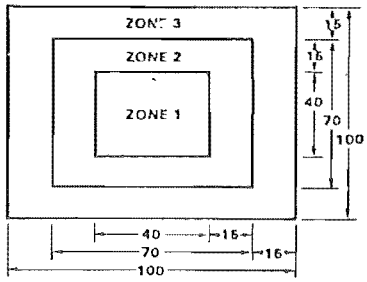

All dimensions in Elements

PACKAGE OUTLINE

24-Pin Dual In-line Hermetic Package

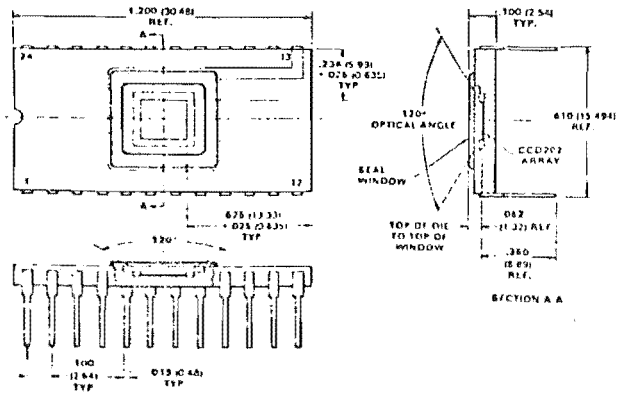

NOTES:
All dimensions in inches (bold) and millimeters (parentheses)
Header is black ceramic (Al_2O_3)
Transparent cover is glass
Photoelement No. 1 is closest to pin 12 on CCD202 die
Photoelement No. 100 is closest to pin 1 on CCD202 die

APPENDIX A2

Calculation of CCD202 performance

1. Number of photons required for 1/256 (one quantization level) of saturation, assume λ = 750 nm and quantum efficiency is 50%

$$n_p = \frac{S_E\ A}{(256)\ h\ \nu\ QE} = \frac{S_E\ A\ \lambda}{(256)\ h\ c\ QE}$$

where S_E = saturation exposure = $0.4 \times 10^{-6}\ \frac{J}{cm^2}$

A = area of one pixel = $5.4 \times 10^{-6}\ cm^2$

h = Plank's constant = $6.6 \times 10^{-34}\ \frac{J\ s}{photon}$

c = velocity of light = $3 \times 10^{8}\ \frac{m}{s}$

QE = quantum efficiency = 0.5

λ = wavelength = 750 nm

$n_p = 6.4 \times 10^{4}$ photons.

APPENDIX B

UNIVERSITY OF CANTERBURY MONITOR COMMANDS

The following brief descriptions are intended as a quick reference to the function and syntax of the University of Canterbury Monitor commands.

A ASSIGN I/O DEVICE

A<logical dev>=<physical dev>

Valid values for <logical dev> and <physical dev> are:

<logical dev>	<physical dev>
C	B or BATCH T or TTY 1 (user-defined device)
L	L or LPT T or TTY 1 (user-defined device)
P	P or PTP T or TTY 1 (user-defined device) 2 (user-defined device)
R	P or PTR T or TTY 1 (user-defined device) 2 (user-defined device)

B BYTE SEARCH

B<low address>,<high address>,<value>,<mask>

Search the memory area between low address and high address for values such that the contents of memory AND mask equal value. When found, the address and contents of memory are displayed on the console. The memory contents may be changed by entering a new value followed by one of the parameters listed below. If value is not to be changed, enter a parameter only.

Parameter	Action
ESCAPE	Continue the search
CARRIAGE RETURN	Display the address and the contents of the next memory location
' ' or ','	Display the contents of the next memory location
'-'	Display the address and the contents of the previous memory location

C BOOTSTRAP LOAD CP/M

D DISPLAY CONTENTS OF MEMORY

D<low address>,<high address>

E PUNCH HEXADECIMAL END-OF-FILE

E<start address>

F FILL RAM WITH CONSTANT

F<low address>,<high address>,<constant>

G EXECUTE PROGRAM (GO)

G<start address>,<breakpoint 1>,<breakpoint 2>

where <breakpoint 1> and <breakpoint 2> are always optional. If <start address> is absent, execution resumes at stored value of user's Program Counter.

H HEXADECIMAL ARITHMETIC

H<number 1>,<number 2>

The two results printed are ((<number 1>+<number 2>) MOD 2**16) and ((<number 1>-<number 2>) MOD 2**16), respectively.

I INPUT FROM A PORT

I<port number>space

The value present at the specified port number will be displayed on the console. A space must be entered after the port number.

M MOVE MEMORY

M<low address>,<high address>,<destination address>

N PUNCH NULL CHARACTERS

N

Each N will punch 6Ø NULL characters.

O OUTPUT TO A PORT

O<port number>, value

Value will be output to the port specified.

P BOOTSTRAP LOAD TAPE OPERATING SYSTEM

Q I/O STATUS QUERY

Q

For meaning of values displayed, see the A command.

R READ HEXADECIMAL FILE

R<bias>

<bias> will be added (MOD 2**16) to indicated load addresses.

S SUBSTITUTE MEMORY

S<address>

The contents of the address specified may be entered followed by one of the parameters listed below. If the memory contents are not to be changed, enter a parameter only.

Parameter	Action
ESCAPE	Terminate the routine and return to monitor
CARRIAGE RETURN	Display the address and the contents of the next memory location
' ' or ','	Display the contents of the next memory location
'-'	Display the address and the contents of the previous memory location

T TRANSFER TO FDOS

U TRANSFER TO USER WRITTEN COMMAND

A call is made to a memory location just above RST 3 RAM area (0018H).

V INVOKE TRACE & DISASSEMBLE ROUTINES

VT<start address>,<number>	Trace <number> of instructions from <start address>.
VN<start address>,<number>	Trace without tracing through calls to subroutines.

<start address>is optional and a default value is taken from the current value of the user program counter.

<number>is optional and when not used the trace continues until a <CTL S>or a<CTL E>is typed.

VL<start address>,<number>	Disassemble number of instructions from <start address>.

<start address>is optional and a default value is taken from the last program location that was disassembled.

<number>is optional and defaults to 16.

The trace and disassembler output may be halted at anytime by typing a <CTL S>. Any character then typed allows the function to be continued from the point at which it was halted. <CTL E>will cause the output to be halted and a return made to the system monitor.

W WRITE HEXADECIMAL FILE

W<low address>,<high address>

X EXAMINE AND MODIFY CPU REGISTERS

X<register identifier>

where<register identifier>has the following meanings:

A,B,C,D,E,H,L	Corresponding 8Ø8Ø CPU register.
M	Contents of the memory location addressed by HL.
P	Program Counter.
S	Stack Pointer.
F	8Ø8Ø CPU flags, packed as follows:

Bit		Flag
7	...	Sign
6	...	Zero
5	...	Always Ø
4	...	Auxiliary Carry
3	...	Always Ø
2	...	Parity
1	...	Always 1
Ø	...	Carry

If register identifier is absent, the Monitor will display each register in alphabetical order. Type a ' ' or ',' to continue command, or a carriage return to terminate.

A branch table has been set up to access the more commonly used monitor routines. They are located at F800H.

Memory Location	Function
F800	Jump to message sign on (SGNON)
F803	Console input (CI)
F806	Reader input (RI)
F809	Console output (CO)
F80C	Punch output (PO)
F80F	List output (LO)
F812	Console status input (CSTS)
F815	I/O system status (IOCHK)
F818	Set I/O configuration (IOSET)
F81B	Compute size of memory (MEMCK)
F81E	Define user I/O entry points (IODEF)
F821	4 bit hex to ASCII conversion (CONV)
F824	Evaluate expressions (EXPR)
F827	Compare DE, HL (HILO)
F82A	HL output to console (LADR)
F82D	A output to console (LBYTE)
F830	ASCII to hex conversion (NIBBLE)
F833	Delay 1 msec (DELAY)
F836	Jump to hardware reset (HWRST)

APPENDIX C

Interactive Image Processing Software

C1. Image Processing Routines Available in PIKKY

Many students have helped with the software development described below. These include: A.J. Ireland (AJI), C.B. Lake (CBL), J.K. Leonard (JKL), J.K.N. Murphy (JKNM), D. Pairman (DP), M.A. Rodgers (MAR) and G.J. Atkinson (GJA).

Notes:

(1) Size includes a 10,000 word intermediate buffer store.

(2) One stays in this routine until the terminating character is typed.

(3) The time depends on the total time for all commands to be executed.

(4) 1 minute, 24 seconds are required to slice through and display all 256 levels.

(5) The time is given for a 180 cps line printer.

(6) Size includes a 20,000 word intermediate buffer store.

(7) The time depends on the baud rate of the console.

Routine	Process	Size bytes	Execution time - s.	Author
G	Continuously execute the program which captures data from the CCD. The process is stopped by a character typed on the keyboard.	10,071	0.16	AJI
SAVE,<file>	Save the picture in buffer #1 on the floppy disk with the name <file>. <file> must be 5 characters or less.	29	20	AJI
LOAD,<file>	Load the image <file> from the floppy disk into buffer #1.	48	6	AJI
R	Restore the last picture that was loaded from the floppy disk.	21	6	MAR
I,X	Increase the intensity of the picture buffer #1 by a shift left of X bits.	26	<1	DP
D,X	Decrease the intensity of the picture buffer #1 by a shift right of X bits.	31	<1	DP
M,X	Mask the picture bitwise by AND-ing each pixel with X, where X is a byte specified in hexadecimal.	23	<1	DP
L,X,I,P,S,M	Plot the intensities along any selected line X. The parameters I,P,S,M are optional and may be given in any order: I - superimpose the plot on the picture. P - leave the plot as points, i.e. do not connect points with lines.	448	<1	DP

Routine	Process	Size bytes	Execution time - s.	Author
	S - superimpose a scale on the vertical axis of the plot. M - put a marker on the line that is plotted.			
P<CR> p_1 p_2...<CR>	Change the VDSI to display either of two pictures. <CR> signifies carriage return, and p_1, p_2 the figures 1 or 2. The display may be switched between buffers by alternating between 1 and 2. On the second carriage return, control is passed back to the command input module within PIKKY.	42	(2)	DP
T, p_1,p_2	Transfer the picture from buffer p_1 to p_2, where p_1 and p_2 may be 1, 2 or 3.	66	<1	DP
EXCH	Exchange buffer #1 and #2.	23	<1	FMC
U or U,plist	Transfer to a previously loaded user module. The plist may be a parameter list required by the user module.	3	<1	MAR
EXPND	Linear contrast expansion. Set the maximum in the picture to OFFH, the minimum to 0, and linearily scale all values in between.	166	<1	FMC
H	Perform a histogram equalized contrast expansion (Pairman 1978; Castleman 1979)	126	3	DP
E	Exit to the system monitor.	3	<1	FMC

Routine	Process	Size bytes	Execution time - s.	Author
F	Bootstrap load the floppy disk operating system.	3	7	DP
ON	Turn on the flashing pixel mode. The flashing pixel is controlled by the ON, OFF and <ESC> commands.	18	<1	FMC
OFF	Turn the flashing pixel mode off. The value of the pixel in the picture is restored to its original value.	13	<1	FMC
<ESC>	<ESC> is the escape key and activates the flashing pixel function keys. When activated, a prompt '^' is written on the console. Then, either the programmable function keys 1, 2, 3, 4 or the keyboard keys L,R,U,D may be used to move the flashing pixel left, right, up, or down respectively. An exit is made from this mode when either <ESC> or <CR> is next pressed. The value of the flashing pixel in hexadecimal and decimal, and the location as a row and column in the picture, are output on the console.	358	(2)	FMC
SET,XX	The value of the flashing pixel is set to the value XXH. The flashing mode must be on for this to be performed correctly.	38	<1	FMC
GO,XXXX	Exit from PIKKY and jump to address XXXXH.	7	<1	DP

Routine		Size bytes	Execution time - s.	Author
BD<CR>C_1<CR>...C_n<CR><ETX>	Define the batch operations string. Valid commands, C_1 - C_n are input and separated by carriage returns <CR>. An <ETX> key <control-C> terminates the BD operation. The string may be up to 100_{10} characters long.	82	(2)	FMC
B	Execute the batch operation string defined in the BD command.	55	(3)	FMC

C2. User Generated Image Processing Routines

		Size bytes	Loading/ Execution time - s.	Author
TITLE,p_1,'text'	Write 'text' into the text buffer display area under the picture. There are four lines of text which are signified by p_1 = 1-4. Two lines of 16 characters are allowed under each of the two VDSI picture buffers.	760	3/<1	FMC
FIGS,'text'	Write 'text' into the picture area beginning at the location of the flashing pixel.	700	2/<1	FMC
WIPE	Erase the text display area under both picture buffers.	27	2/<1	FMC
AVG3	Average out the defective pixels in the CCD. A pre-determined map of the defective locations is used to replace the defective pixel by the average of pixels on each side.	67	2/<1	FMC

Routine	Process	Size bytes	Loading/ Execution time - s.	Author
EDGE	Set the three rows and columns around the periphery to zero. This is done to eliminate extra-sensitive pixels at the outside of the array.	100	2/<1	FMC
DENSY,p_1	A plot of the distribution of intensities is output on the console if p_1 is C, or on the line printer if p_1 is L.	1,100	2/6(5)	FMC
XOR	Exclusive-OR each pixel in picture #1 with the corresponding pixel in picture #2.	23	2/<1	FMC
SCALE,p_1	Generate a gray scale for screen testing. p_1 = 1 - 0-99 in steps of 1. 2 - 100-199 in steps of 1. 3 - 0-99 in steps of 1, top to bottom of display. 4 - 5-255-5 in steps of 5.	150	2/<1	FMC
SLICE,p_1	Display only those pixels above or below a threshold value. The display is above if p_1 is D (slice down through the picture) or below if p_1 is U. The threshold value is set to the maximum/minimum (for D/U) value in the picture and decremented/ incremented for each new display. The normal background of the display is black/white but may be toggled to white/black at any time by depressing the T key.	10,300(1)	3/84(4)	FMC

Routine	Process	Size bytes	Loading/ Execution time - s.	Author
	The operator may stop the process to view the sliced picture at any time by depressing any key. The level of the present threshold is displayed on the console. An exit from the routine is made whenever the operator types an E, or when all values in the picture have been displayed.			
FILTR	Perform a two-dimensional spatial filter on the picture. This filter replaces each pixel with the weighted summation of itself and its eight nearest neighbours. The nine pixel array is numbered 1-9 starting at the top left. The weights are input by the operator in two's complement hexadecimal format at the beginning of the program. This is not required each time the program is run, providing the old weights are still in memory. In this case, <ESC> is typed and the program uses the old values.	20,500(b)	2/12	FMC
L640A	Transfer the contents of picture buffer to the EAI 640 Hybrid Computer.	102	1.5/30	FMC
NUMS	Print in decimal and hexadecimal the values in the 5 x 5 matrix of pixels around the present location of the flashing pixel.	260	2/(7)	FMC

Routine	Process	Size bytes	Loading/ Execution time - s.	Author
FNUMS	Find the maximum value in the picture, cause it to start flashing, and print in decimal and hexadecimal the values of the pixels in a 5 x 5 matrix around this point.	300	2/(7)	FMC
LNUMS	Same as NUMS except the values are listed on the line printer.	400	2/8(5)	FMC
LPIC1	List all the pixels in the picture on the line printer.	140	2/7.6 min. (5)	FMC
LJUST	Left justify all data in the picture.	67	2/<1	FMC
LTMTR	Print on the console the average of the 4 x 8 array of pixels in the centre of the picture.	52	2/<1	FMC
FCNTR	Shift the picture so that the current location of the flashing pixel is moved into the centre of the screen.	1,500	2/3	FMC
BCNTR	Find the brightest point in the picture and move the picture so that this point is in the centre.	525	2/3	FMC
GSUB3,P_1	Same as G except automatically average the defective pixels and subtract a dark picture stored in buffer #3. P_1 = D - take a dark picture and store in buffer #3. L - take normal pictures and subtract the dark picture when a character is typed on the console.	300	2/<1(1)	FMC

Routine	Process	Size bytes	Loading/ Execution time - s.	Author
JOY	Provides a flashing pixel in the displayed picture under control of a joystick connected to port J1. When operating, typing a space causes the output of the current pixel value in hexadecimal and the row and column in decimal. Typing P returns control to PIKKY.	400	2/(2)	JKL
LIST,u,p_1	List the directory of disk in drive u on the line printer if p_1 is L, otherwise on the console. This operates the same as the FDOS command LIST.	866	2/(7)	MAR
VIEW,<file>	List the contents of the disk file <file> on the console. This operates the same as the FDOS command VIEW.	945	2/(7)	MAR
RENAM,<oldfile>,<newfile>	Rename the <oldfile> with the name <newfile>. This operates the same as the FDOS command RENAM.	476	1/<1	MAR
ADD	Add picture #2 to picture #1. Overflow occurs.	21	2/<1	FMC
SUB	Subtract picture #2 from picture #1. Overflow occurs.	23	2/<1	FMC
SUB0	Subtract picture #2 from picture #1. Overflow is set to 0.	27	2/<1	FMC
SUB8	Subtract picture #2 from picture #1. Offset the result to 80H.	32	2/<1	FMC

Routine	Process	Size bytes	Loading/ Execution time - s.	Author
UP	Shift the columns 2-99 in the rows 3-99 up one row. Replace the values in row 99 with 0.	32	2/<1	FMC
RCM,p_1	Calculate the mean pixel value of a row or column. p_1 = Rx where x = row 1 to 100. Cx where x = column 1 to 100.	400	1/<1	GJA
ROT	Rotate the picture 90 degrees anti-clockwise.	53	1/<1	GJA
STORE,p_1	Store the pictures on to the disk. Two modes are available. Single shot - p_1 = file:drive Successive pictures - initially p_1 = NNNXX:drive where NNN = filename, XX = filenumber. For succeeding pictures type U<CR>, the filenumber will be automatically incremented, the new NNNXX displayed and the picture stored on to disk.	200	2/24	GJA
FOTO	Print picture #1 (using double overprinting). The columns are averaged in pairs.	350	2/120(5)	GJA
CALC	Two element stack reverse polish notation calculator which will perform the following operations using floating point arithmetic: <cr> - enter key *,-,*,/ - arithmetic operations N - Negate the X register. C - Clear the X register.	1,700	3.5/(2)	FMC

Routine	Process	Size bytes	Loading/ Execution time - s.	Author

E - Exchange the X and Y registers.

O - Output the X and Y registers.

Hhhhh - Hexadecimal to F.P. conversion.

Ddddd - Decimal input to hexadecimal conversion.

P - Exit to PIKKY (4003H).

F - Exit to FDOS (4000H).

M - Exit to monitor.

APPENDIX C3

Image Processing Examples

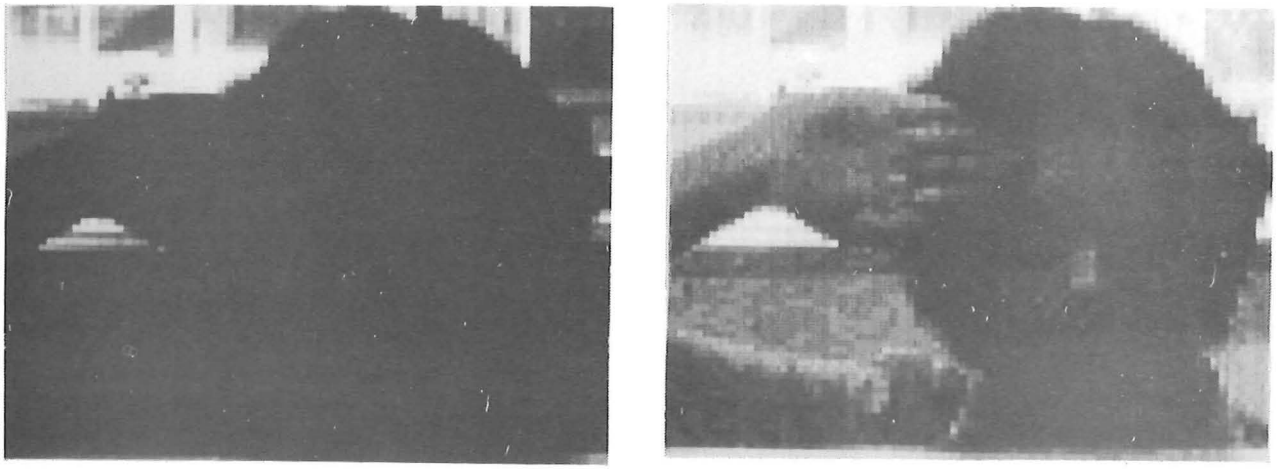

Figure C3-1 Histogram equalization.

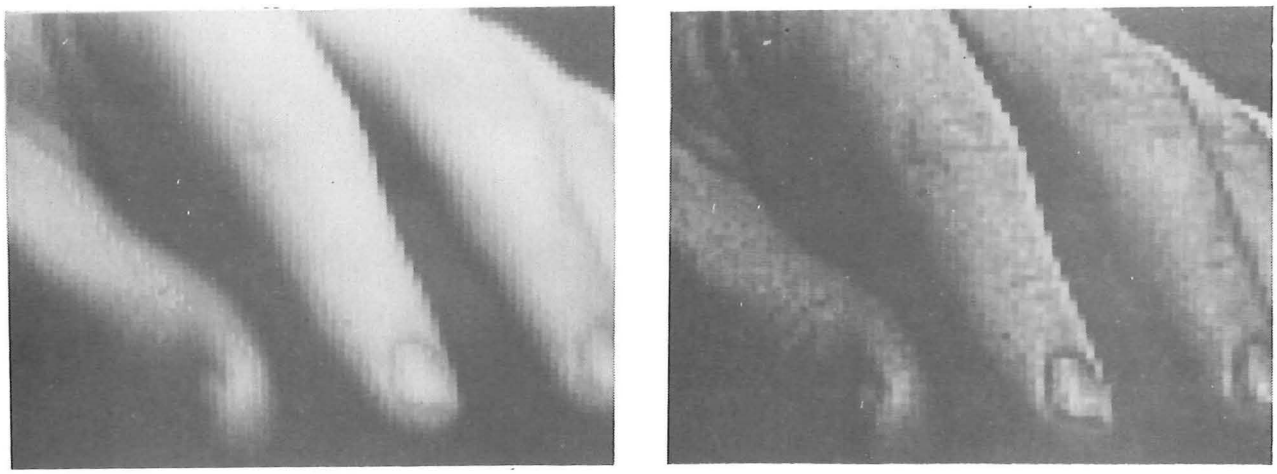

Figure C3-2 Edge enhancement.

C3. Line printer picture output.

Figure C3-3 Line printer picture output.

APPENDIX D

D1. Structure diagram for shift and add

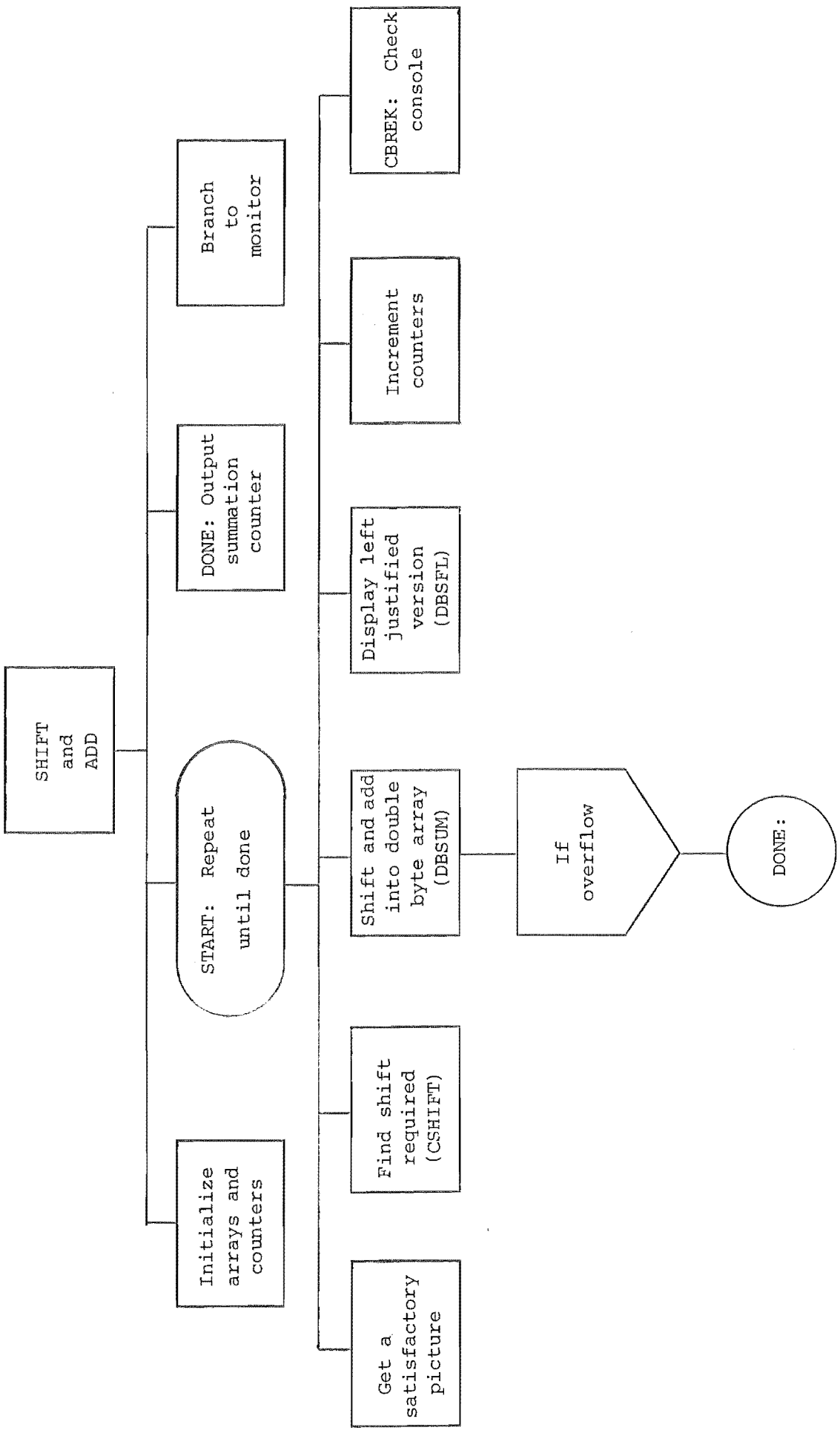

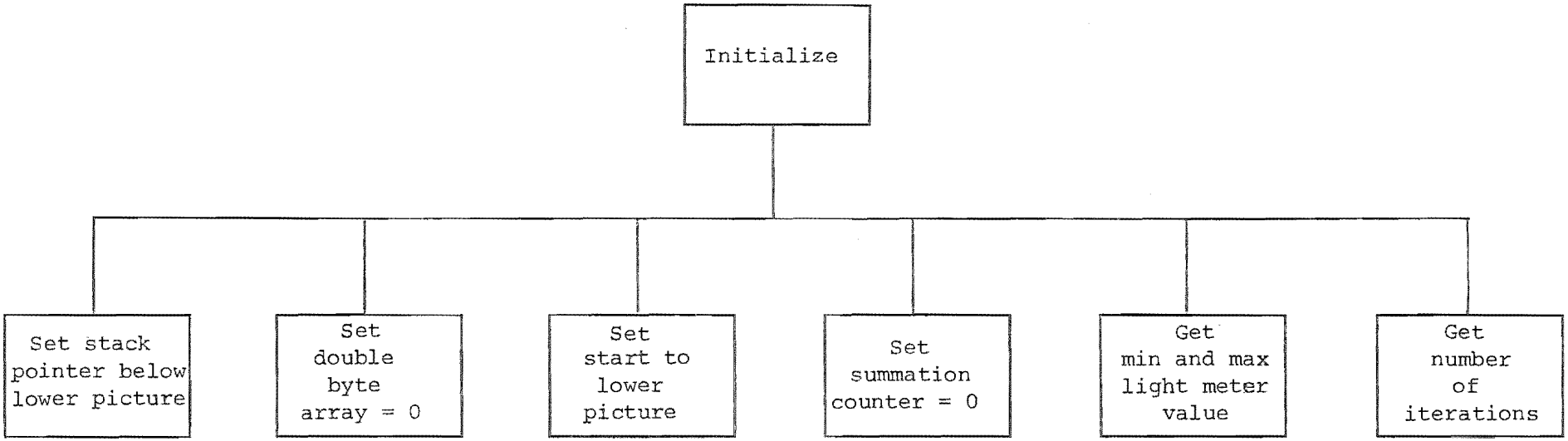
Initialize
Set stack pointer below lower picture
Set double byte array = 0
Set start to lower picture
Set summation counter = 0
Get min and max light meter value
Get number of iterations

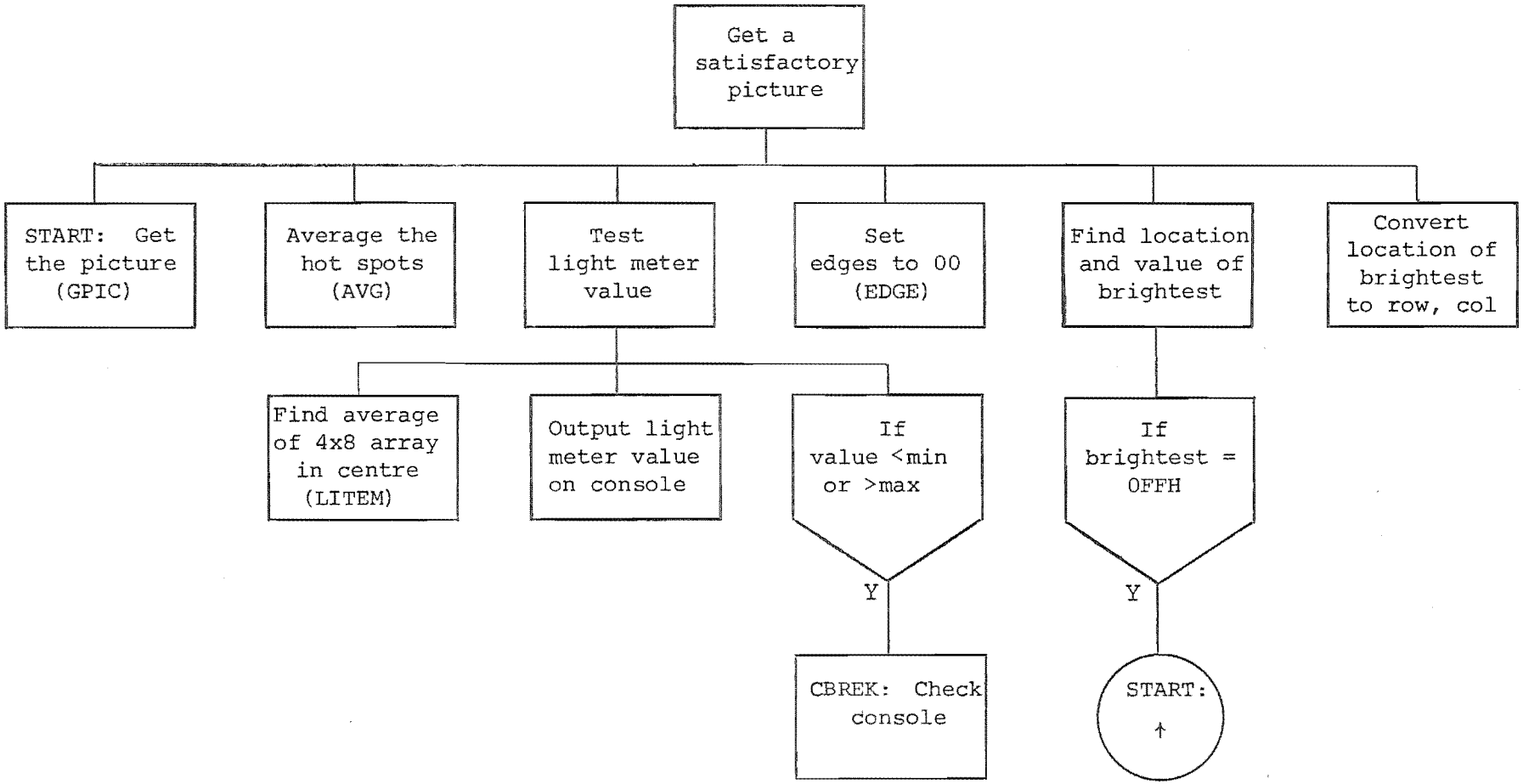
Get a satisfactory picture
START: Get the picture (GPIC)
Average the hot spots (AVG)
Test light meter value
Set edges to 00 (EDGE)
Find location and value of brightest
Convert location of brightest to row, col
Find average of 4x8 array in centre (LITEM)
Output light meter value on console
If value <min or >max
Y
CBREK: Check console
If brightest = OFFH
Y
START:

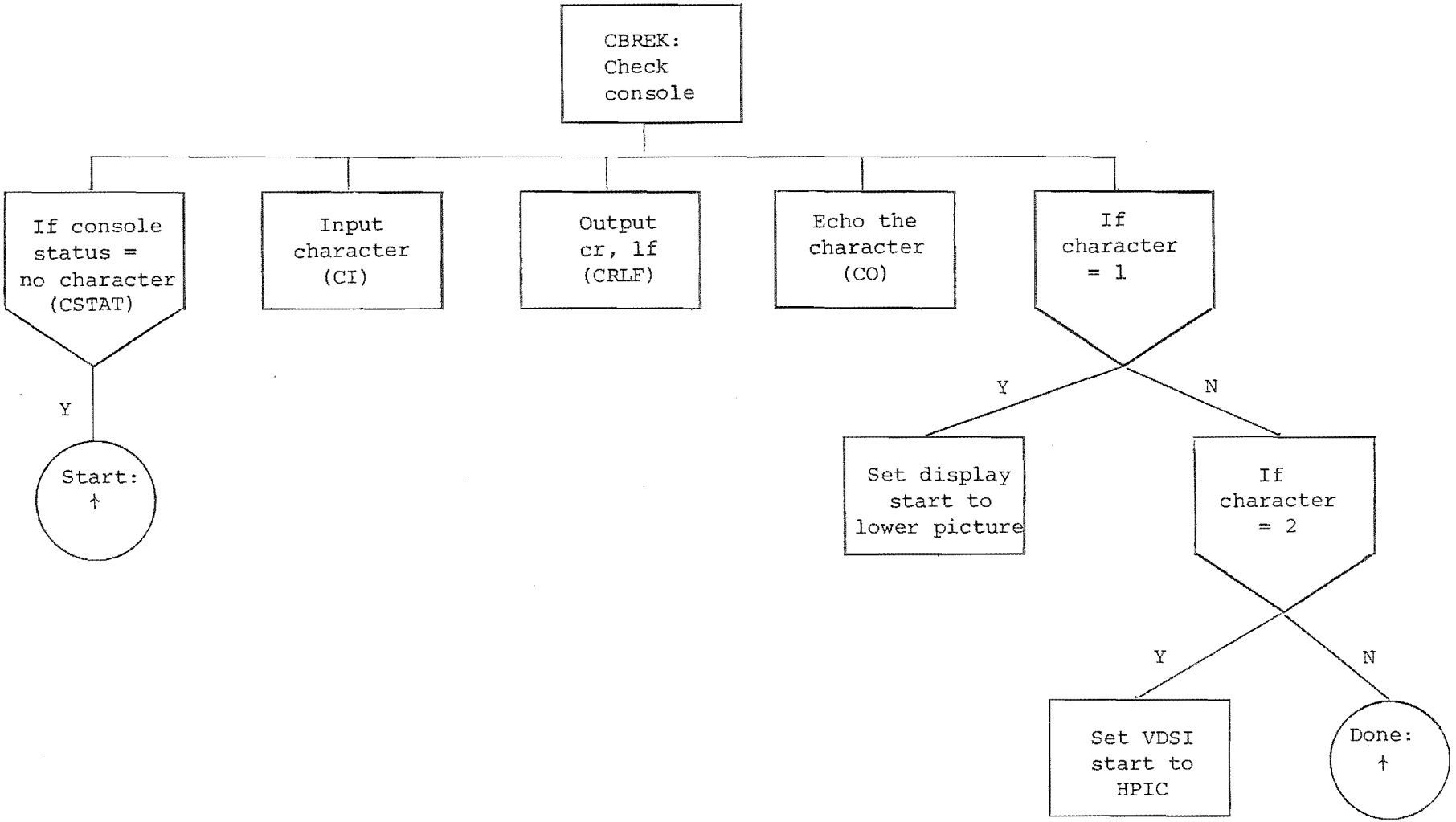
CBREK:
Check
console
If console
status =
no character
(CSTAT)
Y
Start:
Input
character
(CI)
Output
cr, lf
(CRLF)
Echo the
character
(CO)
If
character
= 1
Y
N
Set display
start to
lower picture
If
character
= 2
Y
N
Set VDSI
start to
HPIC
Done:

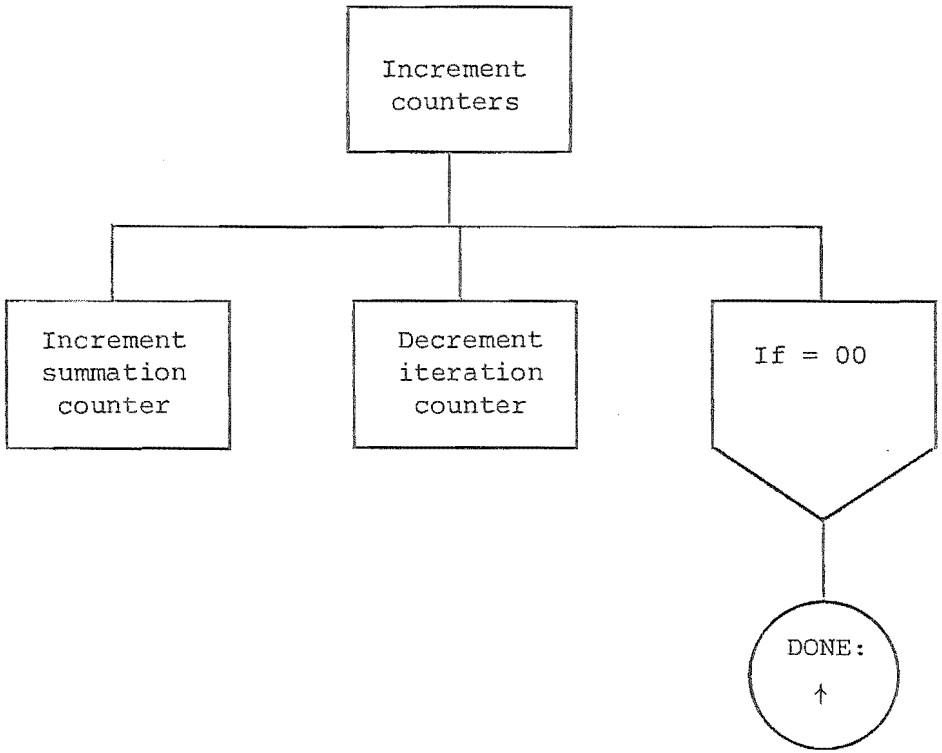
Increment counters
Increment summation counter
Decrement iteration counter
If = 00
DONE:

D2. Operating Shift and Add software

Program Execution

The program loads and executes starting at 100H. An automatic start address has been included allowing the program to be started either from PIKKY or FDOS by typing in the name.

Initialization Input

Valid speckle pictures are determined by calculating the average value in a 4x8 pixel array in the centre of the picture. This array is called the light meter. Speckle pictures are accepted only when this value is between a low and high limit input from the console at the start of the program.

In response to the message

SET LIGHT METER VALUES LOW, HIGH (HEX)

type in the low and high values required, in hexadecimal, separated by a space or comma and terminated by carriage return. The number of iterations to be performed is input, in hexadecimal, terminated by carriage return, in response to the message

SET ITERATION COUNTER (HEX).

If a non-hex character is typed, the program exits to the error routine in the monitor. To recover in this situation, type

G100

When the program is running, the light meter value for the current speckle picture is displayed in hexadecimal on the

console.

Picture Display

The current speckle picture is in buffer #1 and the shift and add in #2. Either display may be selected by typing 1 or 2 on the console at any time during processing. The display is switched at the end of the current iteration.

Program Termination

The program automatically terminates after the number of iterations specified at the beginning. It can be terminated at any time before this by typing any character other than 1 or 2. Whenever the program is terminated, the number of iterations completed is printed on the console in decimal.

Program Restart

After termination, the program can be restarted either at the beginning by typing

G100

or to continue in the loop from where it was interrupted by simply typing

G .

PIKKY or FDOS must be re-booted by typing

T .

D3. Operating instructions for CLEAN and ECLEN

CLEAN or ECLEN

CLEAN uses a single pixel as the clean beam which is added into the clean array. ECLEN uses a 3x3 pixel psf scaled

0.25	0.75	0.25
0.50	1.00	0.50
0.25	0.75	0.25

as the clean beam.

Program Execution

Both programs are PIKKY modules and are loaded and executed by typing the name. The three picture buffer storage areas must be initialized before entering the program.

Buffer Initialization

Buffer #1 must contain the dirty array to be cleaned. Buffer #2 contains the clean array and should be initialized to 0. Buffer #3 contains the psf to be subtracted from the dirty array.

Flashing Pixel Initialization

The flashing pixel must be positioned to the centre of the desired point to be cleaned in the dirty array. It may be left in the flashing mode when CLEAN is entered.

Program Operation

On execution, the message

FRACTION + OR -

is typed on the console. The desired fraction must be

preceded by either a + or - and followed by a carriage return, i.e.

- .3

The decimal value may contain up to 3 digits to the right of the decimal point. The psf in buffer #3 is scaled by the fraction and subtracted from (or added to if +) the dirty array. The scaled value in the centre is added to (or subtracted from) the clean array in the form of the clean beam. When this is complete, the flashing pixel is moved to the maximum value in the dirty array and set flashing. A return is then made to PIKKY.

D4. Operating Instructions for RATIO program

This program determines the ratio of intensities of two stars I_2/I_1.

Program Execution

RATIO is a PIKKY module and is loaded and executed by typing the name.

Initialization

The centres of the two stars are selected by the flashing pixel movement keys. In response to the message

POSITION TO FIRST PIXEL

move the flashing pixel to the centre of the star intensity I_1 and type <ESC>(escape). Position to the star intensity I_2 and type <ESC> after the message

NOW THE SECOND

The centre of the star does not have to be accurately located because the ratio calculation will automatically centre on the maximum value within a 5x5 pixel array centred on the location specified by the action given above.

Ratio Calculation

The two star intensities are output in hexadecimal on the console. Two ratios are also calculated and output. The first is the ratio of the two maxima I_{25}/I_{15} and the second is the ratio

$$R_I = \frac{\sum_{n=1}^{9} I_{2n}}{\sum_{m=1}^{9} I_{1m}} .$$

The format of the output is

$$I_{21}\ I_{22}\ I_{23} \quad I_{11}\ I_{12}\ I_{13}$$
$$I_{24}\ I_{25}\ I_{26} \quad I_{14}\ I_{15}\ I_{16} \quad I_{25}/I_{15} \quad \Sigma I_{2n}/\Sigma I_{1m}$$
$$I_{27}\ I_{28}\ I_{29} \quad I_{17}\ I_{18}\ I_{19}$$

Program Termination

The program returns to PIKKY when through.

APPENDIX E

Experimental Conditions for Results Given in Chapter 6

Figure	Disk file	Light source*	Telescope aperture (mm)	Shift and add light meter limits	Number of iterations
6.1a	O19M3	L	2.75	-	-
6.1c	S19M1	L	2.75	16 - 160	128
6.2a	P28F1	L	2.75	26 - 160	128
6.2c	O19M3	L	2.75	-	-
6.4a	S07M5	L	2.75	32 - 160	128
6.6a	O07D1	L	17.5	-	-
6.6b	L04D1	L	17.5	-	-
6.6c	W04D1	W	17.5	-	-
6.6d	S07D1	L	17.5	26 - 80	442
6.6e	S10D1	W	17.5	21 - 53	1054
6.6g	P29N1	L	17.5	32 - 255	212
	P06D1	W	17.5	26 - 80	919
6.7a	O21F1	L	9.5	-	-
6.7b	O21F3	L	9.5	-	-
6.7c	S21F4	L	9.5	26 - 144	128
6.8	S27F4	W	9.5	37 - 208	128
6.9a	E16M1	L	2.75	-	-
6.9b	S16M1	L	2.75	16 - 160	128
6.9d	S16M2	L	2.75	16 - 160	128
6.11a	S19M1	L	2.75	16 - 160	128
6.12a	E16M1	L	2.75	-	-
6.12b	S16M1	L	2.75	16 - 160	128
6.13a	O05A1	L	multiple	-	-
6.13b	S05A1	L	multiple	16 - 160	128
6.13c	P05A1	L	multiple	16 - 160	128

* L = Laser source

W = Wide band source.

APPENDIX F

Experimental Calculations

F1. Calculation of bandwidth for speckle imaging as in equation (4.1-3).

Consider the field of view θ at the aperture of diameter D.

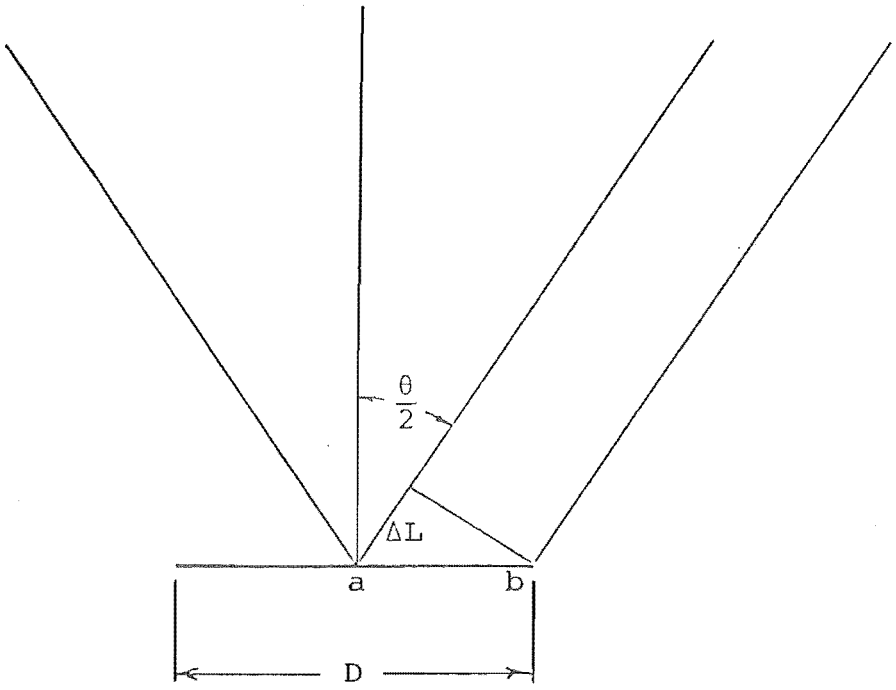

Figure F1.1 Field of view at aperture of diameter D.

The difference in path length for the two rays at (a) and (b) is

$$\Delta L = \frac{D}{2} \sin \frac{\theta}{2} \approx \frac{D\theta}{4} \qquad \text{(F1-1)}$$

To maintain coherence, ΔL must be much less than the coherence length L_c of the radiation, given by

$$\Delta L << L_c = \frac{\bar{\lambda}^2}{\Delta\lambda} \qquad \text{(F1-2)}$$

where $\bar{\lambda}$ is the midband wavelength and $\Delta\lambda$ is the bandwidth. Therefore

$$\frac{D\theta}{4} << \frac{\bar{\lambda}^2}{\Delta\lambda} \qquad \text{(F1-3)}$$

and

$$\frac{\Delta\lambda}{\bar{\lambda}} << \frac{4\bar{\lambda}}{D\theta} \qquad \text{(F1-4)}$$

For a field of view equal to a seeing disk of θ = 1 arc-second, with an aperture diameter of D = 5m, and a midband wavelength $\bar{\lambda}$ = 500 nm,

$$\frac{\Delta\lambda}{\bar{\lambda}} << 8.25 \times 10^{-2}$$

This value is nearly an order of magnitude smaller than that normally used in Speckle Interferometry (§4.1.1b). It indicates that even though coherence is probably not maintained across the entire seeing disk, useful results can be obtained from Speckle Interferometry. The reason for this is that the angular dimensions of objects for which speckle interferometry has been used are generally an additional order of magnitude smaller.

F2. Calculation of the relative intensities of two stars under perfect seeing conditions

The stars are imaged through a 1.75 mm diameter aperture without the simulated atmosphere, and thirty-two iterations of the shift and add process are performed.

The CCD camera is moved slightly between each iteration to reduce the effects of fixed pattern noise in the CCD. A typical print-out of the intensities of the brightest and next brightest star are shown in Figure F2.1. The relative intensity ratio is found by calculating the ratio of the sums of the nine pixels around and including the brightest in each star (equation 5.2-5). The pixels that are used in this example are shown inside the boxes in Figure F2.1

$$R_I = \frac{140 + 163 + \ldots 153 + 131}{38 + 44 + \ldots 46 + 39} = \frac{1385}{375} = 3.69$$

```
R050  C050
077 128 150 128 076
086 140 163 139 085
102 166 195 167 102
080 131 153 131 079
066 111 131 111 066

R050  C041
018 029 033 028 019
024 038 044 037 025
026 042 048 041 028
025 040 046 039 026
019 031 036 030 021
```

Figure F2.1 Intensities of two stars imaged under perfect seeing conditions.

F3. Calculation of the relative intensities of two stars after shift and add processing

The relative intensities are calculated as shown in Appendix F2 and equation (5.2-5) except that the average background level is first subtracted from each of the nine pixel values in the summation. The average background level L_b is found as shown in §5.2.3. Figure F3.1 shows typical intensity values for two stars after the shift and add process. The average of eight corner values shown enclosed in dotted lines are used to calculate L_b.

$$L_{b1} = \frac{50 + 53 + \ldots 49 + 47}{8} = 50.88$$

$$L_{b2} = \frac{45 + 53 + \ldots 49 + 49}{8} = 49.5$$

These values are subtracted from each of the nine pixel values that are used to calculate the relative intensity.

$$R_I = \frac{89 - 50.88 + 119 - 50.88 + \ldots}{57 - 49.5 + 63 - 49.5 + \ldots} = \frac{499.1}{117.5} = 4.24$$

R050 C050

050	064	078	062	053
053	089	119	085	053
056	110	155	108	054
052	089	119	085	050
049	064	077	059	047

R050 C041

045	050	054	052	053
049	057	063	058	051
051	065	076	061	050
051	060	068	057	049
049	051	055	051	049

Figure F3.1 Intensities of two stars after shift and add processing.

F4. Calculation of contrast

The contrast for a star pattern is found by equation (1.2-10) which gives

$$C_m = \frac{|L_t - L_b|}{L_t + L_b} \qquad \text{(F4-1)}$$

where L_b is found as shown in Appendix F3 and §5.2.3, and L_t is simply the maximum value in the star pattern. For example, the contrast for star number 1 in Appendix F3 is

$$C_m = \frac{155 - 50.88}{155 + 50.88} = 0.51$$

F5. Calculation of the defocus width of the stars for Figure 6.7

To determine the relative spreading of the shift and add image when the telescope was defocussed, the background value L_b, as calculated in Appendix F3, was subtracted from each pixel in a column through the centre of the star image. These pixels are shown in the boxes in Figure F5.1. The pixel intensities were then normalised to the maximum value in each star and plotted as a function of row number as shown in Figure F5.2 for the cases of an in-focus telescope and for one suffering from 19λ defocus. The ratio of widths B/A for the arbitrarily chosen 40% level was taken as the measure of relative spreading caused by the defocus aberration.

R049 C050

062	060	062	061	060
060	065	067	062	059
062	064	085	064	055
060	073	177	067	060
056	061	076	059	059
059	058	057	064	058
065	060	064	061	058

R048 C050

061	061	057	060	061
060	061	066	064	063
059	060	077	069	061
063	062	106	073	062
068	070	142	073	063
064	068	102	064	062
064	063	072	062	063
060	063	063	060	066

Figure F5.1 In-focus shift and add image (upper) and 19λ defocussed image.

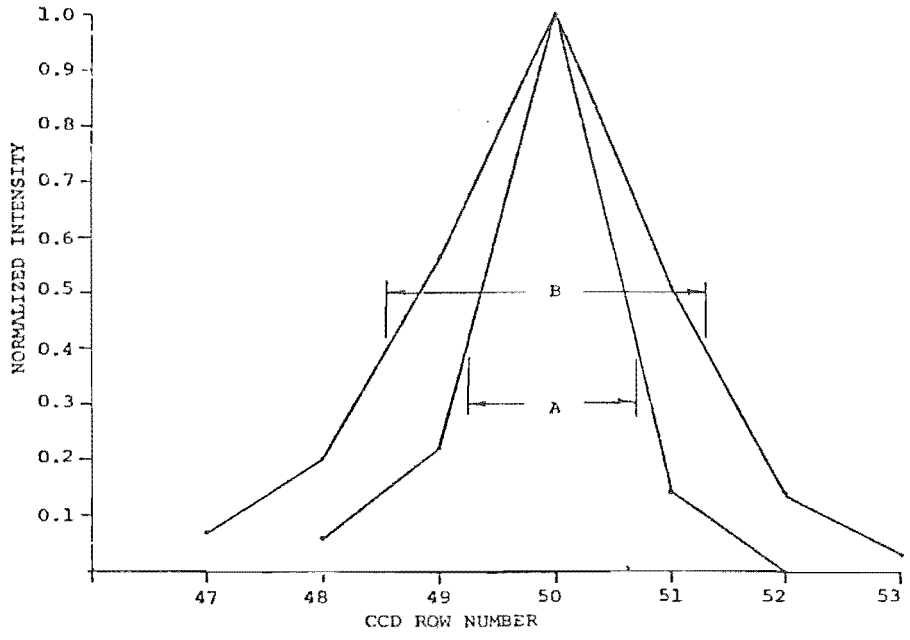

Figure F5.2 Relative intensities in a column through the centre of the star image.

APPENDIX G

Student Projects

A number of student projects have contributed greatly to the development of the University of Canterbury Image Processing System. Their efforts are acknowledged.

1977

A.J. Ireland	A Solid State Fast Area Digitizing Scanner
P.A. Blackburn	Cooling a Charge Coupled Device by a Peltier Effect Cooling Device
M.A. Voss	Image Processing Componentry
N. Wensley	Control Terminal for an Imaging System

1978

G.A. Duncan	Sensor Evaluation and the Design of a Display for an Image Processing System
D. Pairman	Hardware and Software Development for an Image Processing System
M.A. Aitchison	A Visual Display Terminal and Serial Data Interface for an Image Processing Microcomputer

1979

J.K.N. Murphy	Solid State Arrays for Remote Sensing
S.J. Camping and M.A. Savory	Multiplexing a Line Printer to Several Micro-Development Systems
R.A. Cree	A Dual Port Memory System
J. Leonard	A Graphics Input Device for an Image Processing System
S.J. Wilson	Reticon Linear Diode Array Investigation
G. Wong	TRACE, A Software Debugging Package

1980

D. Pairman	Hardware and Software Developments for an Airborne Multispectral Scanning System